

Preparation of polyelectrolyte-coated proteins for controlled drug delivery via supercritical fluid processing

Yu, Miao

DOI

[10.4233/uuid:aa2a287e-e55f-4af5-be23-f0bdb7188512](https://doi.org/10.4233/uuid:aa2a287e-e55f-4af5-be23-f0bdb7188512)

Publication date

2019

Document Version

Final published version

Citation (APA)

Yu, M. (2019). *Preparation of polyelectrolyte-coated proteins for controlled drug delivery via supercritical fluid processing*. [Dissertation (TU Delft), Delft University of Technology].
<https://doi.org/10.4233/uuid:aa2a287e-e55f-4af5-be23-f0bdb7188512>

Important note

To cite this publication, please use the final published version (if applicable).
Please check the document version above.

Copyright

Other than for strictly personal use, it is not permitted to download, forward or distribute the text or part of it, without the consent of the author(s) and/or copyright holder(s), unless the work is under an open content license such as Creative Commons.

Takedown policy

Please contact us and provide details if you believe this document breaches copyrights.
We will remove access to the work immediately and investigate your claim.

**Preparation of polyelectrolyte-coated proteins for
controlled drug delivery via supercritical fluid processing**

Miao YU

ISBN 9789463237017

Printed in the Netherlands by Gildeprint

Copyright © 2019 by M. Yu

All rights reserved. No part of the material protected by this copyright notice may be reproduced or utilized in any form or by any means, electronic or mechanical, including photocopying, recording or by any information storage and retrieval system, without the prior permission of the author.

Preparation of polyelectrolyte-coated proteins for controlled drug delivery via supercritical fluid processing

Dissertation

for the purpose of obtaining the degree of doctor

at Delft University of Technology

by the authority of the Rector Magnificus, Prof.dr.ir. T.H.J.J. van der Hagen,

chair of the Board for Doctorates

to be defended publicly on

13 June 2019 at 12:30 o'clock

By

Miao YU

Master of Science in Environmental Sciences, Wageningen University, the Netherlands

born in Qufu, China

This dissertation has been approved by the promotor:

Prof. dr. G. J. Witkamp

Prof. dr. W. Jiskoot

Composition of the doctoral committee:

Rector Magnificus

Chairperson

Prof. dr. G. J. Witkamp

Delft University of Technology

King Abdullah University of Science and Technology, promotor

Prof. dr. W. Jiskoot

Leiden University, promotor

Independent members:

Prof. dr. ir. W. E. Hennink

Utrecht University

Prof. dr. ir. A. B. de Haan

Delft University of Technology

Prof. dr. R. Verpoorte

Leiden University

Prof. dr. ir. H. J. Noorman

Delft University of Technology

Other member:

Prof. dr. W. Buijs

Delft University of Technology

The picture used in the design of the cover page is adapted from Figure 1 of an open access paper "Insua, I., A. Wilkinson, and F. Fernandez-Trillo, Polyion complex (PIC) particles: Preparation and biomedical applications. *European polymer journal*, 2016. 81: p. 198-215. © 2016 The Authors. Published by Elsevier Ltd. <https://doi.org/10.1016/j.eurpolymj.2016.06.003>" under a Creative Commons Attribution License (CC BY) <https://creativecommons.org/licenses/by/4.0/>.

To my parents

This work was supported by the Dutch Technology Foundation STW (now the Netherlands Organisation for Scientific Research (NWO) Domain Applied and Engineering Sciences (TTW)) [project number 12144], which is partly funded by the Ministry of Economic Affairs.

Contents

Summary	1
Samenvatting.....	4
<i>Chapter 1: Introduction</i>	<i>7</i>
<i>Chapter 2: Towards the development of a supercritical carbon dioxide spray process to coat solid protein particles.....</i>	<i>21</i>
<i>Chapter 3: Molecular structure of dextran sulphate sodium in aqueous environment.....</i>	<i>49</i>
<i>Chapter 4: Molecular modelling of the interactions between lysozyme and dextran sulphate sodium.....</i>	<i>79</i>
<i>Chapter 5: Brownian dynamics simulation of protein-polyelectrolyte particle formation and growth</i>	<i>97</i>
<i>Chapter 6: The investigation of protein diffusion via H-cell microfluidics</i>	<i>123</i>
<i>Chapter 7: The measurement of polyelectrolyte diffusion coefficient via H-cell microfluidics</i>	<i>163</i>
<i>Chapter 8: FlowDensi: a user-friendly Matlab-based toolkit for the density calculation of microparticles analysed by FlowCam®.....</i>	<i>177</i>
<i>Chapter 9: Conclusions and outlook.....</i>	<i>199</i>
<i>Appendix A: Supplementary material for Chapter 2</i>	<i>207</i>
<i>Appendix B: Introduction to molecular modelling</i>	<i>215</i>
<i>Appendix C: Supplementary material for Chapter 5</i>	<i>229</i>
<i>Appendix D: Supplementary material for Chapter 6</i>	<i>239</i>
<i>Appendix E: Supplementary material for Chapter 8.....</i>	<i>247</i>
Acknowledgement	252
List of publications	254
Curriculum Vitae	256

Summary

During the past few decades, numerous protein-based pharmaceuticals to treat chronic and life-threatening diseases have emerged. The short plasma half-life of therapeutic proteins requests frequent administration, usually via parenteral routes. This short-coming is proposed to be solved by the development of an injectable microparticulate drug delivery system (DDS) where the proteins are encapsulated to control the release of the drugs after administration. One way of preparing a protein DDS is through the interaction of proteins and biocompatible coating materials, where the coating materials hinder the quick degradation and release of the proteins.

Conventional encapsulation processes use non-polar polymers such as poly(lactic-co-glycolic acid) (PLGA) as the drug carrier material, but their acid degradants are harmful to the proteins. Moreover, the process of encapsulation requires the use of non-polar organic solvents for the dissolution of the polymers, and freeze-drying or thermal evaporation for particle production, during which the proteins are exposed to interfacial and thermal stress. As an alternative to the conventional coating materials, biocompatible, hydrophilic polyelectrolytes exhibiting complexation with the amphoteric proteins are being investigated. Supercritical fluid processes, typically employing supercritical carbon dioxide (scCO₂), are more suitable for producing formulated protein particles than the conventional methods because of the mild operating conditions.

Only a few studies have been reported on the encapsulation of proteins with polyelectrolytes via the scCO₂ processes. Also, protein-polyelectrolyte interactions on the molecular level and the resulting agglomeration profiles, have been only scarcely investigated. This thesis mainly addresses two targets: protein encapsulation with polyelectrolytes for the purpose of controlled release; and the understanding of the protein-polyelectrolyte interactions and agglomeration. This project was jointly conducted with Ahmad S. Sediq from Leiden University in the framework of an STW project (grant number 12144).

In chapter 2 of this thesis, a scCO₂ spray coating process to coat solid lysozyme particles with dextran sulphate sodium (DSS) as the coating material is presented. The processing schemes and conditions, together with the product morphology, properties and protein release profiles are included. Agglomerated microparticles were produced during the spray coating process. The humidity level in the spray coating vessel had a significant effect on the coating of the solid lysozyme particles. It was demonstrated that the obtained profile of particle release is in correlation with the humidity level in the spray coating vessel. The higher the humidity level to which the lysozyme particles were exposed

during the spray coating process, the more prolonged was the release of the lysozyme from the product particles.

To better understand the behaviours of the protein and polyelectrolyte during their interactions, investigations on the molecular morphology of DSS in an aqueous environment and its interaction with lysozyme are described in chapters 3 and 4. It was found that the DSS has a helix structure in the aqueous environment with a di-sulphate sodium group in each polymerisation unit. Three types of interactions were considered when examining the interactions of DSS with proteins in the aqueous environment: electrostatic interaction; aqueous solvation of the molecules; and steric interactions between the macromolecules. Preliminary results on the reaction energy and the interacted molecular geometry are described.

Chapter 5 describes how a Brownian dynamics method was applied to simulate mathematically the protein-polyelectrolyte particle formation and growth. The simulation was based on an extension of the classical Smoluchowski model. The simulation results on the evolution of the particle size distribution as a function of time are reported. It was found that the average ratio of protein to polyelectrolyte in the formed complexes at the early stage after their mixing is equal to their initial ratio in the system. The comparability of the simulated evolution of particle concentration with experimental observation is discussed. A Monte Carlo method was proposed to simulate the particle agglomeration behaviour by tracking the displacement of the particles in the simulation domain. Another idea proposed to simulate particle agglomeration was based on calculating the inter-particle collision probability.

The dynamics of protein-polyelectrolyte interactions are closely associated with their diffusion behaviour. Chapters 6 and 7 present the determination of the diffusivity of protein and polyelectrolyte using a microfluidics H-cell equipment. The measured diffusion coefficients of the proteins were comparable with those obtained using other (commercially) available techniques reported in the literature. For the model protein (lysozyme in this study), the measured diffusion coefficient decreased with the medium ionic strength and viscosity. At a pH below the pI (isoelectric point) and low ionic strength, the measured diffusion coefficient for lysozyme increased with the inlet concentration gradient between the two streams flowing into the H-cell. The H-cell was also preliminarily applied to determine the diffusion coefficients of polyelectrolytes (chapter 7), in which the DSS (MW 5000 Da) was used as the model polymer. The factors affecting protein diffusion were found to have similar effects on the diffusion of polyelectrolyte.

There has been a method developed to acquire the information on the properties of microparticles such as density and porosity by using flow imaging microscopy (FlowCAM®). The particles settling

down in a stationary liquid medium with a known density can be described by the classical Stokes' law. Based on tracking the particles' displacement and acquiring their velocity, the density of the particles can be calculated. To assist in the analysis of the data exported by FlowCAM®, a Matlab-based toolkit was developed, which is presented in chapter 8. It was demonstrated that this toolkit functions to calculate the particle density based on the particle trajectory in a stationary liquid medium recorded by FlowCAM®.

The scCO₂ spray coating process developed in this study was shown to be a promising alternative to conventional encapsulation processes for proteins. The coating of protein by polyelectrolyte via electrostatic interaction is a competitive strategy to conventional ones using non-polar coating materials. The spray coating mode avoids the dissolution of the protein core particles during the coating process. Moreover, the scCO₂ can work as a drying medium for the production of coated protein particles. The product design of the protein DDS and the process optimisation is aided by information on the molecular behaviour of the protein-polyelectrolyte interaction and their agglomeration profiles. The properties of the encapsulated particles may be examined via flow imaging microscopy techniques, and the data analysis can be assisted by the computation toolkit developed in this study.

Samenvatting

De afgelopen decennia is er een groot aantal op eiwit gebaseerde farmaceutische producten verschenen voor de behandeling van chronische en levensbedreigende aandoeningen. Vanwege de korte plasmahalfwaardetijd van therapeutische eiwitten is veelvuldige toediening noodzakelijk, meestal parenteraal. Deze tekortkoming zou worden verholpen door de ontwikkeling van een geneesmiddelaafgiftesysteem (*drug delivery system*, DDS) met injecteerbare microdeeltjes waarin de eiwitten zijn ingekapseld om de afgifte van de geneesmiddelen na toediening te reguleren. Een van de manieren om een afgiftesysteem voor eiwitten voor te bereiden is door gebruik te maken van de interactie van eiwitten en biocompatibele coatingmaterialen, waarbij de coatingmaterialen het snelle uiteenvallen en de afgifte van de eiwitten belemmeren.

Conventionele inkapselingsprocessen maken gebruik van niet-polaire polymeren als poly(lactideco-glycolide) (PLGA) als drager voor het geneesmiddel. De zure afbraakproducten zijn echter schadelijk voor de eiwitten. Bovendien moeten voor de desintegratie van de polymeren bij het inkapselingsproces niet-polaire organische oplosmiddelen worden gebruikt en is vriesdrogen of thermische verdamping nodig om deeltjes te produceren, waardoor eiwitten worden blootgesteld aan grensvlakspanning en thermische spanning. Als alternatief voor de conventionele coatingmaterialen worden biocompatibele, hydrofiële polyelektrolyten onderzocht die complexvorming met de amfoterische eiwitten vertonen. Processen met superkritische medium, waarbij doorgaans superkritische koolstofdioxide ($scCO_2$) wordt gebruikt, zijn vanwege de milde bedrijfsomstandigheden geschikter voor de productie van samengestelde eiwitdeeltjes dan de conventionele methodes.

Er zijn slechts enkele onderzoeken gemeld naar de inkapseling van eiwitten met polyelektrolyten via processen waarbij gebruik wordt gemaakt van $scCO_2$. Daarnaast zijn ook interacties op moleculair niveau tussen eiwitten en polyelektrolyten en de resulterende profielen voor agglomeratie slechts mondjesmaat onderzocht. Dit proefschrift richt zich voornamelijk op twee hoofddoelen: inkapseling van eiwitten met polyelektrolyten ten behoeve van gereguleerde afgifte en inzicht in de interacties tussen eiwitten en polyelektrolyten en de agglomeratie ervan. Dit project werd uitgevoerd in samenwerking met Ahmad S. Sediq van de Universiteit Leiden in het kader van een STW-project (subsidienummer 12144).

In hoofdstuk 2 van dit proefschrift wordt een $scCO_2$ -sprayproces gepresenteerd voor de coating van vaste lysozymdeeltjes met natriumdextraansulfaat (*dextran sulphate sodium*, DSS) als coatingmateriaal. Ook de processchema's en -omstandigheden worden vermeld, evenals de morfologie, eigenschappen en eiwitafgifteprofielen van het product. Tijdens het proces van

spraycoating werden geagglomerende microdeeltjes geproduceerd. De vochtigheidsgraad in de tank waarin de spraycoating werd uitgevoerd, had een aanzienlijk effect op de coating van de vaste lysozymdeeltjes. Aangetoond werd dat het verkregen profiel van deeltjesafgifte samenhangt met de vochtigheidsgraad in de coatingtank. Hoe hoger de vochtigheidsgraad waaraan de lysozymdeeltjes waren blootgesteld tijdens de spraycoating, hoe langer de afgifte van lysozymen uit de productdeeltjes aanhield.

Voor een beter inzicht in het gedrag van eiwitten en polyelektrolyten tijdens hun interacties, wordt het onderzoek naar de moleculaire morfologie van DSS in waterig milieu en de interactie met lysozymen beschreven in hoofdstuk 3 en 4. Het bleek dat DSS in het waterige milieu een helixstructuur heeft met een natriumdisulfaatgroep in elke polymerisatie-eenheid. Bij onderzoek van de interacties van DSS met aminozuren en peptiden in het waterige milieu werden drie typen interacties bestudeerd: elektrostatische interactie, waterige solvatatie van de moleculen en sterische interacties tussen de macromoleculen. Voorlopige uitkomsten voor de reactie-energie en de geïnteracteerde moleculaire geometrie worden beschreven.

Hoofdstuk 5 beschrijft hoe Brownse dynamiek werd toegepast om mathematisch de vorming en groei van eiwit-polyelektrolytcomplexen te simuleren. De simulatie was gebaseerd op een uitbreiding van het klassieke Smoluchowski-model. Er wordt verslag uitgebracht van de simulatie-uitkomsten voor de ontwikkeling van de deeltjesgrootteverdeling in functie van de tijd. De gemiddelde verhouding van eiwitten en polyelektrolyten in de gevormde complexen in de eerste fase na het mengen van de twee materialen bleek gelijk te zijn aan de initiële verhouding in het systeem. Besproken wordt in hoeverre de experimentele waarneming vergelijkbaar is met de gesimuleerde ontwikkeling van de deeltjesconcentratie. De Monte Carlo-methode werd voorgesteld om het agglomeratiegedrag van de deeltjes te simuleren door de verplaatsing van de deeltjes in het simulatiedomein te volgen. Een ander idee dat als doel had de vorming van deeltjesagglomeratie te simuleren, was gebaseerd op het berekenen van de kans dat deeltjes onderling zouden botsen.

De dynamiek van interacties tussen eiwitten en polyelektrolyten hangt nauw samen met hun diffusiegedrag. Hoofdstuk 6 en 7 presenteren de bepaling van de diffusiviteit van eiwitten en polyelektrolyten met behulp van een microfluidische H-cel. De gemeten diffusiecoëfficiënten van de eiwitten waren vergelijkbaar met de uitkomsten verkregen met commercieel beschikbare technieken. Voor het model eiwit (in dit onderzoek lysozym) nam de gemeten diffusiecoëfficiënt af met de ionsterkte en viscositeit van het medium. Bij een pH onder het pI (iso-elektrisch punt) en een lage ionsterkte nam de diffusiecoëfficiënt voor lysozymen toe met de verschil in concentratie bij de inlaat tussen de twee stromen de H-cel in. De H-cel werd daarnaast preliminair toegepast voor het bepalen

van de diffusiecoëfficiënten van polyelektrolyten (hoofdstuk 7), waar DSS (MW 5000 Da) werd gebruikt als model-polyelektrolyt. De bij de polyelektrolyten waargenomen effecten van de onderzochte factoren waren vergelijkbaar met die bij de eiwitdiffusie.

Er is een methode ontwikkeld om de informatie over de eigenschappen van de microdeeltjes te verkrijgen met behulp van flow imaging microscopy (FlowCAM®), waarmee de dichtheid en porositeit van deeltjes wordt bepaald. De deeltjes die bezinken in een stationair vloeibaar medium met een bekende dichtheid, kunnen worden beschreven aan de hand van de klassieke wet van Stokes. Door de verplaatsing van de deeltjes te volgen en de sedimentatiesnelheid te meten, kan de dichtheid van de deeltjes worden berekend. Om te helpen bij de analyse van de met FlowCAM® gegenereerde gegevens werd een toolkit gebaseerd op Matlab ontwikkeld. Deze toolkit wordt in hoofdstuk 8 gepresenteerd. Aangetoond werd dat met de toolkit de deeltjesdichtheid kan worden berekend op basis van het deeltjestraject in een stationair medium zoals vastgelegd met FlowCAM®.

Het scCO₂-sprayproces dat in dit onderzoek werd ontwikkeld, bleek een veelbelovend alternatief voor conventionele inkapselingsprocessen voor eiwitten. De coating van een eiwit met een polyelektrolyt via elektrostatische interactie is een alternatieve strategie voor conventionele methoden die gebruikmaken van niet-polaire coatingmaterialen. Deze wijze van spraycoating voorkomt de desintegratie van de eiwitkern tijdens het coatingproces. Daarbij kan scCO₂ dienen als droogmedium voor de productie van gecoate eiwitdeeltjes. Het ontwerpen van het afgiftesysteem voor eiwitten en de procesoptimalisatie worden ondersteund door informatie over het moleculaire gedrag van de interactie tussen eiwit en polyelektrolyt en hun agglomeratieprofielen. De eigenschappen van de gecoate deeltjes kunnen worden onderzocht door middel van flow imaging microscopy-technieken, en de berekeningstool die in dit onderzoek werd ontwikkeld, kan helpen bij de data-analyse.

Chapter 1

Introduction

1.1 Development of controlled drug delivery systems for proteins

In the pharmaceutical industry, protein therapeutics have been successfully applied to treat chronic and life-threatening diseases owing to their high specificity and potency [1-6]. To enhance the applicability and efficacy of protein drugs while avoiding degradation in the human body, the development of controlled drug delivery systems (DDS) for therapeutic proteins is an attractive option. Controlled DDS help maintain the drug levels over a relatively long period, thus reducing the need for frequent administration and thereby potentially increasing patient compliance [7]. This is in contrast to traditional drug delivery systems where the drug level in the blood rises after each administration and then decreases until the next administration. The ideal drug delivery system should be inert, biocompatible, convenient for the patient, capable of achieving high drug loading, safe from accidental release, simple to administer and remove, and easy to fabricate and sterilise.

The encapsulation of protein drugs in an injectable microparticulate DDS has been studied previously [8-11]. However, it remains a challenge in practice to find a solution for the controlled delivery of proteins, and there are no commercial products yet available on the market [12-14]. One approach is to involve biocompatible and biodegradable polymers as a complexation or coating material to hinder the direct contact between protein and the bloodstream. This has been the focus of the STW project “Controlled release of protein pharmaceuticals from biodegradable, hydrophilic microcapsules produced by supercritical fluid processing”. The goal of this PhD research has been to investigate the DDS particle formation process in model systems by experiments and by modelling, and to produce coated particles via supercritical carbon dioxide processing.

1.2 Application of biocompatible polyelectrolytes for drug delivery systems

Polymers are widely used in controlled DDS development, as a means to stabilise drugs and modify the drug release characteristics. Non-polar polymers such as poly(lactic-co-glycolic) acid (PLGA) have been used as carriers to encapsulate proteins [15]. The advantage of using these degradable polymers is that they are broken down into biocompatible molecules that are metabolised and removed from the body via normal metabolic pathways. However, there are several drawbacks in using this type of polymers such as i) degradation of proteins (including therapeutic proteins) which come into contact with the polymer as a result of amide bond formation between carboxyl groups of the (degrading) polymer and primary amines of proteins [16]; ii) protein denaturation and aggregation due to the presence of water/organic solvent interfaces when encapsulating the proteins via the commonly-used

emulsion method [17-20]; and iii) protein instability due to the formation of acidic degradation by-products by polymer hydrolysis [21].

As a substitute for the aforementioned non-polar polymers, hydrophilic and biocompatible charged polymers, i.e. polyelectrolytes, have been investigated for protein encapsulation [22-24], but only a few studies have been reported. Polyelectrolytes offer specific benefits over non-polar polymers such as i) the coating process can be conducted in an aqueous environment, helping preserve the bioactivity of the fragile proteins; ii) easy incorporation of the protein via electrostatic interaction because of the charge on the polyelectrolyte and the amphotericity of the proteins; and iii) the potential to build up multi-layer coatings (layer-by-layer (LbL)) by means of alternating positively and negatively charged polyelectrolytes [22]. The coating of proteins by polyelectrolytes enables the control of the release behaviour by selecting appropriate polymers (based on criteria such as pKa, charge group and size) and modifying their interactions [22-24]. Based on these characteristics, it is promising to apply the polyelectrolyte in this project as the coating material for the development of controlled DDS for proteins.

1.3 Protein-polyelectrolyte interaction: mechanism on the molecular level and dynamics of particle formation

The interaction between proteins and oppositely-charged polyelectrolytes tends to cause particle formation and agglomeration. A schematic representation of protein-polyelectrolyte particle precipitation is shown in Figure 1.1. Protein-polyelectrolyte complexes result from the attraction (electrostatic, hydrogen bonding, hydrophobic interactions) between the protein and polyelectrolyte molecules [25, 26]. These complexes then quickly agglomerate to form particles varying in size from sub-micron to a few micrometres [27]. The final stage is the agglomeration of these particles into flocs.

The rate of protein-polyelectrolyte complex formation depends on the particle collision frequency and efficiency (ratio of the number of collisions leading to agglomeration to the total number of collisions). Smoluchowski's theory [28] has been employed to calculate nanoparticle collision frequencies and agglomeration rates. The collision efficiency, however, is more difficult to predict due to the complicated interactions between the particles [29]. Charge neutralisation and polymer bridging affect the collision efficiency between protein and polyelectrolyte. The former is a result of the electrostatic interaction between protein and polyelectrolyte and the gradual domination of van der Waals attraction among the complexes due to the alleviation of electrostatic forces. In the case of

polymer bridging, extended chains of polyelectrolyte adsorbed on the surface of one particle may interact with and adsorb to the surface of another particle.

The successful design of protein-polyelectrolyte DDS product or the production processes relies on understanding the mechanism and dynamics of the macromolecular interactions and complexation, which can be investigated via molecular modelling and Brownian dynamics simulations. The former encompasses theoretical and computational methods to model or mimic the behaviour of molecular systems, ranging from small chemical systems to large biological molecules and material assemblies. By using molecular mechanics or quantum mechanics methods, the morphologies and thermodynamic behaviours of the macromolecules (protein and polyelectrolyte), their complexes at an early stage or even the later agglomerated particles can be predicted. Based on Smoluchowski's theory, the Brownian dynamics simulation is used to describe the collision and agglomeration of molecules or particles following stochastic Brownian motion.

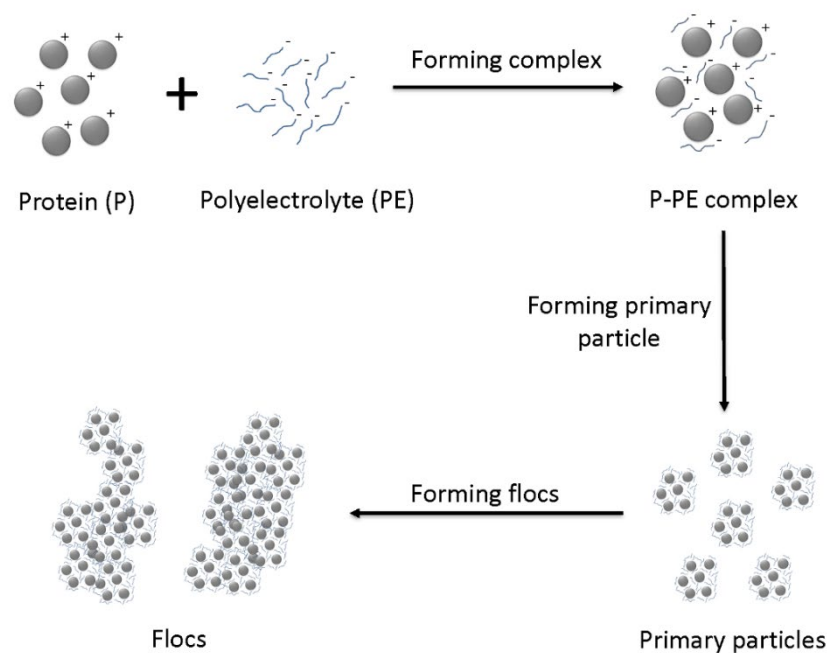


Figure 1.1. Schematic diagram of protein-polyelectrolyte particle formation and growth into flocs (adapted from [26, 30]).

1.4 Supercritical fluid technology: a green alternative to process pharmaceutical proteins

Encapsulation using non-polar polymer materials usually involves emulsion-based methods [15, 31] where an aqueous solution containing the protein is introduced into a non-polar polymer dissolved in an organic solvent. Such encapsulation processes exert interfacial stresses on the labile protein materials that can cause their denaturation. Moreover, organic solvents are costly and harmful to the environment [32, 33], and organic solvent residues in the drug product may be toxic. As an alternative, environmental-friendly techniques using supercritical fluid (supercritical carbon dioxide in this project) are being explored for stabilisation of protein therapeutics. Also, the supercritical carbon dioxide (scCO₂) can be applied as a drying medium for the production of formulated protein-containing microparticles [34, 35].

ScCO₂ processes have been investigated for the purpose of protein encapsulation [36-43]. However, in these studies, hydrophobic materials such as PLA, PLGA and lipids were applied as the coating material, and organic solvents were still used. The application of scCO₂ processes together with the use of hydrophilic polymers as the coating material provides an alternative to encapsulate proteins for the development of controlled DDS.

The encapsulation of solid protein particles can be achieved via emulsion or spray coating methods. The former can be achieved by using the non-polar scCO₂ in place of organic solvents, where a water/scCO₂ emulsion is formed [44, 45] and the solid protein particles are encapsulated by polymer-containing droplets. The latter spray coating method has been applied in the food and pharmaceutical industry [46-50] where core particles are brought in contact with the sprayed polymer-containing droplets. Conventionally, this coating process provides many advantages such as uniform coating, control of coating layer thickness, multilayer coating and particle formation [47, 51].

1.5 Research purpose of this thesis

This thesis aims at encapsulating protein with polyelectrolyte via a scCO₂ process in the absence of organic solvents. This was done by a spray coating process, in which the solid protein microparticles were suspended in a high-pressure vessel filled with scCO₂ and are coated by polyelectrolyte via contacting the atomised polymer droplets sprayed into the vessel. The coating can be achieved without full dissolution of protein in an aqueous medium. The properties of the encapsulated protein product are investigated and correlated to the process conditions. This gives an evaluation of the

operating conditions, especially the critical operating factors that influence the protein encapsulation, and provides guidance for further optimisation of the coating process.

Moreover, this thesis aims to understand the properties of the applied protein and polyelectrolyte and their interaction behaviours via molecular modelling, Brownian dynamics simulation and microfluidic method. These contribute to the design of controlled biopharmaceutical DDS, the improvement of process equipment, and the optimisation of the coating process.

This project was granted by the Netherlands Technology Foundation STW (now is the Netherlands Organisation for Scientific Research (NWO) Domain Applied and Engineering Sciences (TTW)) and has been performed in collaboration with the Division of Drug Delivery Technology from Leiden University. The researchers from Leiden University focused on protein formulation, particle and protein stability, and protein release studies with the extensive characterisation of encapsulated and released proteins.

1.6 Thesis outline

This thesis is divided into nine chapters, and the scheme is shown in Figure 1.2. Chapter 2 describes the investigation of a scCO₂ spray coating process to coat solid protein hydrophilic micron-sized core particles with a biodegradable and hydrophilic polyelectrolyte. Lysozyme microparticles were used as the core particles, and dextran sulphate was used as the coating polymer. The characteristics and principles of the spray coating process are discussed. The encapsulation of the protein by the polyelectrolyte and the protein release behaviours from the coated product particles are evaluated and correlated to the processing conditions.

A better understanding of the interactions between protein and polyelectrolyte contributes to the development of encapsulated biopharmaceuticals and coating process. Molecular modelling was used to study the behaviour of the macromolecules (and complexes after their interaction), and to calculate the energies of the interactions. Chapter 3 addresses the morphology of the dextran sulphate (with sodium as the counterion; DSS). This chapter lays the foundation for studying the molecular interactions of the polymer with lysozyme, which are proposed in Chapter 4. There are three types of interactions considered to occur, i.e. electrostatic interactions where the ion exchange takes place, aqueous solvation of the molecules and steric interactions between the macromolecules. A preliminary calculation of the ion exchange energy under hydrated conditions and the depiction of the geometrical behaviour of the interacting molecules (lysozyme and DSS) when undergoing steric interactions is included.

The dynamics of particle formation and growth have been studied to understand the interaction between proteins and polyelectrolytes, of which the particle formation and growth had been previously studied by a joint investigator in this STW project, Ahmad S. Sediq, via nanoparticle tracking analysis and flow imaging microscopy [52]. In Chapter 5, Brownian dynamics simulations are implemented to understand this perikinetic particle agglomeration profile. One of the simulations performed was based on classical Smoluchowski's model and was extended from the conventional case of monodisperse particles to the one of the system starting with two particle species, i.e. protein and polyelectrolyte. Two other approaches, based on tracking discrete particle trajectories and calculating inter-particle collision probability respectively, are proposed but require further investigation for the simulation of the protein-polyelectrolyte agglomeration.

The diffusivities of protein and polyelectrolyte are important factors when studying their complexation. Chapters 6 and 7 describe a microfluidic method and the results of determining the protein and polyelectrolyte diffusion coefficients, respectively.

Characterisation of the encapsulated proteins is also essential for process and product optimisation. Among the relevant properties are the density and the porosity of the encapsulated particles. A.S. Sediq from Leiden University developed a method to determine the particle porosity based on the particle density measured via flow imaging microscopy [53]. In order to efficiently analyse the data, a MATLAB-based toolkit, named *FlowDensi* was developed to calculate the particle density based on the output database of the flow imaging microscopy device. This toolkit is described in Chapter 8.

Chapter 9 summarises the results and conclusions from the above research. The perspectives of scCO₂ spray coating processes using polyelectrolyte as the coating material for protein DDS development are discussed, together with an outlook of the molecular modelling, Brownian dynamics simulation and microfluidic method to contribute to the encapsulation process and product development.

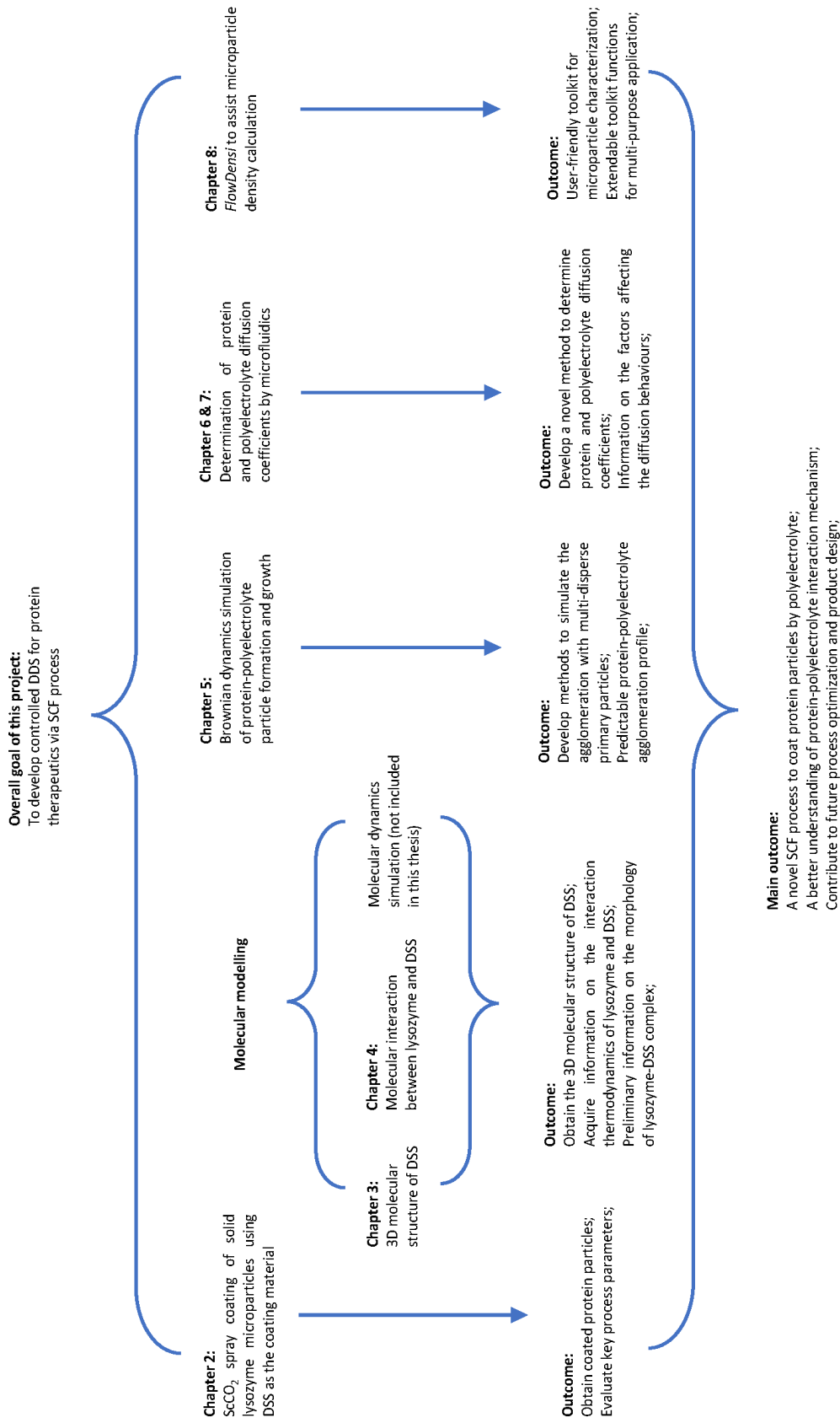


Figure 1.2. Scheme of the thesis chapters and their contributions to the goal of the project.

References

1. Pisal, D.S., M.P. Kosloski, and S.V. Balu-Iyer, Delivery of therapeutic proteins. *Journal of pharmaceutical sciences*, 2010. **99**(6): p. 2557-2575.
2. Dimitrov, D.S., Therapeutic proteins, in *Therapeutic Proteins*. 2012, Springer. p. 1-26.
3. Vaughan, T., J. Osbourn, and B. Jallal, *Protein therapeutics*. 2017.
4. Sahu, K.K., S. Minz, M. Kaurav, and R.S. Pandey, Proteins and peptides: The need to improve them as promising therapeutics for ulcerative colitis. *Artificial cells, nanomedicine, and biotechnology*, 2016. **44**(2): p. 642-653.
5. Wittrup, K.D. and G.L. Verdine, *Protein engineering for therapeutics. Part B*. 2012, San Diego, CA: Elsevier/Academic Press.
6. Lagassé, H.D., A. Alexaki, V.L. Simhadri, N.H. Katagiri, W. Jankowski, Z.E. Sauna, and C. Kimchi-Sarfaty, Recent advances in (therapeutic protein) drug development. *F1000Research*, 2017. **6**: p. 113.
7. Bhowmik, D., H. Gopinath, B.P. Kumar, S. Duraivel, and K.P.S. Kumar, Controlled Release Drug Delivery Systems. *The Pharma Innovation*, 2012. **10, Part A**: p. 24.
8. Pavan Kumar, B., I. Sarath Chandiran, B. Bhavya, and M. Sindhuri, Microparticulate drug delivery system: a review. *Indian J Pharm Sci Res*, 2011. **1**(1): p. 19-37.
9. Madhav, N.S. and S. Kala, Review on microparticulate drug delivery system. *Int J PharmTech Res*, 2011. **3**(3): p. 1242-4.
10. Birnbaum, D.T. and L. Brannon-Peppas, Microparticle drug delivery systems, in *Drug delivery systems in cancer therapy*. 2004, Springer. p. 117-135.
11. Reis, R.L., N.M. Neves, J.F. Mano, M.E. Gomes, A.P. Marques, and H.S. Azevedo, Natural-based polymers for biomedical applications. 2008: Elsevier.
12. Allen, T.M. and P.R. Cullis, Drug delivery systems: entering the mainstream. *Science*, 2004. **303**(5665): p. 1818-1822.
13. Sinha, V. and A. Trehan, Biodegradable microspheres for protein delivery. *Journal of Controlled Release*, 2003. **90**(3): p. 261-280.
14. Antosova, Z., M. Mackova, V. Kral, and T. Macek, Therapeutic application of peptides and proteins: parenteral forever? *Trends in biotechnology*, 2009. **27**(11): p. 628-635.

15. Yeo, Y., N. Baek, and K. Park, Microencapsulation methods for delivery of protein drugs. *Biotechnology and Bioprocess Engineering*, 2001. **6**(4): p. 213-230.
16. Domb, A.J., L. Turovsky, and R. Nudelman, Chemical interactions between drugs containing reactive amines with hydrolyzable insoluble biopolymers in aqueous solutions. *Pharmaceutical research*, 1994. **11**(6): p. 865-868.
17. Cleland, J.L. and A.J. Jones, Stable formulations of recombinant human growth hormone and interferon- γ for microencapsulation in biodegradable microspheres. *Pharmaceutical research*, 1996. **13**(10): p. 1464-1475.
18. Kim, H.K. and T.G. Park, Microencapsulation of human growth hormone within biodegradable polyester microspheres: protein aggregation stability and incomplete release mechanism. *Biotechnology and bioengineering*, 1999. **65**(6): p. 659-667.
19. Sah, H., Protein instability toward organic solvent/water emulsification: implications for protein microencapsulation into microspheres. *PDA journal of pharmaceutical science and technology*, 1999. **53**(1): p. 3-10.
20. Lu, W. and T.G. Park, Protein release from poly (lactic-co-glycolic acid) microspheres: protein stability problems. *PDA journal of pharmaceutical science and technology*, 1995. **49**(1): p. 13-19.
21. van de Weert, M., W.E. Hennink, and W. Jiskoot, Protein instability in poly (lactic-co-glycolic acid) microparticles. *Pharmaceutical research*, 2000. **17**(10): p. 1159-1167.
22. Bijlsma, R., A. Van Well, and M.C. Stuart, Characterization of self-assembled multilayers of polyelectrolytes. *Physica B: Condensed Matter*, 1997. **234**: p. 254-255.
23. Becker, A.L., A.P. Johnston, and F. Caruso, Layer-By-Layer-Assembled Capsules and Films for Therapeutic Delivery. *Small*, 2010. **6**(17).
24. Lankalapalli, S. and V. Kolapalli, Polyelectrolyte complexes: a review of their applicability in drug delivery technology. *Indian journal of pharmaceutical sciences*, 2009. **71**(5): p. 481.
25. Sternberg, M. and D. Hershberger, Separation of proteins with polyacrylic acids. *Biochimica et Biophysica Acta (BBA) - Protein Structure*, 1974. **342**(1): p. 195-206.
26. Chen, W. and S. Walker, The mechanism of floc formation in protein precipitation by polyelectrolytes. *Chemical engineering science*, 1992. **47**(5): p. 1039-1045.

27. Fisher, R.R., Protein precipitation with acids and polyelectrolytes: The effects of reactor conditions and models of the particle size distributions. 1987, Iowa State University.
28. Smoluchowski, M., Versuch einer mathematischen Theorie der Koagulationskinetik kolloider Lösungen. Zeitschrift Für Physikalische Chemie, 1917. **92**(1): p. 129-168.
29. Gregory, J., Flocculation by polymers and polyelectrolytes. Solid/liquid dispersions, 1987. **8**: p. 163-180.
30. Clark, K. and C. Glatz, Polymer dosage considerations in polyelectrolyte precipitation of protein. Biotechnology progress, 1987. **3**(4): p. 241-247.
31. Varde, N.K. and D.W. Pack, Microspheres for controlled release drug delivery. Expert Opinion on Biological Therapy, 2004. **4**(1): p. 35-51.
32. Eckert, C.A., B.L. Knutson, and P.G. Debenedetti, Supercritical fluids as solvents for chemical and materials processing. Nature, 1996. **383**(6598): p. 313.
33. Mohamed, R.S. and G.A. Mansoori, The use of supercritical fluid extraction technology in food processing. Food Technology Magazine, 2002. **20**: p. 134-139.
34. Nuchuchua, O., H. Every, G. Hofland, and W. Jiskoot, Scalable organic solvent free supercritical fluid spray drying process for producing dry protein formulations. European Journal of Pharmaceutics and Biopharmaceutics, 2014. **88**(3): p. 919-930.
35. Darani, K.K. and M.R. Mozafari, Supercritical fluids technology in bioprocess industries: a review. Journal of Biochemical Technology, 2010. **2**(1): p. 144-152.
36. Whitaker, M.J., J. Hao, O.R. Davies, G. Serhatkulu, S. Stolnik-Trenkic, S.M. Howdle, and K.M. Shakesheff, The production of protein-loaded microparticles by supercritical fluid enhanced mixing and spraying. Journal of Controlled Release, 2005. **101**(1): p. 85-92.
37. Jordan, F., A. Naylor, C.A. Kelly, S.M. Howdle, A. Lewis, and L. Illum, Sustained release hGH microsphere formulation produced by a novel supercritical fluid technology: In vivo studies. Journal of Controlled Release, 2010. **141**(2): p. 153-160.
38. Kang, Y., C. Yang, P. Ouyang, G. Yin, Z. Huang, Y. Yao, and X. Liao, The preparation of BSA-PLLA microparticles in a batch supercritical anti-solvent process. Carbohydrate Polymers, 2009. **77**(2): p. 244-249.
39. Tu, L.S., F. Dehghani, and N.R. Foster, Micronisation and microencapsulation of pharmaceuticals using a carbon dioxide antisolvent. Powder Technology, 2002. **126**(2): p. 134-149.

40. Cocero, M.J., Á. Martín, F. Mattea, and S. Varona, Encapsulation and co-precipitation processes with supercritical fluids: Fundamentals and applications. *The Journal of Supercritical Fluids*, 2009. **47**(3): p. 546-555.
41. Kalani, M. and R. Yunus, Application of supercritical antisolvent method in drug encapsulation: a review. *International journal of nanomedicine*, 2011. **6**: p. 1429.
42. Girotra, P., S.K. Singh, and K. Nagpal, Supercritical fluid technology: a promising approach in pharmaceutical research. *Pharmaceutical development and technology*, 2013. **18**(1): p. 22-38.
43. Tran, M.K., L.N. Hassani, B. Calvignac, T. Beuvier, F. Hindré, and F. Boury, Lysozyme encapsulation within PLGA and CaCO₃ microparticles using supercritical CO₂ medium. *The Journal of Supercritical Fluids*, 2013. **79**: p. 159-169.
44. Lee, C.T., P.A. Psathas, K.P. Johnston, J. deGrazia, and T.W. Randolph, Water-in-carbon dioxide emulsions: formation and stability. *Langmuir*, 1999. **15**(20): p. 6781-6791.
45. Johnston, K., K. Harrison, M. Clarke, S. Howdle, M. Heitz, F. Bright, C. Carlier, and T. Randolph, Water-in-carbon dioxide microemulsions: an environment for hydrophiles including proteins. *Science*, 1996. **271**(5249): p. 624-626.
46. Dewettinck, K. and A. Huyghebaert, Fluidized bed coating in food technology. *Trends in Food Science & Technology*, 1999. **10**(4-5): p. 163-168.
47. Werner, S.R., J.R. Jones, A.H. Paterson, R.H. Archer, and D.L. Pearce, Air-suspension particle coating in the food industry: Part I—State of the art. *Powder Technology*, 2007. **171**(1): p. 25-33.
48. Bose, S. and R.H. Bogner, Solventless pharmaceutical coating processes: a review. *Pharmaceutical development and technology*, 2007. **12**(2): p. 115-131.
49. Bolleddula, D., A. Berchielli, and A. Aliseda, Impact of a heterogeneous liquid droplet on a dry surface: Application to the pharmaceutical industry. *Advances in colloid and interface science*, 2010. **159**(2): p. 144-159.
50. Teunou, E. and D. Poncelet, Batch and continuous fluid bed coating—review and state of the art. *Journal of food engineering*, 2002. **53**(4): p. 325-340.
51. Palamanit, A., S. Prachayawarakorn, P. Tungtrakul, and S. Soponronnarit, Performance Evaluation of Top-Spray Fluidized Bed Coating for Healthy Coated Rice Production. *Food and Bioprocess Technology*, 2016. **9**(8): p. 1317-1326.

52. Sediq, A.S., M.R. Nejadnik, B.I. El, G.J. Witkamp, and W. Jiskoot, Protein-polyelectrolyte interactions: Monitoring particle formation and growth by nanoparticle tracking analysis and flow imaging microscopy. *European Journal of Pharmaceutics & Biopharmaceutics*, 2015. **93**: p. 339-345.
53. Sediq, A.S., S.K. Waasdorp, M.R. Nejadnik, M.M. van Beers, J. Meulenaar, R. Verrijck, and W. Jiskoot, Determination of the Porosity of PLGA Microparticles by Tracking Their Sedimentation Velocity Using a Flow Imaging Microscope (FlowCAM). *Pharmaceutical Research*, 2017. **34**(5): p. 1-11.

Chapter 2

Towards the development of a supercritical carbon dioxide spray process to coat solid protein particles

Miao Yu, Ahmad S. Sediq, Shiduo Zhang, M. Reza Nejadnik,
Hayley A. Every, Wim Jiskoot, Geert-Jan Witkamp

Adapted from the Journal of Supercritical Fluids, 141 (2018): 49-59.

Abstract

The aim of this study was to develop a supercritical carbon dioxide (scCO₂) spray process to coat solid protein particles with a hydrophilic polymer. The final purpose is to manufacture drug particles exhibiting controlled release behaviour in patients. Lysozyme microparticles (about 20 µm) were suspended in a vessel into which a dextran sulphate (DS) solution was dispersed by scCO₂ via a nozzle. Upon interaction with the droplets, DS was deposited onto or mixed with suspended lysozyme particles. Particles of about 100 µm were obtained. The zeta-potential analysis and elemental analysis indicated that the top layer of the particles consisted of both lysozyme and DS. Some of the produced particulate materials showed retarded lysozyme release when exposed to water or phosphate buffered saline, holding promise for future production of controlled drug delivery systems for therapeutic proteins.

2.1 Introduction

Protein therapeutics are successfully applied to treat chronic and life-threatening diseases owing to their high specificity and potency. One drawback of these drugs is that they have to be administered parenterally, i.e., intravenously, subcutaneously or intramuscularly, and often require frequent injections or continuous infusion due to rapid clearance from the bloodstream [1]. One way to overcome this is to encapsulate these drugs in an implantable macroscopic or injectable microparticulate drug delivery system (DDS) from which they are slowly released after administration. However, the development of an effective DDS for proteins remains a challenge, as reflected by the low number of such products on the market [2-5].

Up to now, polymers such as polylactic acid (PLA) and poly(lactic-co-glycolic) acid (PLGA) have been used as carriers to encapsulate proteins [6]. The use of these polymers, however, comes with disadvantages such as denaturation of proteins during production because of contact with the polymers, organic solvents and interfaces, and the formation of acidic degradation products causing a local drop in pH during release, leading to protein aggregation and incomplete protein release [7].

As an alternative to the conventionally used polymers, hydrophilic polymers could be employed, which are more protein friendly. In the past decades, the interest for natural or chemically modified polysaccharide-based polymers in the development of controlled drug delivery systems has increased due to their stability, safety, non-toxicity, hydrophilicity and biodegradability [8-12]. Charged polymers such as polyelectrolytes are widely applied in food, biotechnology, pharmaceutical and cosmetic industry and are used as dispersing agents, purification reagents, conditioners, etc. [13-15]. In addition to these applications, polyelectrolytes have been studied as coating materials for food and pharmaceutical purposes [16, 17] with several advantages [18]. One of them is that the coating process can be performed in an aqueous environment under mild conditions without the use of organic solvents, which helps to preserve the bioactivity of sensitive biomolecules like proteins. Proteins can be easily incorporated within polyelectrolyte materials because they are natural polyelectrolytes themselves, and due to their amphotericity the protein charge can be changed through a well-chosen shifted pH [19, 20]. The complex formation with the polyelectrolyte might, however, affect the protein structure and activity [18].

For the purpose of controlled protein release, polyelectrolytes may be employed to build up multi-layer coatings (LbL (layer by layer)) by the application of alternating positively-charged and negatively-charged polyelectrolytes [16]. Compared with conventional encapsulation methods like emulsion-solvent extraction/evaporation [6, 21], i) LbL coating does not require harmful organic solvents; ii)

avoids the use of thermal evaporation steps which can damage the protein; iii) the protein release behaviour can be adjusted by selecting the proper types of polyelectrolytes, arranging the number of coating layers and modifying the interactions among the charged polymers [16-18].

It would be even more advantageous if we were able to carry out protein coating by polyelectrolytes in supercritical carbon dioxide (scCO₂). ScCO₂ has been examined as a solvent to process protein pharmaceuticals because of its mild critical temperature and pressure, nontoxicity, the absence of solvent/water interfaces and it does not leave traces in the product [22]. ScCO₂ can be applied as a drying medium for the production of formulated protein-containing microparticles [23]. Also, via changes in the kinetics of CO₂ depressurisation, the particle morphology can be controlled to generate materials of variable density and surface roughness [24].

Protein encapsulation for controlled release using scCO₂ has been investigated before [24-31]. In these studies, hydrophobic materials such as PLA, PLGA and lipids, were usually selected as the coating materials, and in some cases, organic solvents were applied. As far as we know, there have been no studies on protein coating using polyelectrolytes in scCO₂ processes.

The selection of polymer-based coating methods for microparticle encapsulation depends on many factors like the desired final coating layer thickness and product particle size. Spraying coating involves bringing core particles in contact with the sprayed polymer-containing droplets. Conventionally, this coating process provides many advantages such as uniform coating, coating layer thickness control, and multilayer coating [32, 33]. By combining the advantages above of spray coating and scCO₂ processes (e.g. drying under mild conditions), a novel approach can be developed for producing controlled release protein formulations.

This chapter reports on an exploratory study aimed at evaluating the possibility of developing a scCO₂ process to coat dry protein-containing hydrophilic micro-sized core particles with a shell of a single type of biodegradable and hydrophilic polyelectrolyte. In this study, lysozyme was chosen as a model protein and dextran sulphate (DS) as the coating material. The obtained dry microparticles were characterised for particle morphology, residual moisture content, protein release profile, zeta-potential and surface composition.

2.2 Experimental

2.2.1 Materials and preparations of feed solutions

Hen egg white lysozyme (~70000 U/mg, Sigma-Aldrich, St. Louis, USA) was dissolved in ultrapure water (purified using a Milli-Q ultra-pure water system, Millipore™, Molsheim, France) and was used for the production of lysozyme core microparticles via a scCO₂ spray drying process (see 2.2.2). DS (dextran sulphate) (Sigma-Aldrich, St. Louis, USA) solution (10% w/w) was also prepared in ultrapure water for the spray coating onto lysozyme core particles. For the *in vitro* study on the protein release performance, a phosphate buffer was prepared with phosphate salts (Na₂HPO₄ and NaH₂PO₄) and sodium chloride (NaCl) (Sigma-Aldrich, St. Louis, USA). All liquid formulations were filtered through 0.22 µm cellulose filters (Whatman, GE Healthcare, Freiburg, Germany) before experiments. For all the scCO₂ related processes, CO₂ (99% purity) was purchased from Linde group (Linde Gas Benelux BV, The Netherlands).

2.2.2 Preparation of lysozyme core particles

Prior to the coating experiments, solid spray-dried lysozyme core microparticles were prepared according to previous methods, with uniform spherical morphology and a relatively narrow size distribution [23]. Briefly described, lysozyme solution (10% w/w) was prepared with ultrapure water as the solvent. An amount of 20 ml of this solution was sprayed into a 4-litre scCO₂ spray drying vessel via a co-axial nozzle (inner liquid diameter 0.05 cm and outer scCO₂ diameter 0.24 cm) at a solution flow rate of 0.2 ml/min, scCO₂ flow rate of 30 kg/h, a temperature of 37 °C and a pressure of 130 bar.

2.2.3 Particle suspension & spray coating (PSSC) process

2.2.3.1 Experimental set-up

Figure 2.1 illustrates the scheme of the scCO₂ spray coating process. The scCO₂ was supplied by a diaphragm pump (LEWA, Leonberg, Germany) to a half-litre pressure vessel.

During the process, an amount of solid lysozyme core particles was placed in the vessel, followed by warming and pressurisation with the CO₂. With the help of the agitator (a shaft with both disk turbine and pitched-blade turbine mounted), the lysozyme powder was suspended in the vessel. DS solution was fed into the vessel by a high-pressure piston pump (ISCO, Lincoln, USA). By means of a nozzle-containing T-mixer in which single-hole nozzles were placed, DS solution and scCO₂ were mixed and

sprayed into the vessel, which is explained in detail below. Products from the process were collected at the bottom of the vessel where paper filters were placed. The paper filter was prepared by cutting normal printing paper fitting the inner bottom of the vessel. Ten layers of the paper were fixed at the bottom of the vessel. The paper filter remained intact after the spray coating process.

In order to conveniently describe the process developed in our study, it is named as particle suspension & spray coating (PSSC) process.

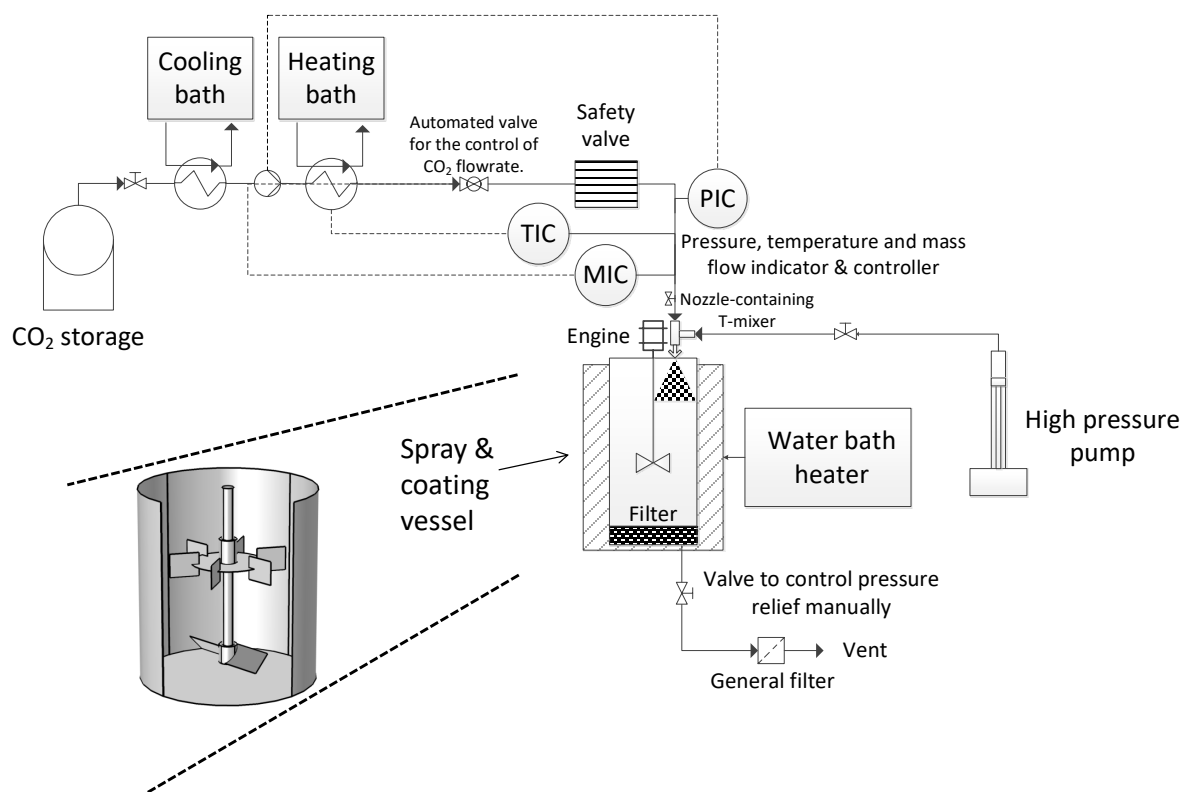


Figure 2.1. Sketch of the PSSC experimental set-up. ScCO₂ was pressurised and heated to a supercritical state (in this study to 130 bar and 37 °C), and introduced into the spray & coating vessel via a nozzle-containing T-mixer, in which the high-speed scCO₂ flow atomises the DS solution (introduced by an ISCO pump) into tiny droplets. A disk turbine and pitched-blade turbine were placed in the spray & coating vessel to mix the core particles (placed in the vessel before pressurisation) and the atomised polymer droplets.

2.2.3.2 Nozzle configurations

These experiments aimed to investigate the influence of different nozzle configurations on the dispersion of the DS liquid. Four types of nozzle arrangement in the T-mixer, named as C1, C2, C3 and C4, respectively, as shown in Figure 2.2, were tested to evaluate the influence of the nozzle configuration on the dispersion of polymer droplets. C1, C2 and C3 had configurations that bend the $scCO_2$ flow while C4 had a configuration of straight flow. In all these experiments, first, the vessel was filled with CO_2 . A $scCO_2$ flow rate of 300 g/min was applied during the spraying process. The operating conditions were maintained at a temperature of 37 °C and a pressure of 130 bar. Ten ml DS solution (10% w/w) was introduced into the vessel at a flow rate of 0.2 ml/min. The agitator rotated at a rate of 500 rpm. The liquid drops were dried as the result of a quick mass transfer between water and $scCO_2$. After the injection of the DS solution, the vessel was flushed for 30 min at 300 g/min with fresh $scCO_2$ to avoid making products with high residual moisture content.

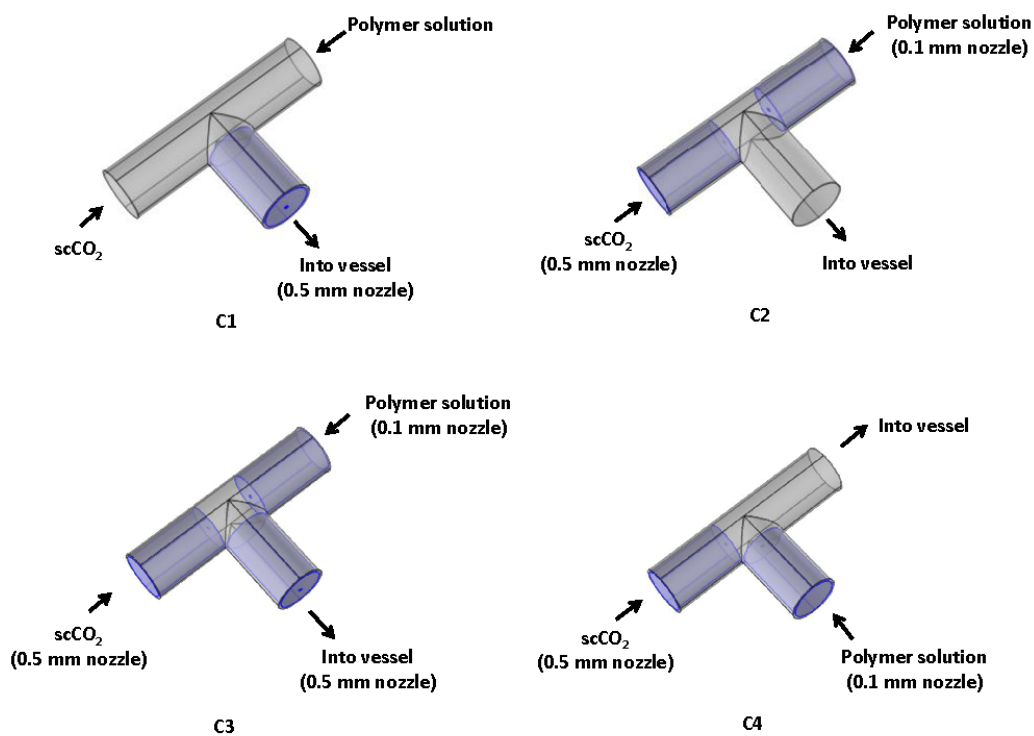


Figure 2.2. Scheme of the configurations (C1, C2, C3 and C4) of the nozzle-containing T-mixers applied in the PSSC process. Nozzles (shown as the hole embedded in the blue cylinders) with different sizes were connected in T-mixers made by cylinder tubes (about 9.5 mm inner diameter). The arrows show the direction of the fluids. The nozzle wall plate thickness was about 1- 2 mm.

2.2.3.3 Processing conditions

Several experiments were performed to evaluate the applicability of the PSSC process for the coating of lysozyme core particles (see Table 2.1).

During these experiments, 1 g lysozyme core particles were suspended in scCO₂ in the half-litre pressure vessel with agitation at 500 rpm, which is higher than the minimum required agitation speed (about 170 rpm) for solid particle suspension based on a classical equation pioneered by Zwietering [34]. The vessel was pressurised with scCO₂ and was regulated at a flow rate of 300 g/min at 130 bar and 37 °C. Once the pressure was stable, 10 ml DS solution (10% w/w) was atomised into the vessel together with the scCO₂ via the T-mixer nozzle. The overall mass ratio of lysozyme to DS during this process was 1:1. The feeding rate of DS was varied to learn about the influence of this parameter on the coating of the core particles. After the injection of DS solution, the vessel was flushed with scCO₂ (300 g/min) for 30 min with agitation for further contact of particles and sprayed DS droplets, as well as the removal of the residual water from the vessel. After depressurisation, the product was recovered from the filter on the bottom of the vessel for further analysis.

The samples collected with different operating conditions are named as Control, S1, S2 and S3, respectively.

Table 2.1. Operating conditions used for the PSSC process.

Sample	DS concentration (% w/w)	Flow rate (ml/min)	Nozzle configuration
Control	0%	1	C4
S1	10%	0.2	C4
S2	10%	0.5	C4
S3	10%	1	C4

2.2.4 Particle characterisation

2.2.4.1 Particle size distribution

DS solution was atomised using different nozzle configurations (see Figure 2.2) and dried in the vessel. The particle size distribution of the spray dried DS microparticles was measured by the tri-laser

diffraction light scattering technique using a Microtrac S3500 particle analyser (Microtrac S3500, Montgomeryville, USA). Microtrac FLEX software (version 10.3.14) was used to calculate the particle size distribution. The device offers two operating modes, i.e., a wet (fluid dispersion) mode and a dry (air dispersion) mode. In the wet mode, the liquid-particle shear and implemented sonification help the homogenisation of the samples; in the dry mode, air flow is used for powder dispersion. In terms of the measurement size range, the wet mode has a lower detection limit (about 0.02 μm) than the dry mode (about 0.2 μm). The wet mode seems to be more favourable for particle size determination. However, a proper liquid medium is needed to avoid sample dissolution and particle-particle interaction.

Methanol was used as the liquid medium as it is a non-solvent for DS. Sonification (2 minutes at an ultrasound power of 25 Watts) was used to improve the homogeneity of the suspension. A refractive index value of 1.59 for particles and 1.33 for methanol was used. A measurement size range of 0.02 to 1408 μm was selected. Each sample was measured in duplicate, and the averaged particle size distribution (each measurement itself was the average of triplicated recycling measurements) was reported.

The size distribution of particles obtained from the PSSC process was measured by the same device in the dry (air dispersion) mode to maintain the solid state of the collected particles and to avoid re-dissolution (as lysozyme can be dissolved in solvents like methanol) and unexpected particle-particle interaction. During the measurement, the dry powder was blown through the beam by means of pressure and sucked into a vacuum cleaner. During the dry mode measurement, the size range of 0.2 to 1408 μm was used, and each sample was measured once.

2.2.4.2 Scanning electron microscope and energy dispersive spectroscopy

A scanning electron microscope (SEM), integrated with Energy Dispersive Spectroscopy (EDS) (JSM-6010LA, JEOL, Tokyo, Japan) was used to examine the morphology of the microparticles as well as the elemental composition of the microparticle surface. Conductive double-sided tape was used to fix the particles to the specimen holder before sputtering them with a thin layer of Au-Pd. All the samples were analysed in map mode during EDS analysis, where the distribution and intensity of elements were measured in the scanned area, and a summarised elemental composition of the scanned area was reported.

The EDS analysis was performed for lysozyme, DS, Control, S1, S2 and S3 at the accelerating voltages of 10 kV), counting rate higher than 1000 cps and dead time lower than 4%. Elemental carbon (C), nitrogen (N), oxygen (O) and sulphur (S) were measured as feature elements to distinguish lysozyme

and DS. For the EDS analysis, at least three different particles were chosen for elemental composition analysis. The average values of the elemental compositions of the measured particles together with their standard deviations are reported.

The influence of different accelerating voltages on the detected elemental composition was investigated. S3 was selected for this measurement due to its relatively high detected sulfur content (see 2.3.5). One particle of S3 was selected; three different positions on the particle were measured for elemental content in the sequence of 5, 10, 15 and 20 kV. The average value of the measured elemental compositions of the three detected positions under each accelerating voltage is reported.

2.2.4.3 Zeta-potential analysis

Zeta-potential measurements are commonly employed to determine whether the electrical charge on the surface of particles is positive or negative, and is used as a means of monitoring the deposition of surface layers [35].

A liquid polar medium has to be used for the zeta-potential measurement. Zeta-potential of the product was measured in ethanol (rather than methanol to avoid the possible dissolution of lysozyme [36]), in which lysozyme and DS are only sparingly soluble, via electrophoretic light scattering (ELS) combined with phase analysis light scattering (PALS) (Zetasizer Nano ZS, Malvern Instruments, Malvern, UK). About 0.01 g sample powder was put in a cuvette filled with 1 ml ethanol, followed by immediate measurement. Refractive indices of 1.36 and 1.59 were used for ethanol and particles, respectively. A voltage of 5 V was applied during the measurement. Each sample was measured in triplicate and the mean zeta-potential value, the standard deviation of the triplicated measurement and the zeta-deviation, which reflects the width of the charge distribution obtained in the experiment [37] and was calculated by Malvern Zetasizer Software v7.11, were reported.

2.2.4.4 Moisture content analysis

The moisture content measurements of the samples were conducted with a Karl-Fischer coulometer (Metrohm 756F, Herisau, Switzerland). An amount of powder (about 0.01 g) was weighed in a chromatography vial, which was sealed after loading the powder, followed by the addition of 1 ml methanol. After half an hour of water extraction by methanol, 0.1 ml of the water-methanol mixture was injected into the coulometer sample chamber for analysis. The measurement was performed in triplicate, and the average value with the standard deviation was reported as the percentage of the sample weight (% w/w).

2.2.4.5 Protein concentration determination

The lysozyme concentration was determined with the use of a UV spectrophotometer (Agilent 8453, Agilent Technologies, Santa Clara, USA). The dissolved lysozyme sample was placed in a cuvette with the path length of 1 cm, and the absorbance at 280 nm was measured. By using an extinction coefficient of $2.64 \text{ ml mg}^{-1} \text{ cm}^{-1}$ [38], the lysozyme concentration in the measured sample was calculated.

2.2.4.6 Protein load determination

In order to determine the total lysozyme content in the product particles (containing both lysozyme and DS), about 2 mg of powder was dissolved in 1 M NaCl solution (at room temperature), in which all the protein-polyelectrolyte complexes were assumed to dissociate at this high ionic strength.

2.2.4.7 Protein release studies

Lysozyme release profiles were achieved with the following procedure: 0.13 g powder was added to a flask, along with 13 ml purified water, or phosphate buffered saline (PBS) (pH 7.4; 10 mM phosphate salts (Na_2HPO_4 and NaH_2PO_4); 150 mM NaCl). The release experiments were performed in an incubator-shaker at 37 °C and 200 rpm. At different time points (1 h, 1 day, 2 days and 4 days) 1.5 ml of the dissolution medium was transferred into an Eppendorf tube and simultaneously 1.5 ml of the corresponding fresh medium was added to the sample flask. After centrifugation for 15 minutes at 18000 x G, the UV spectrum of the supernatant was recorded.

2.3 Results

2.3.1 The configuration of nozzle-containing T-mixer

This section describes the performance of the tested nozzle configurations in the T-mixer with respect to DS droplet dispersion. One of the tested nozzle configurations was selected for the following PSSC process. DS solutions were sprayed by using the different nozzle configurations shown in Figure 2.2. It was aimed to disperse DS liquids into droplets with a size smaller than the core particles while avoiding the presence of droplets larger than the core particles (see 2.4.1.1 for discussions).

The number-based and volume-based size distributions of spray dried DS particles obtained with different nozzle configurations are shown in Figure 2.3. The volume-based particle size is biased toward larger particles.

All the applied four nozzle configurations show comparable number-based particle size distributions with an average particle size of 5 μm . The spray-dried DS particles from C3 have the highest ratio (about 80%) of particles with a (volume-based) size larger than that of the core particles (about 90 μm (volume-based)) among the four nozzle configurations (C1: about 60%; C2: about 63% and C4: about 71%). During the experiments, a blockage of the outlet nozzle sometimes happened due to the rapid drying of tiny droplets by scCO_2 inside the T-mixer. Thus, it was better to avoid the nozzle positioned in the outlet of the T-mixer and C3 was not selected for the PSSC process.

Although there is a presence of large particles of about 1000 μm for C1 and C4, the number of these particles is minimal. To avoid the risk of outlet nozzle blockage, C1 was not selected for the PSSC process. The scCO_2 transport in C2 involves a bend in the tube, while for C4 the tubing is more straight, which is preferable with respect to avoiding hindrance and resistance encountered during scCO_2 transport. Therefore C4 was selected as the configuration for the droplet generation in the PSSC process.

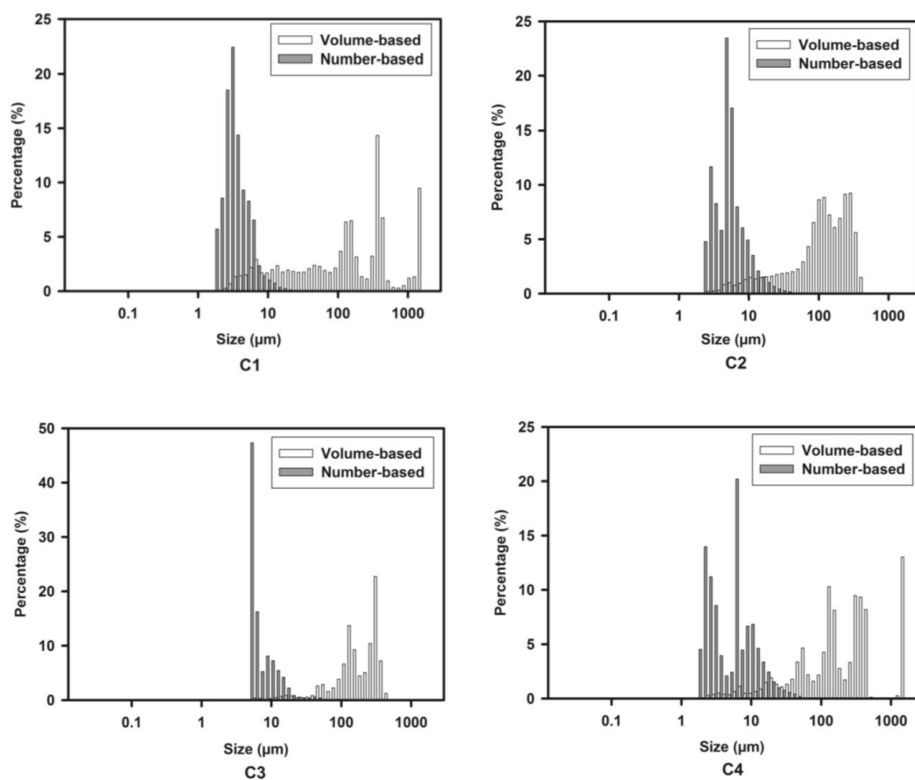


Figure 2.3. Particle size distribution, measured in wet mode by laser diffraction, of spray dried DS particles which were produced via nozzle configurations C1, C2, C3 and C4 (see Figure 2.2 and text for details). This particle size distribution is the average of duplicated measurements. The particle size distributions of each measurement are supplied in Appendix A of this chapter (AppxA-Figure 1).

2.3.2 Morphology and size distribution of particles obtained via the PSSC process

SEM was performed to study i) the morphology of the lysozyme core particles, which were produced via spray drying; ii) particles from the control experiment; and iii) particles formed after spray coating with DS in the PSSC process. The results are shown in Figure 2.4. The used lysozyme core particles were spherical with an average diameter of about 20 μm . After the PSSC process, with either water (Control) or DS spraying, only a few original core particles were found back, and most particles seemed to consist of agglomerates of differently shaped sub-particles, mostly much larger than the core particles (up to hundreds of micrometres). Apparently, some dissolution and reconstitution of the lysozyme had taken place.

It appeared that the sample S2 (where DS solution flow rate was 0.5 ml/min) consisted of agglomerates of a larger size than the other samples. However, these agglomerates consisted of sub-particles with a size similar to the particles in S1 (DS solution flow rate of 0.2 ml/min) and S3 (DS solution flow rate of 1 ml/min).

In the sample of S1, there were many 1-2 μm small particles deposited onto the surface of large particles, while in S2 and S3 such small particles were much less abundant. SEM images of S1 at higher magnification are provided in Appendix A (AppxA-Figure 2).

Laser diffraction particle size analysis was performed to study the size of the sample particles relevant to the PSSC process. The results are shown in Figure 2.5. The lysozyme core particles had an average size of about 20 μm (number-based). After the PSSC process, large particles (often agglomerates) of about hundreds of micrometre size were produced. Although the particles in S2 were visible with SEM as clusters of hundreds of microns, the measured particle size distribution (number-based) shows no significant increase in particle size compared to S1, and S3 was much bigger according to the size distribution. Apparently, the clusters were loose agglomerates of smaller particles (sub-particles). The agglomerates became separated during the particle analysis with air dispersion. As indicated by the size distribution (see Figure 2.5), the Control and S3 samples apparently contain more large particles (i.e., size > 100 μm) than S1 and S2.

Although with SEM small particles could be observed (similar to the core particles, around 20 μm) these small particles were not detected (e.g. in Control, S2 and S3) by the laser diffraction analysis. It may be possible that during laser diffraction analysis the large particles overshadow the small ones during measurement, or the amount of small particles is not enough to induce signal intensity over the detection limit, as recently shown for PLGA microparticles [39].

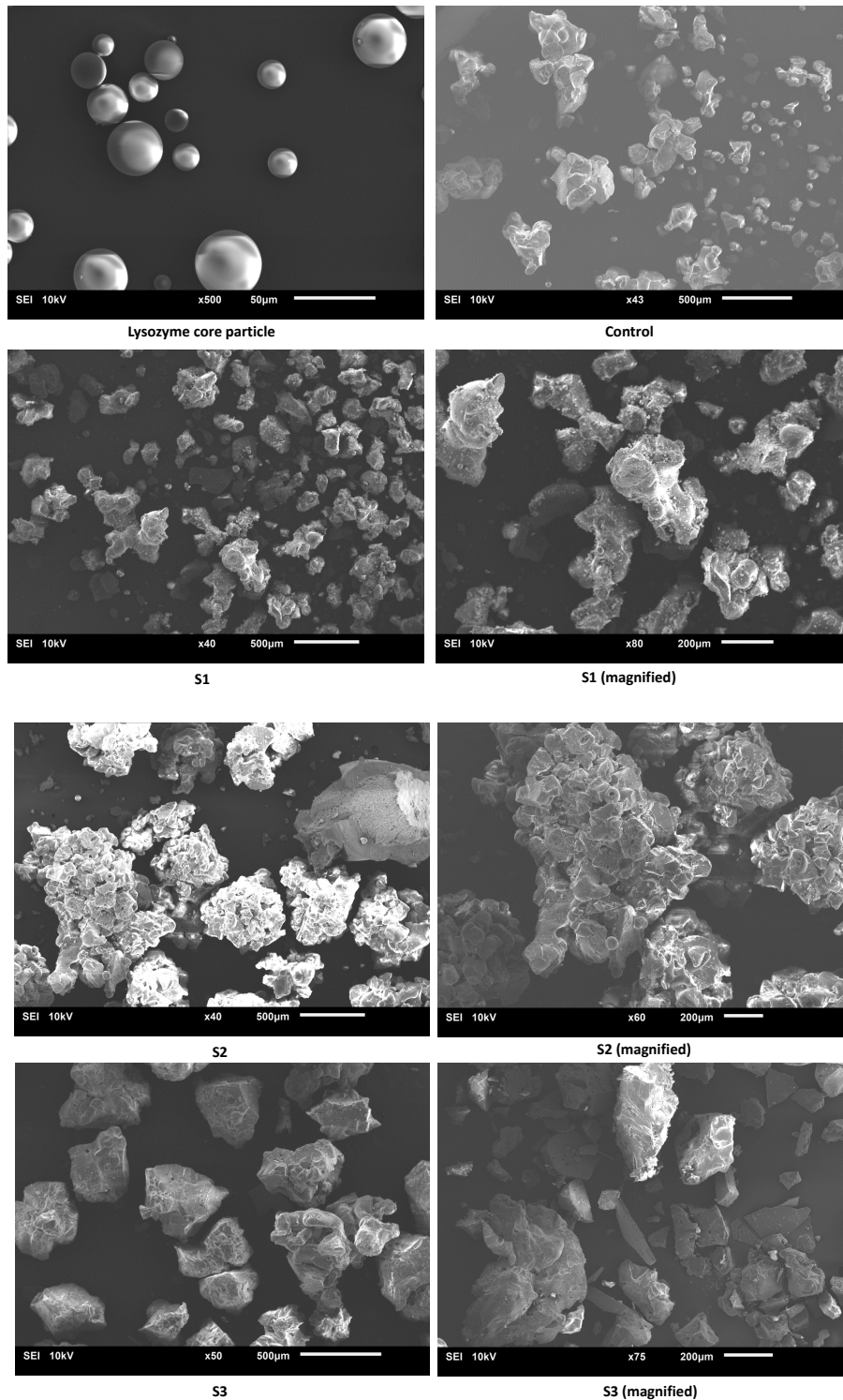


Figure 2.4. SEM images of core lysozyme particles to be coated in the PSSC process (see Figure 2.1 and text for details), Control sample (with water spraying instead of DS spraying) and products from PSSC process (sample S1, S2 and S3) with DS spraying. A magnified image of S1 shows that there are small particles deposited onto the surface of large particles. The magnified image of S2 shows that the large particles are clusters of particles with a size in the same magnitude order as that in S1 and S3. SEM images of S1 at higher magnifications are provided in Appendix A (AppxA-Figure 2).

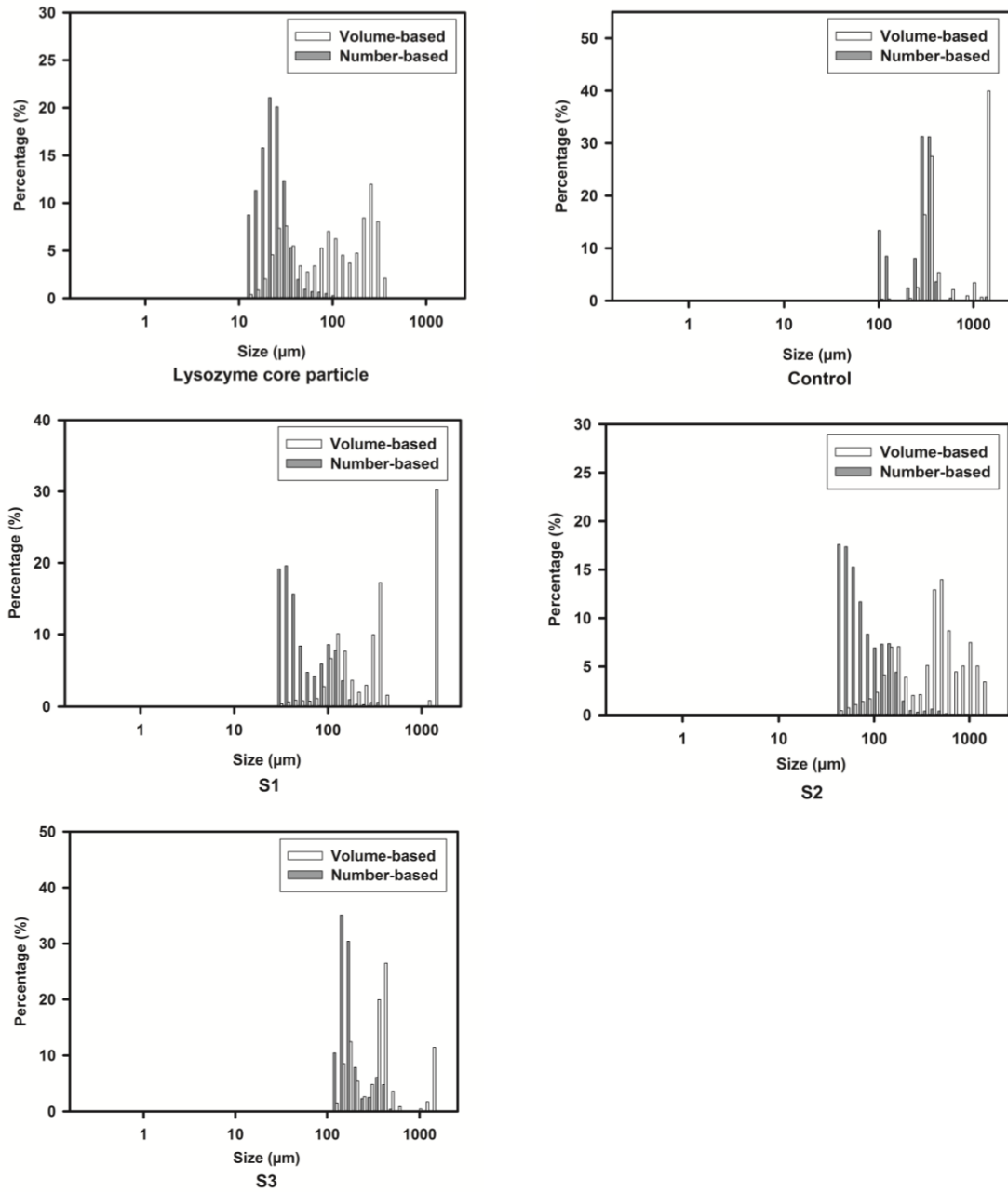


Figure 2.5. Particle size distribution, measured in dry mode by laser diffraction, of lysozyme core particles, Control sample and sample S1, S2 and S3 produced via PSSC process.

2.3.3 Residual moisture content

It has been reported [23] that a residual moisture content below 3% should be low enough to maintain the chemical and conformational stability of protein products over time. However, the influence of

water on the stability of proteins depends on the protein type and its formulation. Thus it cannot be generalised for all situations.

In this study, the residual moisture content is also an indication of the humidity level in the vessel as a result of the DS spraying flow rate. The residual moisture content of the samples is shown in Table 2.2. The average moisture content of lysozyme core particles produced via scCO₂ spray drying was 2.5%, similar to the dried protein formulation moisture content as reported before [23]. For the Control sample as well as the products obtained via the PSSC process with DS, moisture contents of about 3-5% were obtained. According to a T-test (performed via the Data Analysis toolbox of Excel 2010), the moisture contents of the samples S1 and S2 differed insignificantly from that of the lysozyme core particles. There was a statistically significant difference between the moisture content of the lysozyme core particles and S3 (P<0.05), indicating a higher residual moisture content after the particle-droplet interaction at a higher DS flow rate. Moreover, S3 also shows a significant difference from that of the Control sample.

Table 2.2. The residual moisture content of samples of the PSSC process.

Sample	Moisture content (%)
Lysozyme core particles	2.5 ± 1.1
Control	3.0 ± 0.7
S1	3.4 ± 1.1
S2	3.1 ± 0.8
S3	4.9 ± 0.5

2.3.4 Zeta-potential

Table 2.3 shows the zeta-potential of lysozyme, DS, and products from the PSSC process. As expected, lysozyme displayed a positive mean zeta-potential, opposite to that of DS. Control samples from the PSSC process showed a positive mean zeta-potential. The DS-lysozyme products from the PSSC process all showed a negative mean zeta potential, and S1 showed a more negative zeta-potential than S2 and S3. Broad zeta deviations of the sample particles were observed, especially for the products of the PSSC process, of which the zeta deviation was even higher than the mean zeta-potential.

Table 2.3. Zeta-potential of lysozyme, DS and products of the PSSC process.

	Mean zeta potential (mV) ¹	Standard deviation (mV) ²	Zeta deviation (mV) ³
Lysozyme	34.4	7.6	19.2
DS	-42.6	2.3	19.7
Control	16.0	5.9	25.5
S1	-20.8	3.5	21.3
S2	-6.4	2.4	30.9
S3	-5.9	1.5	42.6

¹: average zeta-potential of triplicate measurements.

²: standard deviation of the mean zeta-potential of triplicate measurements.

³: a zeta-potential deviation reported by Malvern Nano-zetasizer, representing the distribution of zeta-potential contributed from differently charged particles [37].

2.3.5 EDS analysis

Energy dispersive (X-ray) spectroscopy (EDS) analysis was conducted to evaluate the composition of the product particle top layer (a few μm depths) in a dry state after the PSSC process. Figure 2.6 shows the elemental compositions of lysozyme, DS and the samples obtained from the PSSC process, including the Control sample and the ones containing DS. Four elements, i.e., C, N, O and S, were selected as representative elements for the identification of materials in the product. In lysozyme, the S content was minimal with about 2% detected mass percentage while C and N dominated, as expected. In DS, N was a trace element where O and S contents were both higher than those in lysozyme, because of the presence of the hydroxyl groups and sulphate groups. The detected elemental compositions of lysozyme and DS are comparable with references [40, 41]. The Control sample shows similar content of elements as lysozyme. In all the products from the PSSC process containing DS, the mass content of S and N fallen between that of lysozyme and DS. At 10 kV accelerating voltage, the EDS analysis can reach a penetration depth of a few micrometres into the sample [42]. Therefore, according to the EDS analysis, on the top layer of the product particles from the PSSC process, there was a combination of lysozyme and DS (as expected from a coating).

The product particles of S3 were (because of the relatively high sulphur content of S3) selected to be measured under different accelerating voltages to study the influence of this factor on the particle

composition. The information is provided in Appendix A (AppxA-Figure 3). According to the results, lysozyme was the dominating material of the detected particles with a mass ratio of over 70%, and the calculated compositions of the detected particles differed slightly as a function of the accelerating voltage.

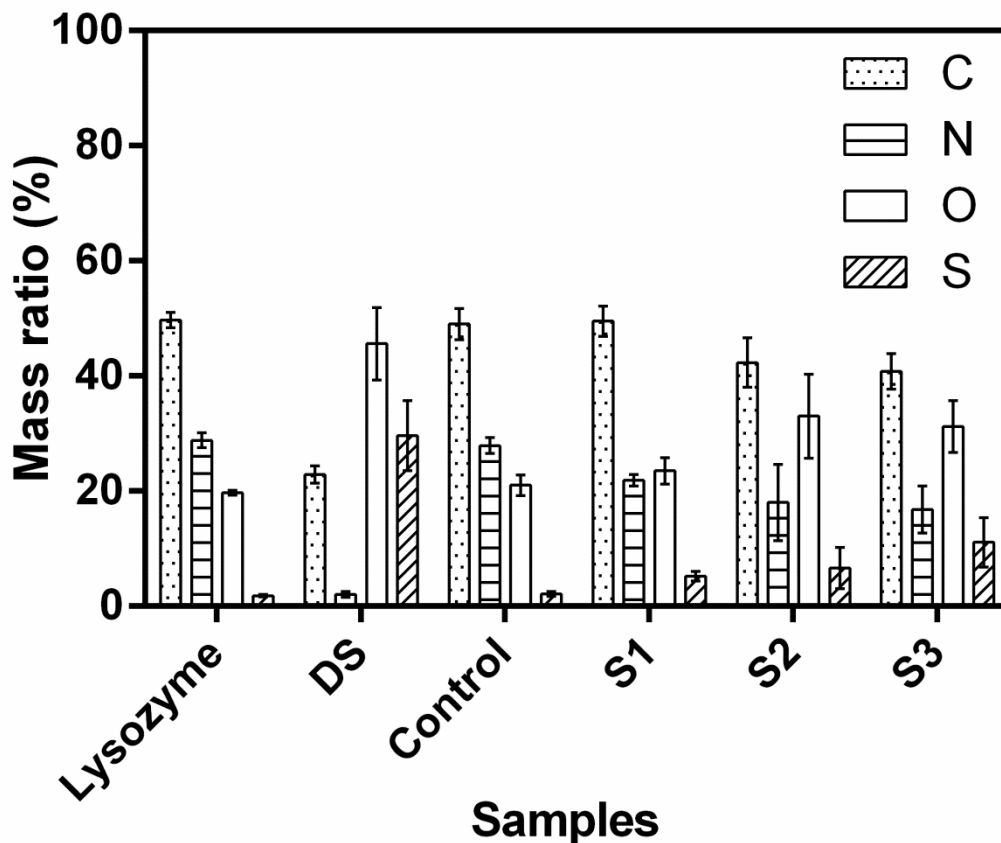


Figure 2.6. Elemental compositions of lysozyme, DS and products of PSSC process detected by EDS at an accelerating voltage of 10 kV.

2.3.6 Protein release profile

The *in vitro* protein release profile of DS-encapsulated lysozyme particles obtained via PSSC process was examined. The sample S1 and S2 showed burst release in PBS of about 80-90% at 1h (the first time point) without showing the expected controlled release behaviour. The lysozyme release profiles of S1 and S2 are provided in Appendix A (AppxA-Figure 4). Only the protein release profile of Control and S3 sample are shown in Figure 2.7. The Control sample, protein without DS, showed an immediate lysozyme release both in water and in PBS, in which 100% protein release was already measured at

first time point. In water, where the ionic strength is low, the release of lysozyme from the S3 particles was limited to about 20% after four days, while in PBS, a quick lysozyme burst release of about 70% was detected after 1 hour and a cumulative release up to 90% was reached after four days.

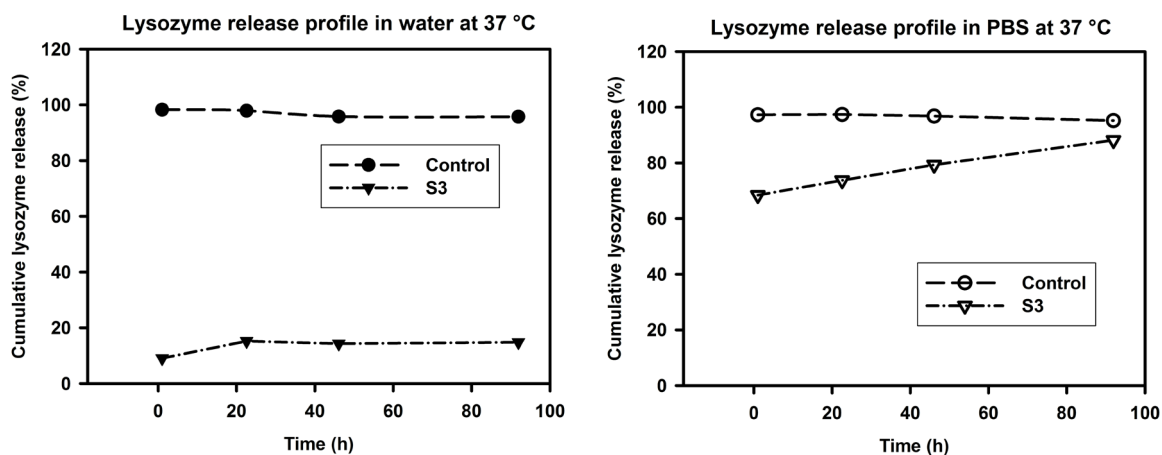


Figure 2.7. Lysozyme release profile from the Control and S3 particles in water and PBS at 37 °C.

2.4 Discussion

2.4.1 Influence of the spraying conditions on particle coating

2.4.1.1 Optimal spraying droplet size

A small (DS) droplet size with a homogeneous size distribution of dissolved coating material is expected to give an optimal coating [32, 43-45]. According to previous studies [18, 46] on the correlation between spraying droplet size and favourable particle coating, it is predicted that the size of droplets must be smaller than that of the core particles (micrometre range) in order to obtain an evenly-distributed surface layer onto the core particle.

Due to the closed high-pressure system, the droplet size could not be observed directly. Therefore, an effort was made here to derive the droplet size indirectly. The size of the dispersed DS droplets was determined based on the size of the spray-dried DS particles. When assuming that one droplet creates one primary DS particle by the process of drying, a mass balance allows for calculating the original droplet size.

According to the number-based particle size distribution, the majority of the spray dried DS particles ranged in size from 2 to 15 μm , with an average size of about 5 μm . DS particles have a density of

about 1.96 g/cm³ [47], and the 10 % (w/w) DS solution has a measured density of about 1.05 g/cm³ (via an Anton Paar DMA 5000 density meter (data not included)). If it is assumed that both the droplets and the spray-dried particles have a spherical shape, the size of the dispersed DS droplets can be calculated to be between 5-40 μm.

In order to assess whether the dispersed DS droplets had been already completely dried before their contact with the core particles, a simple mass transfer simulation based on Fick's law using Comsol Multiphysics software was conducted, using the diffusion coefficients of water and scCO₂ in the corresponding medium that were reported before [48, 49]. The simulation results are displayed in the appendix (Appendix A, AppxA-Figure 5). Based on this simulation, theoretically in fresh scCO₂, it takes about 0.5 ms to 20 ms for the sprayed DS droplet to be dried. The spraying scCO₂ flow rate was about 30 m/s at the nozzle tip, and the travel distance for the dispersed droplets for the contact with suspending particles was about 10 cm, corresponding to a residence time of approximately 3 ms. This means that part of the DS particles might be pre-dried before their contact with the solid core lysozyme particles.

A small fraction of the spray dried DS particles had a large size of hundreds of micrometres, suggesting that the original droplet size was even bigger. These large droplets should dry slowly in scCO₂ and might be one of the factors leading to possible re-dissolution and misshaping of the core microparticles (formation of bridges among the particles and agglomerates), as reflected by the SEM images of the samples (see Figure 2.4).

The average size of the sprayed DS droplets (number-based) was about half the average size of the core particles (about 20 μm). This suggests that the majority of the dispersed droplets were smaller than those of the core particle, which should be favourable for the coating of core particles [18, 46].

2.4.1.2 DS spraying flow rate and residual moisture content

This study aims to produce DS-encapsulated lysozyme particles with the help of scCO₂. In the PSSC process, the scCO₂ flow rate was always 300 g/min while the DS solution injection flow rate was varied from 0.2 ml/min to 1 ml/min in the different experiments. In general, at small volumes of liquid with large volumes of gas using twin-fluid nozzles, a higher liquid flow rate tends to lead to larger droplet sizes [50], implying that the droplet size can be controlled by varying the gas-to-liquid mass ratio (GLR) through the nozzle [51]. From this, we expected to generate larger droplets at higher DS solution flow rates.

Larger droplets may also form by coalescence of the dispersed droplets before drying, and the larger droplets take longer to dry due to the limited mass transfer in the water-scCO₂ binary system. If the

droplets could not leave the system through the paper filter at the bottom of the vessel (something which is not known), this might lead to an increase of the hold-up of water in the vessel.

These combined phenomena resulted in a higher residual moisture content of the particles at a DS flow rate of about 1 ml/min (GLR \approx 300) (about 5% (w/w) moisture content) compared to that at the flow rate of 0.2 and 0.5 ml/min (GLR=1500 and 600, respectively; about 3-3.5% moisture content; see Table 2.2).

At equal flow rates (1 ml/min), the residual moisture content of the particles for the Control experiment with only water spraying was lower (about 3%) than for that of S3 (about 5%). This was probably related to the approximately 20% higher viscosity, and slightly lower (about 6%) surface tension of the 10% DS solution (see AppxA-Table 1), giving rise to larger droplets during the atomization and reduced transport rates. Moreover, the amount of water bound to DS might also contribute to the difference in the residual moisture. Less than two water molecules are bound per sugar ring onto DS [47], representing an amount of residual water of less than 0.08 g for the 1 g of sprayed DS. This would theoretically add maximally 4% to the moisture content of the complex particles, and might explain the higher moisture content of S3 compared to the Control (no DS).

2.4.2 The composition of produced particles and efficacy of the coating

The present study was meant to learn whether lysozyme core particles could be coated with DS through the PSSC process. According to the SEM images, spherical core lysozyme particles (see Figure 2.4) agglomerated into larger particles during the PSSC process ("Control", the sample with the addition of just water in the absence of DS). Only a few original lysozyme particles were still present in the Control sample, and mainly new, agglomerated particles were visible in which the original spherical shapes of the lysozyme core particles were hardly present anymore. This might be explained from a dissolution-growth mechanism. Such a process probably also took place in the presence of DS (see Figure 2.4, S1, S2 and S3), in addition to the coating of the lysozyme by DS.

Whether the protein core particles were indeed coated by DS was evaluated by both the zeta-potential and the elemental composition on the top layer of the product particles.

Zeta-potentials of the samples from the PSSC process were measured (in ethanol) and compared with the measured values for lysozyme (about +34 mV) and DS (about -43 mV). The reverse of the zeta-potential from positive to negative values indicated that there was DS present at the particle surface.

For S1, a low DS injection flow rate was used. According to the discussion in 2.4.1.1, this low DS flow rate might lead to a pre-drying of DS before it came into contact with the lysozyme core particles (see

AppxA-Figure 2). During the zeta-potential measurement, those DS particles which were more loosely attached to the agglomerates, might contribute to the broad zeta-deviation and tend to shift the mean zeta-potential to more a negative value. The samples from the PSSC process contained particles that differed greatly in size, morphology and composition (i.e., lysozyme to DS ratio), which might give rise to different zeta-potential values.

EDS analyses were performed to learn whether the particles from the PSSC process were partly coated by DS. In this study, S was regarded as the representative element of DS. DS has a theoretical S content of 15% (w/w) compared to 2% for lysozyme, and the measured values were 30% and 2%, respectively. Theoretically, lysozyme contains 20% N with 29% measured. By calculating based on the S and N mass contents and the mass ratios of C and O to the feature elements, a mixture of DS and lysozyme was detected on the top layer of the S1, S2 and S3 sample particles whereby the detected DS content of S3 was higher than that of S1 and S2.

Based on the morphology of the product samples, the zeta-potential and EDS analysis, it can be concluded that mixed particles can be produced consisting of lysozyme and DS. However, a conclusion on the homogeneity and completeness of the core particle coating in the PSSC process cannot be drawn yet.

2.4.3 Protein release behaviour from the produced particles

Controlled and retarded protein release is the target of the DS coated lysozyme particles produced via the PSSC process. When exposing the DS-containing PSSC processed particles (S3) to PBS, after one hour about 70% of the lysozyme was released in the solution. When placed in water, however, this initial release was much less (about 10%). One factor causing the burst release of lysozyme was the dissolution of pure protein particles. The product particles of S3, with a higher DS content than S1 and S2, exhibited about 10% less initial (i.e. after 1 hour) burst release in PBS than those of S1 and S2 (see AppxA-Figure 4). The Control sample, protein without DS, dissolved completely in one hour. The much faster release in PBS at a higher ionic strength than in water was expected [52] and probably due to a weak electrostatic interaction between lysozyme and DS.

After the initial burst release, a slow release stage followed. Since the Control sample did not have such a slow phase, this slow release stage had to be related to the involved DS. The polymer apparently hampers the dissolution or the diffusion of the protein, by binding to it or by forming a layer around the protein particle [53-55]. Such a shell type layer would swell when the particle comes into contact with water and form a protein diffusion barrier.

As for the lysozyme release in S1 and S2, after exposing the particles *in vitro* to PBS for about two days, a decrease of free dissolved lysozyme was detected (see AppxA-Figure 4). Complexation of released lysozyme with free polyelectrolyte may account for the detected decrease of the lysozyme concentration [56].

The product particles from the PSSC process formulated with DS show some slow release behaviour. To prolong the release of lysozyme, a next step could be to treat the DS formulated particles with a cationic hydrophilic polymer such as DEAE-dextran (diethylaminoethyl-dextran hydrochloride). This polymer might form a layer on top of a possible DS layer of the current product particles, and the newly-formed particles are expected to exhibit slower release profiles. Thicker layers might be constructed by repeated DS-DEAE-dextran layer deposition.

2.5 Conclusions

In this study, a scCO₂ spray coating process was developed to demonstrate the possibility of coating lysozyme core particles by hydrophilic polyelectrolyte. Core microparticles agglomerated into larger particles during the process, pointing at the interaction between solid protein particles and polymer droplets. Zeta-potential and EDS analysis indicate that DS was deposited onto or mixed with lysozyme in the agglomerated product particles. In some cases, a reduced lysozyme release rate was observed for the product particles, compared to the Control (no DS). This study lays the foundation for the achievement of layer-by-layer encapsulation of protein particles via scCO₂ processes.

References

1. Kamiya, N. and A.M. Klibanov, Controlling the rate of protein release from polyelectrolyte complexes. *Biotechnology and bioengineering*, 2003. **82**(5): p. 590-594.
2. Allen, T.M. and P.R. Cullis, Drug delivery systems: entering the mainstream. *Science*, 2004. **303**(5665): p. 1818-1822.
3. Sinha, V. and A. Trehan, Biodegradable microspheres for protein delivery. *Journal of Controlled Release*, 2003. **90**(3): p. 261-280.
4. Antosova, Z., M. Mackova, V. Kral, and T. Macek, Therapeutic application of peptides and proteins: parenteral forever? *Trends in biotechnology*, 2009. **27**(11): p. 628-635.

5. Mitragotri, S., P.A. Burke, and R. Langer, Overcoming the challenges in administering biopharmaceuticals: formulation and delivery strategies. *Nature reviews. Drug discovery*, 2014. **13**(9): p. 655.
6. Yeo, Y., N. Baek, and K. Park, Microencapsulation methods for delivery of protein drugs. *Biotechnology and Bioprocess Engineering*, 2001. **6**(4): p. 213-230.
7. van de Weert, M., W.E. Hennink, and W. Jiskoot, Protein instability in poly (lactic-co-glycolic acid) microparticles. *Pharmaceutical research*, 2000. **17**(10): p. 1159-1167.
8. Patil, J., M. Kamalapur, S. Marapur, and D. Kadam, Ionotropic gelation and polyelectrolyte complexation: the novel techniques to design hydrogel particulate sustained, modulated drug delivery system: a review. *Digest Journal of Nanomaterials and Biostructures*, 2010. **5**(1): p. 241-248.
9. Liu, Z., Y. Jiao, Y. Wang, C. Zhou, and Z. Zhang, Polysaccharides-based nanoparticles as drug delivery systems. *Advanced drug delivery reviews*, 2008. **60**(15): p. 1650-1662.
10. Prabakaran, M. and J. Mano, Chitosan-based particles as controlled drug delivery systems. *Drug delivery*, 2004. **12**(1): p. 41-57.
11. Pillai, O. and R. Panchagnula, Polymers in drug delivery. *Current opinion in chemical biology*, 2001. **5**(4): p. 447-451.
12. Gombotz, W.R. and D.K. Pettit, Biodegradable polymers for protein and peptide drug delivery. *Bioconjugate chemistry*, 1995. **6**(4): p. 332-351.
13. Yamaguchi, T., Lipid microspheres as drug carriers: a pharmaceutical point of view. *Advanced drug delivery reviews*, 1996. **20**(2-3): p. 117-130.
14. Hall, M. and C. Ricketts, The use of dextran sulphate as a blood anticoagulant in biological research. *Journal of clinical pathology*, 1952. **5**(4): p. 366-366.
15. Bugg, H.M., P.H. King, and C.W. Randall, Polyelectrolyte conditioning of alum sludges. *Journal (American Water Works Association)*, 1970: p. 792-795.
16. Bijlsma, R., A. Van Well, and M.C. Stuart, Characterization of self-assembled multilayers of polyelectrolytes. *Physica B: Condensed Matter*, 1997. **234**: p. 254-255.
17. Lankalapalli, S. and V.M. Kolapalli, Polyelectrolyte complexes: A review of their applicability in drug delivery technology. *Indian journal of pharmaceutical sciences*, 2009. **71**(5): p. 481.

18. Becker, A.L., A.P. Johnston, and F. Caruso, Layer-By-Layer-Assembled Capsules and Films for Therapeutic Delivery. *Small*, 2010. **6**(17).
19. Lvov, Y., K. Ariga, I. Ichinose, and T. Kunitake, Layer-by-layer architectures of concanavalin A by means of electrostatic and biospecific interactions. *Journal of the Chemical Society, Chemical Communications*, 1995(22): p. 2313-2314.
20. Caruso, F., D.N. Furlong, K. Ariga, I. Ichinose, and T. Kunitake, Characterization of polyelectrolyte– protein multilayer films by atomic force microscopy, scanning electron microscopy, and Fourier transform infrared reflection– absorption spectroscopy. *Langmuir*, 1998. **14**(16): p. 4559-4565.
21. Varde, N.K. and D.W. Pack, Microspheres for controlled release drug delivery. *Expert Opinion on Biological Therapy*, 2004. **4**(1): p. 35-51.
22. Jovanović, N., A. Bouchard, G.W. Hofland, G.-J. Witkamp, D.J. Crommelin, and W. Jiskoot, Stabilization of proteins in dry powder formulations using supercritical fluid technology. *Pharmaceutical research*, 2004. **21**(11): p. 1955-1969.
23. Nuchuchua, O., H. Every, G. Hofland, and W. Jiskoot, Scalable organic solvent free supercritical fluid spray drying process for producing dry protein formulations. *European Journal of Pharmaceutics and Biopharmaceutics*, 2014. **88**(3): p. 919-930.
24. Whitaker, M.J., J. Hao, O.R. Davies, G. Serhatkulu, S. Stolnik-Trenkic, S.M. Howdle, and K.M. Shakesheff, The production of protein-loaded microparticles by supercritical fluid enhanced mixing and spraying. *Journal of Controlled Release*, 2005. **101**(1): p. 85-92.
25. Mishima, K., K. Matsuyama, D. Tanabe, S. Yamauchi, T.J. Young, and K.P. Johnston, Microencapsulation of proteins by rapid expansion of supercritical solution with a nonsolvent. *AIChE Journal*, 2000. **46**(4): p. 857-865.
26. Dos Santos, I.R., J. Richard, B. Pech, C. Thies, and J. Benoit, Microencapsulation of protein particles within lipids using a novel supercritical fluid process. *International journal of pharmaceutics*, 2002. **242**(1): p. 69-78.
27. Jordan, F., A. Naylor, C. Kelly, S. Howdle, A. Lewis, and L. Illum, Sustained release hGH microsphere formulation produced by a novel supercritical fluid technology: in vivo studies. *Journal of Controlled Release*, 2010. **141**(2): p. 153-160.

28. Kang, Y., C. Yang, P. Ouyang, G. Yin, Z. Huang, Y. Yao, and X. Liao, The preparation of BSA-PLLA microparticles in a batch supercritical anti-solvent process. *Carbohydrate Polymers*, 2009. **77**(2): p. 244-249.
29. Young, T.J., K.P. Johnston, K. Mishima, and H. Tanaka, Encapsulation of lysozyme in a biodegradable polymer by precipitation with a vapor-over-liquid antisolvent. *Journal of pharmaceutical sciences*, 1999. **88**(6): p. 640-650.
30. Tu, L.S., F. Dehghani, and N. Foster, Micronisation and microencapsulation of pharmaceuticals using a carbon dioxide antisolvent. *Powder Technology*, 2002. **126**(2): p. 134-149.
31. Kluge, J., F. Fusaro, N. Casas, M. Mazzotti, and G. Muhrer, Production of PLGA micro-and nanocomposites by supercritical fluid extraction of emulsions: I. Encapsulation of lysozyme. *The journal of Supercritical fluids*, 2009. **50**(3): p. 327-335.
32. Palamanit, A., S. Prachayawarakorn, P. Tungtrakul, and S. Soponronnarit, Performance Evaluation of Top-Spray Fluidized Bed Coating for Healthy Coated Rice Production. *Food and Bioprocess Technology*, 2016. **9**(8): p. 1317-1326.
33. Werner, S.R., J.R. Jones, A.H. Paterson, R.H. Archer, and D.L. Pearce, Air-suspension particle coating in the food industry: Part I—State of the art. *Powder Technology*, 2007. **171**(1): p. 25-33.
34. Zwietering, T.N., Suspending of solid particles in liquid by agitators. *Chemical Engineering Science*, 1958. **8**(3-4): p. 244-253.
35. Caruso, F. and H. Möhwald, Protein multilayer formation on colloids through a stepwise self-assembly technique. *Journal of the American Chemical Society*, 1999. **121**(25): p. 6039-6046.
36. Bromberg, L.E. and A.M. Klibanov, Transport of proteins dissolved in organic solvents across biomimetic membranes. *Proceedings of the National Academy of Sciences*, 1995. **92**(5): p. 1262-1266.
37. Nobbmann, U. Zeta deviation larger than the mean – how can that be? 2015 [accessed: 2017 22/08]; Available from: <http://www.materials-talks.com/blog/2015/09/24/zeta-deviation-larger-than-the-mean-how-can-that-be/>.
38. Sophianopoulos, A., C. Rhodes, D. Holcomb, and K. Van Holde, Physical studies of lysozyme I. Characterization. *Journal of Biological Chemistry*, 1962. **237**(4): p. 1107-1112.

39. van Beers, M.M., C. Slooten, J. Meulenaar, A.S. Sediq, R. Verrijck, and W. Jiskoot, Micro-Flow Imaging as a quantitative tool to assess size and agglomeration of PLGA microparticles. *European Journal of Pharmaceutics and Biopharmaceutics*, 2017. **117**: p. 91-104.
40. Nagendra, H., C. Sudarsanakumar, and M. Vijayan, An X-ray analysis of native monoclinic lysozyme. A case study on the reliability of refined protein structures and a comparison with the low-humidity form in relation to mobility and enzyme action. *Acta Crystallographica Section D: Biological Crystallography*, 1996. **52**(6): p. 1067-1074.
41. Sigma-Aldrich. Dextran sulphate Product Information. [accessed: 2017 22/08]; Available from: https://www.sigmaaldrich.com/content/dam/sigmaaldrich/docs/Sigma/Product_Information_Sheet/d8906pis.pdf.
42. Cheema, U., *Standardisation in Cell and Tissue Engineering: Methods and Protocols*. 2013, Woodhead publishing.
43. Maronga, S., *On the optimization of the fluidized bed particulate coating process*. 1998, Kemiteknik.
44. Saini, V., Fluidized bed processing for multiparticulates. *J. Chem*, 2009. **2**(2): p. 447-450.
45. Dewettinck, K. and A. Huyghebaert, Top-spray fluidized bed coating: Effect of process variables on coating efficiency. *LWT-Food Science and Technology*, 1998. **31**(6): p. 568-575.
46. Mishra, M., *Handbook of encapsulation and controlled release*. 2015: CRC Press.
47. Lüsse, S. and K. Arnold, Water binding of polysaccharides NMR and ESR studies. *Macromolecules*, 1998. **31**(20): p. 6891-6897.
48. Xu, B., K. Nagashima, J.M. DeSimone, and C.S. Johnson, Diffusion of water in liquid and supercritical carbon dioxide: an NMR study. *The Journal of Physical Chemistry A*, 2003. **107**(1): p. 1-3.
49. Cadogan, S.P., G.C. Maitland, and J.M. Trusler, Diffusion Coefficients of CO₂ and N₂ in Water at Temperatures between 298.15 K and 423.15 K at Pressures up to 45 MPa. *Journal of Chemical & Engineering Data*, 2014. **59**(2): p. 519-525.
50. Omer, K. and N. Ashgriz, Spray nozzles, in *Handbook of Atomization and Sprays*. 2011, Springer. p. 497-579.
51. Masters, K., *Spray drying handbook*. 1985, London: George Godwin Ltd.

52. Kamiya, N. and A.M. Klibanov, Controlling the rate of protein release from polyelectrolyte complexes. *Biotechnology and bioengineering*, 2003. **82**(5): p. 590-594.
53. George, M. and T.E. Abraham, Polyionic hydrocolloids for the intestinal delivery of protein drugs: alginate and chitosan—a review. *Journal of controlled release*, 2006. **114**(1): p. 1-14.
54. Liao, I.-C., A.C. Wan, E.K. Yim, and K.W. Leong, Controlled release from fibers of polyelectrolyte complexes. *Journal of Controlled Release*, 2005. **104**(2): p. 347-358.
55. Shu, S., C. Sun, X. Zhang, Z. Wu, Z. Wang, and C. Li, Hollow and degradable polyelectrolyte nanocapsules for protein drug delivery. *Acta Biomaterialia*, 2010. **6**(1): p. 210-217.
56. Mehrotra, S., D. Lynam, R. Maloney, K.M. Pawelec, M.H. Tuszynski, I. Lee, C. Chan, and J. Sakamoto, Time Controlled Protein Release from Layer-by-Layer Assembled Multilayer Functionalized Agarose Hydrogels. *Advanced functional materials*, 2010. **20**(2): p. 247-258.

Chapter 3

*Molecular structure of dextran sulphate sodium in aqueous environment**

Miao Yu, Hayley A. Every, Wim Jiskoot, Geert-Jan Witkamp, Wim Buijs

Adapted from the Journal of Molecular Structure, 1156 (2018): 320-329.

*An introduction to the theoretical background of molecular modelling is presented in Appendix B.

Abstract

Here we propose a 3D-molecular structural model for dextran sulphate sodium (DSS) in a neutral aqueous environment based on the results of a molecular modelling study. The DSS structure is dominated by the stereochemistry of the 1,6-linked α -glucose units and the presence of two sulphate groups on each α -glucose unit. The structure of DSS can be best described as a helix with various patterns of di-sulphate substitution on the glucose rings. The presence of a side chain does not alter the 3D-structure of the linear main chain much but affects the overall spatial dimension of the polymer. The simulated polymers have a diameter similar to or in some cases even larger than model α -hemolysin nano-pores for macromolecule transport in many biological processes, indicating a size-limited translocation through such pores. All results of the molecular modelling study are in line with previously reported experimental data. This study establishes the three-dimensional structure of DSS and summarises the spatial dimension of the polymer, serving as the basis for a better understanding of the molecular level of DSS-involved electrostatic interaction processes with biological components like proteins and cell pores.

3.1 Introduction

Dextran sulphate sodium (DSS) is a polyanionic derivative of dextran with sodium sulphate groups ($-\text{OSO}_3\text{Na}$) attached to each repeating unit. DSS is widely applied in food, biotechnology, pharmaceutical and cosmetic industry and functions as coating material, anticoagulant agent, purification reagent, and conditioning agent [1-6]. DSS-involved interactions with protein materials have been widely studied with examples like DSS-protein complexation and particle formation for protein delivery purposes [7] and DSS passage through protein nano-channels inserted in a bilayer lipid membrane [8, 9]. A realistic description of the three-dimensional (3D) structure of DSS and its flexibility is of utmost importance for a better understanding of the interaction between DSS and proteins, especially for the study relying on the spatial dimension of the polymer like the translocation via protein nano-channels.

Proposals for the 3D structure of polymeric carbohydrates have been mainly based on X-ray crystallography and nuclear magnetic resonance (NMR) measurements [10-13]. Whenever there is no experimental structure of a polymer available, especially in an aqueous environment, and when it is extremely difficult to study the structure in a liquid environment in sufficient detail by experimental methods, molecular modelling can be an efficient tool to explore the structure. Molecular mechanics performs very well for a wide range of molecules throughout almost the entire periodic table. For large systems, it is the only realistic option for molecular geometry optimisation both with respect to the accuracy of the structure and computational time. In this study, the Merck molecular force field (MMFF) [14] is used. The optimised geometries obtained by MMFF provide good initial points for other studies like quantum mechanics modelling, molecular dynamics simulations, etc.

The molecular structures of monosaccharides, e.g., glucose, in the aqueous environment have been widely studied by molecular modelling via molecular mechanics methods [15-18]. Geometric features like bond distances, bond angles, pyranose ring conformation, and formation of hydrogen bridges with surrounding water molecules were well elucidated. Oligosaccharides or polysaccharides, e.g., dextrans, have not been studied as much by molecular mechanics as monosaccharides [19, 20]. Molecular modelling might shine light on characteristics like the rotation along glycosidic linkages and derived torsional angles, polymer elasticity, and competition among intramolecular hydrogen bridges and intermolecular hydrogen bridges. Up to now, literature reporting the molecular structure of sulphated polysaccharide derivatives is scarce [21], and as far as we know, there are no publications presenting neither the experimentally nor theoretically determined 3D-molecular structure of DSS. In this study, the 3D-structure of DSS is determined using an approach which can be applied to other (carbohydrate) polymers as well. The resulting DSS structure will be used to study the electrostatic interactions and structural dynamic behaviour with biological components like proteins and cell pores.

In this study, it is aimed to establish the molecular structure of DSS with an average molecular weight of 5000 Da, which value was chosen considering the frequent usage of this size of DSS. The parental polymer of DSS, dextran, is a highly-linear polymer of anhydroglucose produced by *Leuconostoc* spp. and related microorganisms, connected mainly via α -1,6-linkages. These α -D-glucans also possess side-chains, connected mainly via α -1,3- and occasionally via α -1,4- or α -1,2- branched linkages [22]. The exact structure of each type of dextran depends on its specific producing microbial strain and hence on the specific type of dextransucrase(s) involved [22, 23]. Dextran, as the parental structure for the production of DSS, according to the manufacturer's information [24], is produced via an enzymatic process from *Leuconostoc mesenteroides*, strain B 512. The produced dextran contains 95% α -1,6-linkages and 5% α -1,3-branch linkages [25, 26]. The sulfur content in DSS is about 17-18%, which is equivalent to approximately two $-\text{OSO}_3\text{Na}$ ester groups per glucose residue [27, 28]. The $-\text{OSO}_3\text{Na}$ moieties can be located on different carbons of the glucose ring [29-32]. Carbon 2 and 3 (C-2,3) appear to be more reactive towards sulphation than the other carbon positions, and carbon 2, 3 and 4 (C-2,3,4) are the common sites for dextran di-sulphation [32, 33]. C-2,3 are more suitable for di-substitution than carbon 2 and 4 (C-2,4) and carbon 3 and 4 (C-3,4) and all the three types of di-sulphation occur in the DSS product [29-33]. In our model, DSS structures with di-sulphation onto C-2,3, C-2,4, and C-3,4 are used for structural determination.

3.2 Approach

An updated version of the Merck Molecular Force Field (MMFF), developed by Merck Research Laboratories [14], was applied. MMFF is an integral part of the Spartan'16 software package [34], which was used for all calculations.

A common DSS, obtained from Sigma Aldrich (Product Number: D7037), has an average molecular weight of 5000. This corresponds approximately to a dodecamer of α -1,6-D-glucose with two $-\text{OSO}_3\text{Na}$ moieties on each glucose ring. Although the material is delivered as a solid, it is commonly used in an aqueous solution. Therefore, particular attention was paid to the role of the aqueous solvent, not only in adding various amounts of H_2O explicitly but also the building and construction of the $-\text{OSO}_3\text{Na}$ units on the sugar rings. They were introduced *in silico* as species in solution, which result in more accurate solvation energies in the molecular modelling calculations.

Starting from the established structure of α -D-glucose monomer, a tetramer was constructed with the correct stereochemistry around the 1,6-glycosidic bond [22-24]. A full conformer distribution (CD) of the tetramer was determined. From the obtained CD, low strain energy head-to-tail conformers were

discarded, as these comprised intramolecular head-to-tail hydrogen bridges, which were considered unrealistic in the aqueous environment. For the same reason, building a dodecamer of dextran based on dimeric or trimeric α -D-glucose was not a good approach. On the other hand, a real systematic search to a conformer distribution of the dodecamer generated a huge number of possible conformers, which would be too costly with respect to computational time. Thus, as an optimal feasible approach, the final conformation for the lowest-energy equilibrium conformer of the dodecamer of dextran was obtained by triplication of the best conformer of the tetramers, using the detailed geometric data of the connection between the second and the third glucose ring to construct the 4,5 and 8,9 couplings in the final dextran dodecamer. This was another strong reason to use the tetramer for building the dodecamer, as the tetramer is the smallest oligomer with 2 internal α -glucose units. Next, the final geometry of the dodecamer was obtained by an unrestricted normal geometry optimisation.

Two (-OSO₃Na) groups in close vicinity on each α -D-glucose unit are the ionic functional groups on DSS. Regarding the fact that the ionic bonds between sodium cation and sulphate anion are subject to hydration, the optimised molecular structure of a sodium sulphate (Na₂SO₄) dimer in the presence of H₂O was studied before introducing these charged groups to the dextran dodecamer. The ionic option for the type of bonds between the sulphate anion and the sodium cation was chosen. Furthermore, explicit solvation with various numbers of H₂O was carried out.

On average, DSS contains two (-OSO₃Na) ester groups per α -D-glucose unit. To study the effect of these strongly ionic groups on the structure of DSS, two (-OSO₃Na) ester groups were added onto the positions C-2,3, C-2,4 and C-3,4 of the α -D-glucose unit. Next, CD's were determined for the three different α -D-glucose units with two (-OSO₃Na) ester groups, while keeping the geometry of the sugar ring intact. Via these CD's, the preferred positions of the di-(-OSO₃Na) ester groups, as well as surrounding H₂O molecules, to the α -D-glucose unit were obtained. In the later building process of the final DSS dodecamers, the preferred positions of the di-(-OSO₃Na) ester groups and surrounding H₂O molecules were initially fixed in the model, followed by cutting them as a whole group. These fixed groups were connected to each α -D-glucose unit along the dextran dodecamer to achieve structures of DSS dodecamers containing 12 di-(-OSO₃Na) ester groups and surrounding H₂O molecules. After completion of the building process, the connected di-(-OSO₃Na) ester groups and surrounding H₂O molecules were unfixed, and an unrestricted full geometry optimisation was carried out.

Statistically, there are about 5% of α -1,3 branched linkages among the DSS polymers. To study the influence of the side chain on the structure of DSS, a two-unit-long DSS moiety was connected to the DSS dodecamer with an α -C-1,3 linkage onto one of the α -D-glucose units, followed by geometry optimisation.

3.3 Results

3.3.1 3D structure of dextran dodecamer

D-glucose, which is the monomeric unit of dextran, exists in two forms, α -D-glucose and β -D-glucose, which differ in the position of the hydroxyl(-OH) group on carbon 1 (C-1) of the glucose ring. The α -form has the -OH group on C-1 on the opposite side of the methyl hydroxyl (-CH₂OH) group on carbon 6 (C-6). The β -form has both chemical groups on the same side. Figure 3.1 shows the two forms with their strain energies from the MMFF calculation. According to MMFF, α -D-glucose is slightly more stable than the β form, in line with previously reported theoretical and experimental results [35, 36].

The molecular structures of the α -D-glucose monomer, the α -D-dextran tetramer and the dodecamer are shown in Figure 3.2. A helix structure was obtained for the dextran dodecamer. This served as the parental structure for the final DSS structures.

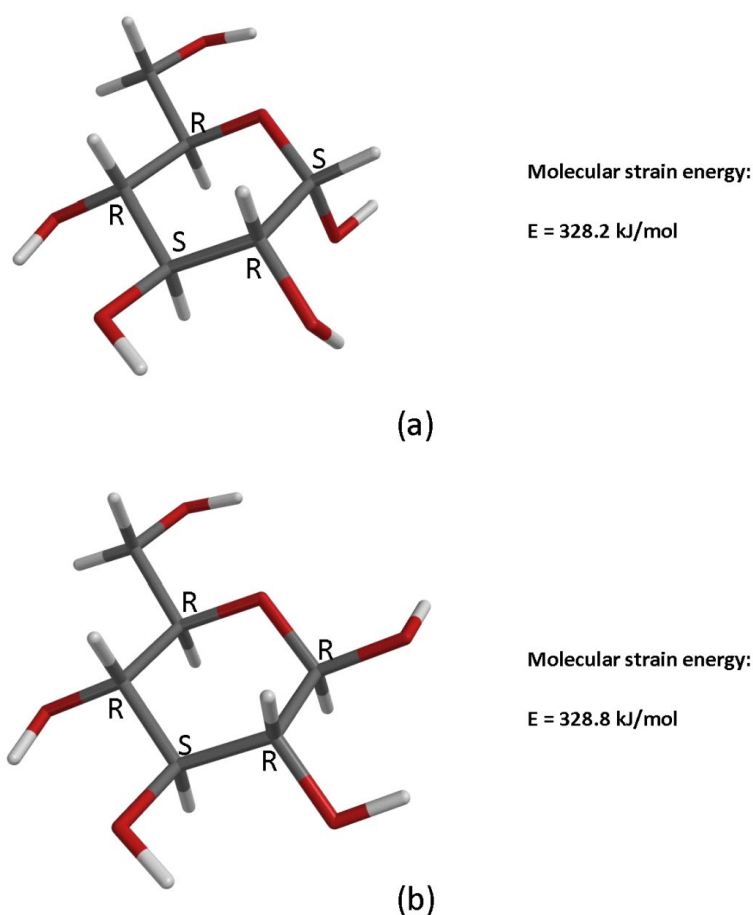


Figure 3.1. Molecular structure displayed in a tube format of α -D-glucose (a) and β -D-glucose (b) and corresponding molecular strain energy. R and S indicate the absolute stereochemistry on the glucose carbons. Grey represents carbon, red oxygen and white hydrogen. This representation is applied in the following figures too.

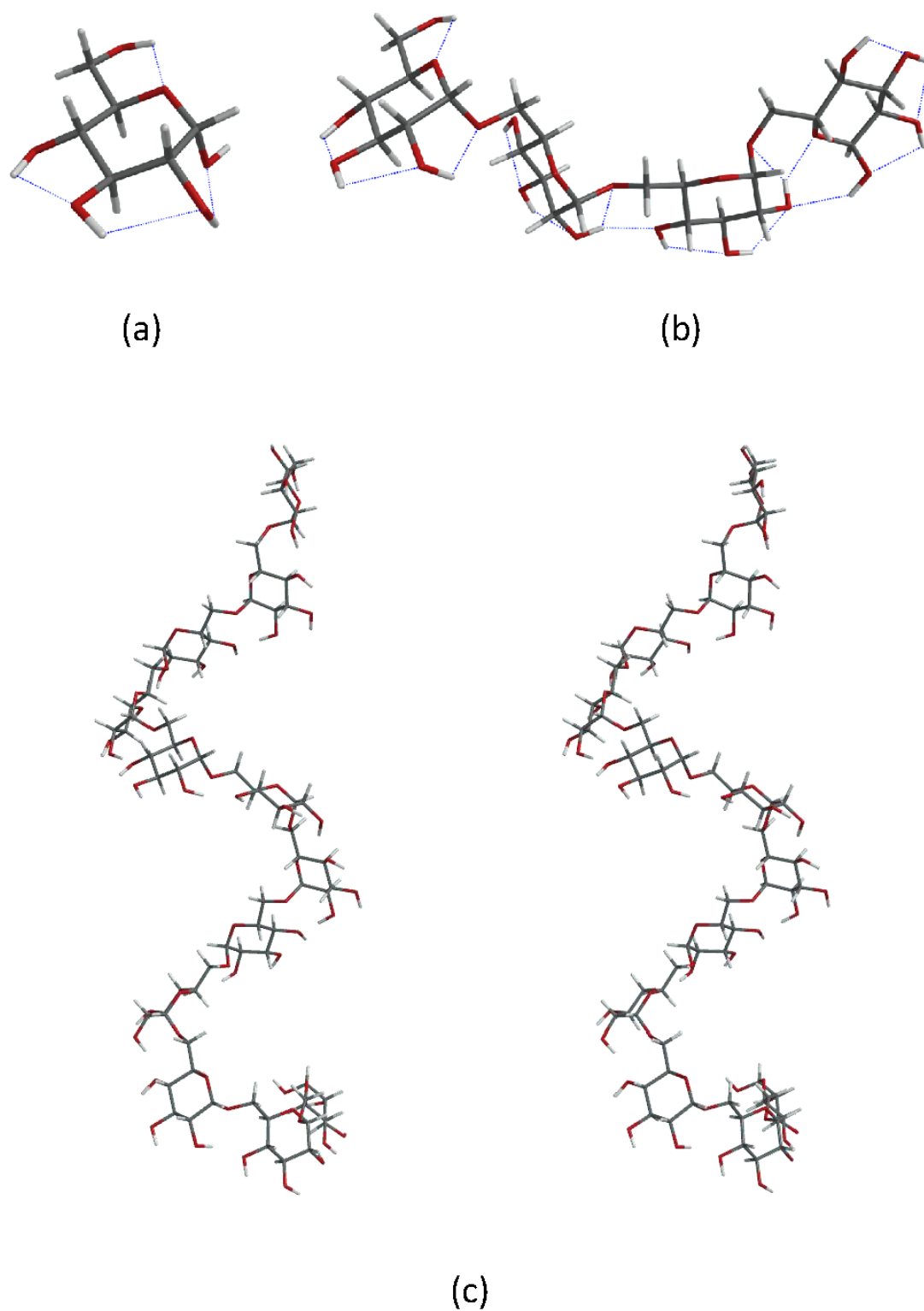


Figure 3.2. MMFF-optimised equilibrium geometry of α -D-glucose monomer (a), tetramer (b) and dodecamer (c), where a cross-eyed stereo-pair picture of the dodecamer is displayed. The blue dashed lines represent hydrogen bridges. See Figure 3.1 for the explanation of the tube colours.

From the tetrameric structure presented in Figure 3.2 (b), it can be seen that the first α -glucose ring shows a hydrogen bridge between the -OH group on carbon 6 (C-6) and the oxygen on C-5 in the ring, and the fourth glucose ring shows a hydrogen bridge between the -OH group on C-1 and the oxygen on C-2 of the third glucose ring. In constructing the final dodecamer of dextran, the geometry of the coupling between the second and the third α -glucose ring was taken, as this connection was influenced by neither head nor tail interactions.

3.3.2 Equilibrium geometry of Na_2SO_4 dimer

Normally, dextran sulphates are supplied as sodium salts. In this study, we wanted to elucidate the structure of the dextran sulphate sodium (DSS) in a neutral aqueous environment. As mentioned before, on average, two ($-\text{OSO}_3\text{Na}$) ester groups are located on one glucose ring in close vicinity. Therefore, the behaviour of two molecules of Na_2SO_4 in an aqueous environment was studied. Figure 3.3 shows the equilibrium geometries of one and two Na_2SO_4 molecules with water as the solvent.

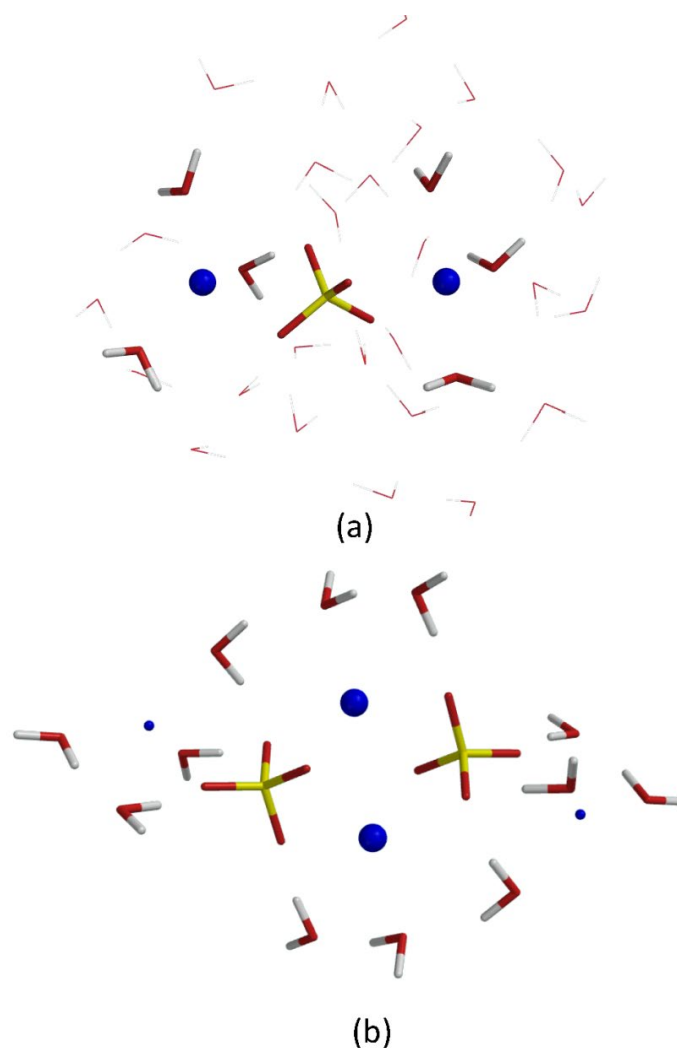


Figure 3.3. (a): Equilibrium geometry of Na_2SO_4 in an aqueous environment (with 32 H_2O molecules); (b) two Na_2SO_4 molecules present with 12 surrounding (coordinating) H_2O molecules. In the figures, blue balls represent Na, S is in yellow and the thin wires represent H_2O . The two Na ions positioned in between the two sulphates are highlighted. All these representations are used for the following figures.

There is a strong interaction between sodium cations and sulphate anions. Three H_2O molecules strongly coordinate to sodium (charge: +1), and with a weaker H-bridge to sulphate-oxygen (charge: about -0.5). Together with the nearby sulphate-oxygen, in total 5 oxygens coordinate to the Na cation. This is in line with previously reported studies on the hydration of the Na cation where 4-6 water-oxygen coordinate to one Na cation [37-39]. In the system of two Na_2SO_4 molecules, two Na cations are located in between the two sulphates (Figure 3.3 (b)). Now the above-mentioned 4-6 coordination of the Na cation is obtained with 2-3 sulphate-oxygens and 3 water-oxygens. Thus, three H_2O

molecules close to one Na cation were used to describe the behaviour of Na₂SO₄ in the aqueous environment.

In DSS, the two Na cations will also be located in between the two sulphates which are held close together by their substitution pattern on the sugar ring.

3.3.3 Equilibrium geometry of DSS

There are documents stating that “DSS is produced via the esterification with sulphuric acid carried out under mild conditions” [24]. However, this cannot be the case as extensive de-polymerisation occurs under these conditions [40]. Therefore a powerful neutral sulphating agent like chlorosulphonic acid pyridine is mostly used to avoid polymer degradation [41, 42]. Chlorosulphonic acid in pyridine was reported for the sulphation of dextran in previous studies [32, 43].

Figure 3.4 shows the monomeric α -D-glucose with different di-sulphation patterns optimised in MMFF with and without solvent water molecules. The sulphate groups are in equatorial position rather than axial position to avoid unfavourable sterical hindrance, similar to what was found before [33]. The two sulphate mono anions hold two Na cations in-between. In the di-sulphated glucose structure in the absence of H₂O, the sulphate-O to Na distance is about 2.1-2.2 Å, and Na-Na distance is about 4.8 Å, while in the presence of H₂O, these values are about 2.1-4.1 Å and 5.2 Å respectively. These differences in atomic distances reflect the solvation power of H₂O. Thus, based on the studies above, combining the best conformer of the glucose with the best geometry of the two (-OSO₃Na) groups leads to the best structure for the monomeric di-sulphated glucose units. The latter was used to build the final DSS structures in the presence of H₂O.

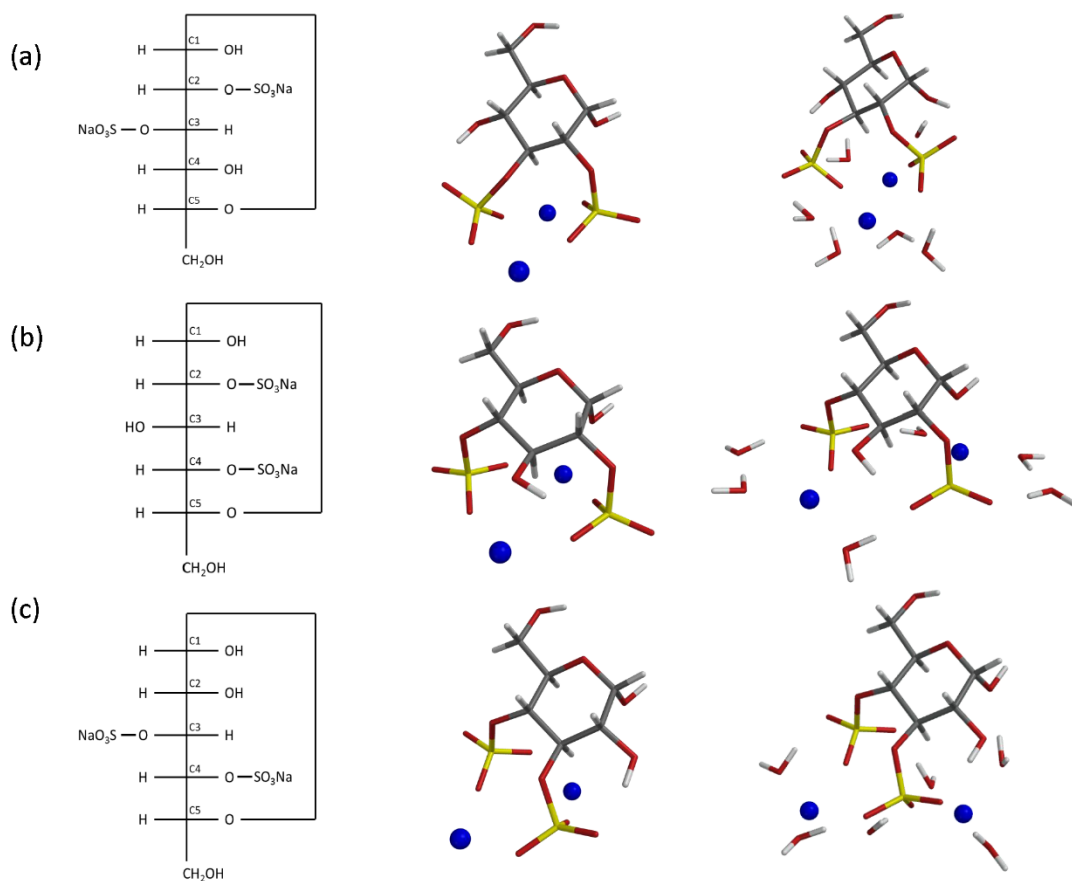
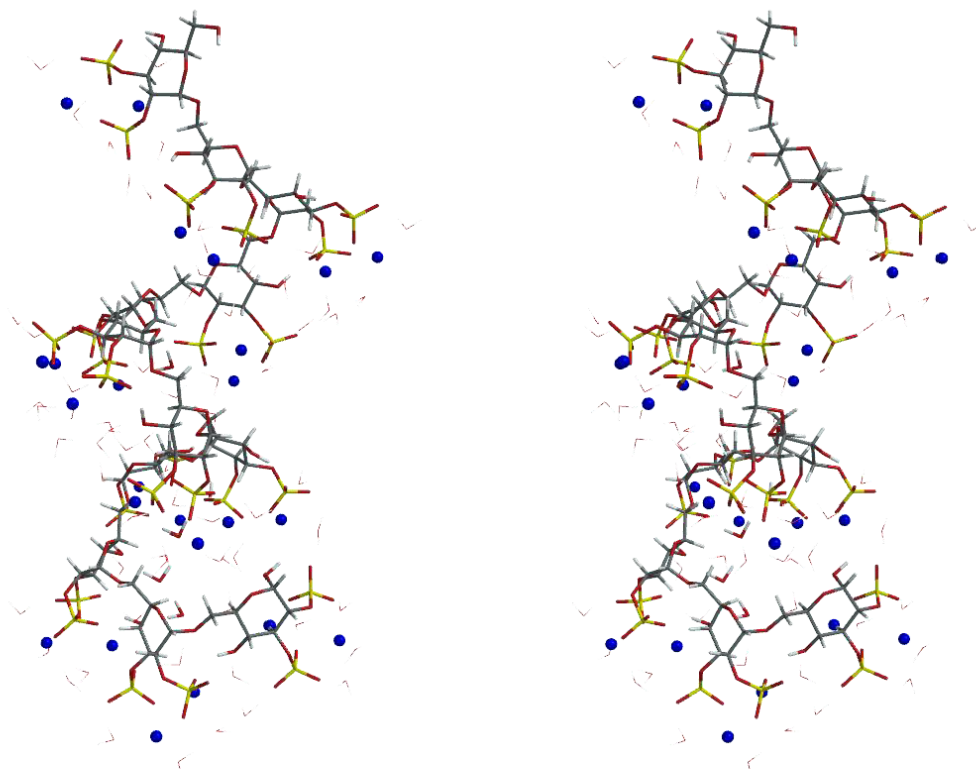
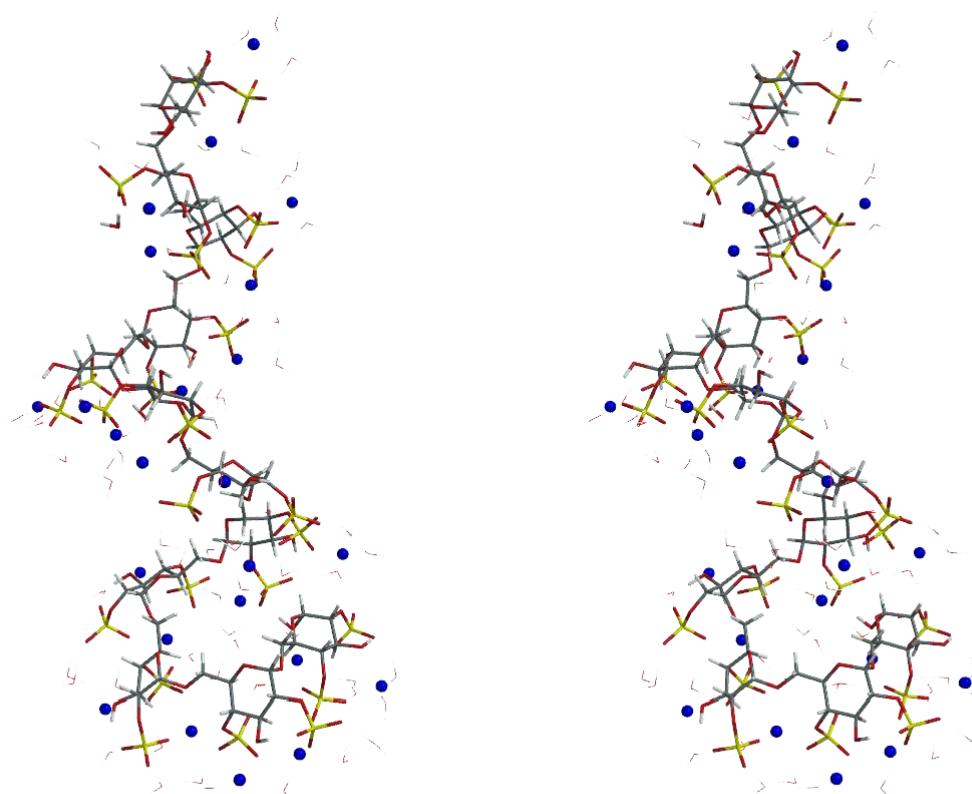


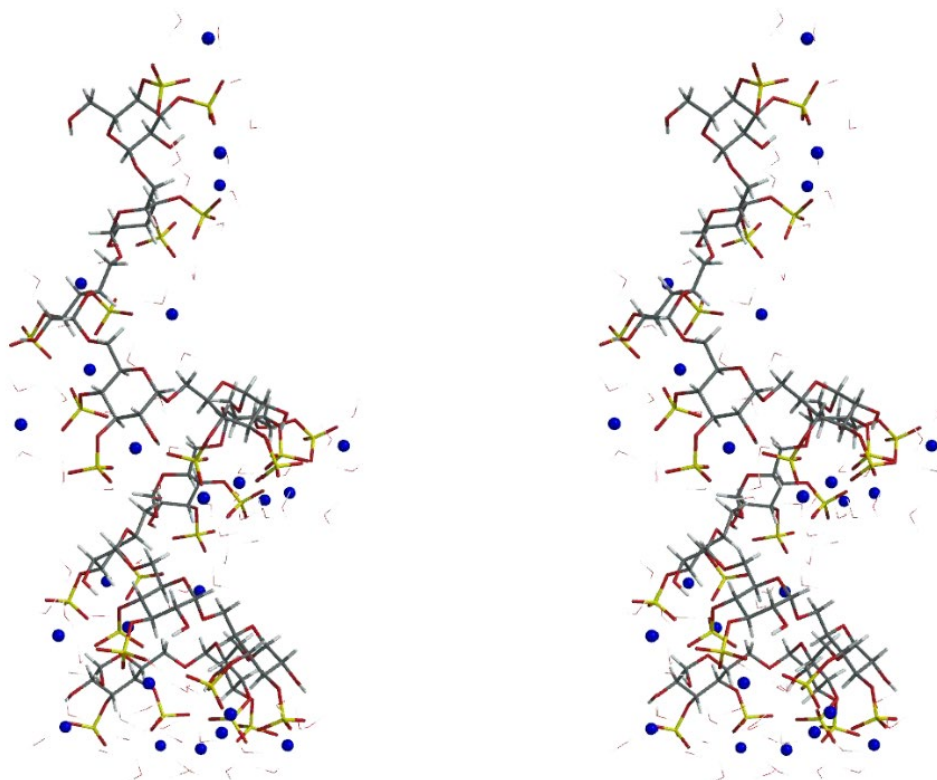
Figure 3.4. The graphs in the left column represent the Fischer projection of di-sulphated monomeric glucose ring. The graphs in the middle are a translation of the Fischer projection images into 3D molecular structures. The graphs on the right show the di-sulphated monomeric glucose in the presence of H₂O. Row (a) represents a glucose with C-2,3 di-sulphation; (b) C-2,4 di-sulphation and (c) C-3,4 di-sulphation. See Figure 3.1 and Figure 3.3 for the explanation of colours.



(a)



(b)



(c)

Figure 3.5. Equilibrium geometries of C-2,3 (a), C-2,4 (b) and C-3,4 (c) DSS dodecamers with 72 surrounding H₂O molecules. Cross-eyed stereo-pair pictures are displayed. See Figure 3.1 and Figure 3.3 for the explanation of colours.

Figure 3.5 shows the DSS dodecamer structure in the presence of 72 H₂O molecules, corresponding to 3 H₂O per Na cation. The three DSS structures are helices, similar to that of the parental dextran structure. In each glucose unit, the two Na cations are located in-between two neighbouring sulphate anions.

Table 3.1. Characteristics of the helix conformation of dextran and DSS dodecamers.

Characteristics	DSS geometric properties in aqueous environment						
	Dextran	Types of di-sulphation ¹					
		C2,3	C2,4	C3,4	Mixed ⁴	Mixed (1000 H ₂ O)	Mixed (side chain) ⁵
Dihedral angle ^{2,3}	120.5°; 153.4°	108.1°	129.1°	151.8°	126.8°	142.7°	-
Na to sulphate-O distance (Å)	-	2.5	3.0	3.1	2.7	3.3	-
Length (Å) ³	43.9	41.5	42.1	42.9	39.0	41.1	41.6
Diameter (Å) ³	16.2	20.3	18.7	19.5	19.8	20.7	22.6
Band width (Å) ³	9.0	11.7	10.0	10.0	10.9	11.6	11.1

¹: if not specified else, the DSS geometry is with 72 H₂O molecules.

²: average of dihedral angles along the DSS dodecamer structure.

³: see Figure 3.6 for the explanation of the various geometric properties.

⁴: Mixed: there is a mixture of different di-sulphation patterns on the pyranose rings of the dodecamer according to statistical information from previously reported experimental results.

⁵: Mixed (side chain): attach a two units long side chain onto the linear DSS dodecamer.

Table 3.1 shows the geometric properties of dextran dodecamer and DSS dodecamer under different conditions, including the dimensions and the average value of the pairs of dihedral angles, which are illustrated in Figure 3.6. The lengths of the various DSS dodecamers are about 40 Å. The length is measured as the distance between the tips of the helix ends. Uniformly substituted DSS dodecamers are longer than mixed substituted DSS dodecamers, however their diameters and band widths are approximately the average of the uniformly substituted DSS dodecamers. In order to get a quantitative impression of the effect of full aqueous solvation, the number of H₂O molecules in the mixed DSS dodecamer was increased to 1000 (see Figure 3.7). The effect is a small increase in the geometric parameters of approximately 5%. Dextran shows energy minima at two dihedral angles of about 121° and 153° between each glucose ring, thus leading to 2¹¹ possible conformers. As the energy difference between the two conformers is about 0.6 kJ/mol only, the dextran helix structure will be very flexible with respect to these dihedrals.

Diameter and band width of DSS dodecamers (about 20 Å and 11 Å respectively) are larger than those of the dextran (about 16 Å and 9 Å respectively). The branched DSS obviously has a larger diameter (about 23 Å) than the linear DSS (about 20 Å).

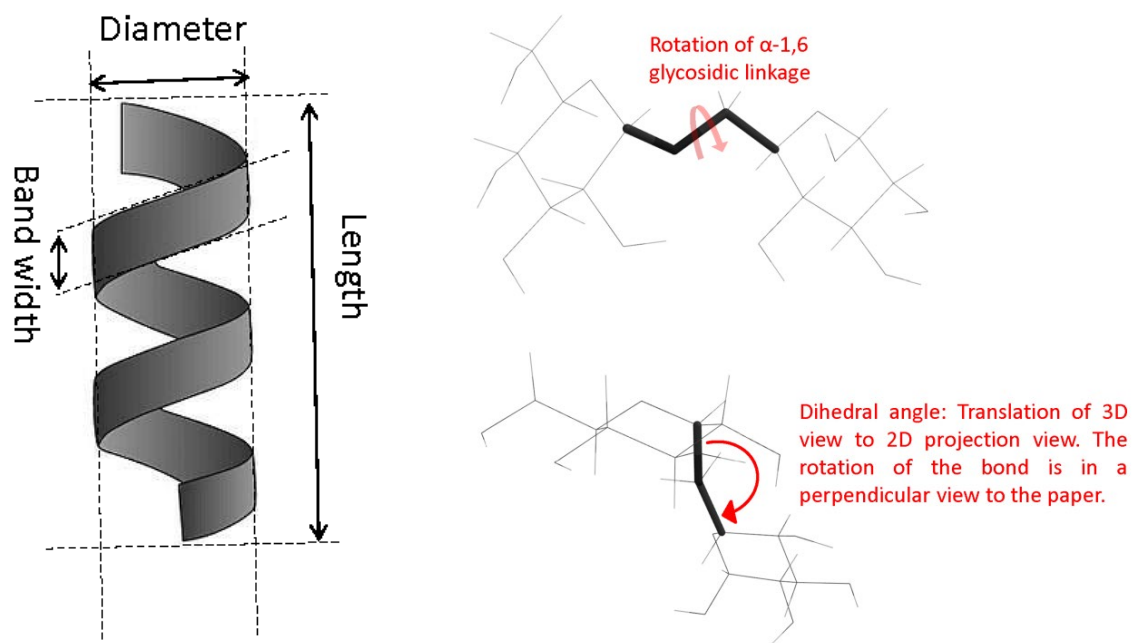


Figure 3.6. Schematic of geometric properties of the DSS helix molecule measured in this study (see Table 3.1).

Table 3.2. The strain energy of di-sulphated glucose and DSS dodecamers with various types of di-sulphation calculated by MMFF.

Compound	Strain energy (kJ/mol)	
	Vacuum	Aqueous
α -D-glucose monomer 2,3-di-Na sulphate	-1433.0	-1854.4
α -D-glucose monomer 2,4-di-Na sulphate	-1419.9	-1840.3
α -D-glucose monomer 3,4-di-Na sulphate	-1393.4	-1802.3
α -1,6-D-dextran dodecamer 2,3-di-Na sulphate	–	-22178.3
α -1,6-D-dextran dodecamer 2,4-di-Na sulphate	–	-22022.5
α -1,6-D-dextran dodecamer 3,4-di-Na sulphate	–	-21954.5
α -1,6-D-dextran dodecamer mixed-type-di-Na sulphate	–	-21898.9

Table 3.2 lists the results of the MMFF strain energies for C-2,3, C-2,4 and C-3,4 di-sulphated α -D-glucose monomers and the corresponding DSS dodecamers. They are in line with previously reported experimental results. It was stated that on the glucose ring, C-2 is the most active site for sulphation, followed by C-3 and then C-4. Thus after di-sulphation, the amount of C-2,3 di-sulphated species is higher than C-2,4 and C-3,4, which reflects the relative stability of the variously di-sulphated molecules [31, 32].

3.3.4 Mixed type of di-sulphation

In reality, DSS contains a mixture of various C-2,3, C-2,4 and C-3,4 di-sulphated polymers of different lengths, with an average chain length of 12. The average substitution pattern on the glucose rings is about C-2,3/C-2,4/C-3,4 = 6/5/1 in a random way [29-31]. The mixed structure shown in Figure 3.7 is thus only one candidate out of thousands of structures with almost equal possibilities.

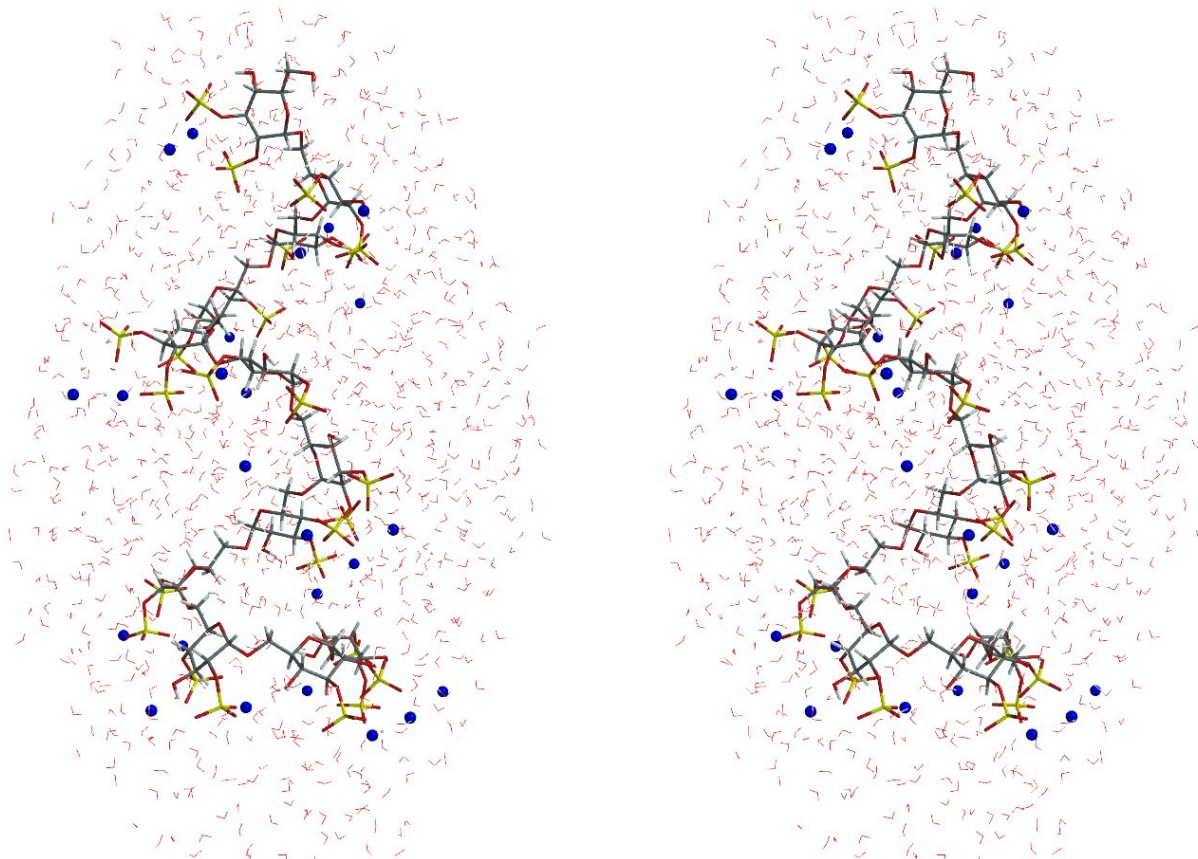


Figure 3.7. Equilibrium geometry of DSS with quasi randomly-arranged mixed sulphation in the presence of 1000 water molecules. In detail, C-2,3 di-sulphation for the polymerisation units of 1, 3, 5, 7, 9 and 11; C-2,4 di-sulphation for unit 2, 4, 6, 10 and 12; C-3,4 di-sulphation for unit 8. A cross-eyed stereo-pair picture is displayed. See Figure 3.1 and Figure 3.3 for the explanation of colours.

Comparing the geometric data of the mixed DSS dodecamer with uniform DSS dodecamer does not reveal large differences. Thus, the simulated DSS dodecamer can be considered as representative for real (mixed) DSS.

With 72 surrounding H₂O molecules (3 per sodium ion), the mixed DSS dodecamer shows a shrinkage compared with the uniform DSS (see Table 3.1). This is due to the closer interaction of –OSO₃Na on adjacent glucose rings within the groove of the helix. The difference between the DSS structure with 72 H₂O and 1000 H₂O molecules is limited, as mentioned before.

3.3.5 DSS with side chain

Dextran is built up mainly based on α -(1,6) linkages (approximately 95%). The remaining 5% are α -(1,3) linkages accounting for the branching of dextran. The length of the side chains of dextran has been studied by sequential degradation, and the results prove that more than 80% of the side chains contain less than 2 glucose units [22, 44-48]. Figure 3.8 shows the result of a structure with a side chain linked at the 6th unit of the DSS main chain via a 1,3 linkage. The side chain consisted of two units of 1,6-linked di-sulphated α -D-glucose. The helix of the main chain structure was preserved. Due to the presence of the side chain and its interaction with the main chain, the pitch of the helix was slightly shortened. Furthermore, the orientation of the glucose planes, as well as the attached (-OSO₃Na) groups, were altered. Some -OSO₃Na groups were positioned outwards, contributing to the increase of the measured length or diameter of the polymer geometry.

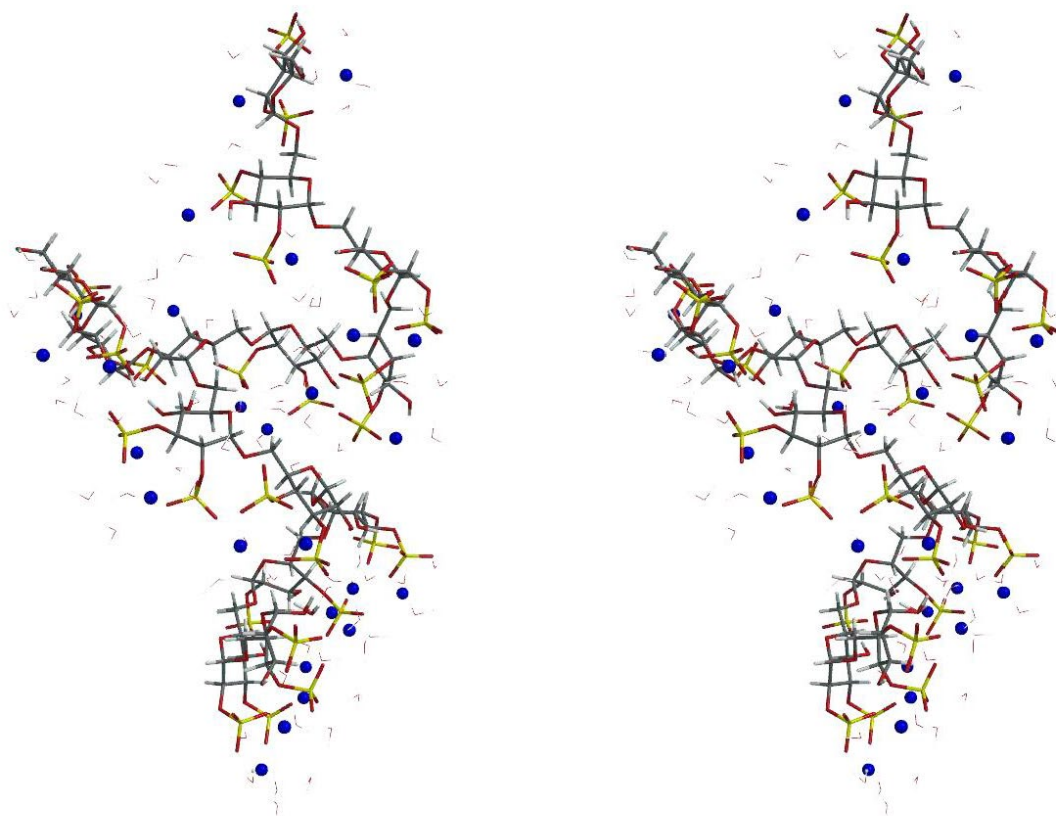


Figure 3.8. DSS structure with a two units side chain connected via 1,3 linkages at the 6th unit of the mixed DSS dodecamer in the presence of 72 H₂O molecules. In detail, C-2,3 di-sulphation for the polymerisation units of 1,3,5,7,9 and 11; C-2,4 di-sulphation for unit 2,4,10 and 12; C-3,4 di-sulphation for unit 8. A cross-eyed stereo-pair picture is displayed. See Figure 3.1 and Figure 3.3 for the explanation of colours.

3.4 Discussion

3.4.1 Molecular structure of dextran

3.4.1.1 Enzymatic synthesis of dextran

Enzymatic synthesis of dextran was reported previously [49, 50]. Dextranase catalyses the synthesis of dextran from sucrose. The proposed mechanism [22, 51, 52] is that dextran is biosynthesised by extrusion from the enzyme wherein glucose units are transferred from sucrose to the active site and inserted between the enzyme and the reducing end of the dextran polymer. The enzyme selectively makes an α -type glycosidic bond between the glucose units during the extension of the dextran chain. The α -1,6 linkage between glucose rings is one of the common types of linkages in the molecule of dextran depending on the type of producing microbial strain. The degree of polydispersity of dextran significantly affects its *in vivo* behaviour [53, 54]. Native isolated dextrans are often polydisperse. The target chain length ranges from approximately 10 to 1000. Either partial acidic or enzymatic hydrolysis is applied to reduce the polydispersity of the dextran polymer and prepare the target size.

3.4.1.2 Conformation of six-membered glucose ring and dextran

The structure of α -D-glucose has been described previously [15, 55, 56]. The glucose ring shows a normal chair conformation with all -OH groups and the $-\text{CH}_2\text{OH}$ group in an equatorial position, and only the glycosidic connection in an axial position due to the stereoselectivity of the enzyme.

Basic features that determine polysaccharide structures, like dextran, have been described in [57]. The 3D structure of dextran is dominated by the α -(1,6) glycosidic linkage, which leads to two similar conformations with a different angle between the imaginary planes of the six-membered rings of about 120 and 150 degrees ($\Delta E \approx 0.6$ kJ/mol). Consequently, dextran adopts a slightly disordered helix structure [58]. The influence of thermal noise ($E \approx 2.4$ kJ/mol) on the rotation of the α -(1,6) glycosidic linkage is limited. Thus the dynamic randomness of dextran is limited to the two possible angles between the imaginary planes of the six-membered rings. The optimised dextran dodecamer structure corresponds to one of the possible 2^{11} very similar conformations of dextran present in the natural aqueous environment.

3.4.1.3 Hydrogen bridges

The influence of hydrogen bridges is an important factor when dealing with modelling of carbohydrates and sugar-derived polymers in aqueous environment regarding the function of the maintenance of their preferred conformational structures. When simulating the carbohydrate in vacuum in the

absence of H₂O, the conformation of the molecule tends to be dominated by energetically favourable intramolecular hydrogen bridges among hydroxyl-hydrogen and neighbouring oxygen with mostly a length of about 2.2-2.3 Å. These are weak hydrogen bridges with an energy of less than 17 kJ/mol [59]. However, in an aqueous environment, the molecule tends to form hydrogen bridges with surrounding H₂O with 1.7-1.9 Å length, corresponding to higher energy of about 17-60 kJ/mol [59]. In the presence of H₂O, intermolecular hydrogen bridges replace the intramolecular hydrogen bridges, but this formation of hydrogen bridges among the glucose moieties and surrounding H₂O does not cause any conformational change of the six-membered rings [12].

3.4.1.4 Hydrogen bridges and –OSO₃Na groups

The electrostatic functional groups (-OSO₃Na) along DSS were proven to not influence the rotational dynamics of H₂O outside the first solvation shells of the ions, so no enhancement or breakdown of the hydrogen-bridge network in liquid water occurs [60]. In the DSS molecular structure worked out by modelling, there were two to three H₂O molecules located around each ionic group. The rest of the H₂O molecules, together with the hydrogen bridges among them, were little influenced by the presence of the polymer with ionised groups.

In conclusion, no literature was found on the influence of hydrogen bridges on the structure of DSS, let alone the function of hydrogen bridges for relevant DSS-involved interaction with other biomolecular assemblies in an aqueous environment.

3.4.2 Molecular structure of DSS

3.4.2.1 Neutral sulphation procedure

Among the existing procedures of production of DSS, the best-known procedure is the sulphation of polysaccharides with SO₃-pyridine [61], *in situ* formed by chlorosulphonic acid pyridine. During the sulphation process, a neutral environment is maintained where the sulphate esterification takes place on the hydroxyl groups of dextran. After cation exchange from pyridinium to sodium, the final DSS is obtained. This sulphation procedure of dextran was shown not to distort the homogeneity of the dextran sample or the NMR spectrum of the poly-glucose structure, which indicates that no detectable degradation occurs in the process [32, 62, 63]. There is a preference of sulphation onto glucose regarding the activity of the -OH groups on different carbons. At low sulphation degrees, the carbon atoms in the glucose ring have the reactivity C-3 > C-2 > C-4 towards sulphation, whereas, at high degrees of sulphation, the order is C-3 >= C-2 > C-4 [32].

3.4.2.2 The geometry of DSS and its polymerisation units

Similar to the explanation of the (dynamic) dextran structure, the structure of DSS is a dynamically-changing molecule with flexibility in the rotational glycosidic linkage.

The introduction of $-\text{OSO}_3\text{Na}$ groups onto glucose rings along dextran influences the dimension of the polymer. Both the diameter and band width of the polymer increase due to the bulky sulphate groups. However, the length of the polymer is little influenced with a difference of 1-3 Å.

A slight increase of size was observed with the addition of 1000 H_2O molecules compared to the DSS geometry with 72 surrounding H_2O molecules. This increase is a result of the formation of DSS- H_2O hydrogen bridges instead of intramolecular ones leading to a slight expansion of the polymer. Also, the distance between Na cation and sulphate-oxygen increases slightly.

In a previous study on molecules containing a Na cation and sulphate [64], it was found that the Na cation tends to form a bridge between sulphate groups through favourable interaction with the negatively charged oxygens. In the DSS case, the two equatorial sulphate ester groups on each glucose ring keep the two corresponding Na cations together.

The types of di-sulphation do not change the overall helical scheme of the molecule. This is in line with earlier reported findings that the molecular structure of heparin, another sulphated polysaccharide chain, is little affected by the varying substitutions and the presence of bulky, charged sulphate substituents [65].

3.4.3 Interactions of DSS with biological structures

3.4.3.1 Aspecific electrostatic interactions

DSS, as a widely applied polyanion, interacts with positively charged materials, like proteins, most likely in an aspecific way. One example may be the development of polyelectrolyte-encapsulated controlled drug delivery systems [66-68]. Whenever oppositely charged protein and polyelectrolyte are mixed, electrostatic absorption takes place, and molecules tend to associate into nano- or micro-particles [7]. In this process, the charge properties of the interacting materials most likely dominate the interactions.

3.4.3.2 Specific size-dependent interaction with protein nano-pores

In some cases, specificity of size-dependent interactions can occur. Transport of macromolecules through membrane channels plays an important role in many biological processes, and there have been studies dealing with the interactions of polyelectrolytes with protein nano-pores [69-71]. Besides the aspecific electrostatic interactions between charged groups or polymer complexation with local membrane functional groups, the topology of the interacting materials is a non-negligible factor, especially when the radius of the polymer is similar to the radius of the target pore. The present study indicates that the simulated DSS polymer has a diameter of about 1.9-2.2 Å, while some model α -hemolysin nano-pores have a size even smaller than the diameter of the DSS polymer (see Table 3.3) especially when there are side chains attached to the polymer. The branched structure of DSS can preclude the entry of the entire molecule in the pore compared with linear polymers. The blockage of the polymer when entering the protein nano-pore is a dominating factor to be taken into account during polymer transport [8, 72, 73].

Table 3.3. DSS dimension according to MMFF modelling and reported dimensions of DSS and protein nano-pores in previous studies on polyelectrolyte translocation.

Reference	Size of DSS	Nanopore size	Comment
MMFF modelling	Mr. 5000 Da; length 4.1 nm; diameter 2.1 nm; band width 1.1 nm;	—	—
Teixeira, et al [70]	Mr. 5000-500,000 Da; Could enter the pore, but the entry of the entire molecule was precluded by branched structure.	Length \approx 10 nm; diameter \approx 2.6 nm.	α -hemolysin mesoscopic ion channel
Brun, et al [8]	Mr. 8000-500,000 Da; Diameter: 0.4 nm	—	An applied voltage-dependent transport was reported.
Pastoriza-Gallego, et al [69]	—	Pore diameter 1.4 - 4.6 nm.	α -hemolysin pore;
Gibrat, et al [71]	—	Pore diameter 2.0- 2.6 nm.	α -hemolysin pore;

3.5 Conclusions

In this work, the 3D-geometry of α -D-dextran dodecamer in an aqueous environment was elucidated *in silico* based on the approach of careful expansion of the corresponding α -D-dextran monomer/tetramer units optimised by MMFF. The connections among the dextran units were based on the ones in the optimised tetramer without head-to-tail interactions. Two Na_2SO_4 moieties in aqueous environment were shown to be dimeric in nature, with 2-3 H_2O per Na cation as a sufficient hydration shell. The dimeric behaviour was maintained in all glucose disulphates. DSS shows a helix structure, just like the parental dextran. The various helix structures of dextran and DSS originate from the two energy minima for the dihedral angle among adjacent sugar rings. The addition of two (-OSO₃Na) ester groups increases the diameter and band width of the polymer but has little influence on the polymer length. In the presence of 1000 surrounding H_2O molecules, a slight expansion of the polymer occurs. Still, the Na cations tend to be positioned between the two (-OSO₃Na) ester groups on each glucose unit. The interaction of DSS involved in an encapsulating process is mainly aspecific and just based on electrostatic attraction among materials with opposite charge. However, size-dependent specific interactions dominate in processes like the interaction with the α -hemolysin nano-pores.

References

1. Samant, S., R. Singhal, P. Kulkarni, and D. Rege, Protein-polysaccharide interactions: a new approach in food formulations. *International journal of food science & technology*, 1993. **28**(6): p. 547-562.
2. Balabushevich, N.G., O.P. Tiourina, D.V. Volodkin, N.I. Larionova, and G.B. Sukhorukov, Loading the multilayer dextran sulfate/protamine micro-sized capsules with peroxidase. *Biomacromolecules*, 2003. **4**(5): p. 1191-1197.
3. Schmitt, C., C. Sanchez, S. Desobry-Banon, and J. Hardy, Structure and technofunctional properties of protein-polysaccharide complexes: a review. *Critical Reviews in Food Science and Nutrition*, 1998. **38**(8): p. 689-753.
4. Miyake, M. and Y. Kakizawa, Morphological study of cationic polymer-anionic surfactant complex precipitated in solution during the dilution process. *Journal of cosmetic science*, 2010. **61**(4): p. 289.

5. Yamagishi, R., M. Niwa, S.-i. Kondo, N. Sakuragawa, and T. Koide, Purification and biological property of heparin cofactor II: Activation of heparin cofactor II and antithrombin III by dextran sulfate and various glycosaminoglycans. *Thrombosis research*, 1984. **36**(6): p. 633-642.
6. Hall, M. and C. Ricketts, The use of dextran sulphate as a blood anticoagulant in biological research. *Journal of clinical pathology*, 1952. **5**(4): p. 366-366.
7. Sediq, A.S., M.R. Nejadnik, I. El Bialy, G.-J. Witkamp, and W. Jiskoot, Protein–polyelectrolyte interactions: Monitoring particle formation and growth by nanoparticle tracking analysis and flow imaging microscopy. *European Journal of Pharmaceutics and Biopharmaceutics*, 2015. **93**: p. 339-345.
8. Brun, L., M. Pastoriza-Gallego, G. Oukhaled, J. Mathe, L. Bacri, L. Auvray, and J. Pelta, Dynamics of polyelectrolyte transport through a protein channel as a function of applied voltage. *Physical review letters*, 2008. **100**(15): p. 158302.
9. Oukhaled, G., L. Bacri, J. Mathe, J. Pelta, and L. Auvray, Effect of screening on the transport of polyelectrolytes through nanopores. *EPL (Europhysics Letters)*, 2008. **82**(4): p. 48003.
10. Mulloy, B., The specificity of interactions between proteins and sulfated polysaccharides. *Anais da Academia Brasileira de Ciencias*, 2005. **77**(4): p. 651-664.
11. Mulloy, B., M. Forster, C. Jones, and D. Davies, Nmr and molecular-modelling studies of the solution conformation of heparin. *Biochemical Journal*, 1993. **293**(3): p. 849-858.
12. Carçabal, P., R.A. Jockusch, I. Hünig, L.C. Snoek, R.T. Kroemer, B.G. Davis, D.P. Gamblin, I. Compagnon, J. Oomens, and J.P. Simons, Hydrogen bonding and cooperativity in isolated and hydrated sugars: mannose, galactose, glucose, and lactose. *Journal of the American Chemical Society*, 2005. **127**(32): p. 11414-11425.
13. Lando, J., H. Olf, and A. Peterlin, Nuclear magnetic resonance and x-ray determination of the structure of poly (vinylidene fluoride). *Journal of Polymer Science Part A-1: Polymer Chemistry*, 1966. **4**(4): p. 941-951.
14. Halgren, T.A., Merck molecular force field. I. Basis, form, scope, parameterization, and performance of MMFF94. *Journal of computational chemistry*, 1996. **17**(5-6): p. 490-519.
15. Jeffrey, G. and R. Taylor, The application of molecular mechanics to the structures of carbohydrates. *Journal of Computational Chemistry*, 1980. **1**(1): p. 99-109.

16. Kroon-Batenburg, L. and J. Kanters, Influence of hydrogen bonds on molecular conformation. Molecular-mechanics calculations on α -D-glucose. *Acta Crystallographica Section B: Structural Science*, 1983. **39**(6): p. 749-754.
17. Barrows, S.E., J.W. Storer, C.J. Cramer, A.D. French, and D.G. Truhlar, Factors controlling relative stability of anomers and hydroxymethyl conformers of glucopyranose. *Journal of computational chemistry*, 1998. **19**(10): p. 1111-1129.
18. Pérez, S., M. Kouwijzer, K. Mazeau, and S.B. Engelsen, Modeling polysaccharides: Present status and challenges. *Journal of Molecular Graphics*, 1996. **14**(6): p. 307-321.
19. French, A.D. and M.K. Dowd, Exploration of disaccharide conformations by molecular mechanics. *Journal of Molecular Structure: THEOCHEM*, 1993. **286**: p. 183-201.
20. Burton, B.A. and D.A. Brant, Comparative flexibility, extension, and conformation of some simple polysaccharide chains. *Biopolymers*, 1983. **22**(7): p. 1769-1792.
21. Mulloy, B. and M.J. Forster, Conformation and dynamics of heparin and heparan sulfate. *Glycobiology*, 2000. **10**(11): p. 1147-1156.
22. Naessens, M., A. Cerdobbel, W. Soetaert, and E.J. Vandamme, Leuconostoc dextransucrase and dextran: production, properties and applications. *Journal of Chemical Technology and Biotechnology*, 2005. **80**(8): p. 845-860.
23. Leathers, T.D., Dextran, in *Biotechnology of Biopolymers, From Synthesis to Patents*. Vol. 1. Lignin, Coal, Polyesters and Polysaccharides, Chapter 20, A. Steinbuchel and Y. Doi, Editors. 2005, Wiley-VCH: Weinheim. p. 575-597.
24. Dextran sulphate product information. Sigma Aldrich: MO, USA.
25. Cheetham, N.W., E. Fiala-Ber, and G.J. Walker, Dextran structural details from high-field proton NMR spectroscopy. *Carbohydrate polymers*, 1990. **14**(2): p. 149-158.
26. Sims, I., A. Thomson, U. Hubl, N. Larsen, and R. Furneaux, Characterisation of polysaccharides synthesised by *Gluconobacter oxydans* NCIMB 4943. *Carbohydrate polymers*, 2001. **45**(3): p. 285-292.
27. Salamone, J.C., *Polymeric Materials Encyclopedia*, Twelve Volume Set. 1996: Taylor & Francis.
28. Balazs, E.A. and R.W. Jeanloz, *Metabolism and Interactions: The Chemistry and Biology of Compounds Containing Amino Sugars*. 2013: Academic Press.

29. Ludwig-Baxter, K.G., R.N. Rej, A.S. Perlin, and G.A. Neville, A novel method for differentiating dextran sulfate from related sulfated polysaccharides. *Journal of pharmaceutical sciences*, 1991. **80**(7): p. 655-660.
30. Neville, G.A., P. Rochon, R.N. Rej, and A.S. Perlin, Characterization and differentiation of some complex dextran sulfate preparations of medicinal interest. *Journal of pharmaceutical sciences*, 1991. **80**(3): p. 239-244.
31. Miyaji, H. and A. MISAKI, Distribution of sulfate groups in the partially sulfated dextrans. *Journal of biochemistry*, 1973. **74**(6): p. 1131-1139.
32. Mähner, C., M.D. Lechner, and E. Nordmeier, Synthesis and characterisation of dextran and pullulan sulphate. *Carbohydrate Research*, 2001. **331**(2): p. 203-208.
33. Cakić, M., G. Nikolić, L. Ilić, and S. Stanković, Synthesis and FTIR characterization of some dextran sulphates. *Chemical Industry and Chemical Engineering Quarterly*, 2005. **11**(2): p. 74-78.
34. Spartan '16 is a product of Wavefunction, Inc., 18401 Von Karman Avenue, Suite 370, Irvine, CA 92612 U.S.A. (<http://www.wavefun.com>). .
35. Damm, W. Molecular Recognition of Carbohydrates [accessed: 2016 31 Oct]; Available from: <http://www.nmr.chem.uu.nl/~abonvin/ToT/damm/>.
36. Mitch, W.E. and T.A. Ikizler, *Handbook of nutrition and the kidney*. 2010, Philadelphia, PA: Lippincott William & Wilkins.
37. Rempe, S.B. and L.R. Pratt, The hydration number of Na⁺ in liquid water. *Fluid Phase Equilibria*, 2001. **183**: p. 121-132.
38. Mähler, J. and I. Persson, A study of the hydration of the alkali metal ions in aqueous solution. *Inorganic chemistry*, 2011. **51**(1): p. 425-438.
39. Van Geet, A.L., Hydration number of sodium ions determined by sodium magnetic resonance. *Journal of the American Chemical Society*, 1972. **94**(16): p. 5583-5587.
40. De Baets, S., E.J. Vandamme, and A. Steinbüchel, *Biopolymers, Polysaccharides II: Polysaccharides from Eukaryotes*. Vol. 6. 2002, Berlin: Wiley VCH.
41. Mauzac, M. and J. Jozefonvicz, Anticoagulant activity of dextran derivatives. Part I: Synthesis and characterization. *Biomaterials*, 1984. **5**(5): p. 301-304.

42. Chaubet, F., J. Champion, O. Maïga, S. Mauray, and J. Jozefonvicz, Synthesis and structure—anticoagulant property relationships of functionalized dextrans: CMDBS. *Carbohydrate polymers*, 1995. **28**(2): p. 145-152.
43. Ricketts, C., The blood anticoagulant effect of short chain-length dextran sulphates. *British Journal of Pharmacology*, 1954. **9**(2): p. 224-228.
44. Zhang, X., J.-C. Wang, K.M. Lacki, and A.I. Liapis, Construction by molecular dynamics modeling and simulations of the porous structures formed by dextran polymer chains attached on the surface of the pores of a base matrix: characterization of porous structures. *The Journal of Physical Chemistry B*, 2005. **109**(44): p. 21028-21039.
45. Rankin, J.C. and A. Jeanes, Evaluation of the periodate oxidation method for structural analysis of dextrans. *Journal of the American Chemical Society*, 1954. **76**(17): p. 4435-4441.
46. Dimler, R., I. Wolff, J. Sloan, and C. Rist, Interpretation of periodate oxidation data on degraded dextran. *Journal of the American Chemical Society*, 1955. **77**(24): p. 6568-6573.
47. Van Cleve, J., W. Schaefer, and C. Rist, The Structure of NRRL B-512 Dextran. *Methylation Studies*. *Journal of the American Chemical Society*, 1956. **78**(17): p. 4435-4438.
48. Larm, O., B. Lindberg, and S. Svensson, Studies on the length of the side chains of the dextran elaborated by *Leuconostoc mesenteroides* NRRL B-512. *Carbohydrate research*, 1971. **20**(1): p. 39-48.
49. Koepsell, H. and H. Tsuchiya, Enzymatic synthesis of dextran. *Journal of bacteriology*, 1952. **63**(2): p. 293.
50. Hehre, E.J., Studies on the enzymatic synthesis of dextran from sucrose. *Journal of Biological Chemistry*, 1946. **163**(1): p. 221-233.
51. Robyt, J.F., B.K. Kimble, and T.F. Walseth, The mechanism of dextransucrase action: Direction of dextran biosynthesis. *Archives of biochemistry and biophysics*, 1974. **165**(2): p. 634-640.
52. Monchois, V., R.M. Willemot, and P. Monsan, Glucansucrases: mechanism of action and structure–function relationships. *FEMS microbiology reviews*, 1999. **23**(2): p. 131-151.
53. Khalikova, E., P. Susi, and T. Korpela, Microbial dextran-hydrolyzing enzymes: fundamentals and applications. *Microbiology and Molecular Biology Reviews*, 2005. **69**(2): p. 306-325.
54. Mehvar, R., Dextrans for targeted and sustained delivery of therapeutic and imaging agents. *Journal of controlled release*, 2000. **69**(1): p. 1-25.

55. Brady, J.W., Molecular dynamics simulations of α -D-glucose in aqueous solution. *Journal of the American Chemical Society*, 1989. **111**(14): p. 5155-5165.
56. Brown, G.M. and H.A. Levy, α -D-glucose: precise determination of crystal and molecular structure by neutron-diffraction analysis. *Science*, 1965. **147**(3661): p. 1038-1039.
57. Oakenfull, D., Polysaccharide Molecular structures, in Polysaccharide association structures in food. 1998, Marcel Dekker, Inc: New York.
58. Hui, Y.H. and F. Sherkat, Handbook of food science, technology, and engineering-4 volume Set. 2005, Boca Raton: CRC press.
59. Jeffrey, G.A., An introduction to hydrogen bonding. Vol. 32. 1997, New York: Oxford university press.
60. Omta, A.W., M.F. Kropman, S. Woutersen, and H.J. Bakker, Negligible effect of ions on the hydrogen-bond structure in liquid water. *Science*, 2003. **301**(5631): p. 347-349.
61. Bochkareva, T., B. Passet, K. Popov, N. Platonova, and T. Koval'chuk, Sulfonation of substituted azoles with sulfur trioxide in dichloroethane. *Chemistry of Heterocyclic Compounds*, 1987. **23**(10): p. 1084-1089.
62. Novikova, E., V. Smychenko, and A. Iozep, Sulfation of dextran with chlorosulfonic acid in organic solvents. *Russian Journal of Applied Chemistry*, 2007. **80**(7): p. 1151-1153.
63. Papy-Garcia, D., V. Barbier-Chassefière, V. Rouet, M.-E. Kerros, C. Klochendler, M.-C. Tournaire, D. Barritault, J.-P. Caruelle, and E. Petit, Nondegradative sulfation of polysaccharides. Synthesis and structure characterization of biologically active heparan sulfate mimetics. *Macromolecules*, 2005. **38**(11): p. 4647-4654.
64. Bruce, C.D., M.L. Berkowitz, L. Perera, and M.D. Forbes, Molecular dynamics simulation of sodium dodecyl sulfate micelle in water: micellar structural characteristics and counterion distribution. *The Journal of Physical Chemistry B*, 2002. **106**(15): p. 3788-3793.
65. Mulloy, B., M.J. Forster, C. Jones, A.F. Drake, E.A. Johnson, and D.B. Davies, The effect of variation of substitution on the solution conformation of heparin: a spectroscopic and molecular modelling study. *Carbohydrate research*, 1994. **255**: p. 1-26.
66. Johnston, A.P., C. Cortez, A.S. Angelatos, and F. Caruso, Layer-by-layer engineered capsules and their applications. *Current Opinion in Colloid & Interface Science*, 2006. **11**(4): p. 203-209.
67. Verma, A. and A. Verma, Polyelectrolyte complex-an overview. *International Journal of Pharmaceutical Sciences and Research*, 2013. **4**(5): p. 1684.

68. Lankalapalli, S. and V.M. Kolapalli, Polyelectrolyte complexes: A review of their applicability in drug delivery technology. *Indian journal of pharmaceutical sciences*, 2009. **71**(5): p. 481.
69. Pastoriza-Gallego, M., G. Gibrat, B. Thiebot, J.-M. Betton, and J. Pelta, Polyelectrolyte and unfolded protein pore entrance depends on the pore geometry. *Biochimica et Biophysica Acta (BBA) - Biomembranes*, 2009. **1788**(6): p. 1377-1386.
70. Teixeira, L.R., P.G. Merzlyak, A. Valeva, and O.V. Krasilnikov, Interaction of heparins and dextran sulfates with a mesoscopic protein nanopore. *Biophysical journal*, 2009. **97**(11): p. 2894-2903.
71. Gibrat, G., M. Pastoriza-Gallego, B. Thiebot, M.-F. Breton, L. Auvray, and J. Pelta, Polyelectrolyte entry and transport through an asymmetric α -hemolysin channel. *The Journal of Physical Chemistry B*, 2008. **112**(47): p. 14687-14691.
72. Heng, J.B., C. Ho, T. Kim, R. Timp, A. Aksimentiev, Y.V. Grinkova, S. Sligar, K. Schulten, and G. Timp, Sizing DNA Using a Nanometer-Diameter Pore. *Biophysical Journal*, 2004. **87**(4): p. 2905-2911.
73. Aksimentiev, A., J.B. Heng, G. Timp, and K. Schulten, Microscopic Kinetics of DNA Translocation through Synthetic Nanopores. *Biophysical Journal*, 2004. **87**(3): p. 2086-2097.

Chapter 4

*Molecular modelling of the interactions between lysozyme and dextran sulphate sodium**

Miao Yu, Hayley A. Every, Wim Jiskoot, Geert-Jan Witkamp, Wim Buijs

*An introduction to the theoretical background of molecular modelling is presented in Appendix B.

Abstract

This study deals with a preliminary examination of the interactions between lysozyme (neutralised by chloride) and dextran sulphate (neutralised by sodium; DSS) via molecular modelling. There are three types of interactions to be taken into account when investigating their interaction behaviours in an aqueous environment: electrostatic interaction where ion exchange takes place; aqueous solvation of the molecules; and steric interactions between the macromolecules. The ion exchange energy among the solvated free ions (NH_4^+ , Cl^- , Na^+ and SO_4^{2-}) is 0 kJ/mol in theory, with ± 80 kJ/mol deviation of the calculated value (by the implicit and explicit solvation method) from the experimental value. In line with these results, for the ion exchange between $\text{R-NH}_3\text{Cl}/\text{R}'\text{-NH}_2\text{Cl}$ and $\text{R}''\text{-(SO}_4\text{Na)}_2$ (R, R' and R'' are small residue groups shown in the main text), reaction energies of 0 ± 80 kJ/mol were calculated by both the implicit and explicit solvation method. For the interaction between DSS monomer (DSS polymerisation unit) with the lysine and arginine, reaction energy of about -150 kJ/mol per ion exchange was obtained by explicit method with 440 H_2O molecules using the Merck Molecular Force Field. The preliminary results on the geometry optimisation of the interacted lysozyme-DSS show a remaining intact structure of the backbone of lysozyme and the helix structure of DSS, although with conformational adjustment of the side chains and dihedral angles of the glycosidic bonds in DSS. Further investigations are needed to explore the geometrical behaviour of lysozyme and DSS and their steric interactions to develop computational strategies for the description of their complexation thermodynamics.

4.1 Introduction

The combination of proteins and polyelectrolytes via electrostatic interaction has been investigated for protein precipitation and separation [1, 2] and controlled drug delivery [3]. The latter case is based on the formation of protein-polyelectrolyte complexes that can protect the protein within the body and enhance the time interval of the bioavailability of protein therapeutics. Although there have been several applications of proteins and polyelectrolytes, knowledge about the mechanisms of the interactions, such as the 3D shape, the interaction potentials, and the driving force for interactions, are still not fully clarified experimentally. Molecular modelling is a powerful tool to explore the behaviour of the interactions among molecules at a down-scale geometrical domain (in nanometer), within a short time profile (fast reaction), and to clarify the contributions of various factors to the interaction (such as the molecular structures, the solvation of the molecules, and the dominating interaction forces (attractive or repulsive)). The molecular modelling helps clarify the interactions among biomacromolecules and give insight into processes taking place in food, pharmaceutical and other biological systems. In this chapter, an investigation on the interaction between the model protein, lysozyme, and the model polyelectrolyte, dextran sulphate, neutralised by sodium (DSS), will be explored via a molecular modelling approach.

The strength and nature of the interactions between lysozyme and DSS affect their complexation and later particle growth. The electrostatic and van der Waals attraction, and the polymer bridging are the two significant particle agglomeration mechanisms [4]. At neutral pH, electrostatic attraction occurs between the amino groups (lysine (Lys) and arginine (Arg) of lysozyme) and the sulphate groups of DSS. This and the van der Waals force facilitate the agglomeration of these macromolecules. Also, the bridging of the extended chains of the polymer among different particles contributes to the agglomeration. Following the above mechanisms, in molecular modelling, one essential aspect to be considered is the electrostatic interaction among the oppositely-charged groups between lysozyme and DSS. Another aspect is the steric interaction between the two macromolecules, which relates to the binding sites, arrangement of the flexible structures, size-(in)dependent interactions and geometries of the complexes.

During the electrostatic interaction, there is the great accessibility of the charged biopolymer groups [5]. The electrostatic nature of the interaction between lysozyme and DSS is also reflected in the effect of pH and especially of ionic strength [5, 6]. It has been reported that there is a possibility of decoupling polymers, e.g. under the condition of high ionic strength where the electrostatic interaction is weakened due to salt screening [7]. In many biopolymer mixtures, the entropic contribution is often more significant than the enthalpic one and phase separation of biopolymers tends to take place [8].

This can be driven by electrostatic interaction, hydrogen bonding, hydrophobic interaction, etc [8]. Aside from these interactions, there is a possibility to form covalent bonds between lysozyme and DSS via the Maillard reaction, and it is not affected by pH or other conditions that might cause dissociation of DSS from lysozyme [9]. However, this is beyond the scope of this chapter.

Ion exchange is ubiquitous in biological systems, also for the process of lysozyme-DSS complexation. When present in a physiological environment, the charged groups of the lysozyme and the DSS are neutralised by mobile counterions, which also take part in the ion exchange reactions. The Na^+ , NH_4^+ , Cl^- and SO_4^{2-} are by far the most common ionic groups involved in the electrostatic interaction, among which Na^+ and Cl^- serve as the counterions of the sulphate groups and the amino groups respectively. Moreover, the Na^+ and Cl^- is the most abundant pair of ions under physiological conditions (about 100 to 150 mM) [10-12]. The thermodynamics of the exchange of these ions help explain the mechanism of the assembling of lysozyme and DSS via electrostatic interaction. During the ion exchange reaction, the number of bonds is conserved, and thus it is defined as an isodesmic reaction. The enthalpies of the isodesmic reaction provide information about any stabilisation/destabilisation of the molecules, based on which the spontaneity and the kinetics of the reaction can be derived.

The binding affinities of proteins with other molecules (such as ligands, polymers) can be figured out using molecular modelling tools [13-15]. The 3D structure of lysozyme can be obtained via databases such as the Protein Data Bank [16, 17]. The molecular structure of DSS in an aqueous environment was determined previously [18]. The complex structures of lysozyme and DSS indicate the possibility of not only nonspecific (ionic/electrostatic) but also specific (morphology/size-dependent) interactions. The former reveals the interactions between charged groups, while the latter involves the adjustment of molecular geometry during their interaction. As summarised in previous literature [8], the optimum interaction between proteins and charged polymers tends to occur at a critical balance between the biopolymer charge density and rigidity. Flexible molecules can form an optimum number of contacts with the other oppositely charged molecules, i.e. an increase in the local concentration of interacting groups is favoured [8].

It has been inherently thought that the most rigorous methods for the approximation of molecular conformations and energy are based on quantum mechanical (QM) methods [19, 20]. However, the molecular mechanics calculation can also give accurate predictions on the molecular structure and energy (such as electrostatic energy and van der Waals energy). This is advantageous over QM methods, which require more computation power and are less accurate in predicting the van der Waals potentials. Nevertheless, QM seems to be the only option to give accurate results when it comes to the calculation of reaction enthalpy and entropic effects of small systems [21].

The MM method has proven to be dominant for fast estimation of the binding affinities among biomacromolecules [20, 22]. Such methods have been used to study the phenomena such as the intrinsic strain of organic molecules, geometries of simple and complex molecules, thermodynamics of the binding of ligands to proteins, and corresponding conformational changes. In contrast to QM methods, MM methods allow computational simulations to be performed on large biomolecular systems and is the most feasible means to model the interactions between ligands and receptor in a physically realistic manner, especially in large-scale applications [19]. To take advantage of both MM and QM, a strategy is developed to carry out MM and QM analysis on appropriate small-scale and recognisable fragments of the macromolecules. Via the correlation that is built between the results of MM and QM for the small systems, additional specific torsional potentials can be added to the MM results to ensure as accurate a representation of the intrinsic conformational energies as possible [22]. This correlation can be extrapolated to approximate the energy of larger molecules, for which only the MM calculations are feasible. Before the extrapolation, it is crucial to have at least qualitative structural data on the molecules or corresponding fragments. This can be obtained by defining the binding cleft in the protein and limiting the conformational flexibility of the polymer.

Most biological processes take place in water. The biopolymer-solvent interaction is also a fundamental and inseparable aspect of the model. In the absence of external electrolytes, H_3O^+ and OH^- , as the counterions, play a role in neutralising the molecular system. The hydrogen bridges formed between water and DSS or lysozyme maintain the molecular structure and avoid the intramolecular interactions. On the other hand, the non-polar groups likely tend to stick together in the presence of water. The hydrophobic interaction between the non-polar groups of protein (lysozyme) and polyelectrolyte (DSS) is still poorly understood. This may be partly clarified via molecular modelling when taking the effects of aqueous solvation into account, in which water forms an integral part of the macromolecule.

Here, a preliminary study was performed on the solvation of ions, the ion exchange that reflects electrostatic interactions, and the geometry of lysozyme and DSS after their interaction. This early-stage research, together with later examination on the electrostatic and steric interaction between the macromolecules, contribute to the description of the lysozyme-DSS complexation mechanism and interaction thermodynamics.

4.2 Approach

This study makes use of lysozyme and DSS as the model protein and polyelectrolyte respectively. The protein's molecular structure was obtained from the RCSB protein data bank [16] with the ID number *1DPX*. The DSS molecular structure was previously determined by the authors of this chapter [18]. The molecular simulations were performed using molecular mechanics (MM) method and quantum mechanics (QM) method. For the MM, the Merck Molecular Force Field (MMFF) was used as it is well parameterised for organic compounds and suitable for large molecular system regarding the high computation efficiency (see Appendix B for more details). For the QM, the semi-empirical (PM6) and density functional theory (DFT) calculations were performed using the hybrid functional (Becke's three-parameter Lee-Yang-Parr hybrid functional, i.e. B3LYP [23, 24]). In all cases, the geometries were optimised and characterised according to their lowest energy minima. After building the initial molecular structure, the equilibrium geometry of the molecule (with the nearest energy minimum) was calculated firstly by MMFF. Based on the obtained geometry, the PM6 and B3LYP geometry optimisation were performed. Both the strain energy of the equilibrium geometry (calculated via MM) and the total energy of the system (calculated via QM) were reported. For the total energy of the system, a correction of the enthalpy to account for finite temperature (298 K) is needed to bring the calculated energy in line with experimentally-measured value. The modelling was performed by using the Spartan 18 software package [25].

4.2.1 Hydration energy

The calculation of the hydration energy of common electrolytes was performed and compared with literature value. There are two types of solvation model to describe the solvation state of a substance: implicit solvation and explicit solvation. The former one applies dielectric continuum to treat the solvent as a continuous and uniform polarizable medium of fixed dielectric constant (in water, the value is about 80). The calculated solvating effects depend on the shape and charge distribution of the molecule (solute) and the dielectric constant of the solvent and do not account for explicit solvent-solute interactions such as hydrogen bridges or hydrophobic interactions. The popular continuum solvation models have been reviewed elsewhere [26, 27]. Among these models, the SM5.4 (universal solvation model) and PCM (polarizable continuum model) were used for MMFF and B3LYP calculation respectively in Spartan (described in this chapter as MMFFaq and B3LYPaq respectively). For MMFFaq, the solvation model does not contribute to the geometry optimisation, but only add the estimated solvation energy to the gas-phase energy obtained from the MMFF after the geometry optimisation. The B3LYPaq allows for the geometry optimisation and calculation of the thermodynamic properties

of the target solvated molecule, whose wavefunction is affected by the solvent dielectric constant. Regarding the latter explicit solvation model, an explicit number of solvent molecules (in this chapter water molecules) are included, and the molecular details of each solvent molecules are considered. The geometries and the thermodynamics of the target solutes in the presence of solvent molecules were depicted.

The hydration of the electrolytes is defined as an isodesmic reaction. Under this condition, the errors on the energy calculation on both sides of the equilibrium are cancelled, and the difference of the steric energy or total energy before and after the reaction corresponds to the difference in enthalpy (ΔH). For infinitely diluted ionic species, the contribution of the dilution to the entropy change is negligible, and thus the ΔH is approximately equal to the reaction Gibbs free energy (ΔG). For the convenience of description, in this study, all the reaction energy is described as ΔE .

The scheme of the solvation of free ions calculated via implicit solvation model is shown as Equation 4.1:



Where A represents the ion bearing positive or negative charge (+/-), g the gaseous state and aq the solvation state. In this study, the B3LYPaq method was used for the hydration energy calculation of the free ions.

Although the implicit solvation method with continuum solvation models is easy to set up and computationally inexpensive, there is a shortcoming of the probable failure to account for chemical interactions between the solute and solvent molecules in the first solvation shell, which are expected to be of particular importance for ionic solutes [28]. Another method of calculation is by B3LYPaq with the addition of explicit water molecules according to the thermodynamic cycle shown in Figure 4.1.

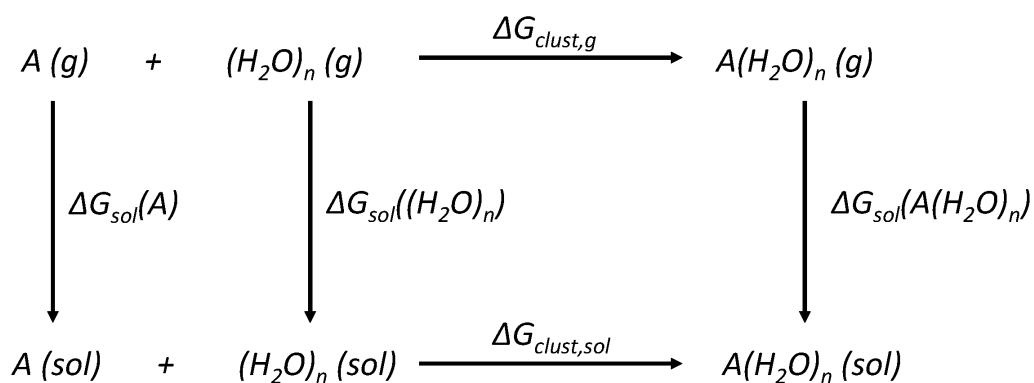


Figure 4.1. Scheme of the thermodynamic cycle of the hydration of ions according to [28].

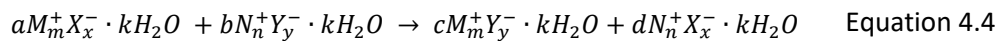
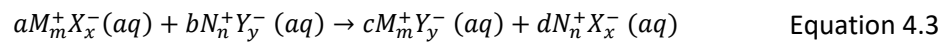
The free energy of solvation of the ion is calculated as:

$$\Delta G_{sol}(A) = \Delta G_{clust,g}(A(H_2O)_n) + \Delta G_{sol}(A(H_2O)_n) - \Delta G_{sol}((H_2O)_n) - RT \ln\left(\frac{[H_2O]}{n}\right) \quad \text{Equation 4.2}$$

Usually, the solvation energy is reported in a standard state (1 mol/L); the last term is a correction term for the free energy change of 1 mol of (H₂O)_n gas from 55.34/n M liquid to 1 mol/L [28]. Total energy by B3LYPaq was calculated. In this study, five water molecules were added for the calculation of the solvation energy of ion according to [28].

4.2.2 Ion exchange

At neutral pH (pH=7), the sulphate groups of DSS bear negative charges with sodium as the counterions, and the amino groups of the Arg and Lys bear positive charges, which are neutralised by chloride. In this chapter, the reaction energy (ΔE) of the ion exchange between the Na₂SO₄ and NH₄Cl, between the R-NH₃Cl/R'-NH₂Cl and R''-(SO₄Na)₂ (R, R' and R'' are illustrated in Figure 4.2), and between the DSS monomer (DSS polymerization unit) and the amino acids are calculated by comparing the sum of energy (of the equilibrium geometry of the molecular systems) before and after the ion exchange. The schemes of the ion exchange process are shown in Equation 4.3 and Equation 4.4, representing the implicit solvation (by MMFFaq and B3LYPaq) and explicit solvation (by MMFF) respectively. For the explicit solvation method, a preliminary trial using a constant number of water molecules (here 440 H₂O) to solvate the ionic species (surround the ionic species in the molecular model) was performed, where the systematic errors before and after the ion exchange were cancelled out. Here it is assumed that the entropy contribution is negligible as the number of atoms or ions before and after the exchange remains the same in the studied solvent environment.



Where M, N, X, Y represent the ionic species in the model; m, n, x, y the composition of the corresponding ion in the model; a, b, c, d the coefficients of the ion exchange reaction; k the number of included water molecules.

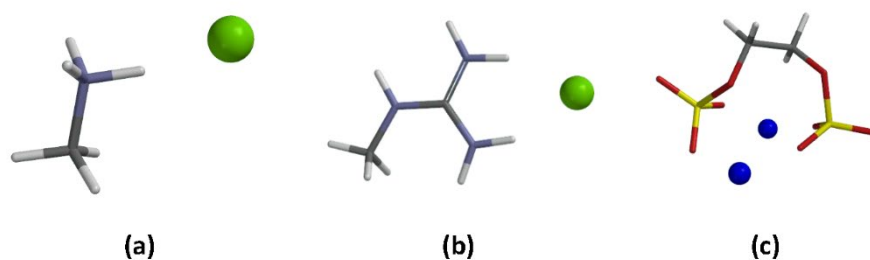


Figure 4.2. The molecular structure of the (a) R-NH₃Cl, (b) R'-NH₂Cl and (c) R''-(SO₄Na)₂ in tube format. The R represents the CH₃- group; the R' represents the CH₃-NH-C(NH₂)-NH₂- group; and the R'' the -CH₂-CH₂- group, in which each -CH₂- is connected with a -SO₄Na. The white tubes represent hydrogen atoms, cyan the nitrogen, grey the carbon, red the oxygen and yellow the sulfur. The green and blue ball represent the chloride and sodium respectively.

4.2.3 Interaction of lysozyme and DSS

A preliminary investigation was performed on the interaction of lysozyme and DSS dodecamer (DSS polymer with 12 polymerisation units; carbon 2,3 di-sulphated). The lysozyme geometry was obtained from online protein data bank with the ID: 1DPX. After growing hydrogen molecules by Spartan, the backbone of the lysozyme was fixed, followed by the docking of DSS at the site with lysine (Lys) and arginine (Arg). Some of the sulphate groups of DSS were targeted to be positioned close to the amino groups of Lys and Arg in the lysozyme molecule. The non-interactive amino groups (of Lys and Arg) and sulphate were neutralised by Cl and Na respectively. After the alignment, the backbone of the lysozyme was unfixed, and the geometry optimisation was performed by MMFF.

4.3 Results and discussion

4.3.1 The hydration energy of common ions

The hydration energy of Na⁺, Cl⁻, NH₄⁺ and SO₄²⁻, calculated via the continuum solvation model with and without the addition of water molecules, are listed and compared with literature values (see Table 4.1). Both the calculated hydration energy and the experimental values reported elsewhere [29] are negative. There are differences in the calculated values from the experimental ones. For the cases with and without water molecules, the standard deviations of the differences between the calculated values and the experimental values are about ±80 kJ/mol.

In an ideal case, for the infinitely diluted ions freely movable in aqueous conditions, the ion exchange energy in equilibrium (ΔE) is 0 kJ/mol. However, concerning the above deviation of the calculated hydration energy by B3LYPaq, the calculated ion exchange energy by the same method is about 0 ± 80 kJ/mol.

Although it has become a common tool for accurate quantum chemical calculations of electronic structures and properties of many molecular systems, the B3LYP still has several shortcomings such as the accumulating errors as the size of the system increases and the breakdown in the description of particularly dispersive van der Waals interactions [30]. Moreover, the applied PCM model tends to perform well in predicting the solvation energy of small neutral species but are less successful for ionic species as a result of the failure to account for chemical interactions between a solute and solvent molecules in the first solvation shell [28], which is of particular significance for ionic solutes. These limitations may account for the deviation of the calculated hydration energy for the studied ions from experimental values. By the way, the high requirement on computation cost limits the application of the B3LYP method to the model of macromolecular systems.

Table 4.1. The hydration energy calculated via B3LYPaq with and without water molecules, and the experimental values from the literature. The deviations of the differences between the calculated values and the experimental values are about ± 80 kJ/mol.

Ions	ΔE (kJ/mol)		
	Addition of 5 H ₂ O molecules	No H ₂ O molecules	Exp [29]
Na ⁺	-460	-252	-365
NH ₄ ⁺	-370	-342	-285
Cl ⁻	-305	-315	-340
SO ₄ ²⁻	-1025	-986	-1080

4.3.2 Ion exchange

The reaction energy (ΔE) of the ion exchange can be calculated via the comparison of the relative energy of the molecular systems before and after the exchange.

Table 4.2 shows the calculated reaction energy of the ion exchange between the electrolytes Na_2SO_4 and NH_4Cl , between the $\text{R-NH}_3\text{Cl/R}'\text{-NH}_2\text{Cl}$ and $\text{R}''\text{-(SO}_4\text{Na)}_2$, and between the DSS monomer and Lys or Arg using different methods. Theoretically, when dissolving the electrolyte infinitely, the free energy of the system is assumed to be zero where all ions are freely movable in the aqueous environment. The ΔE per ion exchange of NH_4Cl and Na_2SO_4 was calculated as 8.7 and 39.6 kJ/mol by MMFFaq and B3LYPq respectively, which is close to zero. The calculation with the explicit method gives the ΔE of 3.2 kJ/mol in the presence of 440 water molecules in the model. When it comes to the reaction of relatively large molecular systems of monomeric DSS unit and Lys or Arg, more negative ΔE (about -150 kJ/mol) was obtained using MMFF explicit method, indicating a spontaneous and full reaction of the DSS and amino acids into DSS-amino acids complexes.

The ΔE calculated by MMFFaq and MMFF with explicit water molecules are closer to the theoretical value. However, the former method is fully geometry-dependent, and the solvation model does not contribute to the geometry optimisation under the solvation condition. For the system of DSS monomer and amino acids, there are van der Waals inter-molecular attractions among the side groups such as the hydroxyl and methyl groups, which is not a realistic physical picture of the system in an aqueous environment. The MMFF calculation with explicit water molecules seems to be the most accessible method with reasonable consideration of the steric and electrostatic forces between the solute and solvent molecules, in which the geometry of the molecular structure is fully relaxed by interacting with the surrounding water molecules, and with acceptable computation duration. The calculation results are assumed to be more reliable when using a constant number of solvent molecules, as the systematic errors before and after the reaction are mostly cancelled out. The calculated ΔE by the MMFF with 440 H_2O is comparable with the literature value and the MMFFaq results for the small molecular systems.

When dealing with macromolecules, for example proteins, it was stated elsewhere that the simulations containing explicit water have apparent advantages over continuum solvent treatments in some respects [31]. For example, detailed bound solvent motifs, such as water H-bridges, require solvent molecules as an integral part of the structural model, while the continuum model tends to take the average specific water interactions and thus cannot show a fine structure [31]. Thus the MMFF explicit method seems to be the only option for the system of large molecules.

In this study, the entropic effect on the ion exchange energy is not included in the case that neither the number of molecules nor the total size of molecules varies before and after the reaction. It is assumed that the entropies of the system before and after ion exchange are roughly the same and the enthalpies of the reaction are approximately equal to their free energy. However, this assumption is not always valid under circumstances such as the internal hydrogen bonding formation occurs, or there are differences in the solvation of the different conformers. The estimation of entropy (i.e., a measure of the relative disorder), requires more extensive knowledge and study about the system.

Table 4.2. The calculated ΔE of the ion exchange reactions.

Ion exchange reaction	ΔE per mol ion exchange (kJ/mol)			
	MMFF	MMFFaq	B3LYPaq	Theoretical
$2\text{NH}_4\text{Cl} + \text{Na}_2\text{SO}_4 \rightarrow (\text{NH}_4)_2\text{SO}_4 + 2\text{NaCl}$	-	8.7	39.6	0
$2\text{NH}_4\text{Cl}\cdot 440\text{H}_2\text{O} + \text{Na}_2\text{SO}_4\cdot 440\text{H}_2\text{O} \rightarrow (\text{NH}_4)_2\text{SO}_4\cdot 440\text{H}_2\text{O} + 2\text{NaCl}\cdot 440\text{H}_2\text{O}$	3.2	-	-	0
$2\text{R-NH}_3\text{Cl} + \text{R}'\text{-(SO}_4\text{Na)}_2 \rightarrow \text{R}'\text{-(SO}_4\text{NH}_3\text{-R)}_2 + 2\text{NaCl}$	-	1.7	52.3	-
$2\text{R-NH}_2\text{Cl} + \text{R}'\text{-(SO}_4\text{Na)}_2 \rightarrow \text{R}'\text{-(SO}_4\text{NH}_2\text{-R)}_2 + 2\text{NaCl}$	-	35.2	58.7	-
$2\text{R-NH}_3\text{Cl}\cdot 440\text{H}_2\text{O} + \text{R}'\text{-(SO}_4\text{Na)}_2\cdot 440\text{H}_2\text{O} \rightarrow \text{R}'\text{-(SO}_4\text{NH}_3\text{-R)}_2\cdot 440\text{H}_2\text{O} + 2\text{NaCl}\cdot 440\text{H}_2\text{O}$	-12.2	-	-	-
$2\text{R-NH}_2\text{Cl}\cdot 440\text{H}_2\text{O} + \text{R}'\text{-(SO}_4\text{Na)}_2\cdot 440\text{H}_2\text{O} \rightarrow \text{R}'\text{-(SO}_4\text{NH}_2\text{-R)}_2\cdot 440\text{H}_2\text{O} + 2\text{NaCl}\cdot 440\text{H}_2\text{O}$	2.0	-	-	-
$\text{Na}_2\text{DS}^+\cdot 440\text{H}_2\text{O} + 2\text{LysCl}^{**}\cdot 440\text{H}_2\text{O} \rightarrow \text{DS(Lys)}_2\cdot 440\text{H}_2\text{O} + 2\text{NaCl}\cdot 440\text{H}_2\text{O}$	-151.3	-	-	-
$\text{Na}_2\text{DS}\cdot 440\text{H}_2\text{O} + 2\text{ArgCl}^{***}\cdot 440\text{H}_2\text{O} \rightarrow \text{DS(Arg)}_2\cdot 440\text{H}_2\text{O} + 2\text{NaCl}\cdot 440\text{H}_2\text{O}$	-165.4	-	-	-

*: a monomeric unit of DSS; Na represents the sodium ions;

** : lysine neutralised by Cl

***: arginine neutralised by Cl;

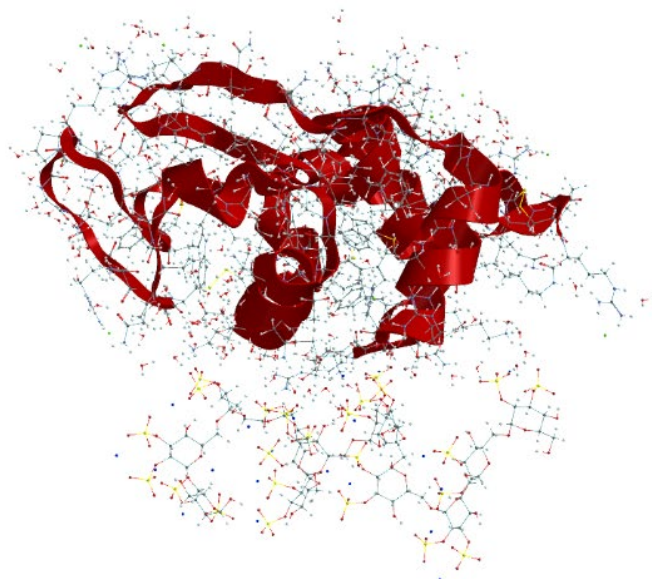
4.3.3 The interaction of DSS with lysozyme

The lysozyme molecule is a compact complex in a shape similar to an ellipsoid with dimensions of about 4.5 x 3.0 x 3.0 nm [5]. It was revealed that there is an almost homogenous distribution of positive charges over the surface, suggesting that the interaction with DSS does not occur at a specific region on the lysozyme molecule [5].

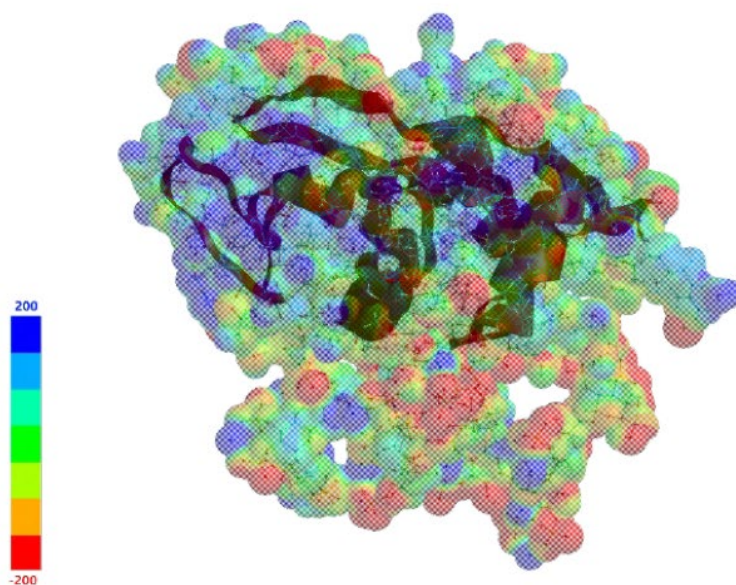
Figure 4.3 displays the MMFF-optimised equilibrium geometry of the lysozyme-DSS structure in the presence of 177 water molecules inherited from the protein structure database (*1DPX*). The DSS was aligned to the lysozyme molecule with four of the sulphate groups in DSS positioned close to the amino groups (Lys or Arg) in lysozyme (each sulphate interacts with one Lys or Arg). Although there is a tendency to reshape for an optimised geometry during energy minimisation, there were slight rearrangements of the structures of lysozyme and DSS. The backbone shape of lysozyme remained. However, there were adjustments of the side chains especially at the location where the interaction with DSS occurs. The helix shape of DSS remained, with rearrangement of the sulphate groups due to the strong electrostatic interaction with the amino groups, and also adjustment of the dihedral angles of the glycosidic bonds connecting the polymerisation units to lower the steric tension of the system.

According to the findings of studies elsewhere, at a low charge ratio of DSS to lysozyme, there was little influence on the protein state when binding with DSS [32, 33]. However, it was stated that at a high charge ratio of DSS to lysozyme, the electrostatic binding with the polyelectrolyte chain could induce tension or “stretching” of the protein molecule [32, 33]. There may also be changes in the tertiary structure of lysozyme at the high charge ratio [5]. Aside from the factor of the charge ratio, the state of the protein also depends on the specific polyelectrolyte-binding site [34, 35].

This lysozyme-DSS interaction is just a preliminary test of the geometry behaviour of the macromolecules optimised by MMFF. In later studies, not only the non-specific ionic interaction but also the specific shape-dependent steric chemical fit of the DSS onto the protein reaction sites (either onto the groove or exposure sites of the protein molecule) are to be examined regarding the flexibility of both structures. Both geometry optimisation and molecular dynamics simulation can be performed to learn the equilibrium geometry, thermodynamic properties and dynamic behaviours of the protein-DSS system in the cases of using different force fields, at different solvation states, with different charge ratios of DSS to lysozyme, at different binding sites, etc.



(a)



(b)

Figure 4.3. The MMFF-optimised geometry of the interacted molecular structure of lysozyme-DSS in the format of ball and wire with the ribbon representing the protein backbone (a), and the electrostatic potential map of the structure (b). In (b), the scale of the electrostatic potential has the unit of kJ/mol, and the blue and red colours represent the positive charge (energy positive; repulsive to a +1 charge) and negative charge (energy negative; attractive to a +1 charge) respectively. The ball or wire in grey represent carbon atom, cyan the nitrogen, red the oxygen, yellow the sulphur, blue the sodium, and green the chloride.

4.4 Conclusions

Here a molecular modelling strategy using molecular mechanics and quantum mechanics methods for the preliminary simulation of lysozyme-DSS interaction is presented. The simulation was used in a predictive manner and compared to experimental data to assess the validity of the methods for the calculation of hydration energy of common ions. There was a deviation of ± 80 kJ/mol of the calculated hydration energy, via implicit or explicit solvation model, from the experimental values. The calculated energy of the ion exchange reactions of small molecules fluctuates around 0 kJ/mol. For one mole ion exchange between DSS monomer and Lys or Arg, there was negative reaction energy with the absolute value of more than 150 kJ/mol, which was calculated by MMFF with an explicit number of water molecules in the model. Regarding the interaction between lysozyme and DSS, the backbone structure of lysozyme and the helix of DSS were maintained, though with conformational adjustment. Further investigations are needed on the lysozyme-DSS interaction with respect to their geometry, and steric and thermodynamic behaviours.

References

1. Cooper, C., P. Dubin, A. Kayitmazer, and S. Turksen, Polyelectrolyte–protein complexes. *Current opinion in colloid & interface science*, 2005. **10**(1-2): p. 52-78.
2. Wang, Y.f., J.Y. Gao, and P.L. Dubin, Protein separation via polyelectrolyte coacervation: Selectivity and efficiency. *Biotechnology Progress*, 1996. **12**(3): p. 356-362.
3. Lankalapalli, S. and V. Kolapalli, Polyelectrolyte complexes: a review of their applicability in drug delivery technology. *Indian journal of pharmaceutical sciences*, 2009. **71**(5): p. 481.
4. Gregory, J., Flocculation by polymers and polyelectrolytes. *Solid/liquid dispersions*, 1987. **8**: p. 163-180.
5. Antonov, Y.A., I.L. Zhuravleva, R. Cardinaels, and P. Moldenaers, Structural studies on the interaction of lysozyme with dextran sulfate. *Food Hydrocolloids*, 2015. **44**: p. 71-80.
6. Chiancone, E., M.R. Bruzzesi, and E. Antonini, Studies on dextran and dextran derivatives. X. The interaction of dextran sulfate with lysozyme. *Biochemistry*, 1966. **5**(9): p. 2823-2828.
7. Vardhanabhuti, B., U. Yucel, J.N. Coupland, and E.A. Foegeding, Interactions between β -lactoglobulin and dextran sulfate at near neutral pH and their effect on thermal stability. *Food Hydrocolloids*, 2009. **23**(6): p. 1511-1520.
8. Doublier, J.-L., C. Garnier, D. Renard, and C. Sanchez, Protein–polysaccharide interactions. *Current opinion in Colloid & interface Science*, 2000. **5**(3-4): p. 202-214.
9. Alahdad, Z., R. Ramezani, M. Aminlari, and M. Majzoobi, Preparation and Properties of Dextran Sulfate– Lysozyme Conjugate. *Journal of agricultural and food chemistry*, 2009. **57**(14): p. 6449-6454.
10. Li, H., S.-r. Sun, J.Q. Yap, J.-h. Chen, and Q. Qian, 0.9% saline is neither normal nor physiological. *Journal of Zhejiang University-SCIENCE B*, 2016. **17**(3): p. 181-187.
11. Milo, R. and R. Phillips, *Cell biology by the numbers*. 2016, New York: Garland Science, Taylor & Francis Group.
12. Silva, J.J.R.F.d. and R.J.P. Williams, *The biological chemistry of the elements : the inorganic chemistry of life*. 2001, Oxford: Clarendon.
13. Grant, G.H. and W.G. Richards, *Computational Chemistry*. 1995: Oxford University Press. 817-818.

14. Leach, B.A.R., *Molecular modelling: principles and applications* (second Edition). 2001: Pearson Education Limited.
15. Hornák, V., R. Dvorský, and E. Sturdík, *Receptor-ligand interaction and molecular modelling*. *General Physiology & Biophysics*, 1999. **18**(3): p. 231.
16. Rose, P.W., A. Prlić, A. Altunkaya, C. Bi, A.R. Bradley, C.H. Christie, L.D. Costanzo, J.M. Duarte, S. Dutta, and Z. Feng, *The RCSB protein data bank: integrative view of protein, gene and 3D structural information*. *Nucleic Acids Research*, 2016. **45**(Database issue): p. D271-D281.
17. Berman, H.M., J. Westbrook, Z. Feng, G. Gilliland, T.N. Bhat, H. Weissig, I.N. Shindyalov, and P.E. Bourne, *The Protein Data Bank*. *Nucleic Acids Research*, 2000. **28**(1): p. 235-242.
18. Yu, M., H.A. Every, W. Jiskoot, G.J. Witkamp, and W. Buijs, *Molecular structure of dextran sulphate sodium in aqueous environment*. *Journal of Molecular Structure*, **1156** (2018): 320-329.
19. Huang, N., C. Kalyanaraman, K. Bernacki, and M.P. Jacobson, *Molecular mechanics methods for predicting protein–ligand binding*. *Physical Chemistry Chemical Physics*, 2006. **8**(44): p. 5166-5177.
20. Gräter, F., S.M. Schwarzl, A. Dejaegere, S. Fischer, and J.C. Smith, *Protein/ligand binding free energies calculated with quantum mechanics/molecular mechanics*. *The Journal of Physical Chemistry B*, 2005. **109**(20): p. 10474-10483.
21. Buijs, W., personal communication. 2018.
22. Cornell, W.D., P. Cieplak, C.I. Bayly, I.R. Gould, K.M. Merz, D.M. Ferguson, D.C. Spellmeyer, T. Fox, J.W. Caldwell, and P.A. Kollman, *A second generation force field for the simulation of proteins, nucleic acids, and organic molecules*. *Journal of the American Chemical Society*, 1995. **117**(19): p. 5179-5197.
23. Becke, A.D., *Becke's three parameter hybrid method using the LYP correlation functional*. *J. Chem. Phys*, 1993. **98**: p. 5648-5652.
24. Lee, C., W. Yang, and R.G. Parr, *Development of the Colle-Salvetti correlation-energy formula into a functional of the electron density*. *Physical review B*, 1988. **37**(2): p. 785.
25. Spartan. Wavefunction, Inc. (www.wavefun.com)
26. Cramer, C.J. and D.G. Truhlar, *Continuum solvation models, in Solvent effects and chemical reactivity*. 2002, Springer. p. 1-80.

27. Tapia, O., J. Bertrán, and J.B. Bertrán, Solvent effects and chemical reactivity. Vol. 17. 1996: Springer.
28. da Silva, E.F., H.F. Svendsen, and K.M. Merz, Explicitly representing the solvation shell in continuum solvent calculations. *The Journal of Physical Chemistry A*, 2009. **113**(22): p. 6404-6409.
29. Marcus, Y., Thermodynamics of solvation of ions. Part 5.—Gibbs free energy of hydration at 298.15 K. *Journal of the Chemical Society, Faraday Transactions*, 1991. **87**(18): p. 2995-2999.
30. Zhang, I.Y., J. Wu, and X. Xu, Extending the reliability and applicability of B3LYP. *Chemical Communications*, 2010. **46**(18): p. 3057-3070.
31. Ponder, J.W. and D.A. Case, Force fields for protein simulations, in *Advances in protein chemistry*. 2003, Elsevier. p. 27-85.
32. Volkin, D.B., P. Tsai, J.M. Dabora, J.O. Gress, C.J. Burke, R.J. Linhardt, and C.R. Middaugh, Physical stabilization of acidic fibroblast growth factor by polyanions. *Archives of biochemistry and biophysics*, 1993. **300**(1): p. 30-41.
33. Ivinova, O.N., V.A. Izumrudov, V.I. Muronetz, I.Y. Galaev, and B. Mattiasson, Influence of complexing polyanions on the thermostability of basic proteins. *Macromolecular bioscience*, 2003. **3**(3-4): p. 210-215.
34. Lookene, A., O. Chevreuil, P. Østergaard, and G. Olivecrona, Interaction of lipoprotein lipase with heparin fragments and with heparan sulfate: stoichiometry, stabilization, and kinetics. *Biochemistry*, 1996. **35**(37): p. 12155-12163.
35. Paulíková, H., M. Molnárová, and D. Podhradský, The effect of heparin and pentosan polysulfate on the thermal stability of yeast alcohol dehydrogenase. *IUBMB Life*, 1998. **46**(5): p. 887-894.

Chapter 5

Brownian dynamics simulation of protein-polyelectrolyte particle formation and growth

Miao Yu, Hayley A. Every, Peter J. T. Verheijen, Wim Jiskoot, Geert-Jan Witkamp

Abstract

Brownian dynamics simulations were performed to describe the perikinetic agglomeration of the system starting primarily with protein and polyelectrolyte, from nano-sized molecules or complexes to micro-sized particles. The simulation was an extension of the classical Smoluchowski's model. The compositions of early complexes (i.e., the content of protein and polyelectrolyte) were found to be in correspondence to the initial ratio of protein and polyelectrolyte in the system. The simulation of the particle agglomeration up to 240 min was performed, and the hypothesis on the collision efficiency was discussed. With a proper value of the collision efficiency factor, the simulation results on the particle concentration profile are comparable with experimental observation. In addition to the simulations based on Smoluchowski's model, there were two other approaches, the Direct Collision simulation and the probability-based simulation, proposed to simulate the protein-polyelectrolyte agglomeration, and are briefly described in this chapter.

5.1 Introduction

The interaction between protein (P) and polyelectrolyte (PE) is being studied for the development of protein drug delivery systems [1] and is an important topic in pharmaceutical sciences [2]. Biocompatible polyelectrolyte has advantages as encapsulation materials as they can bind to biomacromolecular drugs, such as proteins, through electrostatic interactions and allow for flexible coating configurations.

Simulating protein-polyelectrolyte (P-PE) complexation and particle growth pertains to many pharmaceutical and biotechnological processes, such as the design of drug delivery systems formulations. The formation and growth of P-PE complexes (PPE) have been monitored experimentally by nanoparticle tracking analysis (NTA) and flow imaging microscopy (FIM) [3]. The models or numerical simulations which especially describe the P-PE complex formation and growth pattern can contribute to a better understanding of P-PE interaction and agglomeration mechanism.

In the early twentieth century, Smoluchowski firstly developed a model to describe the coagulation of monodispersed spherical aerosols [4]. This model was tested to predict the agglomeration of gold nanoparticles and compared to experimental observations by R. Zsigmondy on the concentration of gold nanoparticles as function of time. In this model, one particle is assumed to be stationary (the reference particle), and the collisions with the other particles diffusing towards it via Brownian motion were considered to be the driving force for their agglomeration. The rate of particle agglomeration depends on the frequency of collisions, which were depicted by Smoluchowski's classical analytical expression. Conventionally, this classical model was widely used for the prediction of particle growth based on the collisions among particles following stochastic Brownian motion and many later studies on this topic are conducted with reference to Smoluchowski's theory [5, 6].

Particle agglomeration can be sub-divided into three mechanisms: perikinetic agglomeration, orthokinetic agglomeration and differential sedimentation, which are considered to be the result of the Brownian motion of particles, sheared dispersions, and the difference in settling velocities of particles, respectively. The perikinetic mechanism dominates when the diameter of the particles is smaller than 1 μm , where the particles follow Brownian motion. When the particle size is greater than 1 μm , gravity and fluid drag force have more of an influence, and as a result, differential sedimentation and orthokinetic agglomeration occur. The present study mainly focuses on the formation and growth of PPE in the nano-size range, where the particles follow perikinetic agglomeration.

The P and PE particle formation and growth generally follows two stages as a result of the attractions such as electrostatic, hydrogen bonding and hydrophobic interactions, and polymer binding among

the molecules or particles: the first stage is the formation of PPE, followed by their quick agglomeration into nanoparticles and the later agglomeration of these nanoparticles (rate-determining step) [7, 8]. In this study, it is assumed that for the system starting with P and PE, the agglomerations only occur for the combinations of P-PE, PPE-P, PPE-PE, and PPE-PPE. There are no agglomerations of P-P and PE-PE. This assumption is illustrated in Figure 5.1. For a convenient description of the composition of the PPE, in this chapter, the PPE is sometimes written in the form of "PPE(i,j)", where i and j represent the number of P and PE composing the PPE.

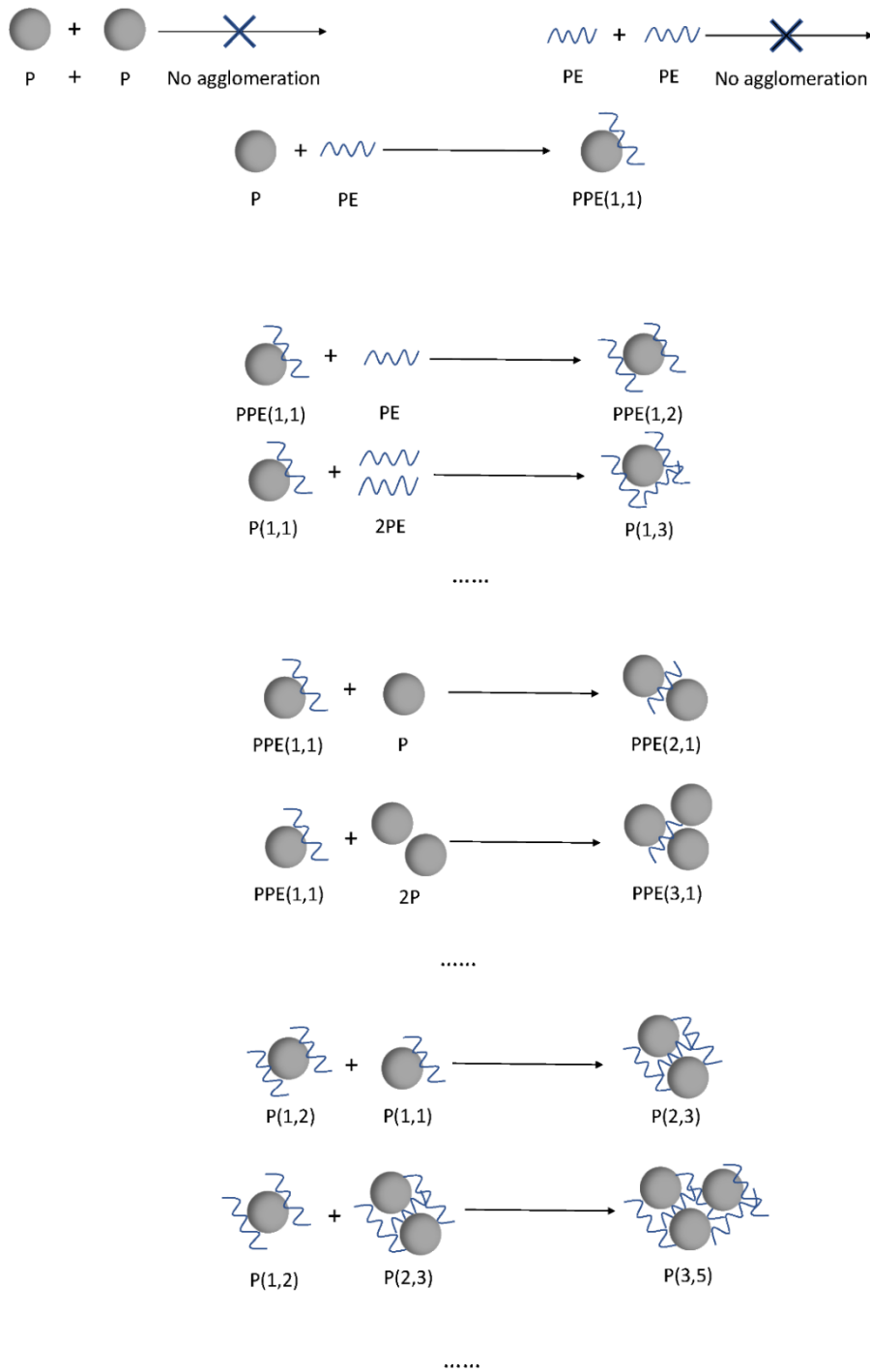


Figure 5.1. Illustration of the assumption made on the agglomeration scheme of the system starting with protein (P) and polyelectrolyte (PE).

Smoluchowski's model deals with the agglomerations of spherical monodisperse primary particles, with constant and uniform collision efficiency factor for all particles during a specific period. For the

modelling of P-PE particle formation and growth, the model needed to be extended to take into consideration the different particle size and complicated particle agglomeration mechanism. In this study, simulations were performed to describe the P-PE agglomeration while differentiating the properties of the colliding particles and enabling the specificity of collision conditions among them.

Aside from the Smoluchowski's analytical solutions, numerical solutions based on the idea of Monte Carlo simulation have also been put forward to describe the evolution of a colliding and coagulating population of suspended particles with the help of computers [9-13]. This method has been used to describe the coagulation mechanism driven by Brownian motion and the development of steady-state size distribution by tracing stochastic particle displacement in the simulation domain. In these studies, topics such as the kinetics of protein-protein association and diffusion-influenced bimolecular reactions have been investigated.

A Direct Collision (DC) simulation, inspired by a previous study of Monte Carlo simulation on particle coagulation [9], has been tried by the authors of this study [14]. Just as the name implies, this method considers that the agglomeration of particles is determined by their direct contact and stickiness (merge to agglomerate). At the start of a simulation, some primary particles are randomly distributed in a volume of a cubical box, where the particle concentration is kept the same as the practical initial condition. In the simulation domain, the particle displacement, collision and agglomeration take place. Each particle follows a straight-line path in stochastic directions during each minimal time step (e.g. 1×10^{-8} s for the gold nanoparticles modelled by Smoluchowski [4], where the particle collision frequency is about $1 \times 10^7 \text{ s}^{-1}$) and after each time step, all the particles are repositioned. The time step of particle displacement was set to be so short that the displacement during each time step is shorter than their effective collision distance, and the missing of contact between the pair of colliding particles is avoided. Whenever the distance between two particles was shorter than the predefined effective collision distance, the two corresponding particles merge and form one particle with a larger volume following the assumption that the newly-formed particle conserves the volumes of the colliding two particles. Simultaneously, the collided particles were removed from the simulation. The particle positions and size were tracked over time during the simulation. At the end of a specific simulation period, the number of particles in the simulation volume was calculated. This represents the particle concentration change of the whole system.

In order to enhance the simulation efficiency and maintain a continuous particle agglomeration profile, a multi-scale approach was developed. For example, for the gold nanoparticle agglomeration detected experimentally by Zsigmondy and modelled by Smoluchowski [4], the DC simulation always starts with tens or hundreds of particles in a mini-volume (about $1 \times 10^{-14} - 1 \times 10^{-13} \text{ m}^3$), followed by step-by-step

expansion into larger volumes (e.g. 8 times, 27 times, 64 times, etc., each increment is the multiplication by the cubic power of an integer) while maintaining the particle number concentration constant (typically about 1×10^{15} particles/m³). Whenever the volume expands, the status of the particles from the smaller volume is copied into the expanded volume. The procedure of volume expansion, as well as particle copying, is consistent with the hypothesis that the particle collision status in the smaller volume is representative of the particle agglomeration in the practical system.

In addition to the DC simulation, the Gillespie algorithm, which is another application of the Monte Carlo approach and was firstly proposed to simulate the stochastic time evolution of a mixture of chemically reacting molecules [15], has provided clues to describe the particle agglomeration in some relevant studies elsewhere [16-19]. The Gillespie algorithm was initially put forward to simulate chemical reaction kinetics. The physical basis of the algorithm is the collision of molecules within a reaction vessel, and each reaction involves at most two molecules. Via this algorithm, the positions and behaviours of the individual particles can be tracked. Unlike Smoluchowski's model, which relies on solving a set of coupled ordinary differential equations for different types of particles, the Gillespie algorithm allows a discrete and stochastic simulation of a system of particles and every reaction is explicitly simulated. Further investigations are needed to apply this idea to simulate the P-PE agglomeration.

Another simulation method, the probability-based method, is proposed in this study to predict the P-PE agglomeration behaviour. The one-dimensional random walk of a particle can be well described by a Gaussian distribution function of the variables x , D and t , which are respectively the distance from the initial position of the particle, the particle diffusion coefficient and the time of the displacement. The probability density function of the occurrence of the particle is given by:

$$P = \frac{e^{-\frac{x^2}{4Dt}}}{\sqrt{4\pi Dt}} \quad \text{Equation 5.1}$$

Where P stands for the probability density. The probability density of a particle along each dimension follows a normal distribution $\sim N(0, 2Dt)$.

Based on this, Uchiyama [20, 21] calculate the joint distribution of the position and the time at which a particle, following standard Brownian motion, hits the surface of another particle for the first time. In the three-dimensional case, the probability density as a function of x and t is expressed as:

$$P_a(x, t) = \frac{x-a}{\sqrt{2\pi t^3}} e^{-\frac{(x-a)^2}{2t}} \left(\frac{a}{x}\right) \quad \text{Equation 5.2}$$

Where a is the inter-particle collision distance.

This chapter aims to simulate the perikinetic P-PE particle formation and growth numerically and to describe the evolution profile of their particle concentration after mixing these two materials. This simulation was based on Smoluchowski's model (SMO-based simulation) and was developed to describe the system starting with two species of particles (P and PE). The simulation results are compared with experimental observation, and their comparisons are discussed. The obtained simulations serve as basis for further investigation on the P-PE agglomeration mechanism and kinetics. Some preliminary results of other methods, the DC method and probability-based method, are described in Appendix C.

5.2 Simulation based on Smoluchowski's model

5.2.1 Theoretical background

The first significant attempt at modelling the particle agglomeration process was made by Smoluchowski [4]. The equations in Smoluchowski's model have formed the core of most subsequent research into agglomeration modelling [5].

The basic equation developed by Smoluchowski is given by

$$\frac{dn_j}{dt} = \frac{1}{2} \alpha \sum_{i=1}^{j-1} \beta(i, j-i) n_i n_{j-i} - \alpha \sum_{i=1}^{\infty} \beta(i, j) n_i n_j \quad \text{Equation 5.3}$$

For perikinetic agglomeration:

$$\beta(i, j) = \frac{2k_B T}{3\mu} \left(\frac{1}{r_i} + \frac{1}{r_j} \right) (r_i + r_j) \quad \text{Equation 5.4}$$

where n represents the particle number concentration; β the collision kernel or frequency (number of collisions per unit volume and time); α the collision efficiency factor; the subscripts i and j represent the discrete particle sizes expressed in terms of the number of monomers (e.g. monomer, dimer, trimer, etc.); k_B the Boltzmann constant; T the absolute temperature; μ the dynamic viscosity of the medium in which the particles diffuse. In Equation 5.3, the first term on the right-hand side indicates the increase in particles of size j by the agglomeration of two particles whose total volume is equal to the volume of a particle of size j . The second term on the right-hand side describes the loss of particles of size j by their agglomeration with other particles. The factor of one half in front of the first term on the right-hand side avoids the double count of particle collisions among the same species of particles. The overall equation thus describes the rate of change in the number concentration of particles of size j . A series of differential equations are then constructed based on Equation 5.3 to describe the whole agglomeration process. Several assumptions are made by Smoluchowski [4, 5]:

1. All particles are spherical and remain so after the collision.
2. Collisions involve only two particles.
3. No breakage of agglomerates occurs.
4. The primary particles are monodispersed (i.e. all of the same size).
5. The collision efficiency factor (shown as α in this chapter) is unity for all collisions.

In this chapter, when the value of α is less than 1, it can be regarded as an indicator of the collision efficiency representing the fraction of collisions that lead to agglomeration. When the value of α is higher than 1, it can be interpreted as the case that there is an extensive influence of the particle that is beyond its geometrical size on the rest of the colliding particles. Hereby the effective collision distance between the two colliding particles (the sum of their effective radius) is longer than the sum of their geometrical radius. Thus the α can be regarded as the ratio of the effective collision radius (R) to its geometrical radius (r).

In this study, the particle agglomeration starts with two types of primary particles, i.e. protein (P) and polyelectrolyte (PE). Regarding the opposite charge carried by the two types of particles, an interaction driven by electrostatic attraction is postulated to occur between P and PE. Assuming that the colliding particles in this study are spherical, the PE, with a size smaller than P, is likely to attach to the surface of P and serves as a sort of shell. The coverage can be calculated by dividing the sum of the cross-sectional area of PE to the surface area of P. The agglomerate (the PPE) has partly the surface covered by PE and the rest surface of P. During later agglomeration driven by electrostatic attraction (the main hypothesis proposed in this study assuming non-neutralisation of charge), when two PPEs collide, it is assumed that the merge of the two particles takes place when P and PE are exposed at the contacting sites of the two particles respectively. Once the two particles merge, there is no breakage of the agglomerate. In this study, it is simply assumed that in the agglomerated particles, the PE is distributed onto the surface with the inner core composed of P, and the value of α was assumed to be roughly constant for all the PPEs. Under these circumstances, the collision efficiency factor (α) can be calculated based on the number of P and PE composed for the PPE when knowing the size of PE and P (to be shown later). Unlike the Smoluchowski's assumption that the α is unity for all collisions, in this simulation for P-PE agglomeration, the α is dependent on the type of the colliding particles and their sizes.

Derived by these thinking, an extension of Equation 5.3 is developed as:

$$\frac{dn_P}{dt} = -\delta(P, PE)n_P n_{PE} - \sum_{i=1}^{\infty} \sum_{j=1}^{\infty} \delta(P, PPE(i, j))n_P n_{PPE(i, j)} \quad \text{Equation 5.5}$$

$$\frac{dn_{PE}}{dt} = -\delta(P, PE)n_P n_{PE} - \sum_{i=1}^{\infty} \sum_{j=1}^{\infty} \delta(PE, PPE(i, j))n_{PE} n_{PPE(i, j)} \quad \text{Equation 5.6}$$

$$\begin{aligned} \frac{dn_{PPE(1,1)}}{dt} = & \delta(P, PE)n_P n_{PE} - \delta(P, PPE(1,1))n_P n_{PPE(1,1)} - \delta(PE, PPE(1,1))n_{PE} n_{PPE(1,1)} \\ & - \sum_{i=1}^{\infty} \sum_{j=1}^{\infty} \delta(PPE(1,1), PPE(i,j))n_{PPE(1,1)} n_{PPE(i,j)} \end{aligned} \quad \text{Equation 5.7}$$

$$\begin{aligned} \frac{dn_{PPE(i,j)}}{dt} = & \delta(P, PPE(i-1,j))n_P n_{PPE(i-1,j)} + \delta(PE, PPE(i,j-1))n_{PE} n_{PPE(i,j-1)} \\ & + \sum_{i_1=1}^{i-1} \sum_{j_1=1}^{j-1} \gamma(i, i_1, j, j_1) \delta(PPE(i_1, j_1), PPE(i-i_1, j-j_1))n_{PPE(i_1, j_1)} n_{PPE(i-i_1, j-j_1)} \\ & - \delta(P, PPE(i,j))n_P n_{PPE(i,j)} - \delta(PE, PPE(i,j))n_{PE} n_{PPE(i,j)} \\ & - \sum_{i_1=1}^{\infty} \sum_{j_1=1}^{\infty} \delta(PPE(i,j), PPE(i_1, j_1))n_{PPE(i,j)} n_{PPE(i_1, j_1)} \end{aligned} \quad \text{Equation 5.8}$$

Where the Equation 5.8 is for $i \geq 1, j \geq 1, i + j > 2$; $\gamma(i, i_1, j, j_1) = 1$ when $i \neq 2i_1$ OR $j \neq 2j_1$; else $\gamma(i, i_1, j, j_1) = \frac{1}{2}$ when $i = 2i_1$ and $j = 2j_1$. Again, the half is necessary to avoid the double count of particle collisions among the same species of particles.

$$\delta(A, B) = \alpha(A, B)\beta(A, B) \quad \text{Equation 5.9}$$

Where P, PE and PPE represent the species of protein, polyelectrolyte and protein-polyelectrolyte complex respectively; α represents the collision efficiency factor, the value of which may change depending on the assumption made on the collision efficiency of the corresponding combinations; the letter i and i_1 represent the number of P in the PPE complex; the letter j and j_1 the number of PE in the complex. Equation 5.5 and Equation 5.6 represent the loss of P and PE, respectively; Equation 5.7 and Equation 5.8 represent the concentration change of PPE; Equation 5.9 shows the calculation of δ where A and B represent the P, PE or PPE species, α refers to Equation 5.10 or Equation 5.11, β refers to Equation 5.4.

As an extension of Smoluchowski's model, the simulation in this study inherits the 1st to the 3rd assumptions of the Smoluchowski's model as mentioned earlier, while replacing the 4th assumption on the monodisperse primary particles to the case of primary particles with multiple sizes and properties (such as size, composition, etc.). For the 5th assumption on the collision efficiency factor, the following assumptions are used instead:

- a. No P-P and PE-PE agglomeration take place.
- b. For the collision of P and PE, electrostatic attraction leads their collision into agglomeration and the value of 1 is used for the α .
- c. For the collision of PE and PPE, the agglomeration takes place either on the sites of PPE that is not covered by PE via electrostatic attraction. The α is calculated as:

$$\alpha = 1 - \frac{jA_{c,PE}}{iA_{s,P}} \quad \text{Equation 5.10}$$

- d. Where $A_{c,PE}$ represents the cross-sectional area of spherical PE; $A_{s,P}$ the surface area of spherical P; and j and i the number of PE and P respectively in the PPE. For the collision of P and PPE, the agglomeration takes place at the site of PPE that is covered by PE via electrostatic attraction. For the collision of PPE and PPE, the polymer bridging dominates the agglomeration of particles. In these cases, the α is calculated as:

$$\alpha = \frac{jA_{c,PE}}{iA_{s,P}} * \left(1 - \frac{jA_{c,PE}}{iA_{s,P}}\right) \quad \text{Equation 5.11}$$

5.2.2 Method

The particle agglomeration simulation is constructed by using the ordinary differential equation (ODE) solver implemented in Matlab (version 2018b, MathWorks). This model has been tested by comparing the numerical results with the results of Smoluchowski's model [4] that was applied to describe the gold nanoparticle agglomeration (data not shown).

In practice, the P-PE agglomeration usually starts with P and PE rather than monodisperse primary particles as assumed in Smoluchowski's publication [4]. To simulate the P-PE agglomeration under a condition closer to reality, an extension of the Smoluchowski's model was developed in which the agglomeration rates among the P, PE and PPE were calculated.

There were experimental investigations on the profile of P-PE particle formation and growth [22]. The experiment started with the mixing of the solution of P and PE with the same concentration (0.01 mg/ml). Thus at the starting time, there is the presence of both P and PE molecules. Monoclonal human IgG subclass (IgG; 150 kDa, pI \approx 8 (isoelectric point)) and dextran sulfate (DS, from Leuconostoc spp., Mw = 5000, pKa \approx 2) were used as the model P and PE, respectively. The P and PE are assumed to be spherical in this study with a radius of 5 nm and 1.5 nm respectively according to the NTA measurement. The primary number ratio of P to PE particles at time zero is 1 to 30. In this study, the simulation was performed with the same starting condition as the experiment.

During the experiment, the particles with the size up to 6 μm were covered during the measurement. If all the particles species from P and PE to PPE of 6 μm , about 0.1 billion ordinary differential equations need to be parallelly solved. This requires vast computation power and is complicated to achieve in practice. Instead, in this study, the simulation was divided into three phases to describe the P-PE agglomeration feasibly (see Figure 5.2). The first phase deals with the complexation of molecular P and PE, which are the basic monomers with which the agglomeration starts. In this phase, the quick agglomeration of P and PE leads to the formation of PPE. In the simulation domain, the concentrations of P and PE decrease in time, meanwhile the concentration of PPE firstly increases, followed by a decrease by agglomerating with the rest of particles. Within a period of up to 0.3 s, the concentration of P and PE drops to below millionth of their initial concentration and the PPE becomes the dominating particles with a concentration of about thousands of times higher. The average value of the ratios of PE to P in the formed PPE at the end of the first phase is the same as the initial ratio of the concentrations of PE to P in the simulation domain (indicated as n_1). Based on this finding, the simulation in the second phase can be simplified into the case of agglomeration based on the monomer PPE(1, n_1). The second phase lasts for about 2 mins, during which all the basic monomers agglomerate into larger particles of PPE(n_2 , n_1n_2), which in turn serve as the basic monomer for the 3rd phase. The simulation of the 3rd phase reflects the behaviour of particles in the experiment as the experimental detection limit only allows for the accurate counting of particles from about 2 mins after the mixing of P and PE.

The idea of dividing the simulating P-PE agglomeration profile into phases can also be extended to further phases (more than 3 phases) by identifying the gradual evolution of the particle behaviours (such as particle size distribution (PSD) and average compositions). This is left for further investigations and may fill the gap between the results of the experiment and the simulation which only covers limited species of PPE particles (with discrete compositions of P and PE).

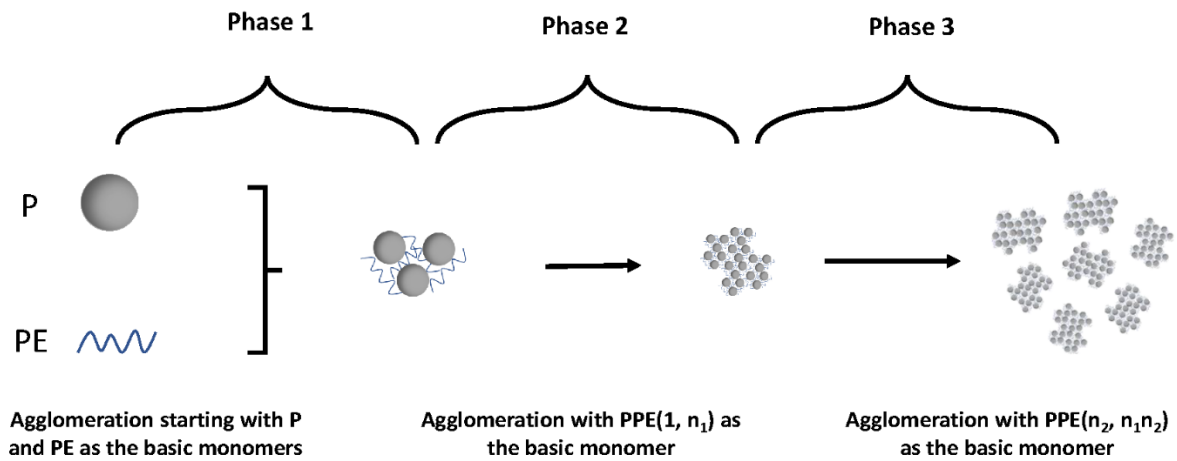
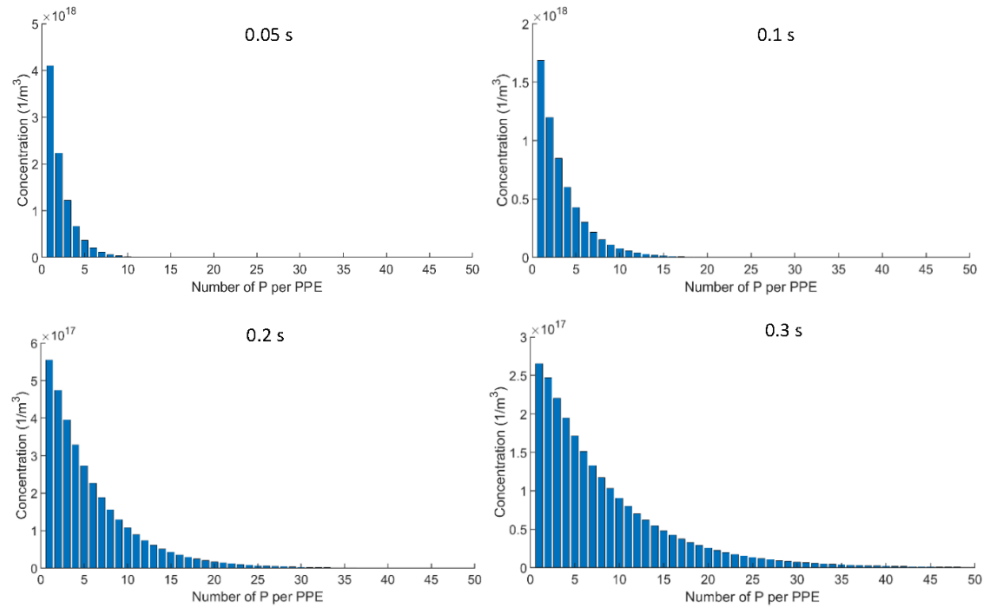


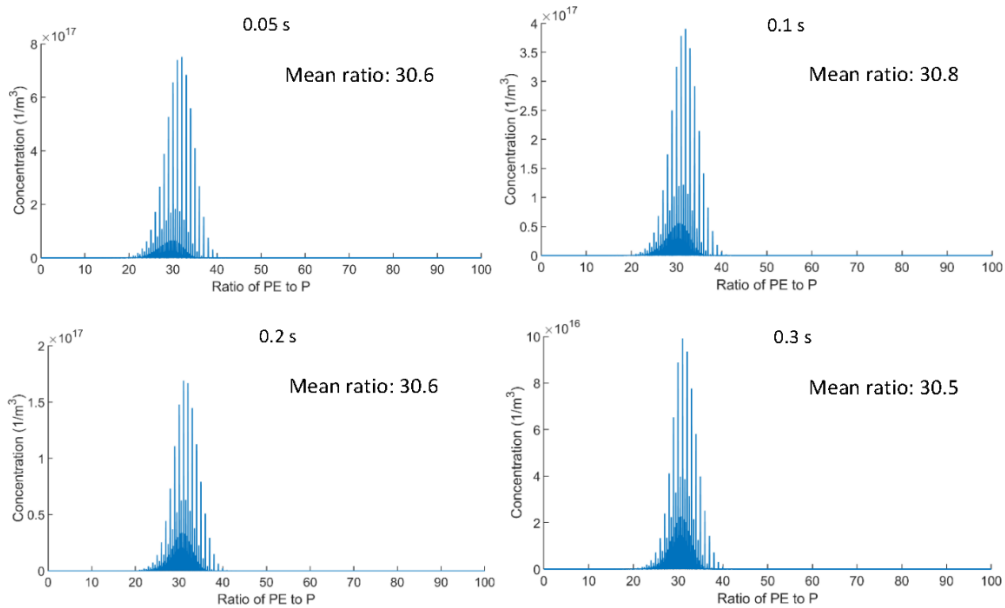
Figure 5.2. The three phases performed to simulate P-PE agglomeration. The n_1 and n_2 are both positive integers where n_1 represents the initial ratio of PE to P in the system and n_2 a value higher than 1.

5.3 Results and discussion

The SMO-based simulation was used to simulate the particle agglomeration profile starting with P and PE. Figure 5.3 shows the calculated particle concentration as function of the number of PE and the ratio of PE to P respectively in the formed PPE after a short period (up to 0.3 s). At 0.3 s, when the P and PE are mostly agglomerated based on the calculation (data not shown), the average composition ratio of P to PE in the formed PPE is 1 to 30, which is the ratio of the starting concentration of P to PE in the simulation domain. This gives an idea that the simulation of P-PE agglomeration can be approximated to the case of simulating the agglomeration of complexes composed of PPE(n , $30n$) (n is a positive integer).



a



b

Figure 5.3. Simulated particle concentration during the 1st phase at 0.05 s, 0.1 s, 0.2 s and 0.3 s as the function of: (a) the P content (represented by the number of P per PPE); and (b) the ratio of PE to P in the complex. The mean value of the ratios of PE to P of the PPE in the simulation are included.

Based on the results above, the simulation on the P-PE agglomeration can be simplified to the scenario of agglomeration among PPE particles with the P to PE ratio of 1 to 30 from 0.3 s onwards.

The evolution of particle size distribution as a function of time up to 2 min is shown in Figure 5.4. Within the simulation period, the total particle concentration decreases while there are particles of larger sizes formed. The starting particle concentration in this simulation is in accordance with the results shown in Figure 5.3, where the PPE(n_2, n_1n_2) (n_1 and n_2 are positive integer values, and n_1 represents the initial ratio of PE to P in the simulation domain) were present. The simulation covers the concentration changes of up to 92000 particle species (i.e. PPE with different P and PE compositions). This corresponds to the particle size ranging from 6 nm to 275 nm. The simulation results are not entirely comparable with the experimental value reported for the 2 min PSD (particle size distribution), where a PSD covering the size range from 100 nm to 800 nm was reported [3]. The simulation results reveal that the shape (e.g. the width) of the PSD (probability density versus the log scale of particle size) is independent of the evolution time, the assumed value of α and the initial PSD with which the evolution starts. Instead, the value of α and initial PSD influences the corresponding particle size of the curve at a specific time. Thus, these two factors cannot thoroughly account for the PSD differences between the simulation and the experimental results. From another point of view, the reported PSD determined in the experiment is not exactly the one taking place at the time point of 2 min. Due to the preparation for and the duration of the measurement (e.g. 1 min), the reported PSD is actually an indicator of the sizes of the particles over a specific period from about 1 min to 3 min after mixing the P and PE. The particle concentration and distribution during this early period of P-PE agglomeration is sensitive to the time of determination regarding the high agglomeration rate as a result of the high particle concentration and collision frequency. In light of this, the comparison of the simulated PSD at 2 min with the experiment is not reasonable.

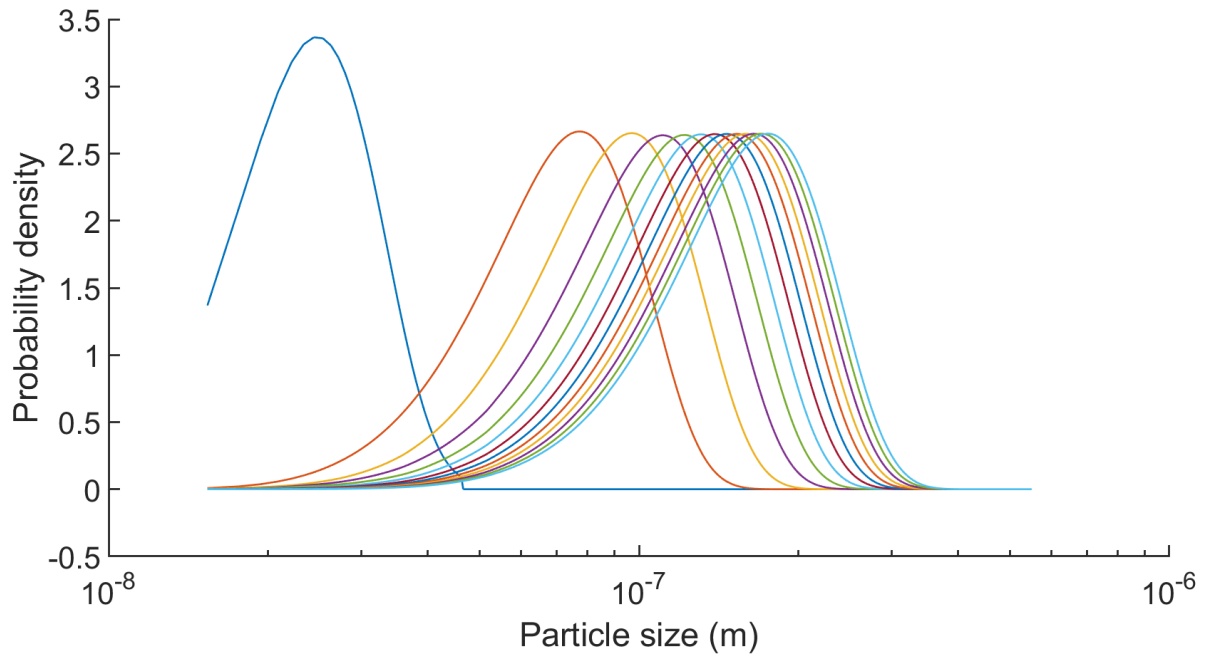


Figure 5.4. The evolution of particle size distribution from 0 s (0.3s) to 120 s with an interval of 10 s (from left to right). The starting particles are PPE(n_2, n_1n_2) (n_1 and n_2 are positive integers, and n_1 is the ratio of the initial concentrations of PE to P) with the size distribution shown in Figure 5.3.

As a further approximation of phase 2, the simulation on the particle concentration as the function of time for the phase from 2 min onwards was performed.

During the experiment, the particles within the size range of 100 to 800 nm and 1 μm to 6 μm were monitored for a period from 2 min up to 430 mins after mixing the P and PE solution. From 240 mins onwards, the majority of particles are in the micro-size range, where the orthokinetic agglomeration rather than perikinetic agglomeration dominates, which is beyond the scope of this chapter. The simulations in this chapter only focus on the particle agglomeration profile up to 240 min.

The monitored particle size distribution at 2 min can be fitted by a lognormal distribution (see Figure 5.5). Based on this fitting, the total particle concentration at 2 min was calculated with the correction of the fraction of the particles in the non-detectable size range of experiment (<100nm; 800-1000 nm; and >6 μm). The corrected total particle concentration was used for the simulation of PPE particle agglomeration from 2 min onwards.

The lognormal model has been used to describe the size distribution of agglomerates driven by Brownian motion [23-25]. However, the measured particle size distribution at a later time point cannot be as well fitted by the lognormal distribution (data not shown), which is not expected when evolving from the lognormal distribution at 2 min. In the experiment, the particle concentrations were measured by two methods --- NTA (from 100 nm to 8000 nm) and FIM (from 1 μm to 6 μm), with specific errors (random or systematic) during the measurement. The NTA is insensitive to the small particles in the sample and instead counts the particle clusters [26, 27]. The laser beam exhibits a Gaussian intensity profile when illuminating the sample. Large and strongly scattering particles at the less intense beam edge may remain detectable and quantifiable, while the scattered light of small particles with a low refractive index contrast may drop below the detection limit [27, 28]. Furthermore, during the experiment, particle concentrations of specific size ranges measured by NTA were recorded. However, the NTA was reported to have a size resolution ratio of 1.33 [29], indicating that the particles out of the specific size range may also be mistakenly included. This gives rise to other probable errors. Last but not least, the presence of large particles in the NTA measurement affects the detection of small particles. The intense light scattering of large particles makes the small particles more difficult to be detected and prevents some of them from being tracked by the NTA software. Thus the spiking with large particles resulted in the underestimation of the number of smaller particles. The presence of a few large particles in a sample has a little impact on NTA sizing accuracy but reduces the number of small particles detected by the software [30]. The FIM also has several errors resulted from: i) the improper adjustment of camera focus, which gives rise to errors of the detected particle size [31]; ii) the possibility of coincidence errors (i.e. multiple particles within the flow cell are counted as a single particle) when measuring at a high concentration [32]; iii) the systematic differences in particle size distribution for each defined particle shape, which may limit the consistency of the particle concentration determination [33].

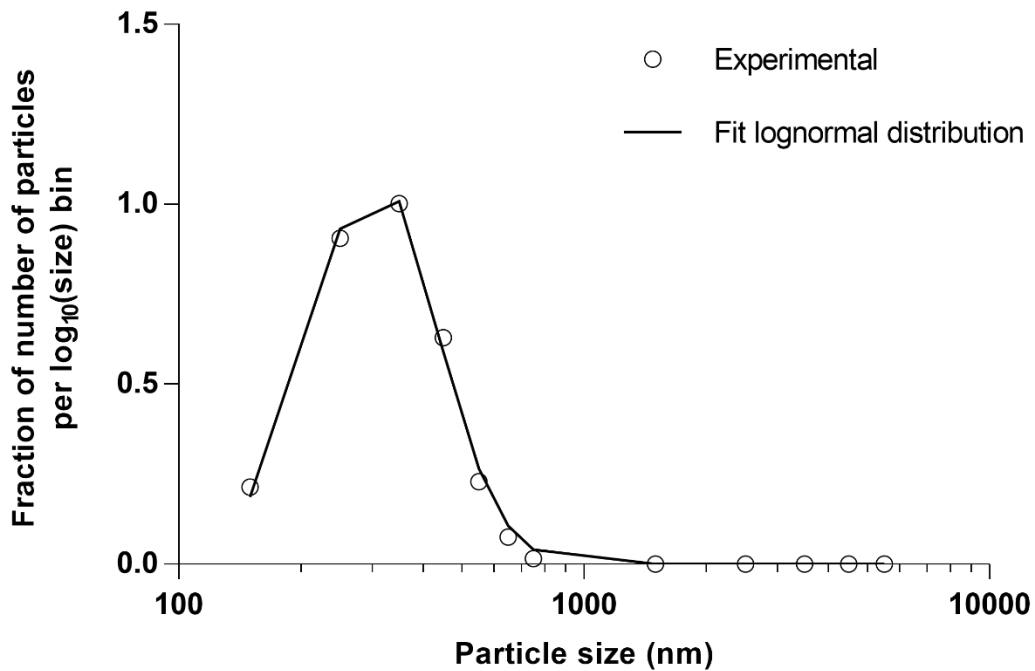


Figure 5.5. Lognormal fitting of the experimentally-determined particle size distribution at 2 min with the geometric mean value of 298 and geometric standard deviation of 1.43.

In the experiment, the primary P and PE finally agglomerated into particles with the size up to about 3 μm within the monitoring time scope (up to 240 min). Each of these particles contains millions of P and PE. The simulation involving all the PPE species formed by the agglomeration starting with millions of P and PE requires high computational power and is not achievable in this study. Instead, a specific number of starting PPE with discrete sizes (discrete compositions of P and PE) were simulated. The agglomerates of these particles thus also have discrete compositions of P and PE.

Figure 5.6 depicts the simulation results starting with PPE composing a discrete number of P and PE. The PPE(20, 20n), PPE(50, 50n) and PPE(100, 100n) (where n is a positive integer value) were simulated respectively, and up to 92000 agglomerate species were involved in the simulation. An almost overlap of the three curves is displayed, indicating the little influence of the composition of the discretely sized PPE on the simulated agglomeration profile.

With the assumption made on the value of α (about 0.22), a slightly quicker agglomeration of the simulated particles was observed than the experimental observation. This deviation can be narrowed a bit by tuning the value of α to 0.19 (data not shown), which is the collision efficiency factor reported elsewhere to fit the experimental data [22].

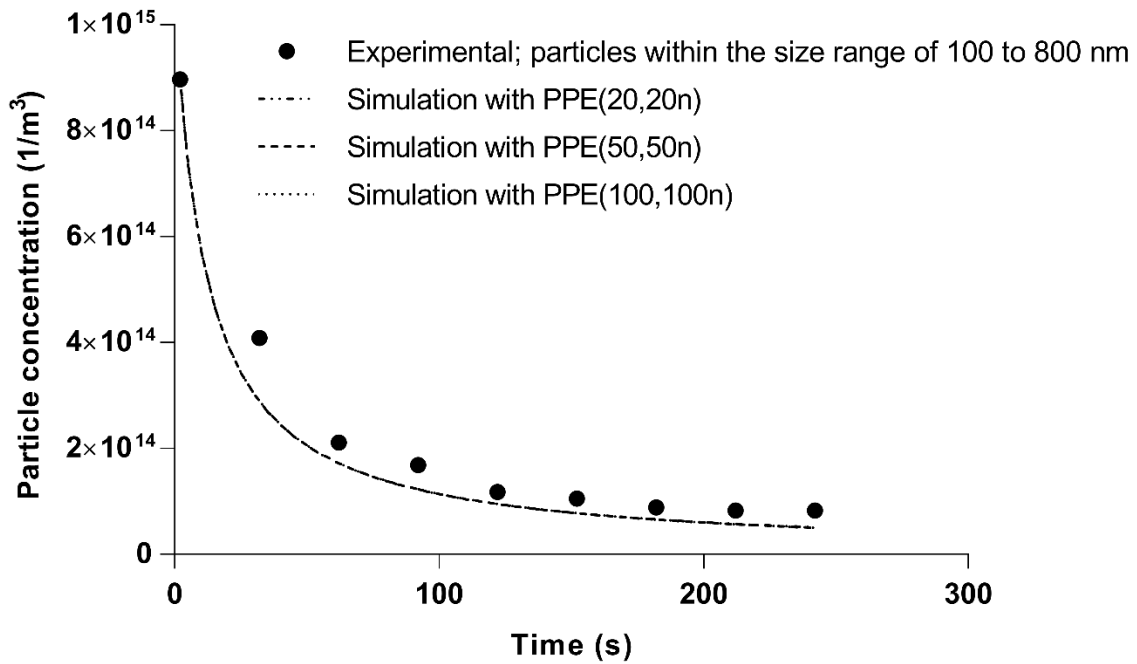


Figure 5.6. Comparison of the experimental result on the particle concentration as the function of time to the SMO-based simulation of PPE with the discrete compositions of P and PE, where n represents the initial ratio of the concentration of PE to P in the simulation domain.

The P-PE agglomeration mechanism is too complicated to achieve a conclusive remark on the value of collision efficiency factor, and it is scarce to find an analogue model or simulation reporting the values of α for the P-PE system. The α depends not only on the strength and nature of the interaction between the colliding particles but also their microstructures. One of the factors affecting the value of α is the distribution of PE in the PPE complex. In the assumption made for the simulation, the ratio of PE coverage on the particle surface is independent of the composition of the PPE and is calculated as the ratio of the sum of cross-sectional area of PE to the surface area of P. This assumption simplifies the scenario of the distribution of PE in the PPE. In principle, not all PE are distributed on the surface regarding the complexity of the PPE structure. Even so, the surface area of the coated P should not have been kept constant without any change with the number of P accumulated in the PPE. Another factor lies in the assumption made on the interaction mechanism. In 5.2.1, the assumption is made based on the mechanism of electrostatic interaction. There is also a mechanism of polymer bridging contributing to the agglomeration of PPE particles [8], where the extended chains of the PE on one complex particle may interact with and adhere to an exposed area on the surface of a second particle, and the polymer functions as a “glue” to bind the particles when colliding.

Thereby, the efficiency of collision should depend on the degree of polymer adsorbate chain extension and the extent of particle surface coverage by the polymer. Even if the bridging of polymers contributes to the agglomeration, not all of them will take part in the “glue” of the complex particles as there may be repulsive forces among the charged groups. Additionally, the reported experimental particle concentration is lower than the practical total particle concentration, therefore in Figure 5.6, the actual α can be even smaller than used for the simulation.

The surface roughness is also a factor to be considered that may affect the particle agglomeration rate [34, 35]. It was observed that the surface roughness, rather than particle size, determines the geometrical factor in the interaction energy of approaching particles. Deviations from a smooth surface ("surface roughness") will affect coagulation rates, if and when their characteristic amplitudes, the interparticle distance, and the range of the interaction forces are commensurate. At the interparticle distance where the interaction energy reaches its maximum, it is not the radius which makes the difference, but the roughness of the particle surfaces to contribute to the details of the interactions. Thus the surface roughness influences the dependence of the coagulation on the particle size. For rather fine roughness, the critical coagulation concentration (the minimum electrolyte concentration that will cause the rapid flocculation of a suspension in a given time [36]) decreases with increasing particle size. For the coarse surface, the critical coagulation concentration depends on the average configuration of the surface roughness in the surface area where two double layers overlap, either increase or decrease.

5.4 Conclusions

The SMO-based simulation proves to be useful to study the kinetics of P-PE particle agglomeration starting from the molecular level. The simulation reveals that at the early stage of P-PE mixing, most of the formed PPE has the ratio of P to PE the same as the initial ratio in the simulation domain. Based on this finding, the simulation of the P-PE agglomeration in the later period can be simplified to the case of collision and agglomeration among PPEs composing the same ratio of P to PE. With proper assumption on the collision efficiency factor, the SMO-based simulation yields comparable results on the P-PE agglomeration profile with experimental observation.

In the SMO-based simulation, the properties of the simulated particles and their binding mechanisms cannot be individually identified and specified. To overcome this limitation, the DC simulation is proposed to simulate the P-PE agglomeration with the particle properties (such as size, composition and charge) discretely distinguished and inter-particle interaction mechanism (such as electrostatic and hydrodynamic interaction) distinctly defined.

For the PB simulation, the inter-particle collision probability rather than their relative position of the particle is used to evaluate the agglomeration among the particles. Further investigations on the algorithms of the PB simulation are needed.

In this study, the collision efficiency factor is based on the assumption that the particles are agglomerated at the sites with opposite charge. However, the collision efficiency cannot be merely limited to the electrostatic effect regarding the complex structure and properties of P, PE and PPE. This requires further study on an explicit description of the collision efficiency among the simulated particles.

Regarding the applications of the developed methods, the SMO-based simulation seems to be a convenient and efficient method to describe the profile of particle formation and growth for practical purposes. The other two proposed methods are more suitable to explicitly distinguish the properties of different particles (in this study P, PE and PPE) during the simulation.

Acknowledgement

Support was given by Dr. Ludolf E Meester for the investigation on the probability-based method for P-PE agglomeration simulation.

References

1. Cooper, C., P. Dubin, A. Kayitmazer, and S. Turksen, Polyelectrolyte–protein complexes. *Current opinion in colloid & interface science*, 2005. **10**(1-2): p. 52-78.
2. Dakhara, S. and C. Anajwala, Polyelectrolyte complex: A pharmaceutical review. *Systematic Reviews in Pharmacy*, 2010. **1**(2): p. 121.
3. Sediq, A.S., M.R. Nejadnik, I. El Bialy, G.-J. Witkamp, and W. Jiskoot, Protein–polyelectrolyte interactions: Monitoring particle formation and growth by nanoparticle tracking analysis and flow imaging microscopy. *European Journal of Pharmaceutics and Biopharmaceutics*, 2015. **93**: p. 339-345.
4. Smoluchowski, M., Versuch einer mathematischen Theorie der Koagulationskinetik kolloider Lösungen. *Zeitschrift Für Physikalische Chemie*, 1917. **92**(1): p. 129-168.
5. Thomas, D., S. Judd, and N. Fawcett, Flocculation modelling: a review. *Water research*, 1999. **33**(7): p. 1579-1592.
6. Meyer, C. and D. Deglon, Particle collision modelling—a review. *Minerals Engineering*, 2011. **24**(8): p. 719-730.
7. Gregory, J., Flocculation by polymers and polyelectrolytes. *Solid/liquid dispersions*, 1987. **8**: p. 163-180.
8. Chen, W. and S. Walker, The mechanism of floc formation in protein precipitation by polyelectrolytes. *Chemical engineering science*, 1992. **47**(5): p. 1039-1045.
9. Pearson, H., I. Valioulis, and E. List, Monte Carlo simulation of coagulation in discrete particle-size distributions. Part 1. Brownian motion and fluid shearing. *Journal of Fluid Mechanics*, 1984. **143**: p. 367-385.
10. Satoh, A., Introduction to practice of molecular simulation: molecular dynamics, Monte Carlo, Brownian dynamics, Lattice Boltzmann and dissipative particle dynamics. 2010: Elsevier.

11. Northrup, S.H., S.A. Allison, and J.A. McCammon, Brownian dynamics simulation of diffusion-influenced bimolecular reactions. *The Journal of chemical physics*, 1984. **80**(4): p. 1517-1524.
12. Northrup, S.H. and H.P. Erickson, Kinetics of protein-protein association explained by Brownian dynamics computer simulation. *Proceedings of the National Academy of Sciences*, 1992. **89**(8): p. 3338-3342.
13. Narsimhan, G. and E. Ruckenstein, Monte Carlo simulation of brownian coagulation over the entire range of particle sizes from near molecular to colloidal: Connection between collision efficiency and interparticle forces. *Journal of Colloid and Interface Science*, 1985. **107**(1): p. 174-193.
14. Miao Yu, A.S.S., Hayley A. Every, M. Reza Nejadnik, Peter Verheijen, Wim Jiskoot, Geert-Jan Witkamp Brownian dynamics simulation of protein-polyelectrolyte particle formation and growth. in 30th Marian Smoluchowski Symposium on Statistical Physics. 2017. Krakow, Poland.
15. Gillespie, D.T., A general method for numerically simulating the stochastic time evolution of coupled chemical reactions. *Journal of computational physics*, 1976. **22**(4): p. 403-434.
16. Trzeciak, T.M., Brownian coagulation at high particle concentrations. 2012, TU Delft, Delft University of Technology.
17. Goodson, M. and M. Kraft, An efficient stochastic algorithm for simulating nano-particle dynamics. *Journal of Computational Physics*, 2002. **183**(1): p. 210-232.
18. Schaafsma, S.H., P. Vonk, P. Segers, and N.W. Kossen, Description of agglomerate growth. *Powder technology*, 1998. **97**(3): p. 183-190.
19. Smith, M. and T. Matsoukas, Constant-number Monte Carlo simulation of population balances. *Chemical Engineering Science*, 1998. **53**(9): p. 1777-1786.
20. Uchiyama, K., Density of Space-Time Distribution of Brownian First Hitting of a Disc and a Ball. *Potential Analysis*, 2016. **44**(3): p. 497-541.
21. Uchiyama, K., Asymptotics of the densities of the first passage time distributions for Bessel diffusions. *Transactions of the American Mathematical Society*, 2012. **367**(4): p. págs. 2719-2742.
22. Sediq, A.S., M.R. Nejadnik, B.I. El, G.J. Witkamp, and W. Jiskoot, Protein-polyelectrolyte interactions: Monitoring particle formation and growth by nanoparticle tracking analysis and flow imaging microscopy. *European Journal of Pharmaceutics & Biopharmaceutics*, 2015. **93**: p. 339-345.

23. Park, S., K. Lee, E. Otto, and H. Fissan, The log-normal size distribution theory of Brownian aerosol coagulation for the entire particle size range: Part I—analytical solution using the harmonic mean coagulation kernel. *Journal of Aerosol Science*, 1999. **30**(1): p. 3-16.
24. Otto, E., H. Fissan, S. Park, and K. Lee, The log-normal size distribution theory of Brownian aerosol coagulation for the entire particle size range: part II—analytical solution using Dahneke's coagulation kernel. *Journal of Aerosol Science*, 1999. **30**(1): p. 17-34.
25. Camejo, M., D. Espeso, and L. Bonilla, Influence of primary-particle density in the morphology of agglomerates. *Physical Review E*, 2014. **90**(1).
26. Nicolet, A., F. Meli, E. Van der Pol, Y. Yuana, C. Gollwitzer, M. Krumrey, P. Cizmar, E. Buhr, J. Pétry, and N. Sebaihi, Inter-laboratory comparison on the size and stability of monodisperse and bimodal synthetic reference particles for standardization of extracellular vesicle measurements. *Measurement Science and Technology*, 2016. **27**(3).
27. Kestens, V., V. Bozatzidis, P.-J. De Temmerman, Y. Ramaye, and G. Roebben, Validation of a particle tracking analysis method for the size determination of nano-and microparticles. *Journal of Nanoparticle Research*, 2017. **19**(8): p. 271.
28. Malloy, A. and B. Carr, NanoParticle tracking analysis—The halo™ system. *Particle & Particle Systems Characterization*, 2006. **23**(2): p. 197-204.
29. NanoParticle Tracking Analysis (NTA) and Dynamic Light Scattering (DLS) - Comparison between NTA and DLS. [accessed: 2018 19 December]; Available from: <https://www.azonano.com/article.aspx?ArticleID=2274>.
30. Filipe, V., A. Hawe, and W. Jiskoot, Critical evaluation of Nanoparticle Tracking Analysis (NTA) by NanoSight for the measurement of nanoparticles and protein aggregates. *Pharmaceutical research*, 2010. **27**(5): p. 796-810.
31. Allen, T., Particle size analysis by image analysis, in *Powder Sampling and Particle Size Determination*. 2003, Elsevier. p. 142-207.
32. Reynolds, R., D. Stramski, V. Wright, and S. Woźniak, Measurements and characterization of particle size distributions in coastal waters. *Journal of Geophysical Research: Oceans*, 2010. **115**(C8).
33. Different measuring techniques provide different results – but what is the truth? [accessed: 2018 19 December]; Available from: <https://www.retsch->

technology.com/applications/technical-basics/different-particle-analysis-techniques-compared/.

34. Shulepov, S.Y. and G. Frens, Surface roughness and the particle size effect on the rate of slow, perikinetic coagulation. *Journal of colloid and interface science*, 1995. **170**(1): p. 44-49.
35. Shulepov, S.Y. and G. Frens, Surface roughness and particle size effect on the rate of perikinetic coagulation: experimental. *Journal of colloid and interface science*, 1996. **182**(2): p. 388-394.
36. Van Olphen, H., *An introduction to clay colloid chemistry : for clay technologists, geologists, and soil scientists*. 1991, Malabar, Fla.: Krieger Pub. Co.

Chapter 6

The investigation of protein diffusion via H-cell microfluidics

Miao Yu, Tiago Castanheira Silva, Andries van Opstal, Stefan Romeijn, Hayley A. Every,
Wim Jiskoot, Geert-Jan Witkamp, Marcel Ottens

Adapted from Biophysical Journal, 116, (2019): 595-609

Abstract

In this study, we developed a microfluidics method, using a so-called H-cell microfluidics device, for the determination of protein diffusion coefficients at different concentrations, pHs, ionic strengths and solvent viscosities. Protein transfer takes place in the H-cell channels between two laminarly flowing streams with each containing a different initial protein concentration. The protein diffusion coefficients are calculated based on the measured protein mass transfer, the channel dimensions and the contact time between the two streams. The diffusion rates of lysozyme, cytochrome c, myoglobin, ovalbumin, bovine serum albumin and etanercept were investigated. The accuracy of the presented methodology was demonstrated by comparing the measured diffusion coefficients with literature values measured under similar solvent conditions using other techniques. At low pH and ionic strength, the measured lysozyme diffusion coefficient increased with the protein concentration gradient, suggesting stronger and more frequent inter-molecular interactions. At comparable concentration gradients, the measured lysozyme diffusion coefficient decreased drastically as a function of increasing ionic strength (from zero onwards) and increasing medium viscosity. Additionally, a particle tracing numerical simulation was performed to achieve a better understanding of the macromolecular displacement in the H-cell micro-channels. It was found that particle transfer between the two channels tends to speed up at low ionic strength and high concentration gradient. This confirms the corresponding experimental observation of protein diffusion measured via the H-cell microfluidics.

6.1 Introduction

Diffusion of proteins is often critical in the design of mass transfer equipment, like protein extraction and fractionation (chromatography) systems, which is widely used in (bio)chemical and biopharmaceutical industries [1]. Moreover, the protein diffusion coefficient is used to estimate its molecular weight and hydration state of proteins, its aggregation state, and its behavior in specific systems where diffusion is the rate-limiting factor, for example, in some controlled drug delivery systems where the release rate of therapeutic protein depends on its diffusion coefficient [1-4].

In the absence of external forces, such as an electric field, at least three forces dominate the dynamics of proteins in a low molecular weight solvent like water [5, 6]: i) Brownian motion; ii) protein-protein (electrostatic) interactions; and iii) hydrodynamic interactions due to perturbation of the solvent velocity by other protein molecules. The protein-protein interactions are dependent on the protein size, shape, surface charge, etc. This makes it complicated to generalise the diffusion behaviour of proteins under various conditions regarding the impact of the forces above on the protein molecular diffusivity.

A summary of various methods for the measurement of solute diffusion coefficient has been listed elsewhere [7, 8]. Among these techniques, dynamic light scattering (DLS), nuclear magnetic resonance (NMR), Taylor dispersion analysis (TDA), Gouy interferometry (GI), Rayleigh interferometry (RI), fluorescence correlation spectroscopy (FCS) have all been used to determine protein diffusion coefficients [9-13]. These techniques are compared in Table 6.1. The drawbacks of some of these techniques, such as the high equipment costs (e.g., NMR) and the need for high-quality equipment parts (e.g., the lens for RI) limit their routine use. Besides, there are some limitations on the detection of some of the listed techniques. As to light scattering methods, there are limiting factors, such as i) a relatively high solute concentration or large solute molecular size is required for a detectable intensity of scattering light; ii) if solute and solvent have the same refractive index, there is no contrast, and thus no scattering light; and (iii) if the turbidity of solutions is too high (e.g., emulsions), multiple scattering of light leads to measurement inconsistencies or errors [7, 14]. As to the Taylor dispersion analysis, the diffusion coefficient is derived from the band broadening measured by the analytical detector (e.g., UV absorbance), thus there is a high requirement on the sensitive detection modality. Additionally, there is a need for large sample injection volume and extended analysis time to fulfil the conditions of validity [13, 15]. Fluorescence methods require the dyeing of protein, which may change its properties and thereby protein-protein interactions [16]. For NMR, local magnetic field gradients and imaging gradients as well as the length of the diffusion period have been reported to affect the

measured diffusion coefficients [17]. In order to relieve some of the drawbacks of these techniques, an orthogonal technique using a microfluidic H-cell is put forward in this study.

Prior research has shown that the application of the microfluidic method is promising for the study of solute diffusion behaviour. The microscale dimensions enable a rapid detectable transport of solute molecules in the fluid. The microfluidics concept has been applied for the diffusion coefficient determination of not only common electrolytes, such as NaCl, but also macromolecules, such as proteins [18-20], where laminar flow tubes or channels were used. The detection methods used in these studies are based on the observation of the spreading of solute bands during transport via the microfluidic devices. This type of diffusion profile in the microfluidic equipment has also been studied to characterize the sizes, interactions and aggregation state of macromolecules (e.g., proteins) [21, 22], and as an indicator of the medium viscosity [23]. When there are two streams introduced to a microchannel at low flow rates (laminar flow at low Reynold number), a fluid interface is formed between the two streams and the solute transfer takes place across the interface [20, 24-27]. In this study, the idea of micro laminar flow is coupled with the quantitative determination of the mass transfer based on the concentration change over the length of the H-cell channel rather than the detection of molecular optical properties, such as with DLS and GI. Therefore, there is less limitation on the selection of the sample materials. Resembling the experimental schemes for solute (e.g., protein) concentration measurement in relevant microfluidics studies [28], a flexibility of mass detection methods, both online and off-line, can be applied during H-cell measurement (e.g., UV-Vis for protein detection in this study and conductivity detection in a previous study [29]), enabling a broader application of the microfluidic H-cell. In our lab, an H-cell (H-shape microfluidic chip) was developed and validated by Hausler, et al. [29] via optimal experimental design (OED) for solute diffusion coefficient measurement. This H-cell was successfully used for the measurement of the diffusion coefficient of common electrolytes as well as polyphenols [29, 30].

The goal of the present study is to determine the diffusion coefficient of proteins, via measuring the mass transfer between the two aqueous streams, by a custom-made micro-fabricated H-cell, and to evaluate the effectiveness of the microfluidic method for the general investigations of biomacromolecular diffusion behaviour. This chapter starts with presenting the measured diffusion coefficients of lysozyme in different solutions (water and buffer), with different inlet concentration profiles for the H-cell and as a function of the medium ionic strength and viscosity. The influence of different operating conditions on the protein diffusivity is shown, and the accuracy of the method is verified via comparison of the results with published values obtained under similar conditions. Next, the applicability of the microfluidics method for a broader range of proteins is validated by measuring the diffusion coefficients of proteins with the molecular weight ranging from about 12 kDa to 150 kDa

(cytochrome c, myoglobin, ovalbumin, bovine serum albumin and etanercept) and comparing the measured values with relevant literature values. Factors that may affect the diffusivity measurement are discussed and exploratory numerical simulations are included.

Table 6.1. Summary of the characteristics of H-cell microfluidics and other techniques for the determination of protein diffusion coefficient.

Characteristics of the technique	DLS	NMR	TDA	GI	RI	FCS	H-cell
	[7, 9, 14, 31, 32]	[7, 8, 17]	[8, 13]	[7, 8, 33]	[7, 33]	[34-37]	
Accuracy	+/- ^c	+ ^d	+/-	+	+	+/-	+/-
Measurement time consumption ^a	+	+/-	+/-	- ^e	-	+/-	+/-
Flexibility	-	-	+/-	NA ^f	NA	-	+
Requirement on sample properties ^b	-	NA	+/-	-	-	-	+
Sample consumption	+/-	+	+	-	-	+	+
Resolution	+	+	+/-	NA	NA	+	+/-
Data analysis	+/-	+/-	+	-	-	NA	+
Set-up cost	+/-	-	+	+/-	-	-	+
Equipment installation	+/-	-	+	-	-	-	+

^a The duration of H-cell measurement depends on the dimension of the microfluidic channel. In this study, it took about 1-2 hours per single run for the measurement of lysozyme diffusion coefficients, where methods like DLS or NMR take about half the time. The length of each measurement can be reduced by using an H-cell of shorter span-wise dimension, where shorter contacting time between the two laminar streams is needed. So the microfluidics method has the potential of shortening the measurement time in the future.

^b such as refractive index, turbidity level, molecular size, etc.

^{c, d, e} The '+' and '-' sign represent the advantageousness and disadvantageousness respectively of the technique for corresponding characteristics, and the medium level is labelled as '+/-'.

^f NA = not available.

6.2 Materials and methods

6.2.1 Materials and preparation of solutions

The proteins used in this study were: lysozyme (LYS) from chicken egg white (14,3 kDa, $pI \approx 11$, Sigma-Aldrich, Zwijndrecht, the Netherlands), cytochrome c (CC) from bovine heart (12.3 kDa, $pI \approx 10-11$, Sigma-Aldrich, Zwijndrecht, the Netherlands), myoglobin (MYO) from horse heart (17 kDa, $pI \approx 6.8-7$, Sigma-Aldrich, Zwijndrecht, the Netherlands), ovalbumin (OVA) from chicken egg white (43 kDa, $pI \approx 4.5-4.9$, Sigma-Aldrich, Zwijndrecht, the Netherlands), bovine serum albumin (BSA) (66.5 kDa, $pI \approx 5-6$, Sigma-Aldrich, Zwijndrecht, the Netherlands), Enbrel[®] (etanercept) (150 kDa, $pI \approx 8$, Pfizer Inc., Capelle aan den IJssel, the Netherlands). Enbrel[®] was supplied at 50 mg/ml (formulation composition is shown later) and the other proteins were supplied as dry powders.

All protein solutions (concentrations shown in Table 6.2) were prepared using ultrapure water (purified using a Milli-Q ultra-pure water system, Millipore™, Molsheim, France) as the solvent. To adjust the pH, phosphate buffer (PB) (Na_2HPO_4 and NaH_2PO_4 , Sigma Aldrich, Zwijndrecht, the Netherlands) and acetate buffer (AC) (acetic acid (Sigma Aldrich, Zwijndrecht, the Netherlands) and sodium acetate (Merck, Darmstadt, Germany)) were used. For etanercept, a placebo buffer was used that contained 10 mg/ml sucrose (Fluka, Sigma Aldrich Steinheim, Germany), 5.8 mg/ml NaCl (J.T. Baker, Deventer, the Netherlands), 5.3 mg/ml arginine hydrochloride Merck (Merck, Darmstadt, Germany) and 3.9 mg/ml $\text{Na}_2\text{HPO}_4 \cdot \text{H}_2\text{O}$ (Sigma, Sigma Aldrich, Steinheim, Germany) (pH 6.3). Furthermore, NaCl (J.T. Baker, Deventer, the Netherlands) and glycerol (Merck, Darmstadt, Germany) were used to change the ionic strength and viscosity of the prepared protein solutions, respectively.

All the prepared solutions were filtered through 0.22- μm cellulose filters (Whatman[®], GE Healthcare, United Kingdom) before the experiments.

6.2.2 Experimental set-up and process description

The experimental set-up is illustrated in Figure 6.1. An H-cell (Micronit[®], Netherlands) made of Borofloat[®] glass with the dimensions 625 mm x 753 μm x 69 μm (L x W x H) was used. The dimensions were measured by using a calibrated ocular micrometre scale implemented in an Olympus microscope (Olympus, Zoeterwoude, the Netherlands).

During the experiments, a syringe pump (Model 270D, KD Scientific, Massachusetts, the USA) introduced two streams with a protein concentration difference into the H-cell. The stream with a higher protein concentration is called the donor stream (DS), while the other stream is named as the

receiver stream (RS). The syringe pump injected and withdrew the streams simultaneously to maintain an equal flow ratio of the two streams during their transport in the H-cell. By implementing both the injecting syringes and sucking syringes, potential pressure drop differences along the outlet tubes were avoided and an equal volumetric split ratio of the DS and RS was achieved at the outlet of the channel [29]. Under this condition, the solute concentration change between the DS and RS is purely a result of the solute diffusion. The input flow rate by the syringe pump was set to achieve a laminar flow profile (Reynold number less than 10). Under this condition, there was a clear interface between the two streams in the middle of the channel (a test of this interface was performed by transporting water (as RS) and an aqueous solution containing dye material (as DS) into the H-cell). The protein diffusion behaviour was examined with different inlet RS and DS concentrations in various liquid media. The operating conditions are summarised in Table 6.2, and there were triplicate measurements for each condition.

For the convenience, in this chapter, the inlet stream concentrations will be described as the “inlet RS concentration vs inlet DS concentration”. For example, 0 vs 2 mg/ml represents inlet concentrations of 0 mg/ml in RS and 2 mg/ml in DS.

Table 6.2. Experimental operating conditions for the H-cell microfluidics study, where the tested proteins, the inlet receiver stream (RS) and donor stream (DS) concentrations, the solvents, the NaCl concentration for ionic strength adjustment and the glycerol concentration for viscosity adjustment are listed.

Experiment	Protein	RS (mg/ml)	DS (mg/ml)	Solvent	NaCl (mM)	Glycerol (w/w%)
1	LYS	0	2	Water	-	-
2	LYS	0	5	Water	-	-
3	LYS	0	10	Water	-	-
4	LYS	2	4	Water	-	-
5	LYS	4	6	Water	-	-
6	LYS	0	2	Water	5	-
7	LYS	0	2	Water	10	-
8	LYS	0	2	Water	500	-
9	LYS	0	2	Water	1000	-
10	LYS	0	0.5	10 mM PB & 100 mM PB *	-	-
11	LYS	0	1	10 mM PB & 100 mM PB	-	-
12	LYS	0	2	10 mM PB & 100 mM PB	-	-
13	LYS	0	5	10 mM PB & 100 mM PB	-	-
14	LYS	0	10	10 mM PB & 100 mM PB	-	-
15	LYS	2	4	10 mM PB	-	-
16	LYS	4	6	10 mM PB	-	-
17	LYS	0	2	10 mM PB	200	-
18	LYS	0	2	10 mM PB	500	-
19	LYS	0	2	10 mM PB	-	10
20	LYS	0	2	10 mM PB	-	20
21	LYS	0	2	10 mM PB	-	40
22	LYS	0	0.5	10 mM AC & 100 mM AC	-	-
23	LYS	0	1	10 mM AC & 100 mM AC	-	-
24	LYS	0	2	10 mM AC & 100 mM AC	-	-
25	LYS	0	5	10 mM AC & 100 mM AC	-	-
26	LYS	0	10	10 mM AC & 100 mM AC	-	-
27	LYS	2	4	10 mM AC	-	-
28	LYS	4	6	10 mM AC	-	-
29	CC	0	2	10 mM PB	-	-
30	MYO	0	2	10 mM PB	-	-
31	OVA	0	2	10 mM PB	-	-
32	BSA	0	2	10 mM PB	-	-
33	etanercept	0	2	placebo buffer	-	-

* The two buffers were used for experiments respectively.

An inline UV-Vis detector (SPD-20AV, Shimadzu, Japan) with a micro flow cell (0.2 μl) was located between the H-cell and the withdrawing syringe of the RS to record the UV-Vis absorbance of the proteins. The UV-Vis detector has a sensitivity limit at the noise level of 0.5×10^{-5} AU. The micro flow cell in the UV-Vis detector enables the inline detection of the proteins in the outlet stream at a low flow rate. A calibration curve was determined to correlate the UV-Vis absorbance with the protein concentration.

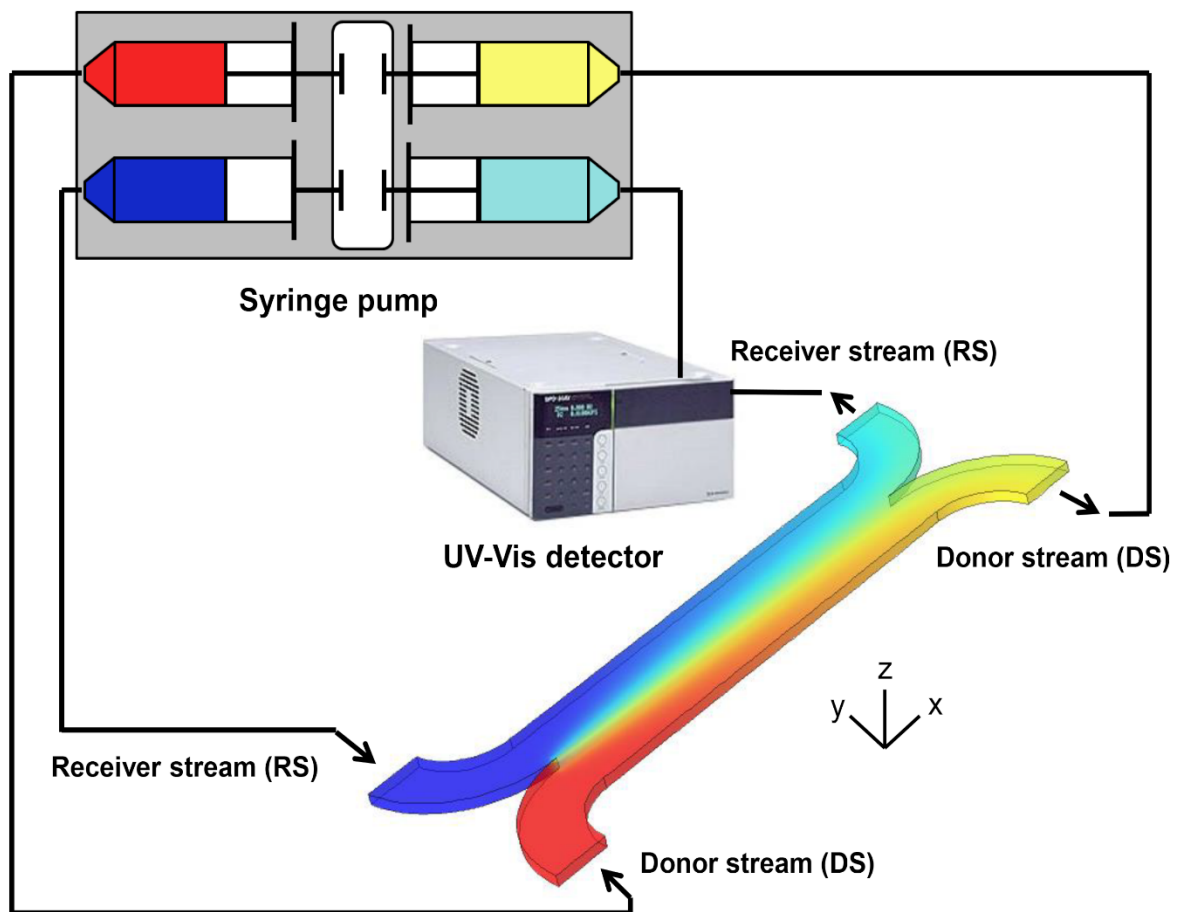


Figure 6.1. Scheme of the H-cell experimental set-up for protein diffusion coefficient measurement. The blue and cyan colours represent the inlet and outlet receiver stream (RS), respectively, and the red and yellow colours represent the inlet and outlet donor stream (DS), respectively.

6.2.3 Protein concentration

Prior to the H-cell microfluidics experiments, the concentration of the prepared protein solutions was determined by a UV-Vis spectrophotometer (UV-1800, Shimadzu, Japan) using the wavelengths and extinction coefficients shown in Table 6.3.

Table 6.3. Wavelengths and extinction coefficients used for the determination of protein concentration measured by UV-Vis spectrophotometer.

Protein	Wavelength (nm)	Extinction coefficient (mL cm ⁻¹ mg ⁻¹)	Reference
LYS	280	2.64	[38]
CC	550	0.68	[39]
MYO	408	11.06	[40]
OVA	280	0.73	[41]
BSA	280	0.66	[42]
etanercept	280	1.49	[43]

6.2.4 Protein mass balance between the DS and RS

During the check of the mass balance between the DS and RS, two UV-Vis detectors were placed between the DS and RS outlets and the corresponding pulling syringes (not as shown in Figure 6.1 where only one UV-Vis detector is placed). Inline detection of the protein concentration in the two streams was performed. The outlet protein concentrations during experiments were obtained based on the calibration curves, which were determined for both detectors. As the syringe pump pushed and pulled the fluid at a consistent flow rate simultaneously, the protein mass recovery was calculated according to Equation 6.1.

$$Recovery (\%) = \frac{C_{outlet,DS} + C_{outlet,RS}}{C_{inlet,DS} + C_{inlet,RS}} \times 100\% \quad \text{Equation 6.1}$$

Where C stands for the protein concentration and the recovery is described as the percentage of the sum of outlet concentration of DS ($C_{outlet,DS}$) and RS ($C_{outlet,RS}$) to the sum of the inlet concentration of both streams ($C_{inlet,DS}$ and $C_{inlet,RS}$).

6.2.5 High-performance size-exclusion chromatography

High-performance size-exclusion chromatography (HP-SEC) was performed to analyse the aggregation state of the protein materials as supplied from the manufacturer. The protein materials were dissolved in PB (10 mM, pH 7.2) (except for etanercept, which was diluted in placebo buffer, pH 6.3) and filtered through a 0.2- μ m filter before measurement.

The protein samples of LYS, CC, MYO, OVA and BSA (50 μ l; \approx 1 mg/ml), were analysed with a Discovery BIO Gel Filtration column (Sigma–Aldrich, St. Louis, USA). A 515 HPLC pump and 717 Plus autosampler (Waters, Milford, USA) were operated at a flow rate of 0.5 ml/min. The mobile phase consisted of 100 mM sodium phosphate buffer, 200 mM sodium chloride, 0.05% (w/v) sodium azide at a pH of 7.2, and was filtered through a 0.2- μ m filter prior to use. Chromatograms were recorded with an SPD-6AV UV detector (Shimadzu, Tokyo, Japan) at a wavelength of 280 nm.

For etanercept analysis (50 μ l; \approx 2 mg/ml), a Yarra SEC-2000 column (Phenomenex, Utrecht, the Netherlands) was used with the running buffer composed of 50 mM phosphate, 150 mM arginine and 0.025% NaN_3 at pH 6.5. UV detection was performed at 280 nm.

6.2.6 Viscosity measurement

The kinematic viscosity of the protein solutions with/without glycerol was determined at room temperature using an Ostwald viscometer (inside tube diameter: 0.26 mm; Roweel Electronic Co., Ltd, Zhengzhou, China). Water was used as the reference.

6.2.7 Calculation of diffusion coefficient

Comsol Multiphysics (version 4.4, Comsol, Sweden), via a Matlab (version 2017a, Mathworks, USA) Livelink, was used to calculate the protein diffusion coefficient based on the outlet RS concentration under steady state. This method of calculation was developed and validated in previous research [29]. The Comsol built-in module of Transport of Diluted Species was used to calculate the mass transfer between the RS and DS. In the case of rectangular cross-section dimension, a simplified solution of the Navier–Stokes equations was used [44].

The z-averaged velocity distribution along the y-axis was calculated according to Equation 6.2:

$$\bar{v}(y) = v\left(\frac{m+1}{m}\right)\left[1 - \left(\frac{y}{a}\right)^m\right] \quad \text{Equation 6.2}$$

Where

$$m = 1.7 + 0.5\left(\frac{b}{a}\right)^{-1.4} \quad \text{Equation 6.3}$$

Where a and b stand for the channel half-width and half-height respectively; v stands for the stream velocity (dividing flow rate by the cross-section area of the channel).

In the simulation of transport of diluted species, Fick's second law was used to correlate the diffusivity with the concentration of solute from the DS to RS.

$$\bar{v}(y) \frac{\partial C}{\partial x} = D \left(\frac{\partial^2 C}{\partial y^2} \right) \quad \text{Equation 6.4}$$

Where D represents the diffusion coefficient of the solute.

The outlet RS concentration, inlet RS and DS concentrations, flow rate and channel dimensions are the input parameters for the calculation. The Matlab's `fminbnd` function was used to determine the minimum value of the least square fitting of the calculated RS outlet concentration (via modelling) and the experimentally measured RS outlet concentration, where the corresponding value of diffusion coefficient was the one measured by the microfluidic H-cell.

The dimensionless Fourier number (Fo), representing the contact time of the RS and DS during transport via the H-cell, was calculated as:

$$Fo = \frac{Dt}{a^2} \quad \text{Equation 6.5}$$

Where D is the diffusion coefficient, t the average residence time in the channel and a the channel half-width. The minimisation of the measurement uncertainty, i.e., the variance of the experimental results, is achieved by operating the experiment at an optimal Fourier number range, in which the H-cell measurement sensitivity and accuracy increase drastically [29]. Empirically, the range of the optimal Fourier number was determined according to Equation 6.6:

$$Fo_{opt} = 0.299\left(\frac{b}{a}\right)^{-0.0983} \quad \text{for } 0.05 < \frac{b}{a} < 0.1 \quad \text{Equation 6.6}$$

Based on the analysis of the Fisher Information (a common factor of ordinary differential equation (ODE) analysis; reciprocal of the variance of measured diffusion coefficients) [29, 45], the experimental check on the correlation of the Fourier number with the variance of measured protein diffusion coefficients (see AppxD-Figure 1), and the empirical correlation (see Equation 6.6), the Fourier number range of 0.3-0.4 was used (where a low level of variance occurs) and the determined diffusion coefficients corresponding to this Fourier number range were reported.

6.2.8 Stokes-Einstein diffusion model

Stokes-Einstein diffusion model (see Equation 6.7) classically correlates the diffusion coefficient of monodisperse spheres at infinite dilution with the viscosity of the medium and the size of the molecule. The solute molecule is considered as a Brownian particle dissolved in a continuous medium. In the model, the microscopic structure of both solute and solvent is neglected, and the only source of dissipative effects is the shear viscosity of the solvent.

$$D = \frac{k_B T}{6\pi\eta R_h} \quad \text{Equation 6.7}$$

Where k_B represents the Boltzmann constant, T the absolute temperature, η the viscosity of the medium, R_h the hydrodynamic radius.

For non-ideal solutions like protein solutions, intermolecular interactions have an impact on the diffusion coefficient, whereby the diffusion coefficient is corrected for the concentration factor via a linear correlation (see Equation 6.8):

$$D = D_0(1+k_D C) \quad \text{Equation 6.8}$$

Where D_0 is the protein diffusion coefficient at infinite dilution and k_D is the diffusion interaction parameter summarising protein-protein intermolecular interactions [46, 47]. The term k_D is used to represent the level of both direct (e.g., electrostatic, dipole-dipole, van der Waals, hydrophobic interactions) and solvent-mediated hydrodynamic interactions among the protein molecules that alter the purely thermally-driven protein motion. The value of k_D depends on factors such as the temperature and salt concentration in the medium.

6.2.9 Numerical simulation of particle diffusion

In the present study, the H-cell microfluidics results indicate different diffusion behaviours of protein molecules in different buffers and protein concentrations. It is assumed that the diffusivity of protein molecules in the H-cell is affected by the protein charge, intermolecular interaction cut-off distance (Debye length), protein concentration and concentration gradients between RS and DS. To give support to this assumption, an exploratory and illustrative numerical simulation of particle displacement (which represents the diffusion of globular protein molecules) between two contacting domains was performed.

This simulation was conducted by the particle tracing module of Comsol Multiphysics (version 5.2). The geometrical configurations and boundary conditions of the simulation are shown in the appendix (see AppxD-Figure 2). The simulation geometry was divided into two domains, donor fluid domain (DD) and

receiver fluid domain (RD), where DD has a higher initial concentration than RD. In the simulation, spherical particles were used to represent protein molecules. Due to the limit on computation power, the particle displacement was simulated within a down-scaled geometry rather than the full scale of the H-cell.

In the simulation, the particle displacement was dominated by three forces: Brownian force, drag force, and particle-particle interaction force (electrostatic repulsive force in this case) [48].

The amplitudes of the Brownian force at every time step was modelled as a Gaussian white noise process [49] given by Equation 6.9:

$$F_b = \zeta \sqrt{\frac{12\pi k_B \eta T r_p}{\Delta t}} \quad \text{Equation 6.9}$$

The drag force was given by Equation 6.10:

$$F_d = \left(\frac{1}{\tau_p}\right) m_p (v - v_p) \quad \text{Equation 6.10}$$

Coulombic force dominates particle-particle interaction and is repulsive with particles of the same sign of charge. The Coulombic force was calculated with Equation 6.11 as the interaction of point charges, where the charge number was used as the charge exposed to the surface of the protein molecule.

$$F_i = -\frac{1}{4\pi\epsilon_0\epsilon_r} e^2 \sum_{j=1}^N Z_i Z_j \frac{(r_i - r_j)}{|r_i - r_j|^3} \quad \text{Equation 6.11}$$

Where m_p is the particle mass, r_p , the particle radius, τ_p , the particle velocity response time, v_p the velocity of the particle, v the fluid velocity, Δt the magnitude of the time step taken by the solver and ζ is a vector of independent normally distributed random numbers with zero mean and unit standard deviation, e is the elementary charge, ϵ_0 is the permittivity of free space, ϵ_r is the relative permittivity of water, Z is the particle charge number, r_i is the position vector of the i -th particle, and r_j is the position vector of the j -th particle.

The diffusion of LYS in 10 mM AC, 100 mM AC, 10 mM PB and 100 mM PB was simulated. The simulation conditions are listed in Table 6.4.

Table 6.4. The conditions used for Comsol particle tracing simulation.

Simulation	Simulated solvent	RD concentration ^a (mg/ml)	DD concentration (mg/ml)	Medium viscosity ^b (mPa·s)	Particle charge number ^c	Cut-off distance (nm) ^d (Coulombic interaction)
1	AC (10 mM; pH 4.2)	0	2	1.00	15.2	6.8
2	AC (10 mM; pH 4.2)	0	10	1.00	15.2	6.8
3	AC (10 mM; pH 4.2)	2	4	1.00	15.2	6.8
4	AC (10 mM; pH 4.2)	4	6	1.00	15.2	6.8
5	AC (100 mM; pH 4.2)	0	2	1.02	15.2	2.0
6	AC (100 mM; pH 4.2)	0	10	1.02	15.2	2.0
7	PB (10 mM; pH 7.2)	0	2	1.00	11.1	2.1
8	PB (10 mM; pH 7.2)	0	10	1.00	11.1	2.1
9	PB (10 mM; pH 7.2)	2	4	1.00	11.1	2.1
10	PB (10 mM; pH 7.2)	4	6	1.00	11.1	2.1
11	PB (100 mM; pH 7.2)	0	2	1.06	11.1	0.6
12	PB (100 mM; pH 7.2)	0	10	1.06	11.1	0.6

^a The experimental solute concentration is converted to the number of particles per volume for the simulation via the correlation $C_n = C_e * N_A / M_w$, where C_n represents the particle number concentration used for the simulation, C_e the experimental solute concentration, N_A the Avogadro number, M_w the molecular weight of solute.

^b The medium viscosity is calculated based on the table of the properties of the aqueous solutions of common electrolytes shown in [50].

^c The particle surface charge is calculated based on the pKa of protein amino acid residues and their corresponding buried percentage obtained from the online PDB2PQR Server (PDB2PQR Version 2.0.0, [51]).

^d The calculated ionic strength of 10 mM AC and 100 mM AC is 2 mM and 24 mM, respectively; for phosphate buffer the value is 21 mM and 221 mM, respectively (calculated via [52]). The Debye length is calculated based on these ionic strengths using the equation $\delta = \sqrt{\frac{\epsilon_r \epsilon_0 k_B T}{2 N_A e^2 I}}$, where δ represents the Debye length, ϵ_r the relative permittivity of water, ϵ_0 permittivity of free space, k_B Boltzmann constant, T the temperature, N_A the Avogadro number, e the elementary charge, I the ionic strength.

6.3 Results

6.3.1 The relative size and aggregation state of proteins

Figure 6.2 shows the HP-SEC chromatograms of the proteins used in this study. According to the retention time, the size of proteins follows the following order: LYS < CC < MYO < OVA < BSA < etanercept. This order is in line with the molecular weight of the proteins, except for the LYS and CC, where CC theoretically should have a slightly smaller size (about 2 kDa difference).

Narrow sharp peaks in the chromatogram of LYS and CC indicate monodisperse protein molecules. For the other proteins, some aggregations occur, based on the multi-peaks shown in Figure 6.2. However, the proteins are primarily in the monomeric form, based on the areas of the peak (LYS and CC: about 100%; MYO: about 88%; OVA: about 83%; BSA: about 70%; etanercept: about 95%). The determined diffusion coefficients in this study reflect majorly the diffusion behaviour of monomeric protein molecules.

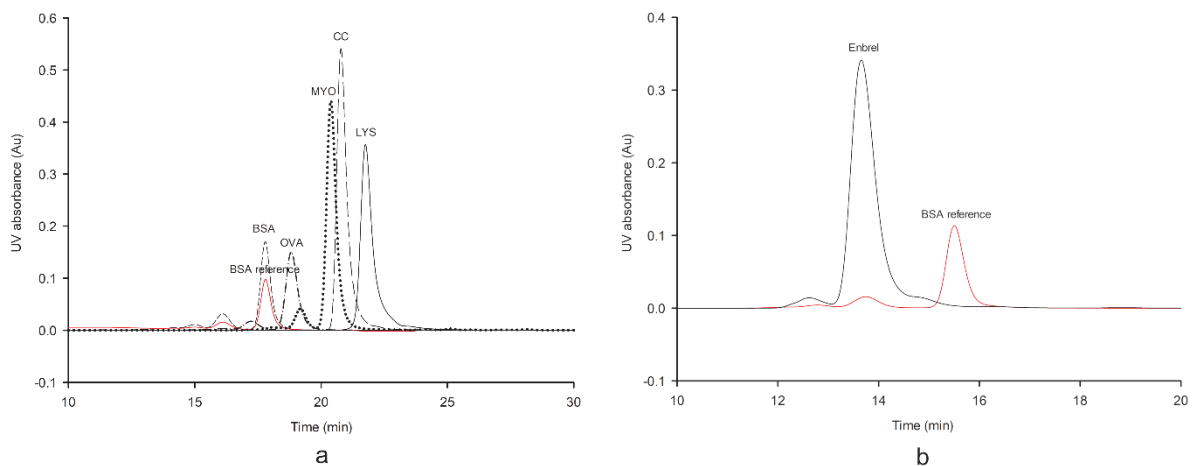


Figure 6.2. HP-SEC chromatograms of proteins used for the H-cell diffusion experiments: (a) chromatogram of LYS, CC, MYO, OVA and BSA, together with a BSA reference; (b) chromatogram of etanercept and the corresponding BSA reference.

6.3.2 Protein mass balance

The recovery of proteins after flowing through the H-cell is shown in Appendix D (see AppxD-Table 2). Under all test conditions, the protein recoveries at the outlets of the DS and RS were not significantly different from 100% according to the t-test ($p > 0.05$).

6.3.3 Lysozyme diffusion coefficient as a function of concentration, pH and buffer type

LYS diffusion coefficients in water, PB and AC were measured by the H-cell microfluidics device at different inlet concentrations of the DS and RS. The results are shown in Figure 6.3.

6.3.3.1 Lysozyme diffusion in water

For LYS, a diffusion coefficient of $4.4 \times 10^{-10} \text{ m}^2/\text{s}$ was measured at 0 vs 2 mg/ml, which is in line with published data [10] [53, 54]. More than 50% increase of the measured diffusion coefficient was observed at 0 vs 5 mg/ml and 0 vs 10 mg/ml.

When the inlet concentration gradient between the RS and DS was kept at 2 mg/ml, almost no difference in the diffusion coefficient was observed between 0 vs 2 mg/ml, 2 vs 4 mg/ml and 4 vs 6 mg/ml. LYS was reported to have a diffusion coefficient of about $5.5 \times 10^{-10} \text{ m}^2/\text{s}$ in water via DLS and GI measurement at similar level of concentrations (<10 mg/ml) [53, 54]. However, even with the same diffusion measurement method (GI), a diffusion coefficient of $2.2 \times 10^{-10} \text{ m}^2/\text{s}$ was reported in another previous study [10]. The measured LYS diffusion in water was more influenced by the protein concentration gradient between the RS and DS than by the absolute protein concentrations in the H-cell channel.

6.3.3.2 Lysozyme diffusion in acetate buffer

In 10 mM AC, LYS diffusion coefficients in the range of $1.6\text{-}2.1 \times 10^{-10} \text{ m}^2/\text{s}$ were obtained at 0 vs 0.5 mg/ml to 0 vs 2 mg/ml. Similar diffusion coefficients have been reported in previous publications under the condition of similar pH and ionic strength [32, 55]. Inlet concentration gradients of up to 2 mg/ml did not substantially affect the measured diffusion coefficients. However, at higher concentration gradients (0 vs 5 and 0 vs 10 mg/ml), higher diffusion coefficients up to about $3.4 \times 10^{-10} \text{ m}^2/\text{s}$ were observed.

At constant inlet concentration gradients, the measured diffusion coefficients increased with increasing LYS concentration from 0 vs 2 mg/ml to 4 vs 6 mg/ml. This trend differs from the case in water.

The measured LYS diffusion coefficients in 100 mM AC were similar to those in 10 mM AC from 0 vs 0.5 mg/ml to 0 vs 2 mg/ml. There was no obvious trend of increasing diffusion coefficient from 0 vs 2 mg/ml to 0 vs 5 mg/ml and 0 vs 10 mg/ml. The diffusion of LYS in AC at low buffer concentration tended to be more influenced by the concentration gradient between RS and DS than that at high buffer concentration. Also at low buffer concentration, the LYS concentration in the H-cell channel proportionally affected its measured diffusion coefficient.

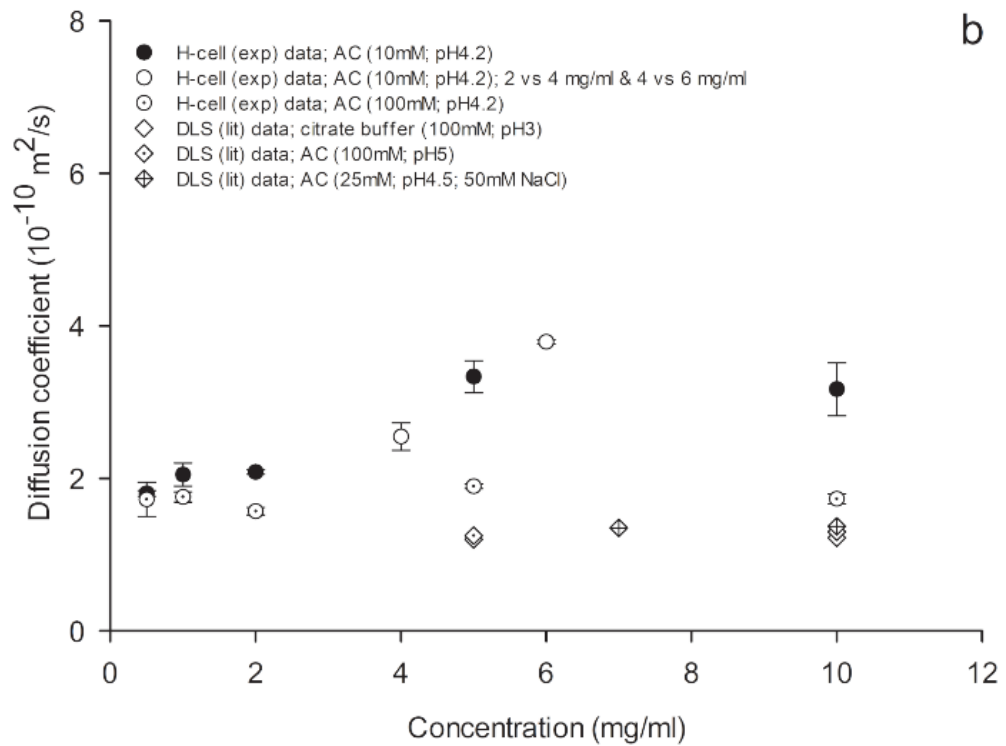
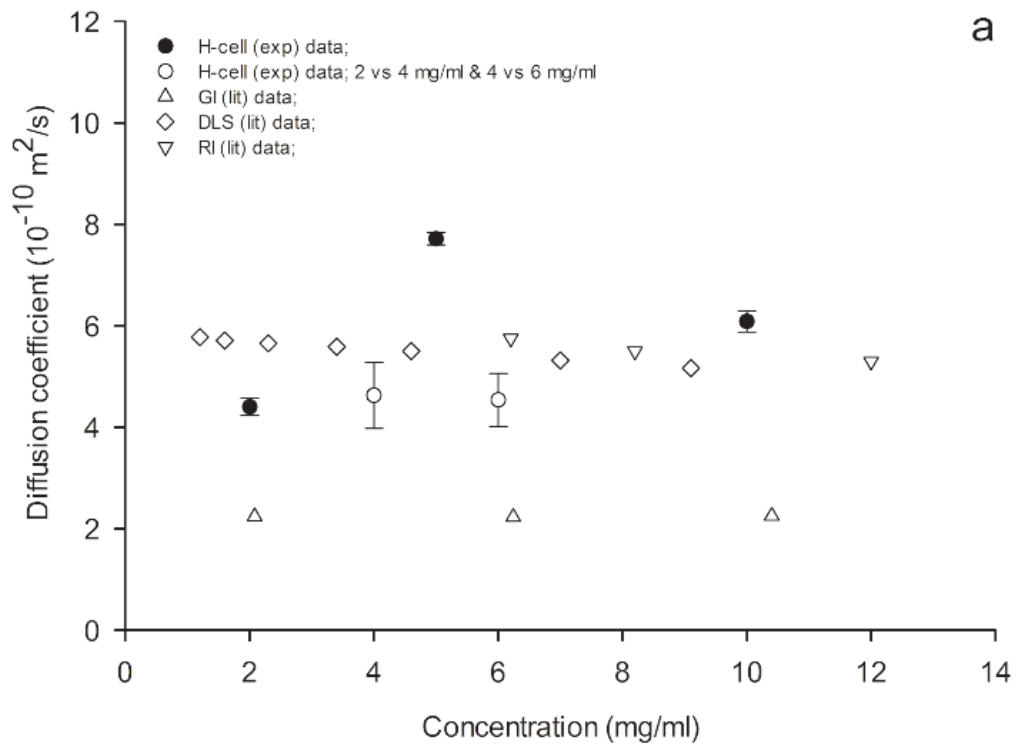
6.3.3.3 Lysozyme diffusion in phosphate buffer

The measured diffusion coefficients of LYS in PB were comparable with those in AC at inlet concentrations of 0 vs 0.5, 0 vs 1 and 0 vs 2 mg/ml. At the inlet concentrations of 0 vs 5 and 0 vs 10 mg/ml, the measured values in PB were similar to those in 100 mM AC, but lower than those in 10 mM AC. In 100 mM PB, the measured diffusion coefficients of LYS decreased by about 25% from a low concentration gradient (0 vs 0.5 to 0 vs 2 mg/ml) to a high concentration gradient (0 vs 10 mg/ml). This decrease was not obvious under the other tested conditions.

When keeping the inlet concentration gradient at 2 mg/ml, an increasing diffusion coefficient with LYS concentration was observed, similar to that in AC. This trend of concentration-dependency was also reported elsewhere in a low ionic strength media (with the ionic strength lower than the 10 mM PB) [56].

The diffusion of LYS in PB at low and high buffer concentration was both not much affected by the concentration gradient between RS and DS. However, the measured diffusion coefficients rised with LYS concentration in the H-cell channel.

In light of the results above, the measured diffusion coefficients of LYS are affected by the concentration gradient between the RS and DS, the concentration of protein in the H-cell channel, and the buffer pH and concentration. It seems that at low protein concentration and concentration gradient (e.g., 0 vs 0.5 mg/ml, 0 vs 1 mg/ml and 0 vs 2 mg/ml), the H-cell performs well in the measurement of protein diffusion coefficients, which are comparable with literature data.



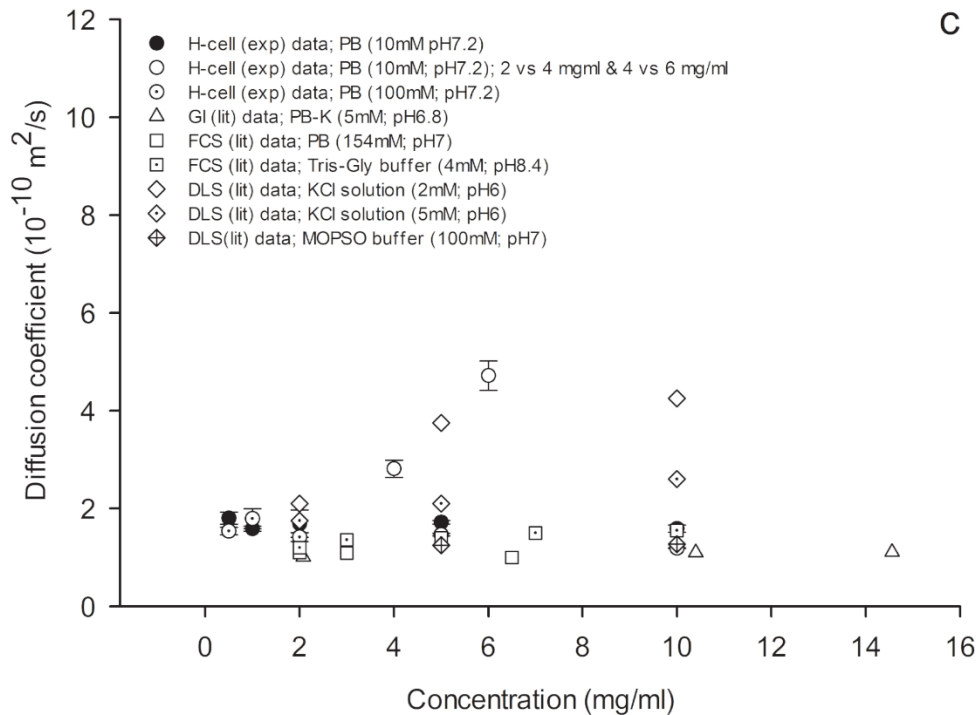


Figure 6.3. H-cell microfluidics experimental results of LYS diffusion coefficients in water (a), acetate buffer (AC) (b) and phosphate buffer (PB) (c) as a function of inlet concentrations. The error bars represent the standard deviation of the measurements. The x-axis corresponds to the inlet LYS concentration in the DS. If not explicitly stated, the inlet LYS concentration in the RS is 0 mg/ml. The literature-reported LYS diffusion coefficients, measured by other techniques under similar conditions, are shown for comparison. In (a), the data of the triangles are collected from [10], diamonds from [53], and inverted triangle from [54]. In (b), the data of the diamonds and dotted diamonds are collected from [32] and the crossed diamonds from [57]. In (c), the data of the triangles are collected from [10], crossed diamonds from [32], square and dotted squares from [58], and the others from [56].

6.3.4 Lysozyme diffusion coefficient as function of ionic strength

The results in the last section indicate that there is a correlation between the measured LYS diffusion coefficient and the buffer concentration. In this section, the H-cell is used to examine the LYS diffusion coefficients at different salt concentrations, to elucidate whether specific buffer effects or general ionic strength effects are responsible for the above observation.

The ionic strength of the medium was changed by adjusting the salt (NaCl) concentration. The measured LYS diffusion coefficients in corresponding media are reported (see Figure 6.4 (a) and (b)).

As indicated by both the H-cell results and literature data, the value of the LYS diffusion coefficient sharply decreased with increasing salt concentration from 0 to about 10 mM, followed by levelling off at higher salt concentrations. In the absence of salt, the H-cell gave a diffusion coefficient of $4.4 \times 10^{-10} \text{ m}^2/\text{s}$ for LYS in water. When the NaCl concentration increased to 10 mM, the H-cell measured LYS diffusion coefficient dropped to lower than $2 \times 10^{-10} \text{ m}^2/\text{s}$. This value was similar to that in 10 mM PB. At higher NaCl concentrations (up to 1 M for water and 500 mM for PB), the LYS diffusion coefficient levelled off at about $1.6 \times 10^{-10} \text{ m}^2/\text{s}$.

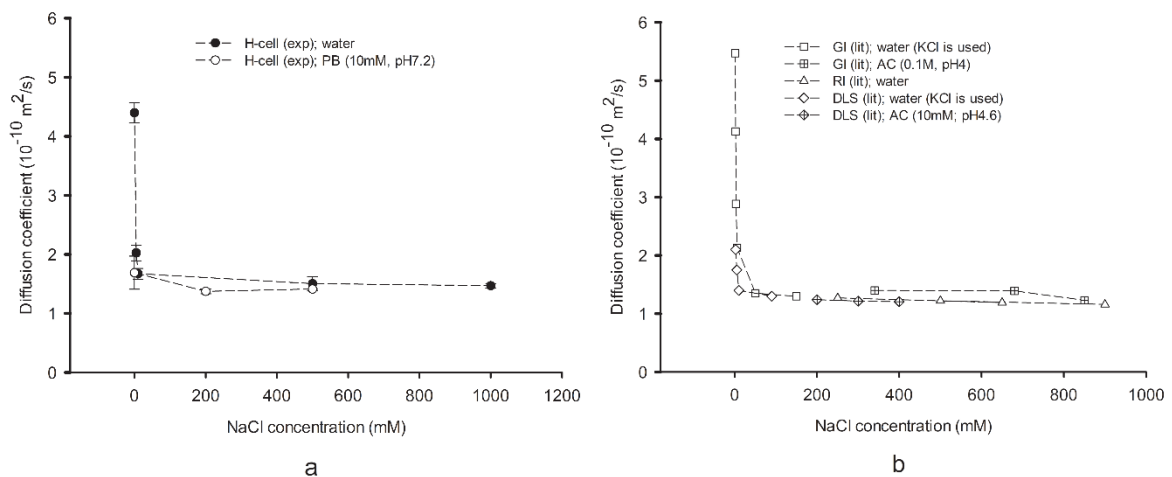


Figure 6.4. Measured diffusion coefficients of LYS via the H-cell as a function of salt concentration in the medium (a). The error bars represent the standard deviation of the measurements. The literature-reported LYS diffusion coefficients measured by other techniques under similar conditions (b) are shown for comparison, where the data of square are collected from [53], crossed squares from [59], triangles from [9], diamonds from [56] and crossed diamonds from [60]. The solvents used in these references are depicted in the legend of the graph. The dashed lines are meant for visual guidance.

6.3.5 Lysozyme diffusion coefficient as function of medium viscosity

The diffusion coefficient is inversely proportional to the medium viscosity, as indicated by the Stokes-Einstein model. Measuring the LYS diffusion coefficients in different viscous media can be used as a further validation of the H-cell. The diffusion coefficients of LYS are plotted against the viscosity of the solution containing glycerol (see Figure 6.5). As expected, the diffusion coefficients decrease with increasing medium viscosity. A comparison of the measured diffusion coefficients to the values calculated by classical Stokes-Einstein model is presented. The molecule of LYS can be considered to be roughly spherical, due to its compact nature and rapid rotational tumbling in solution [61]. The

reported hydrodynamic radius (R_h) of LYS differs in the literature, ranging from about 16 to 21 Å depending on the solvent conditions such as pH, salt types and concentrations, and experimental techniques [9, 46, 57, 62]. This size range was used for the Stokes-Einstein modelling of the diffusion coefficients in this study. The modelling results are also displayed in Figure 6.5. The H-cell results are in accordance to the modelling results at the R_h of 1.6 nm. The modelling results are lower than the H-cell results at a higher R_h . The correction of concentration effect based on empirical Equation 6.8 slightly lifts the value of modelling diffusion coefficients, where an approximate value of 10 was used for the diffusion interaction parameter (kD) for a buffer condition at about pH 7 and low ionic strength (<10 mM) [57, 60]. According to the results corrected for concentration, the hydrodynamic radius of LYS is predicted to be between 1.6 and 1.8 nm, which is consistent with the previously reported value of the hydrodynamic size of LYS measured in phosphate buffer via Taylor Dispersion Analysis [63]. The difference of the diffusion coefficient between measurement and modelling depicted in this study was also observed in a previous publication [64]. According to the analysis above, one of the possible factors causing this deviation is the value of the hydrodynamic radius used for the calculation.

The independence of the calculated protein size on the medium viscosity is another verification of the applicability of the H-cell for the diffusion coefficient measurement. A Spearman correlation analysis was conducted (IBM SPSS 24; IBM, Armonk, NY) on the variables of the viscosity and the hydrodynamic radius (R_h) of protein calculated via the Stokes-Einstein equation based on the H-cell measured diffusion coefficients. It was demonstrated that there was no significant statistical correlation ($p > 0.05$) between the medium viscosity and the calculated protein hydrodynamic radius based on the measured diffusion coefficients.

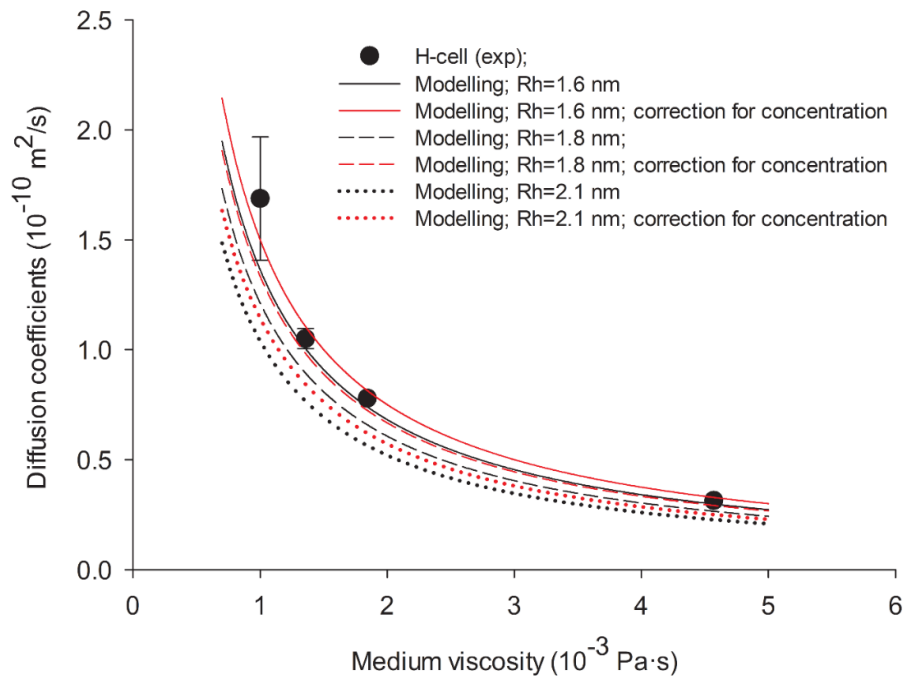
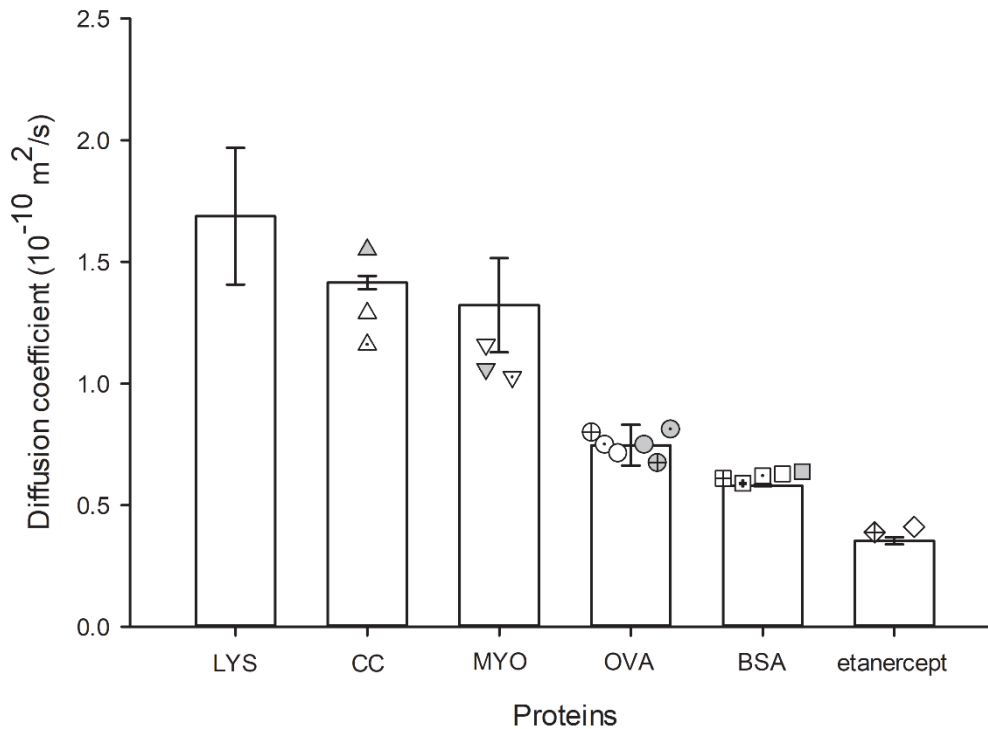


Figure 6.5. Diffusion coefficients of LYS measured by H-cell as a function of medium viscosity adjusted by glycerol. The error bars represent the standard deviation of the measurements. The diffusion coefficients calculated by the Stokes-Einstein equation are shown with the hydrodynamic radius (R_h) of 1.6~2.1 nm. A correction of protein concentration by diffusion interaction parameter [57, 60] is also included.

6.3.6 The diffusion coefficient of other proteins

Besides LYS, five other proteins with different molecular size and properties (e.g., pI) were measured via H-cell for their diffusion coefficients (see Figure 6.6). As expected, the diffusion coefficients of proteins were inversely related to the molecular size, where the larger the protein (as indicated by HP-SEC results shown in Figure 6.2), the slower the detected protein diffusion. For CC and MYO, at most 20% deviation of the H-cell results with literature value was found. For OVA, BSA and etanercept, quite similar values were reported in previous research (less than 10% difference) to the H-cell results. The fraction of monomeric BSA was separated and collected (see chromatogram in AppxD-Figure 4), and was measured by H-cell microfluidics. The obtained diffusion coefficient ($6.7 \times 10^{-11} \text{ m}^2/\text{s}$) was slightly higher than that of the unfractionated BSA ($5.8 \times 10^{-11} \text{ m}^2/\text{s}$), which includes dimers and trimers. In light of the comparable results generated by H-cell and other available techniques, the effectiveness and validity of the H-cell for the evaluation of protein diffusion behaviour are further demonstrated.



- H-cell (exp); PB (10 mM; pH 7.2)
- △ Diffusion across porous membrane (lit); Water (10 mM NaCl)
- △ Schlieren cylindrical lens (lit); PB (20 mM; pH 7.6; 10 mM NaCl)
- △ Micro-tube (lit); AC (10 mM; pH 7.0; 80 mM Na₂SO₄)
- ▽ Diffusion across thin porous plate (lit); K-PB (100 mM; pH 6.8)
- ▽ Referenced value (lit);
- ▽ Micro-tube (lit); AC (10 mM; pH 7.0; 80 mM Na₂SO₄)
- ⊕ Light scattering (lit); AC (4 mM; pH 5.5)
- ⊙ FCS (lit); MES buffer (50 mM; pH 6.4)
- Micro-tube (lit); AC (10 mM; pH 7.0; 80 mM Na₂SO₄)
- Micro-sensor (lit); Tris-HNO₃ buffer (100 mM; pH 7.9)
- ⊕ Micro-chip (lit); 10 mM NaCl solution
- ⊙ Micro-chip (lit); 40 mM NaCl solution
- ⊞ Gouy optics (lit); PB (pH 6.8; 100 mM IS)
- ⊠ DLS (lit); PB (100 mM; pH 7.2)
- Light scattering (lit); PB (150 mM; pH 7.4)
- Micro-tube (lit); AC (10 mM; pH 7.0; 80 mM Na₂SO₄)
- Micro-chip (lit); water;
- ⊕ IgG; photon-correlation spectroscopy (lit); Tris-HCl buffer (50 mM; pH 7.6)
- ◇ IgG; Micro-tube (lit); AC (10 mM; pH 7.0; 80 mM Na₂SO₄)

Figure 6.6. Diffusion coefficients of different proteins measured in phosphate buffer (PB; 10 mM; pH 7.2; except for etanercept in placebo buffer) and literature-reported value under similar conditions. The error bars represent the standard deviation of the measurements. The data of the grey triangle are collected from [65], blank triangle [66], dotted triangle [18]; grey inverted triangle [67], blank

triangle [68], dotted triangle [18]; crossed circle [69], dotted circle [12], blank circle [18], grey circle [20], crossed grey circle and dotted grey circle [19]; crossed square [70], x-haired square [71], dotted square [72], blank square [18], grey square [19]; crossed diamond [73], blank diamond [19]. Due to limited information on the diffusion coefficient of etanercept, the diffusion coefficient of IgG with similar molecular size (about 150 kDa) is used for comparison to the H-cell measurement results.

6.3.7 Particle tracing simulation

Particle tracing simulation provides support for a better understanding of the protein diffusion results by counting particle transport between two contact simulation domains with an initial concentration difference. According to the simulation results (see AppxD-Figure 3 and AppxD-Table 1 in Appendix D), the particles diffused faster in 10 mM AC than in the other buffers. In 10 mM AC, the diffusion rate of LYS at 0 vs 10 mg/ml was higher than that at 0 vs 2 mg/ml. This increment as a function of concentration gradient was also observed in the case of 100 mM AC and slightly 10 mM PB, but did not occur for the 100 mM PB, where the diffusion rate decreased with the increasing concentration gradient. In the case of 10 mM AC and 10 mM PB, particles diffused faster at 4 vs 6 mg/ml than that at 2 vs 4 mg/ml, and both were faster than that at 0 vs 2 mg/ml.

6.4 Discussion

6.4.1 General

When present in solution, protein diffusion depends not only on the viscosity of the medium but also the protein-protein interactions, which are related to the strength of the interaction and the concentration of the solutes. In order to provide an overview of the applicability and potential of the H-cell microfluidics device on the determination of protein diffusivity, the diffusion coefficients of model protein (LYS) were measured in different media (water, PB, AC) at different pH (4.2 and 7.2), ionic strength (about 0 to 1 M), viscosity (about 1 to 5 mPa·s) and at different protein concentration profiles (0 vs 2 mg/ml to 0 vs 10 mg/ml; 2 vs 4 mg/ml; 4 vs 6 mg/ml). For the proof of the H-cell applicability to a broad scope of proteins with different properties (e.g., molecular weight), five other proteins were also tested via H-cell and the measured diffusion coefficients were comparable to studies elsewhere (the characteristics of the techniques applied to determine the protein diffusion coefficients are summarised in Table 6.1). The key factors that influence protein diffusion and the interpretation of the H-cell results are discussed in the following sections.

6.4.2 Interaction among protein molecules in different media

The diffusion behaviour of LYS, depicted in Figure 6.3, varied in water, AC (10 mM and 100 mM) and PB (10 mM and 100 mM). The measured diffusion coefficients of LYS as function of the solvating medium followed the order of water > 10 mM AC > 100 mM AC >= 10 mM PB > 100 mM PB in the cases where the inlet RS concentration is 0 mg/ml. The differences in different media were more evident at high concentration gradients than at low gradients. When in the concentration profile of 2 vs 4 mg/ml and 4 vs 6 mg/ml, similar diffusion behaviours were found in 10 mM AC and 10 mM PB.

There is a slight change of the viscosity of different media. The 100 mM PB and 100 mM AC have about 6% and 2% higher viscosity than that of water, 10 mM PB and 10 mM AC, which have almost similar viscosity. Thus the slight viscosity change cannot explain all the differences of the measured diffusion coefficients, especially the ones in water and 10 mM AC (0 vs 5 mg/ml & 0 vs 10 mg/ml), which show more than 50% higher value than the ones in the other media.

Besides viscosity, inter-molecular interactions (e.g., electrostatic repulsion) among the protein, which are influenced by both the pH and ionic strength of the medium, contribute partly to the aforementioned diffusivity difference. The impact of pH depends on the specific surface configuration (such as the fraction of exposed amino acid residues chargeable at the specific pH) of the studied protein and its resulting isoelectric point (pI ; representing the pH at which the protein is electrically neutral). In water, AC (pH 4.2) and PB (pH 7.2), LYS molecules (isoelectric point $pI \approx 11$) are positively charged and repulsive electrostatic interactions likely occur [10, 74]. However, when the pH is closer to the proteins' pI , the inter-molecular electrostatic interaction is reduced meanwhile the attractive short-range interactions (interaction force decreases with distance quickly), such as van der Waals or hydrophobic forces, are relatively dominant [75]. This is reasonable as the pH influences the protonation of ionizable amino acids and thus the charge distribution on the protein surface, and the hydrophobic surface patches [76, 77]. These forces tend to hinder the dispersion and displacement of the protein molecules, opposite to the effect of repulsive interactions. As a result, relatively low diffusion coefficients tend to occur at high pH than at low pH.

The aforementioned inter-molecular electrostatic repulsion can be relieved by salt screening in a medium with a relatively high ionic strength. The addition of salt is known to promote attractive hydrophobic protein interactions due to the shielding of electrostatic charges (with the same sign) [46, 78].

The H-cell results of LYS diffusion with different ionic strengths (adjusted by NaCl) show slower LYS diffusion at high NaCl concentration. In this study, the LYS diffusion coefficient was observed to drop

markedly from 4.4×10^{-10} to 2.0×10^{-10} and then to 1.7×10^{-10} m²/s as the salt concentration increased from 0 to 5 mM and then to 10 mM (see Figure 6.4), which was also observed elsewhere [53, 79].

In water, the measured LYS diffusion coefficients were higher than that in AC and PB. The electrostatic free energy of the charged macromolecule increases due to that the charges on the macromolecule are no longer shielded from one another [53]. The increased inter-molecular repulsive electrostatic interactions drive the molecules strongly to displace quicker and more frequent towards the location with fewer repulsions, which is depicted as the higher measured molecular diffusion coefficient via the H-cell.

The measured diffusion coefficients of proteins in AC were in most cases higher than that in PB. Apart from the aforementioned ion shielding effect, the type of salt may also contribute to the different diffusion behaviour in different buffers. Hofmeister, et al. [80] pioneered the study and proposed the series of salts that have different ability to salt out proteins. The mechanism of the Hofmeister series has not been entirely clarified. It was put forward that the interactions between ions and proteins as well as ions and the water molecules that directly contact the proteins play a role [81]. According to the research, phosphate anions ($\text{HPO}_4^{2-}/\text{H}_2\text{PO}_4^-/\text{PO}_4^{3-}$) have a stronger tendency of salting out protein than acetate anions [82, 83]. This tendency may partly help explain why the LYS molecules diffuse slightly faster in AC than in PB.

Based on the analysis above, the diffusion behaviour of the protein depends on the present solution condition (e.g., pH, ionic strength, salt type) and the resulting molecule properties. Electrostatic as well as additional short-range interactions play a role for the samples investigated in this study.

6.4.3 Concentration-dependent protein diffusion coefficients

In the present study, the measured protein diffusion coefficients by H-cell depend both on the initial protein concentration gradient and the protein concentrations.

In water and AC (10 mM; pH 4.2) where the ionic strength is low, the measured diffusion coefficients of LYS increased as the concentration gradient increased (from 0 vs 2 mg/ml to 0 vs 5 mg/ml as shown in Figure 6.3). However, for the other buffers with a relatively high ionic strength, this elevation was not detected. The particle tracing simulation results supported the phenomena above in which the inlet concentration gradient influences the measured diffusion coefficient more in the situation of longer particle-particle interaction cut-off distance (Debye length). For example, in 10 mM AC the cut-off distance is about 6.8 nm, which is longer than the other buffers, and the particle diffusion rate is higher. When the inter-molecular interaction is weakened (e.g., in 100 mM AC and 10 mM PB in which

the cut-off distance is shorter (≈ 2 nm)), the concentration gradient seems to exert less influence on the measured molecular diffusion coefficient.

The diffusion coefficients of LYS were also studied as a function of the protein concentration at consistent inlet concentration gradient (2 mg/ml). In AC and PB, the measured diffusion coefficient values increased with increasing concentration. It has previously been reported that for AC [60, 84] and PB [56] at low ionic strength, the diffusion coefficient of LYS increases with concentration, and at higher ionic strength, this trend becomes weaker or is even independent of protein concentration. However, the level of increase reported elsewhere is less than the H-cell findings at similar pH and ionic strength. This is probably due to that the high protein concentrations cause a higher frequency of collisions and thus the faster displacement of the molecules.

Under the investigated diffusion conditions, the effect of excluded volume (the volume that is inaccessible to other molecules in the system as a result of the presence of the first molecule; steric hindrance) seems to be less significant than the electrostatic effects. In previous research, there were statements pointing out that the increase in protein concentration promotes the impact of excluded-volume effects and additional attractive short-range interactions, therefore impeding the diffusion of the macromolecules [85, 86]. Usually when the concentration of protein molecules increases to an even higher level (e.g., 20-30% v/v), the protein diffusion is retarded by the crowding of molecules (in the strict sense of excluded-volume), as a result, the stronger the electrostatic repulsions among the molecules, the more decrease of the diffusivity with the similar increase of concentration [87, 88].

In water, the measured diffusion coefficients of LYS were slightly affected by the concentration (0 vs 2, 2 vs 4 and 4 vs 6 mg/ml). Similar behaviour was also reported previously [10, 53, 54] at this low concentration range. Although there is strong electrostatic repulsive interaction among the molecules and low level of excluded volume effect occurs in this situation, there is no similar trend of increasing diffusion coefficients as that in 10 mM PB and 10 mM AC. Scarce theoretical support for this observation is collected up to now. Regarding the presence of external salts in AC and PB, the diffusion of proteins can be accelerated by the presence of more counterions, which is a thermodynamic effect brought about by an increase in the free energy gradient of the solutes, which is the driving force for isothermal diffusion [89]. Moreover, the diffusion of proteins is likely to be enhanced or hindered by gradients of other diffusing species in the multicomponent system. The flux of the protein is related to its own concentration gradient without disturbance of extra ions in the binary system of LYS and water. In the ternary systems of protein-salt-water, there are many counter-ions in the motion sphere of the protein molecule. Directly proportional to the LYS gradient, there is also an effective concentration

gradient of salt. This raises the likelihood that the protein diffusion is enhanced or hindered by gradients of other diffusing species and thus a variation of the diffusion coefficients occurs [54, 90].

The analysis above on the correlation of the concentration-dependence of the protein diffusion coefficients with the inter-molecular interactions provides an insight of the possible reasons explaining the H-cell observations. As the H-cell results only reflect the overall interactions among the protein molecules, the impact of each specific factor on the determined diffusion coefficient cannot be independently distinguished.

6.4.4 Model to calculate the diffusion coefficient

Fick's law was used to describe the diffusion of solute in the H-cell and to calculate the corresponding diffusion coefficient based on mass transport in the micro-scale geometry within a period. The diffusion behaviour was a result of a protein concentration difference, especially for binary systems.

If we take into account the diffusion of the solvent molecules (e.g., water) besides the protein molecule transport, there is a drift flux caused by the displacement of the solvent simultaneously when protein diffuses. This drift flow is usually taken into account for gas transport rather than for liquid system [91] and a correction factor for Fick's law diffusion is applied. However, due to the low concentration of proteins applied in the H-cell study (e.g., 10 mg/ml in water), this correction factor only causes about 1% difference to the value predicted by Fick's law.

The aforementioned drift flux is covered by the theory of Maxwell-Stefan (M-S) for the description of multi-component diffusion behaviours (mostly applied for gas conditions). The M-S approach differs from the Fickian case as the transport is driven by a gradient in chemical potential and provides a physically-based comprehensive framework to describe multicomponent mass transport. The approach relates the driving force for diffusion of one component (i.e. the chemical potential gradient at constant temperature and pressure) to friction forces of the molecules of other components [92]. Regarding the non-ideal effects of mixing, the molar-based concentrations used in Fick's law are not convenient forms of thermodynamic activity variables [93]. The M-S framework separates the ideal and non-ideal effects of diffusion and a thermodynamic factor is used to correlate the M-S with Fickian case. In the case of LYS diffusion in water at 0 vs 10 mg/ml, the M-S diffusion coefficient is calculated to be about 10% lower than by Fick's law due to the thermodynamic factor by applying the LYS activity as shown in [94]. However, it was pointed out in a previous study that the thermodynamic factor involves the first derivative of the activity coefficient with respect to the composition, and errors of about 20% are expected for this derivative [92]. Even taken these errors into account, the correction of the diffusion coefficient predicted by M-S theory is not sufficient to explain some of the observed

phenomena, such as the elevation of the measured diffusion coefficients between 0 vs 2 mg/ml and 0 vs 10 mg/ml in water and 10 mM AC.

6.5 Conclusions

A microfluidic H-cell was used for the determination of protein diffusion coefficients based on the mass transport via the interface between the two laminar co-current fluid streams in the channel. For lysozyme as a model protein, the measured diffusion behaviour in the microfluidic H-cell was found to be influenced not only by the buffer type, pH, viscosity and ionic strength, but also by the operating conditions such as the inlet concentration gradients between the receiver stream and donor stream. There was the presence of inter-molecular (protein-protein) interactions during the protein diffusion in the channel. In good agreement with relevant research, the H-cell performed well to measure the diffusion coefficients of not only lysozyme but also some other common proteins with different molecular sizes and properties. These results prove the potential of this technique to be used as a general and promising approach for the determination of (macromolecular) diffusion coefficients.

Symbol list

a : H-cell channel half-width (m);

b : H-cell channel half-height (m);

C : solute concentration (mg/ml or mol/l or g/m³);

D : diffusion coefficient of target solute (m²/s);

d_p : the particle diameter (m);

e : the elementary charge ($\approx 1.60 \times 10^{-19}$ C);

F_b : Brownian force;

F_d : drag force;

F_i : coulombic force exerting on particle i ;

Fo : Fourier number;

I : the ionic strength (mol/l);

k_B : Boltzmann constant ($\approx 1.38 \times 10^{-23} \text{ m}^2 \text{ kg s}^{-2} \text{ K}^{-1}$);

k_D : diffusion interaction parameter;

m_p : the particle mass (g);

N_A : the Avogadro number ($\approx 6.02 \times 10^{23}$);

R_h : hydrodynamic radius (m);

r_i : the position vector of the i -th particle;

r_j : the position vector of the j -th particle.

T : thermodynamic temperature (K);

t : average residence time of stream in the channel (s);

v : the fluid velocity (m/s);

v_p : the velocity of the particle (m/s);

Z : the particle charge number;

Δt : the time step taken by the Comsol solver (s);

δ : Debye length (m);

ϵ_0 : the permittivity of free space ($\approx 8.85 \times 10^{-12} \text{ C}^2 \text{ N}^{-1} \text{ m}^{-2}$);

ϵ_r : the relative permittivity of water (≈ 80);

ζ : a vector of independent normally distributed random numbers with zero mean and unit standard deviation;

η : viscosity (Pa·s or mPa·s);

τ_p : the particle velocity response time (s);

References

1. Brune, D. and S. Kim, Predicting protein diffusion coefficients. Proceedings of the National Academy of Sciences, 1993. **90**(9): p. 3835-3839.

2. Nesmelova, I.V., V.D. Skirda, and V.D. Fedotov, Generalized concentration dependence of globular protein self-diffusion coefficients in aqueous solutions. *Biopolymers*, 2002. **63**(2): p. 132-140.
3. Price, W.S., Diffusion - Based Studies of Aggregation, Binding and Conformation of Biomolecules: Theory and Practice. eMagRes, 2002.
4. Langer, R., New methods of drug delivery. *Science*, 1990: p. 1527-1533.
5. Gallagher, W.H. and C.K. Woodward, The concentration dependence of the diffusion coefficient for bovine pancreatic trypsin inhibitor: a dynamic light scattering study of a small protein. *Biopolymers*, 1989. **28**(11): p. 2001-2024.
6. Pecora, R., Dynamic light scattering: applications of photon correlation spectroscopy. 2013: Springer Science & Business Media.
7. Cussler, E.L., Diffusion: mass transfer in fluid systems. 2009: Cambridge university press.
8. Bedeaux, D., S. Kjelstrup, and J. Sengers, Experimental Thermodynamics Volume X: Non-equilibrium Thermodynamics with Applications. 2015: Royal Society of Chemistry.
9. Annunziata, O., D. Buzatu, and J.G. Albright, Protein diffusion coefficients determined by macroscopic-gradient Rayleigh interferometry and dynamic light scattering. *Langmuir*, 2005. **21**(26): p. 12085-12089.
10. Kim, Y.-C. and A.S. Myerson, Diffusivity of lysozyme in undersaturated, saturated and supersaturated solutions. *Journal of crystal growth*, 1994. **143**(1): p. 79-85.
11. Yao, S., D.K. Weber, F. Separovic, and D.W. Keizer, Measuring translational diffusion coefficients of peptides and proteins by PFG-NMR using band-selective RF pulses. *European Biophysics Journal*, 2014. **43**(6-7): p. 331-339.
12. Krouglova, T., J. Vercaemmen, and Y. Engelborghs, Correct diffusion coefficients of proteins in fluorescence correlation spectroscopy. Application to tubulin oligomers induced by Mg²⁺ and paclitaxel. *Biophysical journal*, 2004. **87**(4): p. 2635-2646.
13. Hawe, A., W.L. Hulse, W. Jiskoot, and R.T. Forbes, Taylor dispersion analysis compared to dynamic light scattering for the size analysis of therapeutic peptides and proteins and their aggregates. *Pharmaceutical research*, 2011. **28**(9): p. 2302-2310.
14. Øgdenal, L., Light Scattering a brief introduction. 2016.

15. Saetear, P., J. Chamieh, M.N. Kammer, T.J. Manuel, J.-P. Biron, D.J. Bornhop, and H. Cottet, Taylor Dispersion Analysis of Polysaccharides Using Backscattering Interferometry. *Analytical chemistry*, 2017. **89**(12): p. 6710-6718.
16. Toseland, C.P., Fluorescent labeling and modification of proteins. *Journal of chemical biology*, 2013. **6**(3): p. 85-95.
17. Hrabe, J., G. Kaur, and D.N. Guilfoyle, Principles and limitations of NMR diffusion measurements. *Journal of medical physics/Association of Medical Physicists of India*, 2007. **32**(1): p. 34.
18. Walters, R.R., J.F. Graham, R.M. Moore, and D.J. Anderson, Protein diffusion coefficient measurements by laminar flow analysis: method and applications. *Analytical biochemistry*, 1984. **140**(1): p. 190-195.
19. Culbertson, C.T., S.C. Jacobson, and J.M. Ramsey, Diffusion coefficient measurements in microfluidic devices. *Talanta*, 2002. **56**(2): p. 365-373.
20. Kamholz, A.E., E.A. Schilling, and P. Yager, Optical measurement of transverse molecular diffusion in a microchannel. *Biophysical Journal*, 2001. **80**(4): p. 1967-1972.
21. Arosio, P., T. Müller, L. Rajah, E.V. Yates, F.A. Aprile, Y. Zhang, S.I. Cohen, D.A. White, T.W. Herling, and E.J. De Genst, Microfluidic diffusion analysis of the sizes and interactions of proteins under native solution conditions. *ACS nano*, 2015. **10**(1): p. 333-341.
22. Kopp, M.R., A. Villosio, U. Capasso Palmiero, and P. Arosio, Microfluidic Diffusion Analysis of the Size Distribution and Microrheological Properties of Antibody Solutions at High Concentrations. *Industrial & Engineering Chemistry Research*, 2018. **57**(21): p. 7112-7120.
23. Arosio, P., K. Hu, F.A. Aprile, T. Müller, and T.P. Knowles, Microfluidic diffusion viscometer for rapid analysis of complex solutions. *Analytical chemistry*, 2016. **88**(7): p. 3488-3493.
24. Hatch, A., E. Garcia, and P. Yager, Diffusion-based analysis of molecular interactions in microfluidic devices. *Proceedings of the IEEE*, 2004. **92**(1): p. 126-139.
25. Kamholz, A.E. and P. Yager, Theoretical analysis of molecular diffusion in pressure-driven laminar flow in microfluidic channels. *Biophysical journal*, 2001. **80**(1): p. 155-160.
26. Kamholz, A.E., B.H. Weigl, B.A. Finlayson, and P. Yager, Quantitative analysis of molecular interaction in a microfluidic channel: the T-sensor. *Analytical chemistry*, 1999. **71**(23): p. 5340-5347.

27. van Leeuwen, M., X. Li, E.E. Krommenhoek, H. Gardeniers, M. Ottens, L.A. van der Wielen, J.J. Heijnen, and W.M. van Gulik, Quantitative determination of glucose transfer between cocurrent laminar water streams in a H-shaped microchannel. *Biotechnology progress*, 2009. **25**(6): p. 1826-1832.
28. Yates, E.V., T. Müller, L. Rajah, E.J. De Genst, P. Arosio, S. Linse, M. Vendruscolo, C.M. Dobson, and T.P. Knowles, Latent analysis of unmodified biomolecules and their complexes in solution with attomole detection sensitivity. *Nature chemistry*, 2015. **7**(10): p. 802.
29. Häusler, E., P. Domagalski, M. Ottens, and A. Bardow, Microfluidic diffusion measurements: The optimal H-cell. *Chemical engineering science*, 2012. **72**: p. 45-50.
30. Berends, C., Determination of the diffusion coefficient of phenolic compounds using microfluidics, in Department of Biotechnology. 2015, Delft University of Technology: Delft.
31. Arzenšek, D., R. Podgornik, and D. Kuzman. Dynamic light scattering and application to proteins in solutions. in Seminar, Department of Physics, University of Ljubljana. 2010.
32. Bauer, K.C., M. Göbel, M.-L. Schwab, M.-T. Schermeyer, and J. Hubbuch, Concentration-dependent changes in apparent diffusion coefficients as indicator for colloidal stability of protein solutions. *International journal of pharmaceutics*, 2016. **511**(1): p. 276-287.
33. Cussler, E.L., *Multicomponent diffusion*. 2013: Elsevier.
34. Petrášek, Z. and P. Schwille, Precise measurement of diffusion coefficients using scanning fluorescence correlation spectroscopy. *Biophysical journal*, 2008. **94**(4): p. 1437-1448.
35. Tian, Y., M.M. Martinez, and D. Pappas, Fluorescence correlation spectroscopy: a review of biochemical and microfluidic applications. *Applied spectroscopy*, 2011. **65**(4): p. 115A-124A.
36. Elson, E.L., Fluorescence correlation spectroscopy: past, present, future. *Biophysical journal*, 2011. **101**(12): p. 2855-2870.
37. Shahzad, A., M. Knapp, I. Lang, and G. Köhler, The use of fluorescence correlation spectroscopy (FCS) as an alternative biomarker detection technique: a preliminary study. *Journal of cellular and molecular medicine*, 2011. **15**(12): p. 2706-2711.
38. Aune, K.C. and C. Tanford, Thermodynamics of the denaturation of lysozyme by guanidine hydrochloride. II. Dependence on denaturant concentration at 25. *Biochemistry*, 1969. **8**(11): p. 4586-4590.

39. Van Gelder, B. and E. Slater, The extinction coefficient of cytochrome c. *Biochimica et biophysica acta*, 1962. **58**(3): p. 593-595.
40. Castro-Forero, A., D. Jiménez, J. López-Garriga, and M. Torres-Lugo, Immobilization of myoglobin from horse skeletal muscle in hydrophilic polymer networks. *Journal of applied polymer science*, 2008. **107**(2): p. 881-890.
41. Ross, J.R., *Practical Handbook of Biochemistry and Molecular Biology*: Edited by G D Fasman. pp 601. CRC Press, Boca Raton, Florida, USA. 1989. \$00 ISBN 0-8493-3705-4. *Biochemical Education*, 1991. **19**(2): p. 95-96.
42. Pace, C.N., F. Vajdos, L. Fee, G. Grimsley, and T. Gray, How to measure and predict the molar absorption coefficient of a protein. *Protein science*, 1995. **4**(11): p. 2411-2423.
43. Hawe, A., V. Filipe, and W. Jiskoot, Fluorescent molecular rotors as dyes to characterize polysorbate-containing IgG formulations. *Pharmaceutical research*, 2010. **27**(2): p. 314-326.
44. Rohsenow, W.M., J.P. Hartnett, and Y.I. Cho, *Handbook of heat transfer*. Vol. 3. 1998: McGraw-Hill New York.
45. Walter, É. and L. Pronzato, Qualitative and quantitative experiment design for phenomenological models—a survey. *Automatica*, 1990. **26**(2): p. 195-213.
46. Kuehner, D.E., C. Heyer, C. Rämisch, U.M. Fornefeld, H.W. Blanch, and J.M. Prausnitz, Interactions of lysozyme in concentrated electrolyte solutions from dynamic light-scattering measurements. *Biophysical journal*, 1997. **73**(6): p. 3211-3224.
47. Lehermayr, C., H.C. Mahler, K. Mäder, and S. Fischer, Assessment of net charge and protein–protein interactions of different monoclonal antibodies. *Journal of pharmaceutical sciences*, 2011. **100**(7): p. 2551-2562.
48. Kim, M.-m. and A.L. Zydney, Effect of electrostatic, hydrodynamic, and Brownian forces on particle trajectories and sieving in normal flow filtration. *Journal of Colloid and Interface Science*, 2004. **269**(2): p. 425-431.
49. Li, A. and G. Ahmadi, Dispersion and deposition of spherical particles from point sources in a turbulent channel flow. *Aerosol science and technology*, 1992. **16**(4): p. 209-226.
50. Haynes, W.M., *CRC handbook of chemistry and physics*. 2014: CRC press.

51. Dolinsky, T.J., J.E. Nielsen, J.A. McCammon, and N.A. Baker, PDB2PQR: an automated pipeline for the setup of Poisson–Boltzmann electrostatics calculations. *Nucleic acids research*, 2004. **32**(suppl_2): p. W665-W667.
52. Buffer calculator. [accessed: 2018 17 July]; Available from: <https://www.liverpool.ac.uk/pfg/Research/Tools/BufferCalc/Buffer.html>.
53. Cadman, A.D., R. Fleming, and R.H. Guy, Diffusion of lysozyme chloride in water and aqueous potassium chloride solutions. *Biophysical journal*, 1982. **37**(3): p. 569.
54. Albright, J.G., O. Annunziata, D.G. Miller, L. Paduano, and A.J. Pearlstein, Precision Measurements of Binary and Multicomponent Diffusion Coefficients in Protein Solutions Relevant to Crystal Growth: Lysozyme Chloride in Water and Aqueous NaCl at pH 4.5 and 25 C \pm . *Journal of the American Chemical Society*, 1999. **121**(14): p. 3256-3266.
55. Svanidze, A.V., I.P. Koludarov, S.G. Lushnikov, A. Asenbaum, C. Pruner, F.M. Aliev, C.-C. Chang, and L.-s. Kan, Specific features of the temperature behavior of lysozyme diffusivity in solutions with different protein concentrations. *Journal of Molecular Liquids*, 2012. **168**: p. 7-11.
56. Sorret, L.L., M.A. DeWinter, D.K. Schwartz, and T.W. Randolph, Challenges in predicting protein-protein interactions from measurements of molecular diffusivity. *Biophysical journal*, 2016. **111**(9): p. 1831-1842.
57. Parmar, A.S. and M. Muschol, Hydration and hydrodynamic interactions of lysozyme: effects of chaotropic versus kosmotropic ions. *Biophysical journal*, 2009. **97**(2): p. 590-598.
58. Szymański, J.d., E. Poboży, M. Trojanowicz, A. Wilk, P. Garstecki, and R. Hołyst, Net charge and electrophoretic mobility of lysozyme charge ladders in solutions of nonionic surfactant. *The Journal of Physical Chemistry B*, 2007. **111**(19): p. 5503-5510.
59. Myerson, A.S., Diffusivity of protein in aqueous solutions. *Korean Journal of Chemical Engineering*, 1996. **13**(3): p. 288-293.
60. Saluja, A., R.M. Fesinmeyer, S. Hogan, D.N. Brems, and Y.R. Gokarn, Diffusion and sedimentation interaction parameters for measuring the second virial coefficient and their utility as predictors of protein aggregation. *Biophysical journal*, 2010. **99**(8): p. 2657-2665.
61. Grigsby, J., H. Blanch, and J. Prausnitz, Diffusivities of lysozyme in aqueous MgCl₂ solutions from dynamic light-scattering data: effect of protein and salt concentrations. *The Journal of Physical Chemistry B*, 2000. **104**(15): p. 3645-3650.

62. Prinsen, P. and T. Odijk, Fluid-crystal coexistence for proteins and inorganic nanocolloids: Dependence on ionic strength. *The Journal of chemical physics*, 2006. **125**(7): p. 074903.
63. Hulse, W. L. and R. T. Forbes, Taylor Dispersion Analysis to Gain an Insight into Formulation Buffer Salts on the Stability and Aggregation Behaviour of Proteins. [accessed: 2018 05 January]; Available from <https://www.brad.ac.uk/biopharmaceutical/media/biopharmaceuticalformulationgroup/allfiles/documents/TDA-to-Gain-an-Insigh-intoto-Formulation-Buffer-Salts-on-the-Stability.pdf>.
64. Tanaka, H., S. Takahashi, M. Yamanaka, I. Yoshizaki, M. Sato, S. Sano, M. Motohara, T. Kobayashi, S. Yoshitomi, and T. Tanaka, Diffusion coefficient of the protein in various crystallization solutions: The key to growing high-quality crystals in space. *Microgravity Science and Technology*, 2006. **18**(3): p. 91-94.
65. Kontturi, A.-K., K. Kontturi, P. Niinikoski, A. Savonen, and M. Vuoristo, The effective charge number and diffusion coefficient of cationic cytochrome c in aqueous solution. *Acta Chem Scand*, 1992. **46**: p. 348-353.
66. Nozaki, M., Studies on Cytochrome C. *The Journal of Biochemistry*, 1960. **47**(5): p. 592-599.
67. Riveros-Moreno, V. and J.B. Wittenberg, The self-diffusion coefficients of myoglobin and hemoglobin in concentrated solutions. *Journal of Biological Chemistry*, 1972. **247**(3): p. 895-901.
68. Choi, J. and M. Terazima, Denaturation of a protein monitored by diffusion coefficients: myoglobin. *The Journal of Physical Chemistry B*, 2002. **106**(25): p. 6587-6593.
69. Gibbs, S.J., A.S. Chu, E.N. Lightfoot, and T.W. Root, Ovalbumin diffusion at low ionic strength. *The Journal of Physical Chemistry*, 1991. **95**(1): p. 467-471.
70. Scott, D.J., S.E. Harding, and D.J. Winzor, Concentration dependence of translational diffusion coefficients for globular proteins. *Analyst*, 2014. **139**(23): p. 6242-6248.
71. Medda, L., M. Monduzzi, and A. Salis, The molecular motion of bovine serum albumin under physiological conditions is ion specific. *Chemical Communications*, 2015. **51**(30): p. 6663-6666.
72. Meechai, N., A.M. Jamieson, and J. Blackwell, Translational diffusion coefficients of bovine serum albumin in aqueous solution at high ionic strength. *Journal of colloid and interface science*, 1999. **218**(1): p. 167-175.
73. Jøssang, T., J. Feder, and E. Rosenqvist, Photon correlation spectroscopy of human IgG. *Journal of protein chemistry*, 1988. **7**(2): p. 165-171.

74. Marlowe, R.L., a Study of the Concentration Dependence of Macromolecular Diffusion Using Photon Correlation Spectroscopy. 1983.
75. Papadopoulos, K.N., Food chemistry research developments. 2008, New York: Nova Science Publishers.
76. Amrhein, S., K.C. Bauer, L. Galm, and J. Hubbuch, Non-invasive high throughput approach for protein hydrophobicity determination based on surface tension. *Biotechnology and bioengineering*, 2015. **112**(12): p. 2485-2494.
77. Bigelow, C.C., On the average hydrophobicity of proteins and the relation between it and protein structure. *Journal of Theoretical Biology*, 1967. **16**(2): p. 187-211.
78. Curtis, R., J. Ulrich, A. Montaser, J. Prausnitz, and H. Blanch, Protein–protein interactions in concentrated electrolyte solutions. *Biotechnology and bioengineering*, 2002. **79**(4): p. 367-380.
79. Fair, B., D. Chao, and A. Jamieson, Mutual translational diffusion coefficients in bovine serum albumen solutions measured by quasielastic laser light scattering. *Journal of Colloid and Interface Science*, 1978. **66**(2): p. 323-330.
80. Hofmeister, F., About the science of the effects of salts: About the water withdrawing effect of the salts. *Arch. Exp. Pathol. Pharmacol.*, 1888. **24**: p. 247-260.
81. Zhang, Y. and P.S. Cremer, Interactions between macromolecules and ions: the Hofmeister series. *Current opinion in chemical biology*, 2006. **10**(6): p. 658-663.
82. Tietze, A.A., F. Bordusa, R. Giernoth, D. Imhof, T. Lenzer, A. Maaß, C. Mrestani-Klaus, I. Neundorff, K. Oum, and D. Reith, On the Nature of Interactions between Ionic Liquids and Small Amino-Acid-Based Biomolecules. *ChemPhysChem*, 2013. **14**(18): p. 4044-4064.
83. Salis, A. and B.W. Ninham, Models and mechanisms of Hofmeister effects in electrolyte solutions, and colloid and protein systems revisited. *Chemical Society Reviews*, 2014. **43**(21): p. 7358-7377.
84. Muschol, M. and F. Rosenberger, Interactions in undersaturated and supersaturated lysozyme solutions: static and dynamic light scattering results. *The Journal of chemical physics*, 1995. **103**(24): p. 10424-10432.
85. Minton, A.P., Influence of excluded volume upon macromolecular structure and associations in ‘crowded’ media. *Current opinion in biotechnology*, 1997. **8**(1): p. 65-69.

86. Saluja, A. and D.S. Kalonia, Nature and consequences of protein–protein interactions in high protein concentration solutions. *International journal of pharmaceutics*, 2008. **358**(1-2): p. 1-15.
87. Han, J. and J. Herzfeld, Macromolecular diffusion in crowded solutions. *Biophysical journal*, 1993. **65**(3): p. 1155-1161.
88. Dwyer, J.D. and V.A. Bloomfield, Brownian dynamics simulations of probe and self-diffusion in concentrated protein and DNA solutions. *Biophysical journal*, 1993. **65**(5): p. 1810-1816.
89. Leaist, D.G., Counterion-accelerated diffusion of aqueous serum albumin. *Journal of solution chemistry*, 1987. **16**(10): p. 805-812.
90. Gosting, L.J., Measurement and interpretation of diffusion coefficients of proteins, in *Advances in protein chemistry*. 1956, Elsevier. p. 429-554.
91. den Akker, V. and R.F. Mudde, *Transport Phenomena: The Art of Balancing*. 2014: Delft Academic Press
92. Liu, X., A. Martín-Calvo, E. McGarrity, S.K. Schnell, S. Calero, J.-M. Simon, D. Bedeaux, S. Kjelstrup, A. Bardow, and T.J. Vlugt, Fick diffusion coefficients in ternary liquid systems from equilibrium molecular dynamics simulations. *Industrial & Engineering Chemistry Research*, 2012. **51**(30): p. 10247-10258.
93. Fowler, K., P.J. Connolly, D.O. Topping, and S. O'Meara, Maxwell–Stefan diffusion: a framework for predicting condensed phase diffusion and phase separation in atmospheric aerosol. *Atmospheric Chemistry and Physics*, 2018. **18**(3): p. 1629-1642.
94. Willis, P., L. Nichol, and R. Siezen, The indefinite self-association of lysozyme: consideration of composition-dependent activity coefficients. *Biophysical chemistry*, 1980. **11**(1): p. 71-82.

Chapter 7

*The measurement of polyelectrolyte diffusion coefficient via H-cell microfluidics**

Miao Yu, Tiago Castanheira Silva, Hayley A. Every, Wim Jiskoot, Geert-Jan Witkamp, Marcel Ottens

*The structure and text of this chapter are adapted from Chapter 6.

Abstract

A novel H-cell microfluidic method is investigated to measure the diffusion coefficient of polyelectrolyte. Via the measurement of the mass transfer between two contacting streams, which flow laminarily in micro-fabricated channels and contain different polymer concentrations, the diffusion coefficient of the polymer can be determined. Dextran sulphate sodium (DSS), with a molecular weight of 5000 Da, was used as the model polyelectrolyte. The diffusion coefficient was determined over a range of concentrations, medium ionic strengths and viscosities. In water, the measured diffusion coefficient of DSS was $8.6 \times 10^{-10} \text{ m}^2/\text{s}$ at the inlet concentrations of the receiver stream (with lower polymer concentration) and the donor stream (with higher polymer concentration) of 0 mg/ml and 2 mg/ml respectively. The diffusion coefficient was also influenced by the DSS concentration gradient between the two streams. The increasing medium ionic strength and viscosity lead to decreasing DSS diffusion coefficient. Preliminary tests of the H-cell for the measurement of the diffusion coefficient of long-chain polyelectrolytes (DSS (500,000 Da) and diethylaminoethyl dextran (DEAE-dextran; 500,000 Da)) were also performed, and the preliminary results are presented.

7.1 Introduction

Polyelectrolytes are polymers with electrolyte groups attached to the polymerisation units. The dissociation of the electrolyte groups in aqueous solutions (e.g. water) allows the polymer to bear charges, and therefore their solutions are electrically conductive. The polyelectrolytes are used in a variety of industries such as food, biotechnology, pharmaceuticals and cosmetics and function as coating materials, anticoagulant agents, purification reagents, conditioning agents, etc. [1-6]. Among these applications, their complexation with therapeutic proteins via electrostatic interactions for controlled drug delivery has been a popular topic in recent decades [7-9].

Knowledge of the diffusion coefficient of polyelectrolyte provides insight into the mechanisms of polymer motion, structure-property relations, and electrostatic interactions with oppositely-charged materials. The polyelectrolyte diffusivity is one of the important factors in the fields such as biochemical synthesis, biophysics and separation technology.

This chapter reports a novel method for determining the polyelectrolyte diffusion coefficient using a microfluidic device: H-cell. During the measurement, two streams with different solute concentrations flow laminaarily in the microfabricated channel with known dimensions. An entropy increase process takes place, and the system tends to be closer to equilibrium. By detecting the mass transfer of the solute during the passage of the streams via the channel, the diffusion coefficient of the solute can be calculated. This method has been applied to determine the diffusion coefficients of small molecules such as common electrolytes and polyphenols [10, 11] and macromolecular proteins [12]. In this study, the diffusion coefficient of dextran sulphate sodium (DSS; 5000 Da) was determined by the H-cell. The concentration of the polyelectrolyte was determined by building a calibration curve to the conductivity of the polymer solution. The H-cell was also tested to measure the diffusion coefficients of DSS with the size of 500,000 Da and diethylaminoethyl dextran (DEAE-dextran) (500,000 Da). One bottleneck hindering the determination of the long-chain polymer diffusion coefficient was the apparent viscosity difference between the donor stream and receiver stream with higher and lower inlet polymer concentrations respectively.

7.2 Materials and method

The polyelectrolytes used in this study were: dextran sulfate sodium (DSS) salt from *Leuconostoc* spp. (5000 Da, Sigma-Aldrich, Zwijndrecht, the Netherlands), DSS salt from *Leuconostoc* spp. (500,000 Da, Sigma-Aldrich, Zwijndrecht, the Netherlands), Diethylaminoethyl-dextran hydrochloride (DEAE-

dextran) (500,000 Da, Sigma-Aldrich, Zwijndrecht, the Netherlands). All the polymer materials were supplied in dry powder form and used as received.

The polyelectrolyte solutions (concentrations shown in Table 7.1) were prepared using ultrapure water (purified using a Milli-Q ultra-pure water system, Millipore™, Molsheim, France) as the solvent. To control the pH, phosphate buffer (PB) (Na_2HPO_4 and NaH_2PO_4 , Sigma Aldrich, Zwijndrecht, the Netherlands) and acetate buffer (AC) (acetic acid (Sigma Aldrich, Zwijndrecht, the Netherlands) and sodium acetate (Merck, Darmstadt, Germany)) were used. NaCl (J.T. Baker, Deventer, The Netherlands) and glycerol (Merck, Darmstadt, Germany) were used to change the ionic strength and viscosity respectively. All the prepared solutions were filtered through 0.22 μm cellulose filters (Whatman®, GE Healthcare, United Kingdom) before the experiments.

The H-cell microfluidic set-up is similar to the one used for the protein diffusion coefficient determination (see Chapter 6). A microfluidic H-cell (Micronit®, Netherlands) made of borofloat glass with the dimension of 625 mm x 753 μm x 69 μm (L x W x H) was used. The concentration of the outlet stream was determined using an inline conductivity flowcell (GE healthcare pH/C900 with Consort C832 analyzer). Calibration curves were established as a function of polymer concentration. The experimental operating conditions are summarised in Table 7.1. For convenience, the inlet stream concentrations will be described as the “inlet receiver stream (RS) concentration vs inlet donor stream (DS) concentration”. For example, 0 vs 2 mg/ml represents the inlet concentrations of 0 mg/ml in RS and 2 mg/ml in DS.

The kinematic viscosities of the polyelectrolyte solutions with and without glycerol were determined at room temperature using an Ostwald viscometer (inside tube diameter: 0.26 mm; Roweel Electronic Co., Ltd, Zhengzhou, China). Water was used as the reference.

Comsol Multiphysics (version 4.4, Comsol, Sweden), via a Matlab (version 2017a, Mathworks, USA) livelink, was used to calculate the diffusion coefficient based on the H-cell dimensions, the concentrations of inlet RS and DS, and the concentration of outlet RS under steady state, as described in Chapter 6.

Table 7.1. Experimental conditions for the H-cell study, in which the tested polyelectrolytes, the inlet receiver stream (RS) and donor stream (DS) concentrations, the solvents, the NaCl concentrations for ionic strength adjustment and the glycerol concentrations for viscosity adjustment are listed.

Experiment	Polyelectrolyte	Mw (Da)	RS (mg/ml)	GS (mg/ml)	Solvent	NaCl (mM)	Glycerol (w/w%)
1	DSS	5000	0	2	Water	-	-
2	DSS	5000	0	5	Water	-	-
3	DSS	5000	0	10	Water	-	-
4	DSS	5000	1	3	Water	-	-
5	DSS	5000	4	6	Water	-	-
6	DSS	5000	0	2	Water	10	-
7	DSS	5000	0	2	Water	20	-
8	DSS	5000	0	2	Water	50	-
9	DSS	5000	0	2	Water	-	10
10	DSS	5000	0	2	Water	-	20
11	DSS	5000	0	2	Water	-	40
12	DSS	5000	0	2	10 mM PB	-	-
13	DSS	5000	0	5	10 mM PB	-	-
14	DSS	5000	0	10	10 mM PB	-	-
15	DSS	5000	1	3	10 mM PB	-	-
16	DSS	5000	4	6	10 mM PB	-	-
17	DSS	5000	0	2	10 mM AC	-	-
18	DSS	5000	0	5	10 mM AC	-	-
19	DSS	5000	0	10	10 mM AC	-	-
20	DSS	5000	1	3	10 mM AC	-	-
21	DSS	5000	4	6	10 mM AC	-	-
22	DSS	500,000	0	0.08	Water	-	-
23	DEAE-dextran	500,000	0	0.04	Water	-	-

7.3 Results and discussion

7.3.1 Diffusion coefficient of DSS as function of concentration, pH and buffer type

Figure 7.1 shows the measured diffusion coefficients of DSS (Mw 5000 Da) in water, AC and PB at different concentration profiles. The diffusion coefficients of DSS were found to be about $4\text{-}10 \times 10^{-10}$ m²/s but varied at different conditions. In water, with the increasing concentration gradient of DSS, there was a decrease in the diffusion coefficient at 0 vs 5 mg/ml before increasing slightly again at 0 vs 10 mg/ml. In PB, an increase of the diffusion coefficient was observed with the increasing concentration gradient from 2 mg/ml to 5 mg/ml, followed by levelling off. In AC, relatively stable diffusion coefficients were obtained when increasing the concentration gradient. When at constant concentration gradient (2 mg/ml), the measured diffusion coefficients in water increased from 0 vs 2 mg/ml to 1 vs 3 mg/ml, followed by a decrease to 4 vs 6 mg/ml. In PB and AC, the measured values increased as a function of concentration before levelling off. At 0 vs 5 mg/ml and 0 vs 10 mg/ml, the measured DSS diffusivity in water, PB and AC were more similar, ranging from 6×10^{-10} to 8×10^{-10} m²/s, than that at 0 vs 2 mg/ml. The measured diffusion coefficients at 4 vs 6 mg/ml in water, PB and AC differed less than those at lower concentrations with the gradient of 2 mg/ml.

The influence of the concentration gradient on the diffusion coefficient of DSS was not as apparent as that shown for protein in Chapter 6. For the protein (e.g., lysozyme), a sharp increase of the measured diffusion coefficients was observed from 0 vs 2 mg/ml to 0 vs 5 mg/ml in water and AC (10 mM pH 4.2 with low ionic strength), in which there was in principle relatively strong repulsion among the charged molecules. For the polyelectrolyte (e.g., DSS), when the concentration increased, there was an increasingly strong internal friction between the randomly coiled and swollen macromolecules and the surrounding solvent molecules, increasing the viscosity of the solution. Under this circumstance, the effect of the increasing concentration gradient on the diffusivity of the polymer may be compromised by the increased drag force between the polymer and the solvent.

At 0 vs 2 mg/ml and 1 vs 3 mg/ml, the measured diffusion coefficients of DSS followed the order that the values measured in water > in AC > in PB. This was the reverse order of the ionic strength of the media (the ionic strength of water < 10mM AC < 10mM PB, as calculated via [13]). In analogue to the behaviour of protein's diffusion, when the macromolecules diffuse in the presence of other electrolytes, the diffusion-induced electric field drives large coupled flows of the relatively mobile ions of the other electrolytes instead of speeding up the macromolecules [14]. Consequently, the other electrolytes sharply reduce macromolecular diffusivity. Furthermore, the lower the ionic strength of the medium, the longer the Debye length and, as a result, the more probable the charged

macromolecules are driven by inter-molecular repulsion, which is one of the main driving forces for their diffusion. When at 0 vs 5 mg/ml, 0 vs 10 mg/ml and 4 vs 6 mg/ml, there were fewer differences among the measured diffusion coefficients in different media than those at other concentration profiles. In this situation, the effect of the ionic strength on the polymer diffusivity was attenuated. This may be the consequence of the increased viscosity due to the increasing polymer concentration.

In the cases of DSS diffusion at a constant concentration gradient (2 mg/ml), the measured diffusion coefficients in water varied less at different concentrations than those in AC and PB, in which the diffusion coefficients increased with concentration. A similar phenomenon was reported in Chapter 6 for protein diffusion. Regarding the presence of external salts in AC and PB, the diffusion of proteins can be accelerated by the presence of counterions, which is a thermodynamic effect brought about by an increase in the free energy gradient of the solutes, which is the driving force for isothermal diffusion [14]. However, it remains a question whether the same explanation can interpret the similar diffusion behaviour for DSS with Na^+ as the counterion. Also, in the ternary systems of DSS-salt-water, the diffusion coefficient of DSS may be not only related to the flux of its concentration gradient but also related to the flux of other components, similar to the behaviour of the protein diffusion reported elsewhere [15]. When increasing the DSS concentration while keeping the buffer concentration consistent, due to the excluded volume effect, the flux of the buffer component relative to the DSS may increase. Directly proportional to the polymer gradient, there is an effective concentration gradient of salt and thus a flux from higher to lower polymer concentration regions, contributing to the variation of the DSS diffusion coefficients calculated based on the flux across the diffusion boundary.

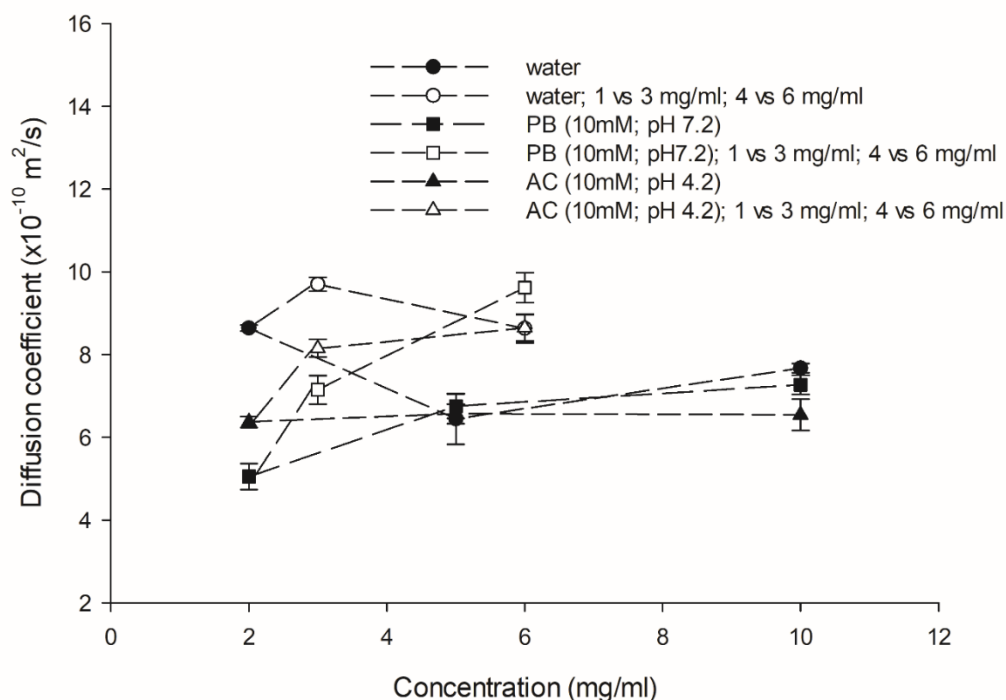


Figure 7.1. The diffusion coefficients of DSS (Mw 5000 Da) measured via microfluidic H-cell in water, PB and AC at different concentration profiles. The x-axis stands for the inlet concentration of DSS in the DS. If not specially indicated, the DSS concentration in the inlet RS is 0 mg/ml.

7.3.2 Diffusion coefficient of DSS as function of ionic strength

The measured DSS diffusion coefficients in an aqueous medium decreased with increasing NaCl concentration (see Figure 7.2). This phenomenon was also observed for protein diffusion as shown in Chapter 6. The decrease of the measured diffusion coefficient was probably a result of the lessened inter-molecular electrostatic repulsion that is hindered by salt screening. However, the level of attenuation on the diffusivity of DSS was not as high as that for the protein. This may be due to the stronger electrostatic interaction among DSS molecules than that among protein molecules.

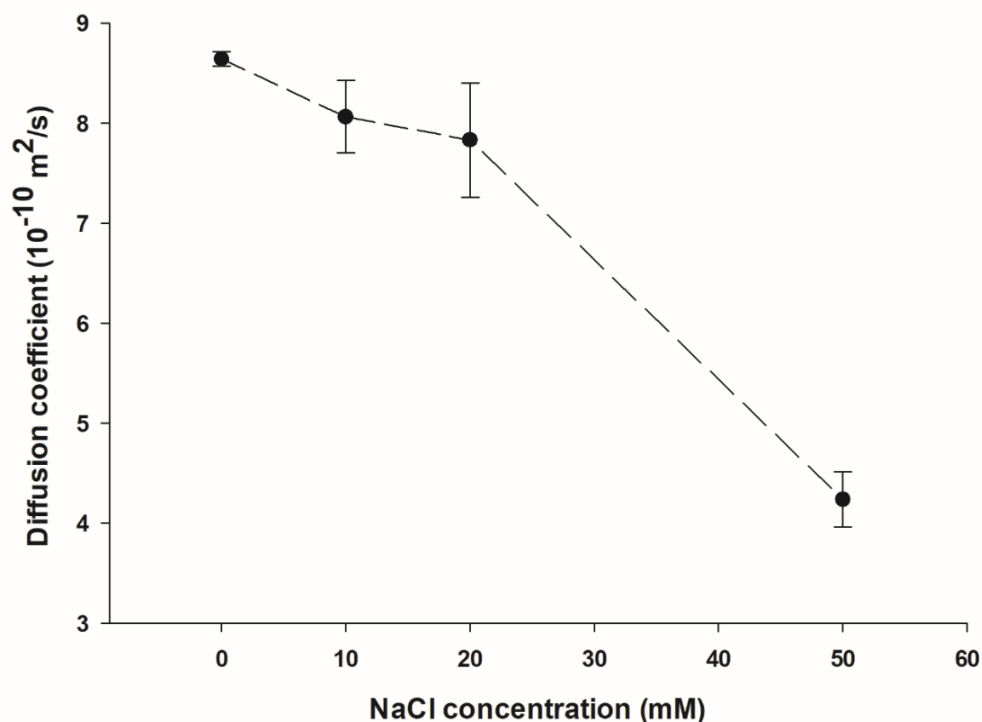


Figure 7.2. The diffusion coefficient of DSS as a function of the NaCl concentration. The dashed line is used to guide the eye.

7.3.3 Diffusion coefficient of DSS as a function of viscosity

There was an expected decrease in the measured DSS diffusion coefficient with the increasing medium viscosity (see Figure 7.3). This trend can be predicted by the Stokes-Einstein model. When inputting 0.5 nm for the term of molecular size in the model, the calculated results were comparable with the experimental values. However, according to the test of Nanoparticle Tracking Analysis (NTA) (data not included) and the results of molecular modelling [16], the size of the DSS (Mw. 5000 Da) is about 3 nm in the aqueous environment.

The size of DSS obtained by fitting the Stokes-Einstein equation is not conclusive yet. The diffusion coefficient determined by the H-cell takes into account the inter-molecular interactions among the charged polymers. However, the Stokes-Einstein model predicts merely the diffusivity of molecules at infinite dilution. There is thus an underestimation of the particle size calculated by the Stokes-Einstein equation based on the H-cell data. Moreover, the Stokes-Einstein equation was theoretically used to predict the diffusivity of globular molecules or particles. However, DSS was found to be helical in aqueous environment [16]. Additionally, it was not clear whether the glycerol

(for viscosity adjustment) in the solution affected the dimension of the DSS. Searches of specific models to predict the DSS diffusion coefficient or simulations on DSS molecular dynamics will be performed in future studies to provide more relevant information on the (diffusion) behaviour of the DSS molecules in the aqueous environment.

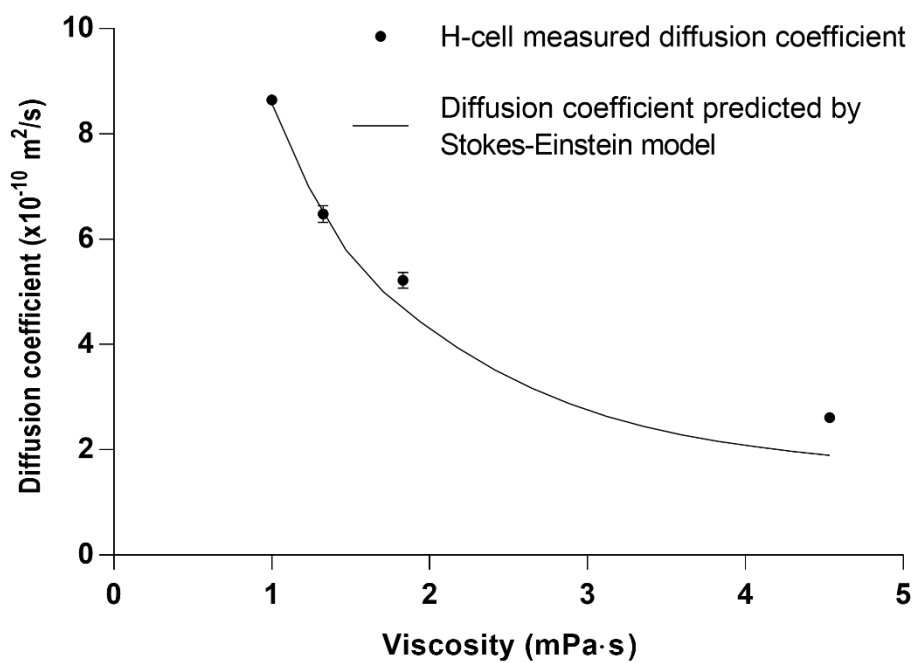


Figure 7.3. The diffusion coefficient of DSS (5000 Da) measured via H-cell as a function of viscosity (solid circle) and predicted by Stokes-Einstein model with the input of the polymer size of 0.5 nm (solid line).

7.3.4 Measured diffusion coefficients of DSS (500,000 Da) and DEAE-dextran

Table 7.2 shows the measured diffusion coefficients of DSS and DEAE-dextran with the molecular weight of 500,000 Da. Compared to the DSS (5000 Da; $8.6 \times 10^{-10} \text{ m}^2/\text{s}$), the measured diffusion coefficient decreases with increased molecular size. For the DSS (500,000 Da), there was literature reporting the radius of about 14.5 nm [17-19] and the calculated free diffusion coefficient of about $6-10 \times 10^{-11} \text{ m}^2/\text{s}$ by Stokes-Einstein law based on this radius [20]. There may be an underestimation of the diffusion coefficient calculated by Stokes-Einstein law due to the negligence of the inter-molecular interactions among the charged polymers. For the DEAE-dextran (500,000 Da), there was literature reporting the measured hydrodynamic radius of about 21 nm with a z-average diffusion coefficient of about $1.01 \times 10^{-11} \text{ m}^2/\text{s}$ determined by a light scattering method [21]. The diffusion coefficient of DEAE-

dextran measured by H-cell is much higher than that measured by light scattering. Different methods may give different results on the determined diffusion coefficients of the polymer. For the light scattering method, the z-average diffusion coefficient is calculated by the method of cumulants and is an intensity weighted diffusion coefficient [22]. This value is affected by the particle size, light intensity, light wavelength and scattering angles. This differs from the principle of the H-cell, which is based on the mass transfer as function of residence time and cell dimensions. Moreover, the concentration of the polymer used for the light scattering determination was not clearly mentioned in the reference paper [21]. The difference of the testing DEAE-dextran concentration may also be one of the reasons explaining the difference of the determined diffusion coefficients.

The obtained H-cell results of the diffusion coefficients of the long-chain polymers (500,000 Da DSS and DEAE-dextran) need to be further tested and validated regarding the non-negligible effect of the viscosity difference between the RS and DS on the microfluidic stream split ratios in the H-cell. The apparent viscosity difference between the two streams can consequently cause an overestimation of the measured polymer diffusion coefficient.

For short-chain polymers, the unentangled chains pass each other without further twisting with other polymer molecules. However, for long-chain polymers, the lateral chain motion is severely restricted by the presence of neighbouring chains due to the entanglements of the polymer chain. When it comes to the polyelectrolyte, the diffusion behaviour is not only affected by the restriction of other polymers due to hindrance, but also electrostatic interactions among the molecules, making the phenomena more complicated to explain.

To reduce the difference between the properties of the DS and RS, such as viscosity, a small inlet concentration gradient was tried. Physically speaking, the dividing line between the two streams is off the channel midline if the input two fluids have different viscosities, although at the same flow rate. This change of the fluidic profile can lead to an overestimation of the measured diffusion coefficients due to the fact that the more viscous fluid (DS) takes over the dimension of the less viscous fluid (RS) in the microfluidic channel, i.e. the contacting interface of the two streams shifts from the middle of the channel to the less viscous side [23]. To alleviate this influence of the viscosity difference, low concentrations of the long-chain polymer solution (0.08 mg/ml DSS (500,000 Da) and 0.04 mg/ml DEAE-dextran) were used for the H-cell measurement. The viscosities of these diluted solutions were about 1.1 mPa·s compared to that of water (about 1 mPa·s). The significance of the influence of this 10 % viscosity difference on the fluidic profiles and the measured diffusion coefficients needs further clarification experimentally and numerically.

Another problem encountered during the experiment was the detection limit of the conductivity meter, which was used to determine the polyelectrolyte concentration. In the experiment, the conductivities of the outlet RS (about 0.02-0.03 $\mu\text{S}/\text{cm}$ for DSS 500,000 Da and 0.09 $\mu\text{S}/\text{cm}$ for DEAE-dextran) were so low that the conductivity meter could not perform the sensitive determination. To overcome this shortcoming, several alternative methods are proposed here: i) to use more sensitive detection methods with a lower detection limit, e.g. spectroscopic methods such as the refractive index spectrometer; ii) to collect offline the RS outlet sample under a steady-state condition, followed by concentrating the collected sample (e.g. freeze-drying and redissolution) before determination; iii) to increase the inlet DS polymer concentration while reducing the viscosity difference by adjusting the viscosity of the RS using glycerol. These possibilities need further investigation and evaluation.

Table 7.2. Experimental and literature values of the diffusion coefficients of DSS (500,000 Da) and DEAE-dextran.

Polyelectrolyte	Diffusion coefficient (m^2/s) (measured by H-cell)	Diffusion coefficient (m^2/s) (literature value)
DSS (500,000 Da)	$3.3 \pm 0.2 \times 10^{-10}$	0.6 to 1×10^{-10} [20]
DEAE-dextran (500,000 Da)	$2.6 \pm 0.4 \times 10^{-10}$	0.101×10^{-10} [21]

7.4 Conclusions

An H-cell microfluidics device was used for the quantitative determination of the diffusion coefficient of polyelectrolyte based on the polymer mass transfer over the contacting liquid-liquid interface of the co-current flowing streams in the diffusion channel. The conductivity and concentration of the polyelectrolyte solution were correlated as a calibration curve, which was used for concentration determination during the experiment. The measured diffusion coefficients of DSS (Mw. 5000 Da) were about 8 to $10 \times 10^{-10} \text{ m}^2/\text{s}$ in water. Different diffusion coefficients were obtained in AC and PB at low polymer concentration and concentration gradient. High ionic strength resulted in low measured diffusion coefficients, which might be due to the attenuated inter-molecular repulsive interaction. The measured polymer diffusion coefficient decreased with increasing viscosity. The preliminary tests on DSS (500,000 Da) gave values of the diffusion coefficient lower than the 5000 Da DSS, but higher than literature values. There are still experimental limitations when applying the H-cell to measure the long-chain polymer diffusion coefficient due to the high viscosity of the polymer solution and the limitation on the detection of the polymer concentration.

References

1. Samant, S., R. Singhal, P. Kulkarni, and D. Rege, Protein-polysaccharide interactions: a new approach in food formulations. *International journal of food science & technology*, 1993. **28**(6): p. 547-562.
2. Balabushevich, N.G., O.P. Tiourina, D.V. Volodkin, N.I. Larionova, and G.B. Sukhorukov, Loading the multilayer dextran sulfate/protamine micro-sized capsules with peroxidase. *Biomacromolecules*, 2003. **4**(5): p. 1191-1197.
3. Schmitt, C., C. Sanchez, S. Desobry-Banon, and J. Hardy, Structure and technofunctional properties of protein-polysaccharide complexes: a review. *Critical Reviews in Food Science and Nutrition*, 1998. **38**(8): p. 689-753.
4. Miyake, M. and Y. Kakizawa, Morphological study of cationic polymer-anionic surfactant complex precipitated in solution during the dilution process. *Journal of cosmetic science*, 2010. **61**(4): p. 289.
5. Yamagishi, R., M. Niwa, S.-i. Kondo, N. Sakuragawa, and T. Koide, Purification and biological property of heparin cofactor II: Activation of heparin cofactor II and antithrombin III by dextran sulfate and various glycosaminoglycans. *Thrombosis research*, 1984. **36**(6): p. 633-642.
6. Hall, M. and C. Ricketts, The use of dextran sulphate as a blood anticoagulant in biological research. *Journal of clinical pathology*, 1952. **5**(4): p. 366-366.
7. Cooper, C., P. Dubin, A. Kayitmazer, and S. Turksen, Polyelectrolyte-protein complexes. *Current opinion in colloid & interface science*, 2005. **10**(1-2): p. 52-78.
8. Lankalapalli, S. and V. Kolapalli, Polyelectrolyte complexes: a review of their applicability in drug delivery technology. *Indian journal of pharmaceutical sciences*, 2009. **71**(5): p. 481.
9. Dumitriu, S. and E. Chornet, Inclusion and release of proteins from polysaccharide-based polyion complexes. *Advanced drug delivery reviews*, 1998. **31**(3): p. 223-246.
10. Häusler, E., P. Domagalski, M. Ottens, and A. Bardow, Microfluidic diffusion measurements: The optimal H-cell. *Chemical engineering science*, 2012. **72**: p. 45-50.
11. Berends, C., Determination of the diffusion coefficient of phenolic compounds using microfluidics, in Department of Biotechnology. 2015, Delft University of Technology: Delft.

12. Yu, M., T.C. Silva, A. van Opstal, S. Romeijn, H.A. Every, W. Jiskoot, G.-J. Witkamp, and M. Ottens, The investigation of protein diffusion via H-cell microfluidics. *Biophysical journal*, 2019. **116**(4): p. 595-609.
13. Buffer calculator. [accessed: 2018 17 July]; Available from: <https://www.liverpool.ac.uk/pfg/Research/Tools/BufferCalc/Buffer.html>.
14. Leaist, D.G., Counterion-accelerated diffusion of aqueous serum albumin. *Journal of solution chemistry*, 1987. **16**(10): p. 805-812.
15. Albright, J.G., O. Annunziata, D.G. Miller, L. Paduano, and A.J. Pearlstein, Precision measurements of binary and multicomponent diffusion coefficients in protein solutions relevant to crystal growth: lysozyme chloride in water and aqueous NaCl at pH 4.5 and 25° C. *Journal of the American Chemical Society*, 1999. **121**(14): p. 3256-3266.
16. Yu, M., H.A. Every, W. Jiskoot, G.J. Witkamp, and W. Buijs, Molecular structure of dextran sulphate sodium in aqueous environment. *Journal of Molecular Structure*, **1156** (2018): 320-329.
17. Leyboldt, J.K. and L.W. Henderson, Molecular charge influences transperitoneal macromolecule transport. *Kidney international*, 1993. **43**(4): p. 837-844.
18. Granath, K.A., Solution properties of branched dextrans. *Journal of Colloid Science*, 1958. **13**(4): p. 308-328.
19. Granath, K.A. and B.E. Kvist, Molecular weight distribution analysis by gel chromatography on Sephadex. *Journal of Chromatography A*, 1967. **28**: p. 69-81.
20. Deen, W.M. and F.G. Smith III, Hindered diffusion of synthetic polyelectrolytes in charged microporous membranes. *Journal of Membrane Science*, 1982. **12**(2): p. 217-237.
21. Hanselmann, R., W. Burchard, R. Lemmes, and D. Schwengers, Characterization of DEAE-dextran by means of light scattering and combined size-exclusion chromatography/low-angle laser light scattering/viscometry. *Macromolecular Chemistry and Physics*, 1995. **196**(7): p. 2259-2275.
22. Koppel, D.E., Analysis of macromolecular polydispersity in intensity correlation spectroscopy: the method of cumulants. *The Journal of Chemical Physics*, 1972. **57**(11): p. 4814-4820.
23. Kamholz, A.E., B.H. Weigl, B.A. Finlayson, and P. Yager, Quantitative Analysis of Molecular Interaction in a Microfluidic Channel: The T-Sensor. *Analytical Chemistry*, 1999. **71**(23): p. 5340-5347.

Chapter 8

FlowDensi: a user-friendly Matlab-based toolkit for the density calculation of microparticles analysed by FlowCam®

Miao Yu, Ahmad S. Sediq, Ruben van Duijvenvoorde, M. Reza Nejadnik, Hayley A. Every,
Wim Jiskoot , Geert-Jan Witkamp

Abstract

According to some previous research, via the analysis of the exported data from the flow imaging microscopy (FlowCAM®), the trajectories and displacement velocities of microparticles can be obtained, based on which the density of microparticles can be calculated. To assist in the time-consuming FlowCAM® data analysis, we have developed and assessed a user-friendly Matlab-based toolkit, the *FlowDensi*. This toolkit was used to analyse the experimental data of polystyrene beads of different sizes with a known density for testing purposes. The program can efficiently extract all the necessary data belonging to one displacing particle from the database, such as coordinates, size and optical focus. Thereafter, the trajectory of each moving particle can be identified as a function of time, from which the displacement velocity and particle density are subsequently calculated.

8.1 Introduction

Polymeric microparticles are commonly used as a drug delivery system to improve the pharmaceuticals of the encapsulated drug substance [1, 2]. Knowledge about the porosity, which can be derived from the density of such microparticles, can contribute to the rational design of a therapeutic product [3, 4]. There have been several techniques developed for the measurement of microparticle density, such as (helium-air) pycnometry [5, 6], density gradient technique [7], sedimentation field flow fractionation [8] and flow imaging microscopy (FlowCAM®) [3]. The last technique is based on the method of tracking the displacement of microparticles in a stationary liquid and using Stokes' law to calculate the density from the velocity of the particles [3].

In a static liquid, the vertical displacement of micron-sized particles as a result of gravity (settling) or buoyancy (floatation) is greater than the random motion due to bombardment by liquid molecules (Brownian motion). Gravity and buoyancy are in opposite directions and their net force drives the motion of the particle. In addition, there is a drag force acting on the moving particle, which is influenced by the projected area of the particle (cross-section area), the viscosity of the liquid and the velocity of the particle. Whenever the drag force is equal to the gravitational or buoyant force, the particle ceases to accelerate and moves at a constant speed, namely the terminal velocity. Stokes' law correlates the terminal velocity to the densities of the solid particle and the liquid according to Equation 8.1 [9].

$$\rho_p = \rho_l + \frac{9\mu v_w}{2gr^2} \quad \text{Equation 8.1}$$

Where ρ_p (kg/m³) is the density of solid particle, ρ_l (kg/m³) is the density of the liquid, μ (Pa·s) is the viscosity, v_w the particle terminal velocity corrected for the wall effect (explained later), g (m/s²) is the gravitational acceleration rate, and r the particle radius. So, the density of the particle can be calculated based on the measurement of its velocity in a liquid of known density and viscosity. The velocities of the displaced particles can be obtained from their trajectories in the flow cell [3, 10]. This lays the foundation of the method of microparticle density determination using FlowCAM®.

When using FlowCAM®, the microparticles move in a flow cell and are imaged at fixed time intervals. Depending on the coordinates of the microparticles at different time, the displacement of the microparticles along the direction of gravity or buoyancy per time interval can be determined and the corresponding velocity calculated. This velocity is then used to calculate the particle density according to Stokes' law.

One drawback of this method is that the data analysis part is laborious and time-consuming [3]. In short, the FlowCAM® chronologically captures images of the flow cell in which the microparticles are displaced. In these images of the flow cell, the microparticles were displayed as sort of dots as indicated in previous studies [3, 10]. The equipment sequences the particles appearing in the captured images and reports information such as their coordinates and optical properties. As multiple particles can be recorded at the same time, it can be difficult to differentiate these within the database as the data is grouped by the time interval. Under these circumstances, the information about each particle is disorderly arranged in the exported database and must be sorted manually. This can be particularly challenging when dealing with a sample containing a high concentration of particles with similar properties.

One possible solution to simplify this process is to make use of a computer program to accelerate data analysis. Bach et al. [10] applied FlowCAM® to determine the sedimentation velocity of marine particles. Small ($\approx 10 \mu\text{m}$) and large (75-400 μm) polystyrene (PS) beads, monospecific phytoplankton cultures and sediment trap materials were used for the investigation. Instead of manual data analysis, a Matlab script was developed to automatically distinguish the particles within a mixed sample and analyze the particles that fulfilled the defined criteria. However, this Matlab script was only able to calculate the particles' sedimentation velocity and lacked other functionalities such as the calculation of particle densities. Furthermore, no evaluation of the applied parameters in the scripts for the sorting of particle information was conducted. The efficiency of the used criteria and their limitations were not reported. Moreover, since the script was a command-driven program, it is not readily accessible to researchers and students with a lack of Matlab knowledge but an interest in investigating the microparticle properties via FlowCAM®.

To overcome these shortcomings, a robust and easy-to-use Matlab-based toolkit, named as *FlowDensi*, with a user-friendly graphical user interface (GUI), was developed to simplify the determination of microparticle density based on particle displacement velocity recorded by FlowCAM®. In this study, the developed toolkit i) provides a platform for the automated selection of relevant data from the FlowCAM® database that belong to each moving particle according to the inclusion of user-defined criteria; ii) allows for routine analysis of microparticle batches with high temporal resolution and improved efficiency to retrieve data with respect to time; and iii) provides the possibility to extend the application of FlowCAM®-based methods for other purposes, such as the determination of particle porosity and optical properties.

In this study, the particle sorting algorithms used by *FlowDensi* and corresponding GUI functions are presented. The toolkit was used to process the database of microparticle displacement recorded by

FlowCAM®. Standard sized PS beads (30 µm, 50 µm and 70 µm) were equilibrated in static liquids with a known density and their moving trajectories and optical properties were recorded. Different input parameters of *FlowDensi* were used to sort the information about the recorded microparticles and to calculate their densities. Comparison of *FlowDensi* results to reference values was used to determine the accuracy of the toolkit in investigating microparticle density.

8.2 Experimental

8.2.1 Materials and sample preparation

Non-porous polystyrene (PS) sizing standards of different sizes (30, 50 and 70 µm) with a density of 1050 kg/m³ were purchased from Duke Scientific (through Thermo Scientific, Fremont, CA, USA). Ultrapure water (18.2 MΩ.cm) was dispensed from a Purelab Ultra water purification system (ELGA LabWater, Marlow, UK). Caesium chloride (CsCl) was purchased from Sigma (Sigma-Aldrich, Steinheim, Germany). CsCl was dissolved in water to prepare the CsCl solution with a higher density than the PS beads (concentration and density shown in Table 8.1). Before use, both the water and CsCl solution were filtered through 0.2 µm filters (Millipore Corporation, Bedford, MA, USA). These filtered media were used to pre-rinse the equipment and set the background. The PS beads were suspended in either water or CsCl solution before FlowCAM® measurement.

8.2.2 Particle displacement determined by FlowCAM®

A FlowCAM® VS1 equipment (Fluid Imaging Technologies, Yarmouth, ME, USA) installed with a 300 µm-deep flow cell (FC300FV: 300 µm depth and 1500 µm width or FC300: 300 µm depth and 3000 µm width) and 4× magnification lens was used in this study. The set-up was controlled by the Visual Spreadsheet software version 3, which was also used to export the database. An illustration of the FlowCAM® set-up during measurement and the positions of a particle being photographed during transport in the flow cell is shown in previous literature [10].

Before each measurement, the flow cell was rinsed with 2 mL of the suspending medium (particle-free) that was also used for the measurements. The background was calibrated by manually priming 0.5 mL of the same particle-free suspending medium. The PS beads were diluted to a specific concentration with the medium and suspended by pipette. Afterwards, 1.5 mL of the sample was loaded to fill the flow cell and tubing. The tubing was then disconnected from the pump, and both ends were clamped to create a closed system in which there is no liquid flow. The FlowCAM® measurement was performed with a camera rate of 3, 4 or 20 frames/s for the 30, 50 and 70 µm PS beads respectively. A higher camera rate was used for the larger particles with theoretically high velocity, so that more dots (each one representing one of a particle's images recorded at a specific

time) composing the trajectory of the particle were recorded when particles passed the flow cell. The analysis was stopped manually as soon as a sufficient number of particles was tracked (50 to 100 particles).

Table 8.1 shows the experimental conditions for the PS samples. Each sample was measured five times according to the procedure above. The exported databases of the five experiments were merged and processed by *FlowDensi*.

Table 8.1. Experimental conditions for PS beads density measurement.

Sample	Flow cell type	Frame rate (frames/s)	Medium	Medium density (kg/m ³)	Medium viscosity (Pa·s)
30 µm PS beads	FC300FV	4	Water	1003.35	1.00x10 ⁻³
50 µm PS beads*	FC300FV	3**	CsCl solution	1060.00	0.99x10 ⁻³
70 µm PS beads	FC300***	20	Water	1003.35	1.00x10 ⁻³

*For the experiment with the 50 µm PS beads, the density of the CsCl solution was higher than the beads. Therefore floatation of the particles rather than sedimentation was observed.

**The velocity of the 50 µm PS beads was assumed to be lower than the other two beads due to the smaller difference of the medium density from the particle density (1050 kg/m³ according to the manufacturer). Thus a low frame rate was applied.

*** FC300 and FC300FV have the same cell depth. FC300 has a broader cell size (3000 µm width) than the FC300FC (1500 µm width).

8.3 FlowDensi: GUI, algorithm and theoretical background

FlowCAM® characterises microparticles during their transport in a liquid medium via a flow cell placed in front of a microscope camera. The microparticles in the detected sample are photographed at a constant time interval as they pass through the flow cell. Each particle is displayed as a dot in the photograph. At every time step, each particle is automatically characterised by a number of properties via the software Visual Spreadsheet (Fluid Imaging Technologies Inc.). This information can be exported as a database in comma-separated values (CSV) format, in which parameters such as the x-y coordinates, sizes (e.g., projected area) and optical properties (e.g., aspect ratio and edge gradient) of the particles are listed. This file is used for the analysis by *FlowDensi*.

The algorithm of *FlowDensi* is shown in the flowchart in Figure 8.1, together with the corresponding sections on the GUI. A two-step process is used: primary sorting and refinement. In the primary sorting step, *FlowDensi* consolidates the data based on: i) the deviation of the x coordinates (*Delta X*), where the particle dots with similar horizontal positions are grouped; ii) the deviation of the particle area (*Delta area*), where particle dots with similar size are grouped; and iii) the deviation of aspect ratio (AR) (*Delta AR*), which is the ratio of the length to width of the imaged particle (dot), where particles with the similar shape are grouped. After this primary sorting, a coarse generalisation of the trajectories of the transporting particle can be determined.

Further refinement steps are implemented to exclude any inconsistent dots obtained from the primary sorting. FlowCAM® records the image of the flow cell at a constant time step and each image has an image number. In this case, each dot of a travelling particle has a corresponding image number. With the parameter of *Delta SIN* (source image number), the user can define the allowable difference of the image number of the dots every time interval and exclude the ones with abnormal value.

Another parameter, the *Delta Y*, is implemented to determine the proper vertical moving distance of a particle per time interval. During sedimentation or floatation, each particle displaces vertically in the flow cell at an almost constant velocity. During the experiment, the camera continuously records the field of view at a constant time interval. As a result, the difference between the y coordinates of a particle every time interval should be stable. By constraining the stepwise change in y, the possibility of consolidating data belonging to different particles is reduced.

The parameter *Edge gradient* is implemented to set the range of the camera focus of the captured particles. The value of the edge gradient represents the intensity of the pixels making the outer border of the particles in the picture. The blurring or over-sharpening of the particle border indicates that the particle is out of the camera focus. Very blurred or very sharp particle borders (corresponding to very

low or high edge gradients respectively) can lead to an overestimation or underestimation of the particle size respectively. Therefore, both a lower and an upper limit of the edge gradient are needed in order to size the PS beads accurately.

In addition, refinement parameters related to the effective range of the camera view (*Eff X range* & *Eff Y range*) are implemented, via which particles on the borders of the flow cell are excluded.

Upon implementing these refinements, the trajectory of one travelling particle can be well depicted. The final trajectory of one particle is composed of a number of dots. Each dot represents the particle in the view cell photographed at a specific time during its transport. When plotting the vertical path of one particle against time, the slope of this plot by linear regression represents the velocity. When moving in the flow cell, the closest cell walls may exert a drag force on the particle [11] and thus potentially influence the particle velocity [12]. Under this circumstance, the velocity may need to be corrected for the wall retardation effect depending on the size of the particle. After the correction, the velocity can then be used to calculate the density of the particle based on the known liquid viscosity and density according to Stokes' law (see Equation 8.1).

The correction of the wall retardation effect on the velocity can be calculated based on Equation 8.2 [3, 10, 13].

$$V_w = \frac{V_m}{1 - k \left(\frac{2+r}{D} \right)} \quad \text{Equation 8.2}$$

Where V_w (m/s) represents the particle velocity corrected for the wall retardation effect, V_m is the measured particle velocity, k (dimensionless) is the coefficient of drag, and D (m) is the shortest distance between the particle edge and the wall. Brenner, H [14] studied the effect of wall proximity on the Stokes' resistance of an arbitrary particle. Assuming that the particles travel midway between two walls, the value of 1.004 can be used for the coefficient of drag (k) in the equation.

After the above steps and calculations, four types of files are exported by *FlowDensi*: i) parameters, which includes the input criteria for particle sorting; ii) summary, which includes the data of the general properties of sorted particles (corresponding to the sorted trajectories), such as their velocity, density, area, diameter and so on; iii) plots, which depict the particle trajectory and some user-defined plots (an example is given in AppxE-Figure 2); iv) matrix, in which the information from the FlowCAM® database of the dots composing each sorted trajectory is included.

FlowDensi allows the user to export the data of the particle trajectories based on the number of dots composing the trajectory or the zone of the trajectory in the camera view. The former criterion avoids the output of redundant sorted particles with too short moving paths. The latter allows the user to

focus on the analysis of particles passing by a specific region of the flow cell. In this study, only the former criterion was used to control the export of the data of the sorted particles.

In this study, the *FlowDensi* was tested to process the FlowCAM® database of PS beads. Firstly, the parameters of primary sorting were tested to evaluate their effect on the sorting of particle trajectories. *Delta X* was set at 5, 10, 20, 30 and 40 μm respectively for different *Delta area* values. For the 30 μm PS beads, the *Delta area* (relative) was set at 0.025, 0.05, 0.075, 0.1 and 0.15 respectively; for the 50 μm and 70 μm beads, the *Delta area* (relative) was set at 0.01, 0.03, 0.05 and 0.1 respectively. For the spherical PS beads, the detected aspect ratio (AR) of the particles mostly lies in the range of 0.98-0.99 with little variance. Thus, the AR was not taken as a significant factor affecting the primary sorting, and a constant *Delta AR* of 0.1 (relative) was used in this work. In the case of irregular-shape particles, the effect of particle shape on the calculated particle density needs to be taken into account, and the AR value may play a role in that scenario [3, 15].

Each exported trajectory included at least 100 dots. The effective range of the camera view recording the position of the dots (*Eff X range* and *Eff Y range*) were set at 100-1200 μm and 100-1500 μm respectively, which cover most of the camera scope and exclude the border. Coarse refinement criteria were used during this primary sorting. The *Delta Y* was set at a broad range (from 0 to 10 μm), where the top limit is higher than the theoretical travelling distance of the particle per time interval (calculated by Stokes' law under the assumption that the particle density is 1050 kg/m^3). A high value of 100 was given to the *Delta SIN*. Although this is not the maximum value that can be set, this high *Delta SIN* allows for loose control on the consecutiveness of the image index (a maximum allowable gap of 100) for the dots composing the trajectory of one moving particle. An unconstrained *Edge gradient* (0-255, the full range) was used.

Followed by the primary sorting, the function of the refinement parameters (the *Delta SIN*, *Edge gradient* and *Delta Y*) are tested and discussed.

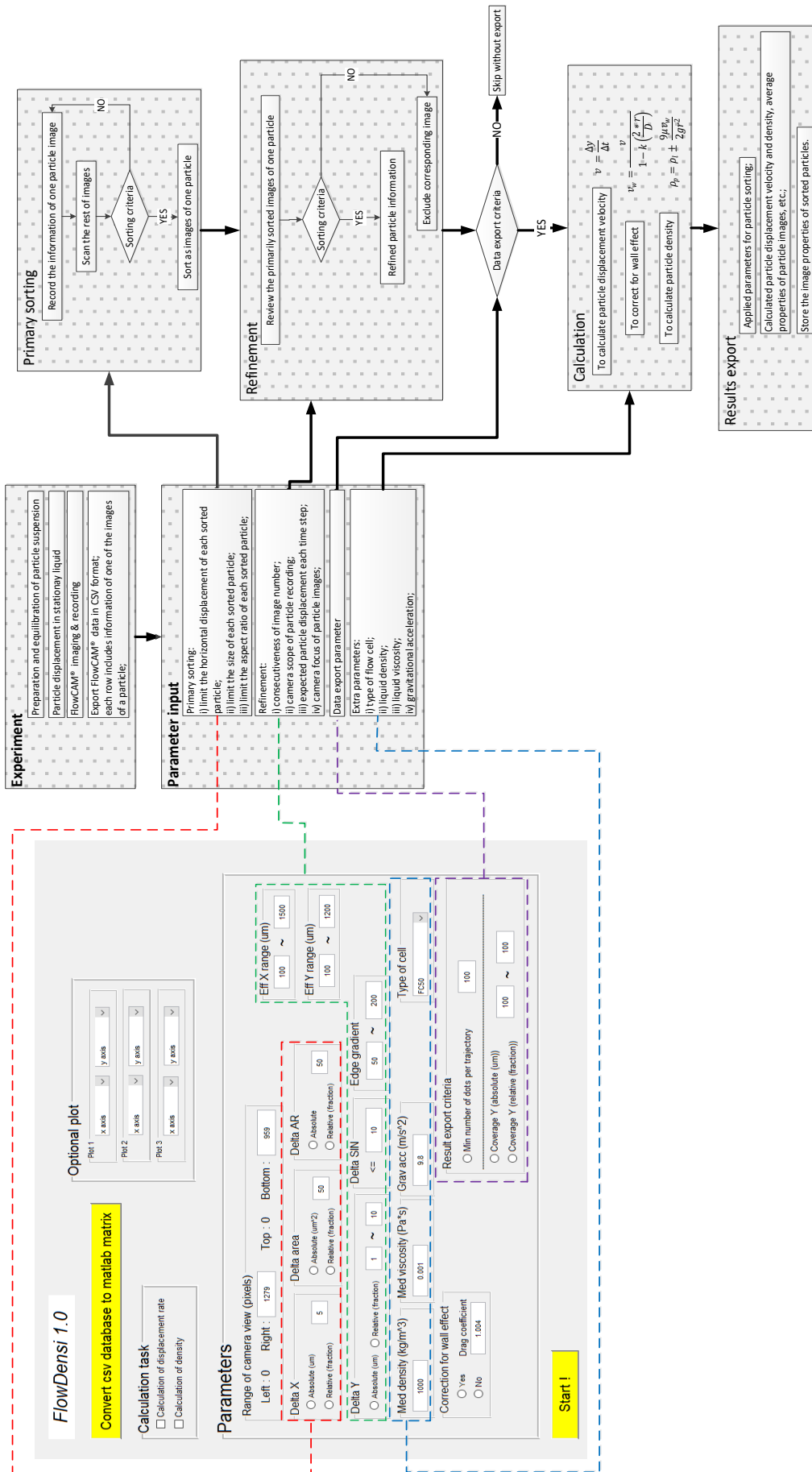


Figure 8.1. The flowchart of the *FlowDensi* algorithm and the graphical user interface (GUI). The magnified pictures of the GUI and the key sections of the flowchart are displayed in the appendix (see Appendix E, AppxE-Figure 1).

8.4 Results

8.4.1 Primary sorting

The effect of the applied parameters on the primary sorting of particle trajectories was evaluated by analysing the exported results of *FlowDensi*. Figure 8.2 shows the number of the sorted particles' trajectories and the calculated particle density (average value and standard deviation (SD)) at different values of the input *Delta X* and *Delta area* for the 30 μm , 50 μm and 70 μm PS beads, respectively. The values of the average density at different input parameters are similar. The SD and the number of sorted particles' trajectories are the key aspects to consider to evaluate the effectiveness of the *FlowDensi* for the sorting of particles' trajectories.

For the 30 μm PS beads, based on the sorted trajectories, the average densities of the particles were calculated to be about 1043.7 kg/m^3 with a relative SD of 2%. The calculated SD depended on *Delta X* and *Delta area*. When keeping the input *Delta X* of 5 μm , there is an SD of 12-18 kg/m^3 when inputting different *Delta area*, while at a *Delta X* of 40 μm , the deviation narrowed to 16-18 kg/m^3 . For the 50 μm PS beads, the calculated average density is about 1045.0 kg/m^3 , with an SD of only about 3-6 kg/m^3 at different *Delta X* and different *Delta area*. For the 70 μm PS beads, an average density of $1044.1 \pm 20.6 \text{ kg/m}^3$ was obtained. The value of SD increases with *Delta X*, except for the ones at the *Delta area* of 0.05 and 0.1 where there was a drop from the *Delta X* of 30 μm to 40 μm .

For the 30 μm PS beads, an increasing number of sorted trajectories was detected with *Delta X* from 5 to 20 μm , followed by a level-off or slight decrease at higher *Delta X*. There were more trajectories exported at the *Delta area* of 0.025 to 0.15, where slight differences occur, than that at 0.01. For the 50 μm PS beads, a similar trend was found for the number of particles at different *Delta X*. The number varies at different input *Delta area*. There is a smaller number of sorted trajectories at the *Delta area* of 0.01 than the others at the *Delta X* of 5 μm . At the *Delta X* of 40 μm , the number at the *Delta area* of 0.1 is less than the rest. For the 70 μm PS beads, there is a slight difference in the number of sorted trajectories at the *Delta area* of 0.01. However, at a higher *Delta area*, the number decreases from 70 to 40 with increasing *Delta X*. There are fewer particles exported at higher *Delta area* (higher than 0.03) than at 0.01 and the numbers at the higher *Delta area* are similar.

In addition to the primary sorting of the particles' trajectories, the subsequent refinement steps were performed to find out the correlation of the input refinement parameters to the calculated particle density based on the sorted trajectories.

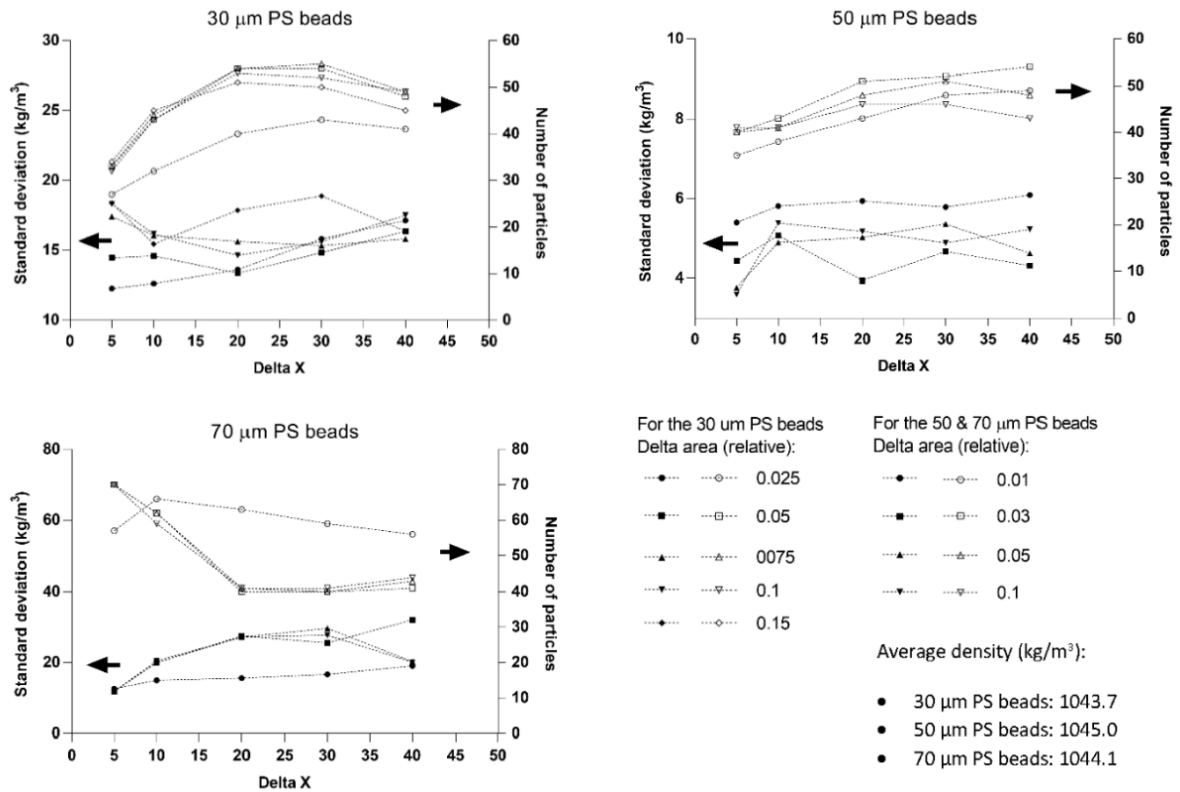


Figure 8.2. The particles' average density, and the number and standard deviation (SD) of the sorted particles (corresponding to the sorted trajectories) at different values of ΔX and Δ area exported after the primary sorting of 30 μm , 50 μm and 70 μm PS beads database. The solid markers represent the SD, and the blank markers represent the number of sorted particles. The dashed lines are used to guide the eye.

8.4.2 Refinement

8.4.2.1 Δ SIN

The refinement parameter of Δ SIN was implemented to limit the difference of source image number (SIN) between every two consecutive dots composing the trajectory of a settling particle. Each dot represents a particle in one picture of the flow cell taken by the camera, and for one moving particle the SIN of the dots is usually sequential. In the aforementioned primary sorting stage (section 8.4.1), the Δ SIN was set to 100. Under this condition, there was no strict limitation on the time continuity of the dots along the particle path, and the particles travelling in the flow cell at different time but with similar sizes and coordinates may be mistakenly assembled as one. To refine the results,

the *Delta SIN* was set at 1, indicating that the dots composing the sorted trajectory of one particle are successively recorded by FlowCAM®.

Figure 8.3 displays the results with the *Delta SIN* of 1. When compared with the results shown in Figure 8.2, there are only slight differences in the number of sorted trajectories and the calculated average density. However, the SD has decreased by about 40%, 25% and 20% to 10, 4 and 16 kg/m³ for the 30 μm, 50 μm and 70 μm PS beads, respectively. This decrease of the SD reveals that the particles' trajectories (y coordinates versus time) after refinement are more consistent and the values of the slopes are less varied.

The other two refinement parameters, *Edge gradient* and *Delta Y*, were also evaluated and are shown in the following sections, in which the values of 40 μm and 1 are used as the input parameters for the *Delta X* and *Delta SIN*, respectively. The values of 0.15 and 0.1 are used for the *Delta area* of the 30 μm PS beads and the 50 μm and 70 μm PS beads, respectively. These parameters were selected as they gave rise to relatively high SD of the calculated particle densities based on the sorted particle trajectories.

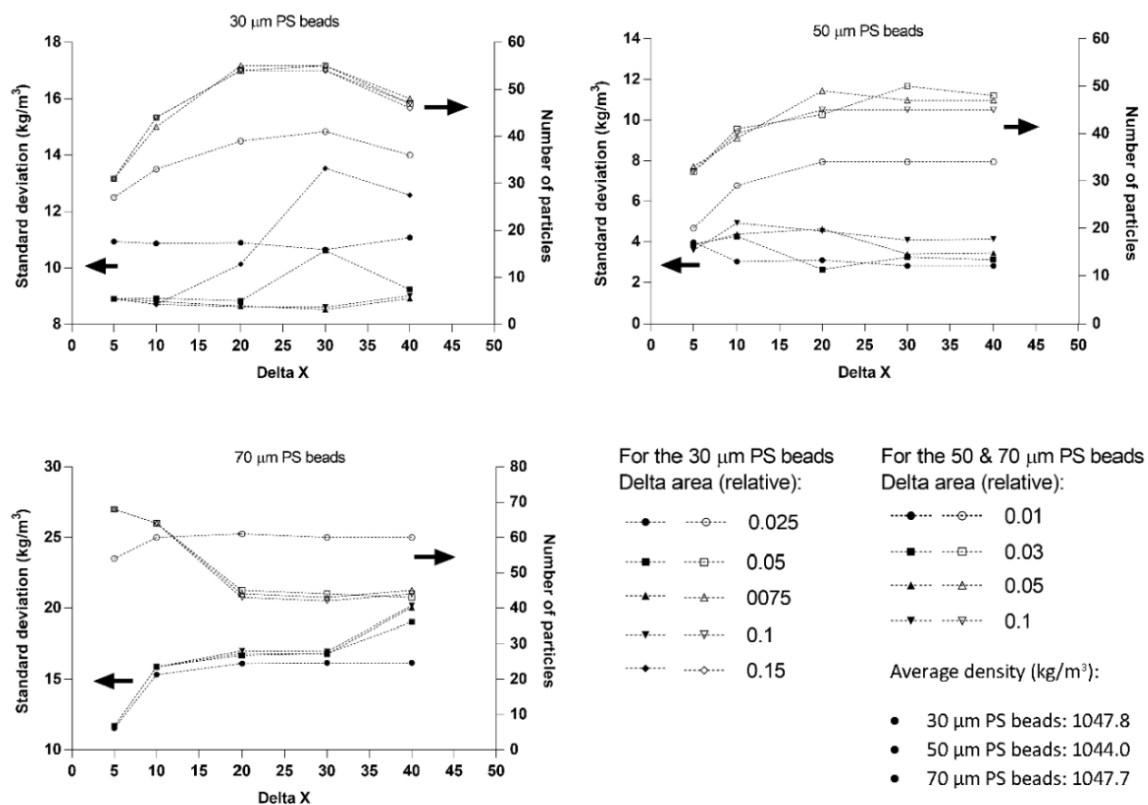


Figure 8.3. The average density, and the number and standard deviation (SD) of the sorted particles at different *Delta X* and *Delta area* of the 30 μm, 50 μm and 70 μm PS beads. The solid markers

represent the SD, and the blank markers represent the number of sorted particle trajectories. The dashed lines are used to guide the eye. The value of *Delta SIN* was 1.

8.4.2.2 Edge gradient

By implementing the parameter of *Edge gradient*, the dots composing the trajectory of one particle obtained from the primary sorting step can be differentiated by the focus of the microscope. The dots with the edge gradient out of the input range were excluded from the trajectory, and the remained ones are more likely affiliated to one moving particle. Figure 8.4 shows the average density, diameter and velocity of the sorted particles exported by *FlowDensi* as a function of edge gradient, which is presented with the intervals of 50.

For the 30 μm PS beads, the particle density increased with edge gradient, from 1033 kg/m^3 at a value of 50-100 to 1058 kg/m^3 at a value above 200. A similar trend was observed for the 70 μm PS beads, where an edge gradient higher than 150 resulted in a density of about 1097 kg/m^3 , which is larger than for the particles detected at a lower edge gradient ($\approx 1050 \text{ kg}/\text{m}^3$). However, regarding the 50 μm PS beads, only slight differences for the average density of the sorted particles were observed at different edge gradient ranges (less than 0.5 %).

In order to correlate the calculated particle density to the edge gradient, the sorted particles' diameter and velocity, which are the key parameters in the Stokes' equation to calculate the particle density, at different *edge gradient* are also included in Figure 8.4.

For the tested PS beads, the detected diameters decreased with increasing edge gradient. This correlates with a transition from blurred to sharp focus of the camera. For the 30 μm PS beads, a difference of about 13% was found between the diameter detected at the low and the high edge gradient range. For the range 100-150, the size of the particles was about $29.8 \pm 0.6 \mu\text{m}$, which is closer to the reference value of 30 μm than at other edge gradients. For the 50 μm PS beads, the size of the particles decreases by about 8% for an edge gradient higher than 200 compared to the ranges of 50 to 100. At the range of 100 to 150, the detected particle size of the PS beads was $50.5 \pm 0.8 \mu\text{m}$, which is the closest to the manufacturer's reference. For the 70 μm PS beads, the detected particle size decreased from 68 to 66 μm from the low to the high edge gradient, so slightly different from the manufacturer's reference value ($69.1 \pm 0.8 \mu\text{m}$). In this study, it is assumed that the value of the calculated particle density at the optimum camera focus is closest to the manufacturer's reference value. Therefore, when determining the density of a sample of microparticles, it is suggested to

calculate the particle density based on the sorted trajectories composed of dots captured by the microscope at the optimum focus.

According to Stokes' law (Equation 8.1), for a particle settling in a medium, the calculated particle density is proportional to the particle velocity and inversely proportional to the size of the particle. The experimental results, analysed by *FlowDensi*, is in accordance with this correlation (see Figure 8.4).

There is an additional parameter implemented in *FlowDensi* for particle sorting refinement. *Delta Y* differentiates the particles based on their vertical displacement per time step. By inputting the range of vertical displacement per time interval, the information of beads moving at different velocities can be distinguished. This is presented in the following section.

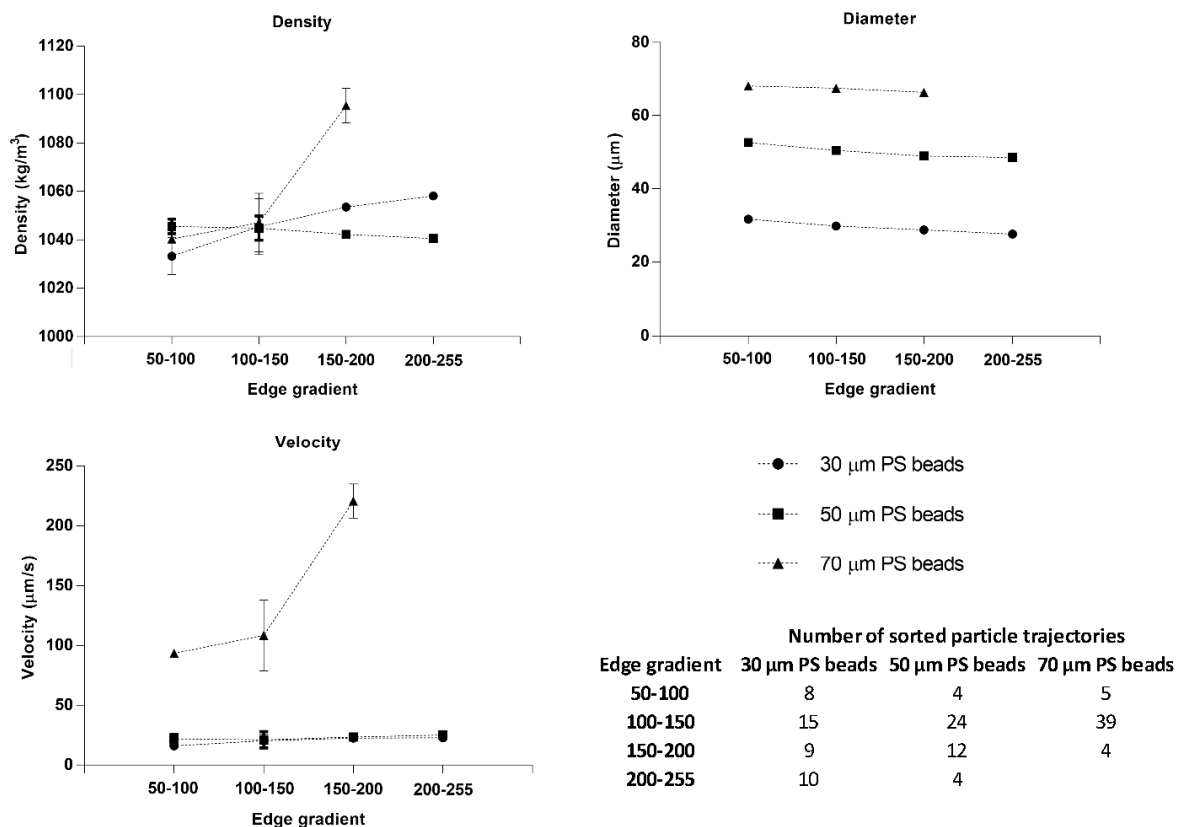


Figure 8.4. The average density, diameter and velocity of the sorted particles of the 30 µm, 50 µm and 70 µm PS beads exported by *FlowDensi* as a function of the *Edge gradient*. The number of the sorted particle trajectories is included. The dashed lines are used to guide the eye. The error bars represent the standard deviation of the corresponding value.

8.4.2.3 *Delta Y*

Figure 8.5 displays the average density based on the sorted trajectories of the particles as a function of the *Delta Y* and their corresponding diameter and edge gradient.

Under the condition of a fixed time step, the higher the particle velocity, the higher the value of *Delta Y*. For the 30 μm and 70 μm PS beads, the calculated particle density increased with the value of *Delta Y*. As to the 50 μm PS beads, a slight decrease in density was observed with *Delta Y* due to flotation as the density of the medium was higher than that of the particle. Theoretically speaking, if assuming the density of PS beads is 1050 kg/m^3 , the 30 μm , 50 μm and 70 μm PS beads respectively should have a vertical displacement distance of about 5.7 μm , 2.5 μm , and 2.4 μm per 0.25 s, 0.3 s and 0.05 s respectively, with the correction of wall effect for 50 μm and 70 μm PS beads. However, the results show that not all particles followed the theoretical displacement per time interval. The diameter of the sorted particles and their edge gradient value, which are also included in Figure 8.5, are inversely correlated, where the smaller the particle size, the higher the edge gradient. This fits the earlier observation that FlowCAM[®] tends to underestimate the particle size in sharp images and vice versa. The change of the value of edge gradient reflects the change of the focal distance of the detected particles and the wall-normal positions of the particles when moving in the flow cell. The correlation of the particle diameter and edge gradient to the particle velocity (*Delta Y*) reflects the effect of the particles' wall-normal shift on their displacement velocity and thus the calculated particle density. This effect may be due to the frictions between the wall of the flow cell and the particles. However, here the number of sorted trajectories at a specific *Delta Y* is not enough to give sound statistical support on this effect.

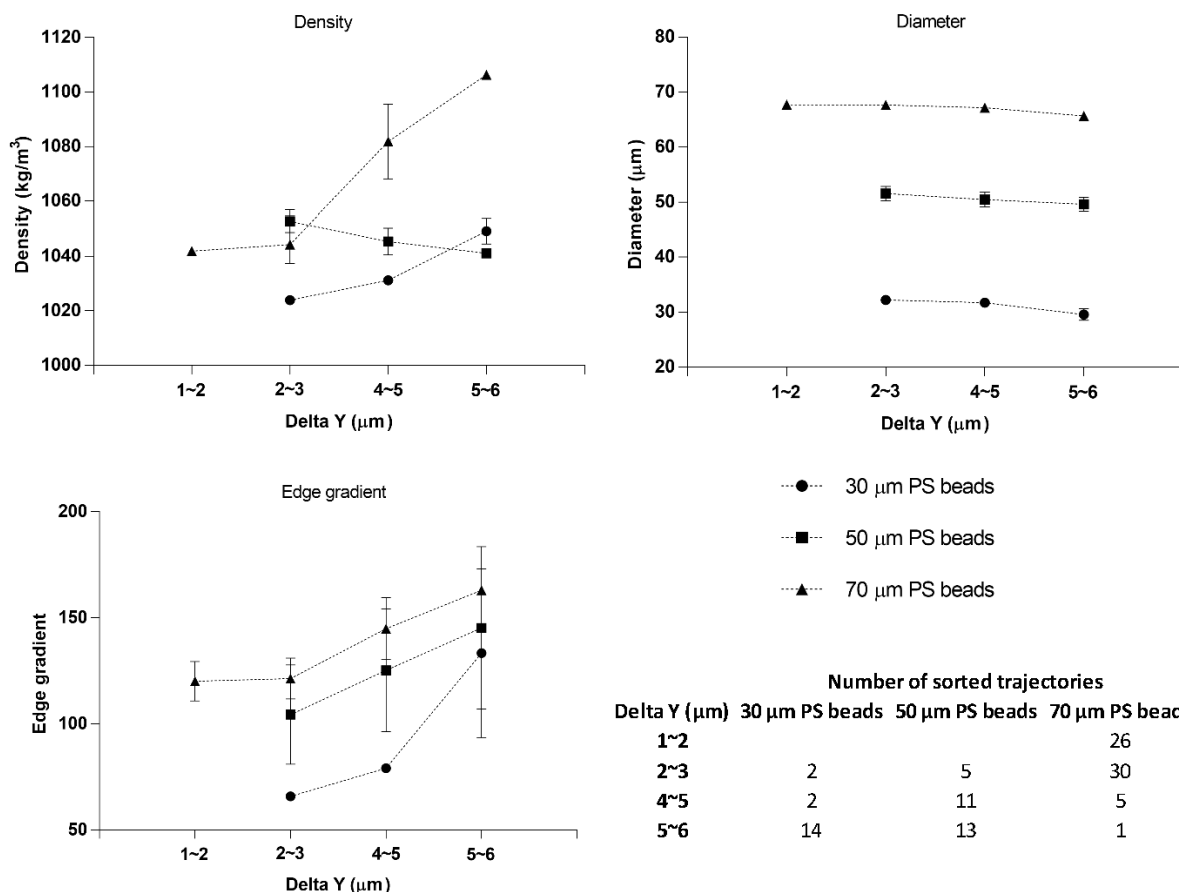


Figure 8.5. The average density, diameter and edge gradient of the sorted particles of the 30 µm, 50 µm and 70 µm PS beads exported by *FlowDensi* as a function of the *Delta Y*. The number of the sorted particle trajectories is also included. The dashed lines are used to guide the eye. The error bars represent the standard deviation of the corresponding value.

8.5 Discussion

This chapter describes a toolkit (*FlowDensi*) developed for the calculation of particle density based on the FlowCAM® data of recording the particle displacement in a stationary medium. The sorting of particle trajectories by *FlowDensi* was based on several parameters. The functions and limitations of these parameters are discussed. Some recommendations are included for later updates of the toolkit.

8.5.1 The parameters to sort particles' trajectories

During measurement of particle displacement in a stationary liquid phase, the flow cell, in which the particles displace, is tightly closed and placed vertically in front of the video microscope. There is no friction from the mobile liquid phase, and the particle displacement is driven by gravity or buoyancy.

This ensures that the particle paths are vertically aligned when they pass by the camera's view scope, and the horizontal positions (x-coordinates) should change very slightly in theory. However, there are several reasons that can lead to a shift of the horizontal position of the displacing particle, such as i) hydrodynamic interactions that arise due to neighbouring particles perturbing the velocity of the liquid at the location of the measured particle; ii) obstruction or distortion of some stuck particle or dust in the flow cell; and iii) distortion due to any unevenness of the surface of particle or the inner surface of the flow cell.

The setting of the parameter, *Delta X*, restricts the horizontal spread of the sorted dots along the particle trajectory, which influences both the number of the sorted trajectories and the calculated particle density (see Figure 8.2). During the primary sorting, a low value of *Delta X* may result in the division of a particle path into several ones. When the number of dots per path is lower than the export limit (100 in this work), these paths are not included in the final results. When using a high *Delta X*, several particles' paths, which are closely located in terms of horizontal position, may be mistakenly consolidated. This can lead to either an increase in the number of exported trajectories (more paths meet the export limit) or a decrease when multiple trajectories are exported as one. The above situations affect the calculation of the average and the standard deviation of the particle density statistically. An example of this scenario of the latter case is shown in the appendix (see Appendix E, AppxE-Figure 3). In this example, even though the dots of the particles share similar coordinates and consolidated by *FlowDensi* for the trajectory of one particle, they belong to different particles' paths passing the flow cell at different time. The primary sorting alone is not enough to distinguish one path from the rest. To help the users check the results, the exported files of *FlowDensi* include the correlation coefficients representing the linearity of the particle trajectory as a function of time.

The mistaken consolidation of particle paths at different time can be alleviated by setting a low value for the *Delta SIN (source image number)*. This is revealed by the obvious lower standard deviation of the density in Figure 8.3 than in Figure 8.2. However, this problem cannot be completely avoided due to the mistaken labelling or sequencing of dots. In some cases agglomerated or overlapping particles may be labelled as one big dot, or a stuck particle may shield part of the camera view during calibration. Such problems can be avoided during the experiment by reducing the particle concentration in the medium and identifying 'blind' regions for each measurement.

The parameter of the edge gradient is essential for the particle density calculation. All pixels within the edge border contribute to the projected area of the particle in the image and thus the diameter of the particle (area-based diameter (ABD)). This area-based diameter (ABD) is used as one of the variables by *FlowDensi* in the Stokes' law formula. Thus, the selected edge gradient range, i.e., the

focus of the particles, influences the sizing of the displacing particles, and as a result the calculated particle density. The extent of this influence depends on the size of the particle and it is assumed that the smaller the particle, the more influence of the blurring on the size determination. In addition, the focal plane in the flow cell is ideally positioned in the middle of the depth of field of view, where particles in focus are assumed to be furthest from the front and rear wall of the flow cell, and hence experience the lowest resistance effects. Based on Stokes' law, the calculated particle density at different edge gradient ranges is not only affected by the particle size, which depends on the camera focus, but also by the displacement velocity. The results of *FlowDensi* suggest the edge gradient of 100-150 as the optimal range for the detection of 30 μm and 50 μm PS beads as the particle diameter observed with this range is the closest to the reference value. For the 70 μm PS beads in this study, the detected diameter deviates slightly in and out of the edge gradient range of 100-150, and are comparable to the reference value. The findings in this study are also supported by the proposal in the previous literature [3] that an edge gradient range from 100 to 200 indicates an optimal camera focus of particles.

The parameter of *Delta Y* is used to differentiate the particles based on their vertical displacement per time step. By inputting the expected range of vertical distance per time step, the trajectories of particles moving at different velocities can be separated. The analyses in this study are based on the results of experiments carried out with diluted samples. When dealing with concentrated samples, there is a higher probability of particles close to each other with similar optical properties. By setting a proper *Delta Y*, these particles may be distinguished as their velocities differ due to factors such as the density, size, and proximity to the wall of the flow cell.

In this study, a drag coefficient value of 1.004 was used for the correction of the wall effect, by assuming an ideal situation where the particle is positioned midway between the two parallel walls (the front & back walls of the flow cell). However, not all particles follow this ideal path and the effect of wall proximity on the Stokes' resistance of the particle may differ. Researchers in a previous study [3] provided a solution to this phenomenon by selecting particles within the focus of the camera (limiting the edge gradient from 100 to 200) and neglecting the particles at other focal distances. However, the out-of-focus particles may contain specific physical properties (e.g. specific affinity to cell wall material) and optical information (e.g., distinctive refractive index) that may be useful to understand their compositions and surface characteristics. Moreover, the drag coefficient is limited to only spherical particles. It is therefore desirable to have analogous wall-effect corrections for non-spherical particles to achieve more practical significance of the calculation, as the particles encountered in practice are rarely of ideal spherical shape [14].

It is worthwhile noting that different sorting criteria give rise to a different number of output particles, which can affect the statistics of the results. All the statistical analyses above are based on the results obtained in this study. These analyses can be further validated in future investigations with larger datasets.

8.5.2 Recommendations for *FlowDensi* updates or other relevant toolkits

This study releases the first version of *FlowDensi* (version 1.0), which allows for the post-processing of the FlowCAM® database. Although the current toolkit can meet most needs for the particle density analysis, some recommendations to improve this toolkit for more convenient and concrete daily routine use and extended applications are made:

1. Include a function for the pre-assumption of particle velocity and provide suggestions on parameters such as the *Delta Y*. Although it is not easy for the user to give a presumable density of the particles, *FlowDensi* can make a prediction by including a list of common materials for the user to choose from and requesting the expected size range of the particles from the user.
2. Include a time scope parameter in the primary sorting step, to distinguish the particles displacing at different periods through the flow cell. This can help avoid the inclusion of several particles with similar coordinates and graphical properties but moving at different time.
3. Include a shape factor to make correction on particle velocity. No shape correction factor was included in the current study as uniform spherical PS beads were used for the experiment. For non-spherical particles, a correction of the shape effect on particle displacement is needed.
4. Include an input of the onsite magnitude, latitude and altitude where the FlowCAM® experiments are performed. This is for a more accurate calculation of the value of gravitational acceleration, which is a function of the three parameters. This enables a more accurate calculation of the tested microparticle density.

FlowDensi was developed to calculate the density of moving particles recorded by FlowCAM®. Knowledge of the particle density can be further utilised to calculate other particle properties such as porosity or void fraction of the particle, which are critical parameters for drug delivery systems, and in particular, the release kinetics of encapsulated drugs. A pioneering study has been performed by A.S. Sediq [3] to correlate the microparticle density with the porosity. The density of each component of a microparticle contributes proportionally to the total microparticle density and can therefore be used to calculate the porosity of a microparticle, which can be obtained based on the knowledge of the particle density in the presence and absence of loaded material. This correlation can be

implemented in the next version of *FlowDensi* or any derivative toolkit focusing on the porosity calculation.

8.6 Conclusions

Flow imaging microscopy can be widely applied for microparticle characterisation, for example, particle density determination. The proposed *FlowDensi* toolkit offers a user-friendly operation window and assists in the analysis of the FlowCAM® database. Useful information about the trajectories of particles can be quickly sorted, and the density can be calculated accordingly. All sorted particle information was comparable to those sorted manually in research elsewhere, and was exported into excel files for users' convenient check and analysis. The *FlowDensi* toolkit, as well as its derived versions, can be packaged into a platform and serve as a complementary tool for the post-analysis of experimental data obtained by FlowCAM®.

Acknowledgement

Support was given by Stephan K. Waasdorp for performing the FlowCAM® experiments and sharing the experimental data.

References

1. Hines, D.J. and D.L. Kaplan, Poly (lactic-co-glycolic) acid- controlled-release systems: experimental and modelling insights. *Critical Reviews™ in Therapeutic Drug Carrier Systems*, 2013. **30**(3).
2. Makadia, H.K. and S.J. Siegel, Poly lactic-co-glycolic acid (PLGA) as biodegradable controlled drug delivery carrier. *Polymers*, 2011. **3**(3): p. 1377-1397.
3. Sediq, A., S. Waasdorp, M. Nejadnik, M. van Beers, J. Meulenaar, R. Verrijck, and W. Jiskoot, Determination of the porosity of PLGA microparticles by tracking their sedimentation velocity using a flow imaging microscope (FlowCAM). *Pharmaceutical research*, 2017. **34**(5): p. 1104-1114.
4. Sediq, A.S., S.K. Waasdorp, M.R. Nejadnik, M.M. van Beers, J. Meulenaar, R. Verrijck, and W. Jiskoot, A Flow Imaging Microscopy-Based Method Using Mass-to-Volume Ratio to Derive the

- Porosity of PLGA Microparticles. *Journal of pharmaceutical sciences*, 2017. **106**(11): p. 3378-3384.
5. Kawashima, Y., T. Niwa, H. Takeuchi, T. Hino, and Y. Itoh, Hollow microspheres for use as a floating controlled drug delivery system in the stomach. *Journal of pharmaceutical sciences*, 1992. **81**(2): p. 135-140.
 6. Rosca, I.D., F. Watari, and M. Uo, Microparticle formation and its mechanism in single and double emulsion solvent evaporation. *Journal of Controlled Release*, 2004. **99**(2): p. 271-280.
 7. Canada, D.C. and W. Laing, Use of a density gradient column to measure the density of microspheres. *Analytical Chemistry*, 1967. **39**(6): p. 691-692.
 8. Giddings, J.C. and M.H. Moon, Measurement of particle density, porosity, and size distributions by sedimentation/steric field-flow fractionation: application to chromatographic supports. *Analytical Chemistry*, 1991. **63**(24): p. 2869-2877.
 9. Batchelor, G.K., *An Introduction to Fluid Dynamics*. 1973: Cambridge University Press.
 10. Bach, L.T., U. Riebesell, S. Sett, S. Febiri, P. Rzepka, and K.G. Schulz, An approach for particle sinking velocity measurements in the 3–400 μm size range and considerations on the effect of temperature on sinking rates. *Marine biology*, 2012. **159**(8): p. 1853-1864.
 11. Happel, J. and H. Brenner, *Low Reynolds number hydrodynamics: with special applications to particulate media*. Vol. 1. 2012: Springer Science & Business Media.
 12. Uhlherr, P. and R. Chhabra, Wall effect for the fall of spheres in cylindrical tubes at high Reynolds number. *The Canadian Journal of Chemical Engineering*, 1995. **73**(6): p. 918-923.
 13. Ristow, G.H., Wall correction factor for sinking cylinders in fluids. *Physical review E*, 1997. **55**(3): p. 2808.
 14. Brenner, H., Effect of finite boundaries on the Stokes resistance of an arbitrary particle. *Journal of Fluid Mechanics*, 1962. **12**(1): p. 35-48.
 15. Deo, S. and S. Datta, Stokes flow past a fluid prolate spheroid. *Indian Journal of Pure and Applied Mathematics*, 2003. **34**(5): p. 755-764.

Chapter 9

Conclusions and outlook

9.1 The main findings and strategies of this thesis

This study steps towards the goal of developing a controlled drug delivery system (DDS) for protein therapeutics. The strategic path of this research project is shown in Figure 1.2 in Chapter 1.

As an alternative to the conventional encapsulation methods using non-polar coating materials and organic solvents, in this study, a hydrophilic polyelectrolyte (dextran sulphate sodium (DSS)) was used for coating, and the encapsulation and product particle formation were performed in a supercritical carbon dioxide (scCO₂) environment. A scCO₂ spray coating process was developed, in which the encapsulation was achieved via the contact of solid protein (lysozyme) particles with the atomised polymer-containing tiny droplets. Dry encapsulated particles were collected after the water removal by scCO₂. A retarded protein release from the coated protein particles was observed. The humidity level in the spray coating vessel was one of the critical factors affecting the encapsulation.

Concerning the interaction among the macromolecules, investigations on the molecular level were performed via molecular modelling, in which the molecular behaviours are visualizable, and the steric and electrostatic interactions are quantifiable. The molecular structure of the DSS in an aqueous environment was resolved via molecular mechanics methods, and a helix structure was established. In the helix, each polymerisation unit contains two sulphate groups with the sodium positioned in-between as an ionic bridge. Next, the research headed for an elucidation of the complexation between the protein (lysozyme) and polyelectrolyte (DSS) in terms of the interaction thermodynamics and the geometries of the complexes using molecular mechanics and quantum mechanics methods. The calculated reaction energies of the exchange of ions represent conditions close to equilibrium. The interaction between DSS (monomeric unit) and amino acids was found to be exothermic and spontaneous. The backbone structures of lysozyme and DSS remained after their interaction, with adjustments of the molecular conformation to lower the steric potential for the energy minimisation of the system. Although the molecular dynamics (MD) simulation is beyond the scope of this thesis, it will be useful to apply this method to simulate the natural motion of the macromolecules and determine the macroscopic thermodynamic properties of the system.

Along with the microscopic view on the molecular interactions, Brownian dynamics simulations of protein-polyelectrolyte particle formation and growth, based on Smoluchowski's theory, were developed and performed to gain insight into the collisions and stickiness among the particles. The evolutions of the particle size distribution were calculated. The average ratio of the protein to polyelectrolyte in the formed complexes was found to be in accordance with their initial ratio in the system. The simulated evolutions of particle concentration were found to be comparable with experimental results. Moreover, this thesis proposes a direct collision simulation to describe the

protein-polyelectrolyte agglomeration based on tracking the particle displacement, and an idea to simulate the agglomeration based on calculating the inter-particle collision probability.

The diffusivity of proteins and polyelectrolytes in an aqueous environment is a crucial parameter affecting their complexation and the release of proteins from the developed DDS. A microfluidic H-cell was investigated to determine the diffusion coefficients of the macromolecules. It was found that the diffusion coefficients of proteins depend not only on the size of the molecules but also on the inter-molecular interactions, which are influenced by the pH and ionic strength. These factors were also found to exert similar effect on the diffusion of polyelectrolytes. Regarding the complicated structures of the polyelectrolytes and their interactions, it remains a challenge to make appropriate estimation on their diffusion coefficients, and there is a scarcity of relevant literature information to compare with the H-cell results. Further investigations are needed to improve the microfluidics method, such as using more sensitive detection methods and lowering the viscosity difference of the streams into the H-cell, to determine the diffusion coefficients of the long-chain polyelectrolytes, the solutions of which are highly viscous

Flow-imaging microscopy technique is a powerful and promising tool to determine the properties of the DDS microparticles. To provide assistance and enhance the efficiency for the data analysis, a supplementary toolkit, the *FlowDensi*, was developed to calculate the density of the detected particles based on their trajectories in a stationary liquid in a micro flow cell. The application of this toolkit is extendable by preparing it for the routine daily analysis of other microparticle properties (e.g. porosity) derived from the measurements of the flow-imaging microscopy.

9.2 Research topics for future investigations

The work described in this thesis has led to some accomplishments such as i) the development of a novel scCO₂ process for the preparation of protein DDS; ii) the interpretation of the protein and polyelectrolyte interaction mechanism; iii) the understanding of the dynamics of the particle formation and growth; and iv) the application of a microfluidic method to determine the diffusion behaviour of protein and polyelectrolyte. These accomplishments also open the door for some future research topics.

9.2.1 Optimisation of the scCO₂ spray coating process

The early-stage research provides information on the critical parameters for the optimisation of the scCO₂ spray coating process to achieve complete encapsulation of the core protein particles and to achieve homogeneous micron-sized product particles.

Firstly, more attention needs to be paid on the control of the size of the sprayed droplets. The size of the sprayed droplets affects their contact pattern with the core microparticles, the humidity level in the spray coating vessel and the agglomeration state of the product particles. The control of the droplet size requires not only a proper type of nozzle for the atomization but also a proper liquid to scCO₂ mass ratio. Secondly, the appropriate ratio of the size of the core particles to the droplets calls for further investigation. The proper size of the core particles relative to the sprayed droplets leads to thorough and homogeneous contact between the particles and the droplets, and can also help prevent the agglomeration of the particles. Thirdly, the contacting time of the particles and the sprayed droplets needs adjustment for the complete mixing and coating. After optimising these factors to coat the protein core particles with one polyelectrolyte layer, this spray coating process can be extended for layer-by-layer encapsulation with the implementation of both positively and negatively charged polymers that are alternately-aligned in the final product.

An idea on the lab-scale equipment with a half-litre vessel for an optimal spray coating is put forward in accordance with the aforementioned propositions. The piping and instrumentation diagram (P&ID) is shown in Figure 9.1. In this equipment, a coaxial nozzle is implemented into the top lid of the vessel for the efficient atomisation of the polyelectrolyte solution into the vessel. A powerful agitation engine is implemented at the bottom of the vessel for the homogeneous suspension of the core particles. As an advancement of this spray coating equipment, three transparent high-pressure sapphire windows are embedded into the wall of the vessel. This is advantageous over opaque standard steel vessel in which the liquid spraying and droplet-particle contact are enclosed and non-observable. The

installation of transparent windows allows the user to perceive the spray coating process in a direct way. With the help of high-speed imaging techniques, liquid atomisation and droplet-particle contact can be easily captured to provide first-hand information on the mechanism of the coating process. A preliminary conceptual design of this new spray coating equipment is displayed in Figure 9.2.

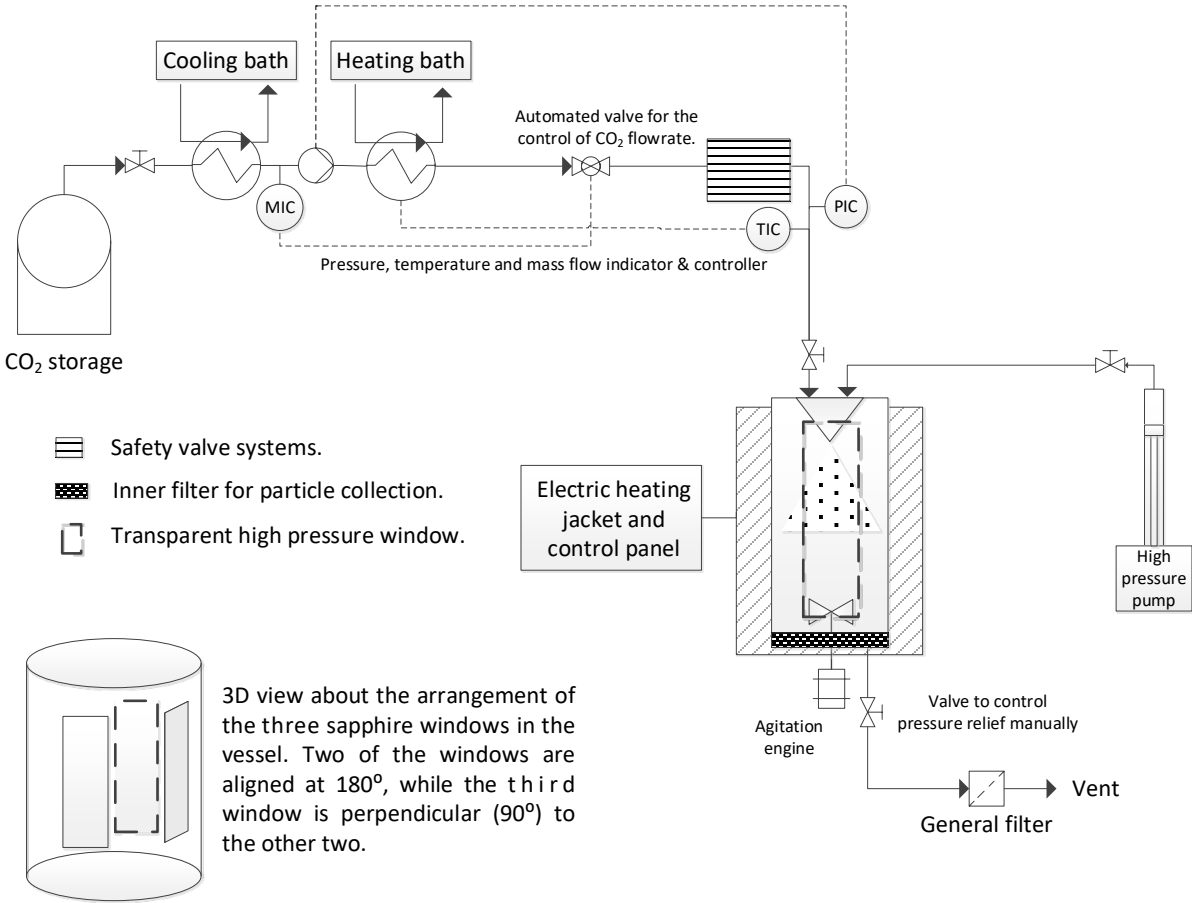


Figure 9.1. P&ID diagram of the lab-scale equipment planned for an optimal spray coating. The spray coating vessel is installed with transparent windows.

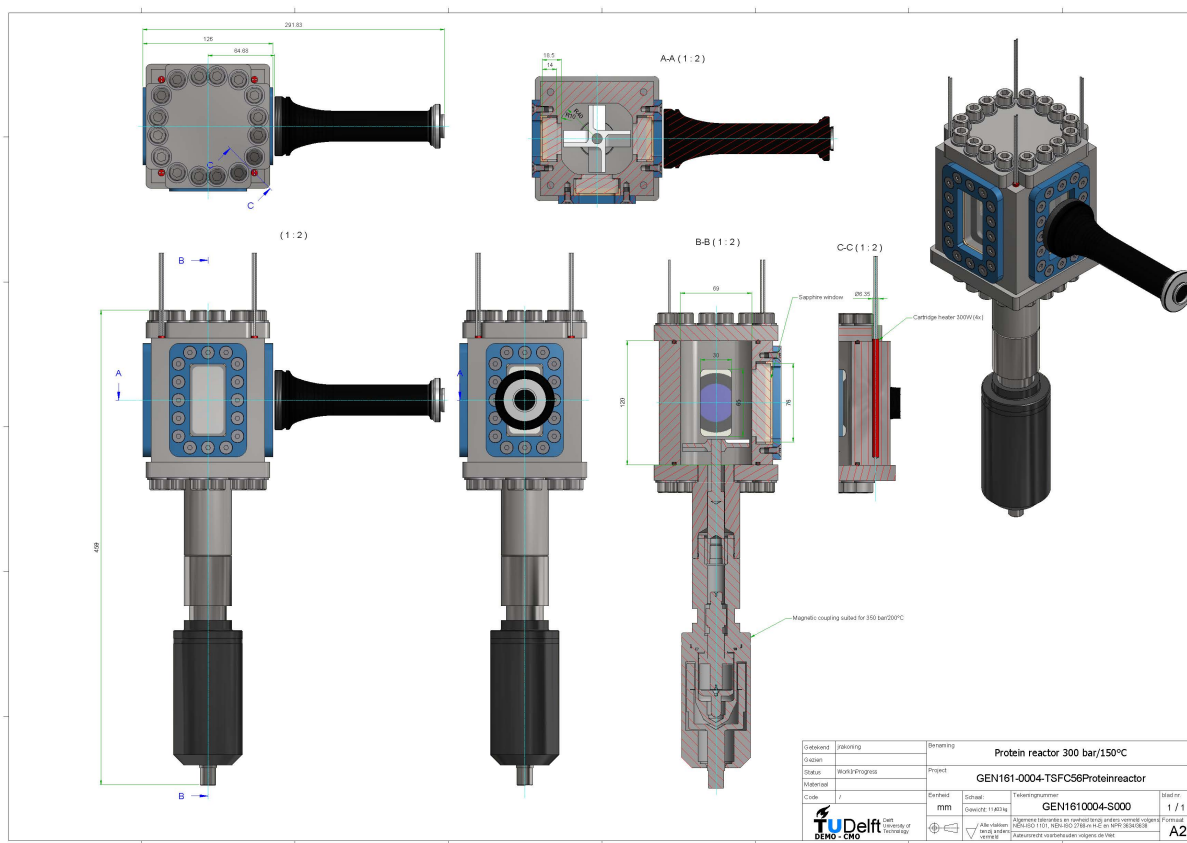


Figure 9.2. Conceptual design of the lab-scale spray coating vessel with transparent windows installed (designed by Jeroen Koning from Electronic and Mechanical Support Division, Delft University of Technology). A high-speed camera with special lens will be used for the observation of micron-sized particles or droplets.

9.2.2 Scale-up of the scCO_2 spray coating process

Once the optimal operating conditions for the lab-scale spray coating process are established, the extension of the process from lab scale to (semi)industrial scale can be the next topic to be investigated.

One of the aspects to be considered when scaling up a scCO_2 spray coating process is the delivery of the liquid containing the coating materials. The product size is in correlation with the sprayed droplet size, which is dependent on the design of the spray nozzle. The sprayed droplet size, the relativity to the core particle size and the uniformity in the size distribution need to be taken into account to achieve the overall and homogeneous coating of the core particles. If the sprayed droplet size is too big, there is a tendency of the product particles to coalesce into agglomerates. This regime is considered to be undesirable, as it adversely affects the protein particle coating, product particle drying, and particle size distribution in the final product. These factors can be adjusted by appropriately

configuring the liquid and scCO₂ flow rate into the nozzle, the mass ratio of liquid to scCO₂, and the size of the nozzle holes (the path of the liquid and the scCO₂). In large machines, multiple nozzles (or multi-headed nozzles) may be used to spread the liquid over as many of the suspended particles as possible. Moreover, the nozzle height and spray cone angles also need to be considered for the scale-up. These two factors affect the contacting region of the droplets and the suspended particles in the vessel. To enhance the coating efficiency, it is desired to disperse the liquid over an as large fraction of the suspended particles as possible.

Another factor to be considered is the drying power of the upscaled equipment. The removal of water from the spray coating vessel depends on the delivery of fresh CO₂ into the vessel. When the water addition is excessive, the agglomeration of particles is likely to occur due to their affinity to moisture, compromising the homogeneous size distribution of the particles. It is favourable if the liquid delivery rate and the drying capacity are compatible to avoid the accumulation of moisture in the vessel.

The design of the impeller for the off-bottom suspension of a larger batch of protein particles is also a crucial factor. The particles, either in a wet or dry state, require a shear force to break the cohesive bonds among the particles and allow all the particles to be fully suspended in the spray coating vessel. The propeller type and dimension, and the geometrical arrangement of the propeller relative to the vessel impact the mixing of the particles and the required power consumption.

9.2.3 Molecular dynamics simulation of protein-polyelectrolyte interaction

Static molecular mechanics and quantum mechanics simulations can provide information on the optimised molecular morphology, molecular strain energy, and thermodynamic potential changes during reactions. The difference in the thermodynamic properties of the protein-polyelectrolyte system calculated via static and dynamic simulations remains a question to be figured out. The proper selection of force field, the calculation of the electrostatic potentials with solvating effects, and the calculation of the diffusion tensor of the molecules and complexes are among the topics to be investigated.

9.2.4 Using a microfluidic device to determine the diffusivity of the product DDS particles

The diffusion coefficient of the product DDS particles (in this thesis the encapsulated protein particles) provides information on the particle properties such as particle size, thickness of the encapsulation layers, inter-particle interaction (attractive or repulsive), tendency of particle agglomeration, particle degradation kinetics, porosity and loading of proteins in the encapsulated particles. The developed H-cell microfluidics system is likely suitable to determine the diffusion coefficient of the DDS

microparticles, in which various detection techniques are applicable to detect the particle concentration.

9.3 Potential of the results of this project for practical applications

This study brings forward a scCO₂ spray coating process to encapsulate solid protein particles for the development of DDS. Instead of conventional non-polar polymers, biocompatible hydrophilic polyelectrolyte is applied as the coating material for the hydrophilic amphoteric protein. This idea is of practical significance in the food and pharmaceutical industries, in which protein encapsulation (with sugar as the stabilising excipient) is one major approach for protein storage, maintenance and retarded release, which are common aspects to be considered for protein product development. The present study also provides an idea of the preliminary design of the scCO₂ spray coating equipment as well as a discussion on the key factors affecting the coating of the core particles. This contributes to the later optimisation of the high-pressure spray coating process.

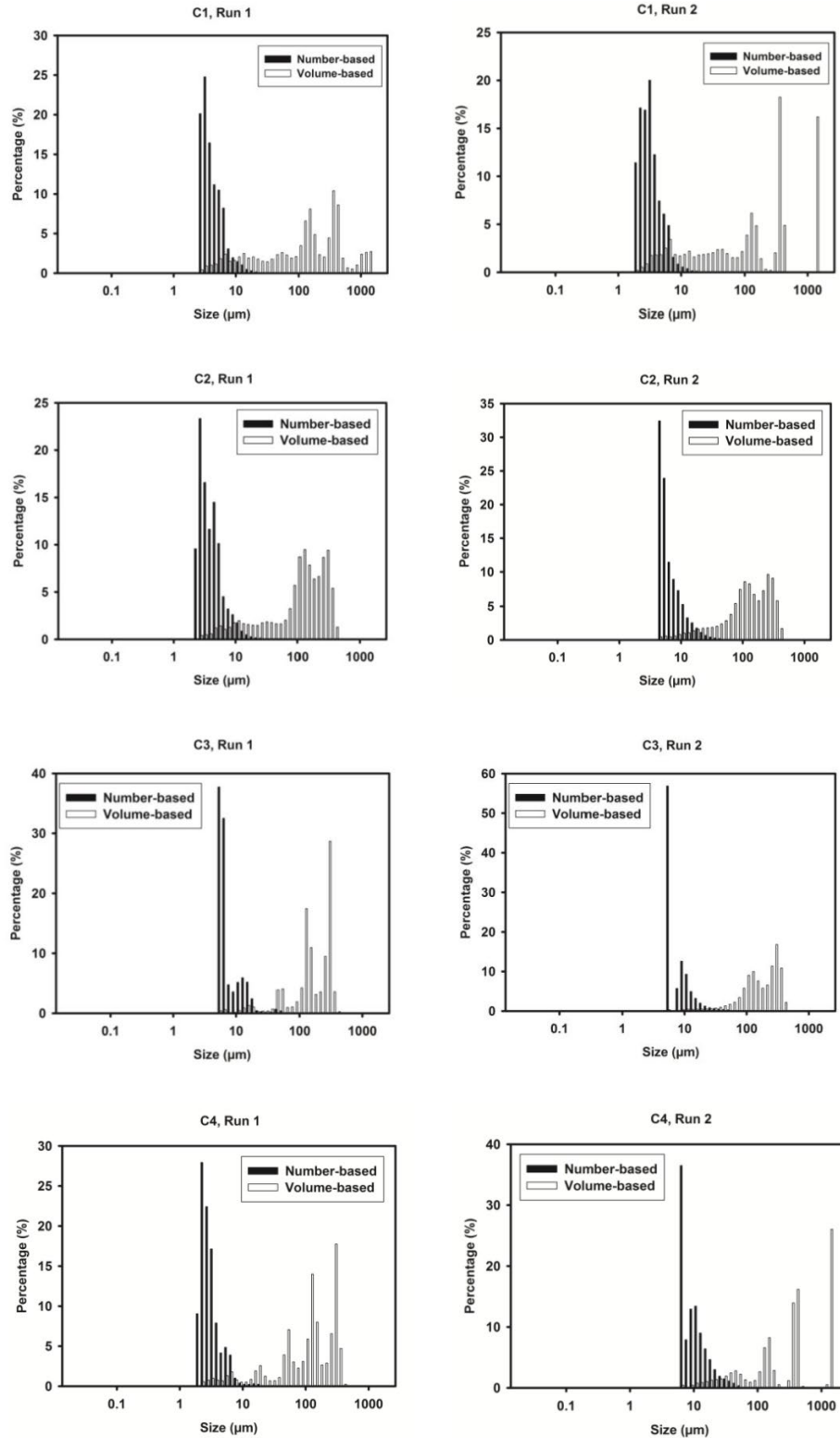
The method to establish the DSS molecular structure via molecular modelling provides guidance for elucidating polymer structures accordingly in the case of lacking experimental information. The finding of the helix structure of DSS contributes to the protein product design when the polymer properties (such as charge distribution) and behaviours (such as conformational change) are essential factors to be considered. The Brownian dynamics simulation can be applied to predict the evolution of particle concentration and size distribution in the process starting with various interactive materials.

The microfluidic H-cell described in this study has the potential to be developed into a commercialised instrument for accurate, convenient, versatile (with respect to detectors) and high-throughput determination of macromolecular diffusive properties. The H-cell is also applicable for the purpose of separation or as micro-scale reactors.

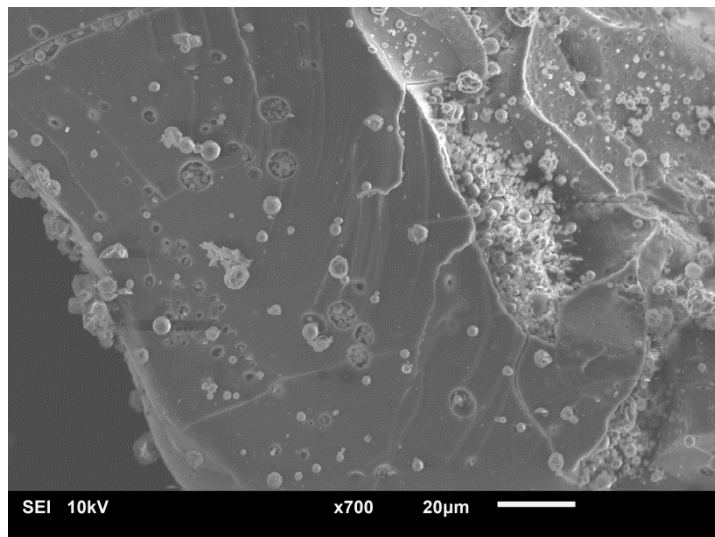
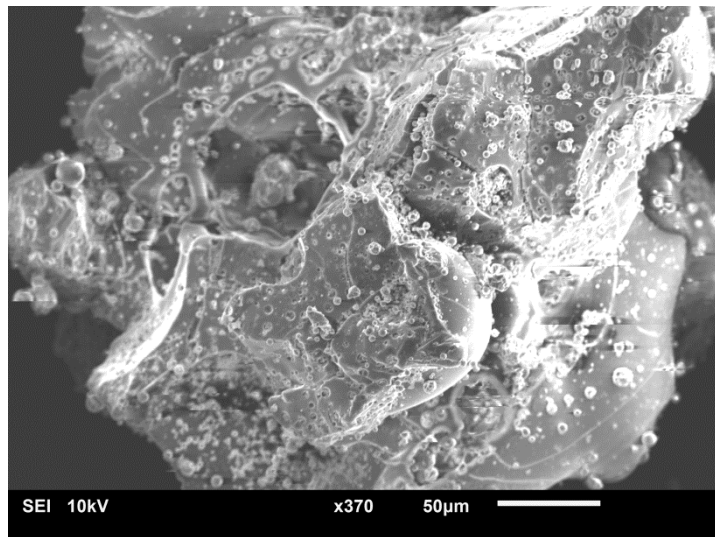
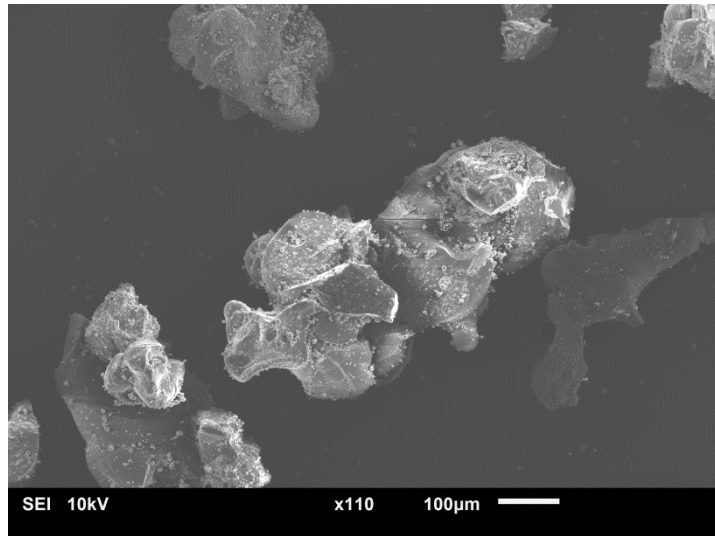
Another potential of this thesis work for practical application is to develop the *FlowDensi* toolkit into a supplementary software for the convenient and efficient analysis of the data of FlowCAM® (commercial equipment of flow imaging microscopy) for the determination of microparticle density, based on which some other particle properties such as the porosity can be derived (also using the same toolkit).

Appendix A

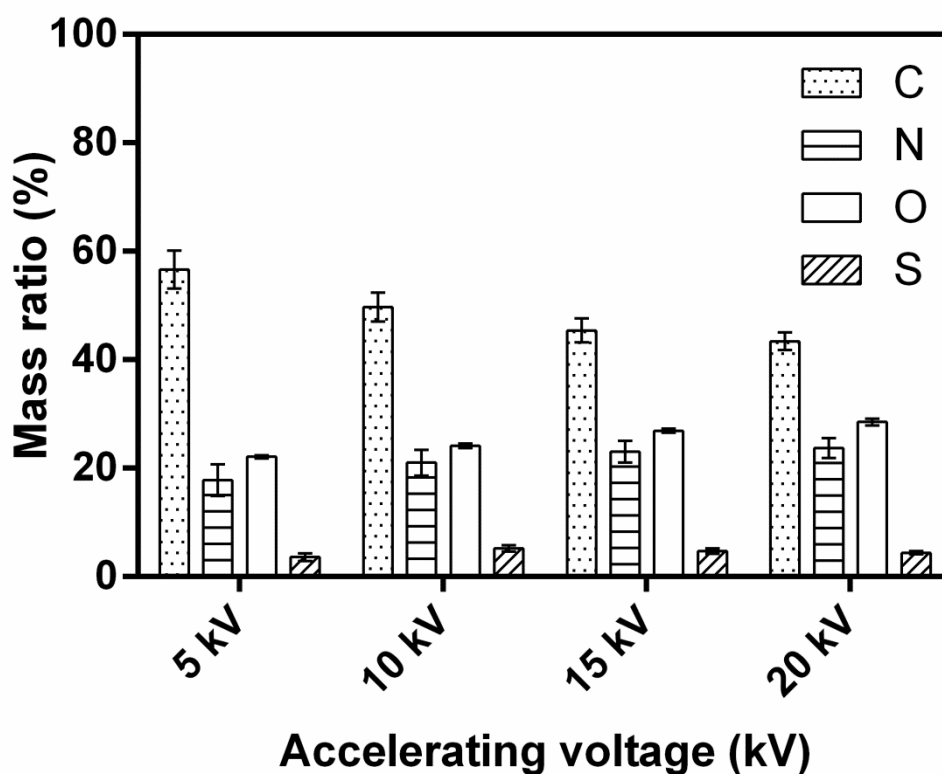
Supplementary material for Chapter 2



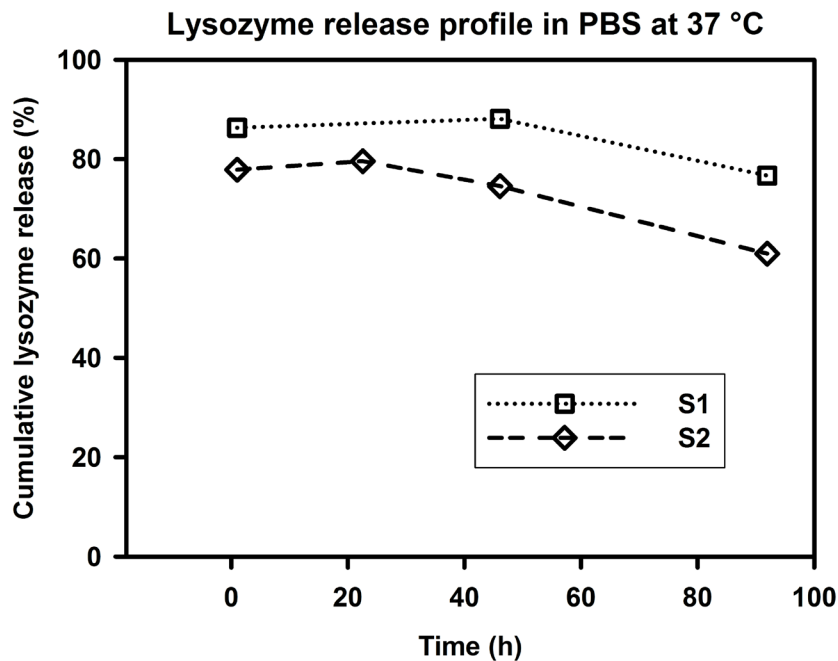
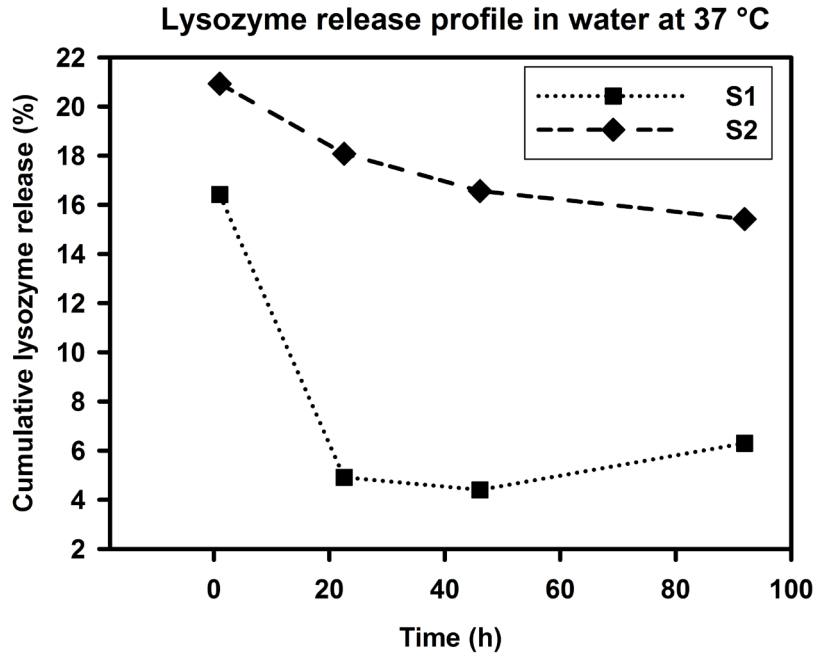
AppxA-Figure 1. Particle size distribution, measured in wet mode by laser diffraction, of spray dried DS which were produced via nozzle configurations C1, C2, C3 and C4.



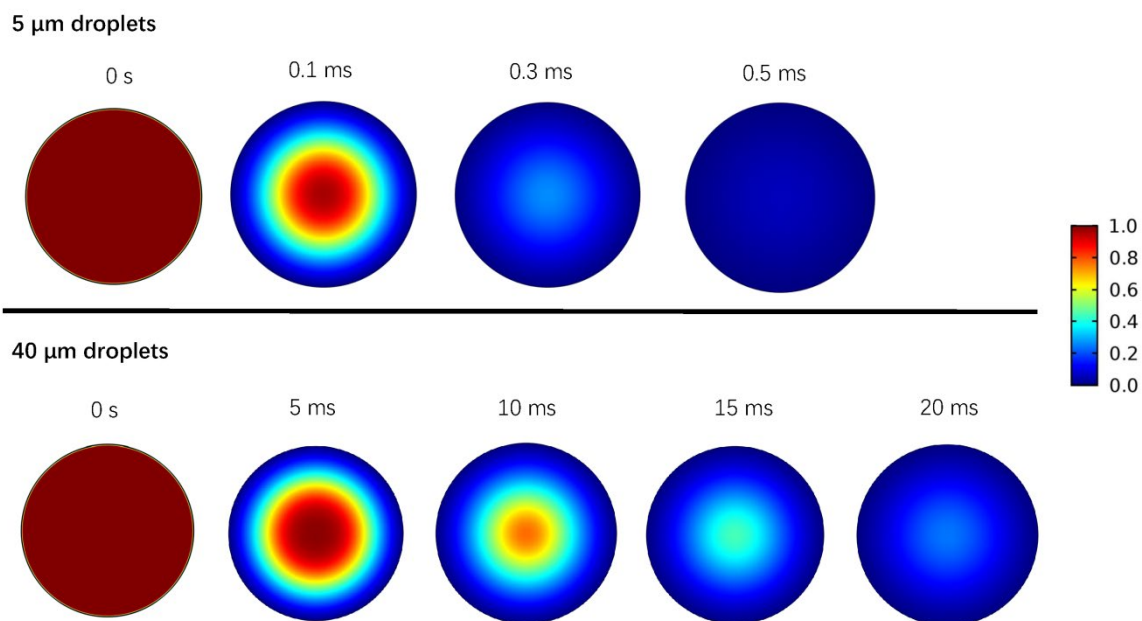
AppxA-Figure 2. SEM images of sample S1 from PSSC process at high magnifications. The tiny particles deposited onto the larger particles are clearly observed.



AppxA-Figure 3. Apparent elemental composition of S3 product particles (on the top layer) from PSSC process as function of accelerating voltage. One particle in S3 was selected for this measurement. Three different positions on the selected particles were scanned. At low accelerating voltage (5 kV), the detected S content was lower than that at higher accelerating voltages due to the relatively low excitation energy of the electron beam. The sulphur excitation energy is about 2.3 keV. The ratio of the accelerating voltage (kV) to the excitation energy (keV) should be at least 2 and optimally 2.5 to 3 to achieve a trade-off between elemental EDS spectral resolution and electron excitation [1, 2]. The composition of DS and lysozyme was calculated based on the mass content of S and N, which were used as representative elements of DS and lysozyme, respectively. The mass ratios of C and O to N and S were also applied for the calculation of composition. Based on the 10-20 kV measurements, it can be concluded that in sample S3, lysozyme was the major compound (about 70-90% mass ratio). It was determined that for a bulk carbon sample, at an accelerating voltage of 5 to 20 kV, the penetration depth increases from about 0.3 μm to 4 μm [3]. For particles of 150-200 μm , the limited penetration depth of the X-ray beam only allows for the detection of elements on the top layer of the particle.



AppxA-Figure 4. Lysozyme release profile from the S1 and S2 sample particles in water and PBS at 37 °C. A limited lysozyme release occurred in water. In PBS, a burst lysozyme release of 80-90% was observed at 1h. After 1 or 2 days exposure to PBS, the amount of detected released lysozyme decreased, which may be due to the complexation between released lysozyme and free DS in the aqueous environment. This interaction was also pointed out in a previous controlled release study where it was mentioned that the interactions between the released protein and free polyelectrolyte may sequester the released lysozyme by forming complexes in the solution [4].



AppxA-Figure 5. Water mass fraction profiles in the 5 μm and 40 μm droplets at different times in the mass transfer simulation between water and scCO₂. This simulation was based on Fick’s law using Comsol Multiphysics software where the approximate diffusion coefficients of water and scCO₂ in corresponding medium at 37 °C and 130 bar were used [5, 6].

AppxA-Table 1. Surface tension and viscosity of water and DS solutions of different concentrations measured at 37 °C. The surface tension was measured by the capillary rise method (Surface tension apparatus, KIMBLE CHASE, New York, USA). The viscosity was measured by an Ostwald viscometer (Roweel Electronic Co., Ltd, China) at 37 °C using water as reference.

Sample	Surface tension (mN/m)	Viscosity (mPa·s)
Water	69.7	0.69*
DS solution (1% w/w)	67.5	0.65
DS solution (5% w/w)	67.6	0.72
DS solution (10% w/w)	65.8	0.85

* Data from [7].

References

1. Russ, J.C., Fundamentals of Energy Dispersive X-Ray Analysis: Butterworths Monographs in Materials. 2013: Butterworth-Heinemann.
2. Energy-dispersive X-ray microanalysis: an introduction. 1999, Wisconsin NORAN Instruments Middleton.
3. Lee, S., H. Younan, Z. Siping, and M. Zhiqiang. Studies on electron penetration versus beam acceleration voltage in energy-dispersive X-ray microanalysis. in Semiconductor Electronics, 2006. ICSE'06. IEEE International Conference on. 2006. IEEE.
4. Mehrotra, S., D. Lynam, R. Maloney, K.M. Pawelec, M.H. Tuszynski, I. Lee, C. Chan, and J. Sakamoto, Time Controlled Protein Release from Layer - by - Layer Assembled Multilayer Functionalized Agarose Hydrogels. Advanced functional materials, 2010. **20**(2): p. 247-258.
5. Xu, B., K. Nagashima, J.M. DeSimone, and C.S. Johnson, Diffusion of water in liquid and supercritical carbon dioxide: an NMR study. The Journal of Physical Chemistry A, 2003. **107**(1): p. 1-3.
6. Cadogan, S.P., G.C. Maitland, and J.M. Trusler, Diffusion Coefficients of CO₂ and N₂ in Water at Temperatures between 298.15 K and 423.15 K at Pressures up to 45 MPa. Journal of Chemical & Engineering Data, 2014. **59**(2): p. 519-525.
7. Viscopedia | A free encyclopedia for viscosity. [accessed: 2017 13 September]; Available from: <http://www.viscopedia.com/viscosity-tables/substances/water/>.

Appendix B

Introduction to molecular modelling

General

One of the fascinating levels of chemistry research is to explore the complexities of chemistry at the invisible molecular level, and numerous representations of molecular interactions and structures have been devised in the recent decades [1]. The scientists can correlate the properties of one mole chemicals to the behaviours of one (set of) molecules, laying the foundation for the success of molecular modelling. With the development of modern computers with ameliorated performance of CPU, GPU, memory, etc., the chemistry research capabilities have been enhanced with the help of powerful visualisation and modelling tools [1]. These allow for a more accurate and informative description of the behaviours of molecules regarding their structure and participating interactions.

Molecular modelling is a computer-based technique for deriving and interpreting the structures and behaviours of molecules, as well as their reactions and interactions. The modelling targets at both small chemical systems and large (biological) molecules and their complexes. It has been applied to the fields of drug design, biomaterials, emerging materials, and spectroscopy [2].

The molecular modelling can be either time-independent (static) or time-dependent (dynamic). The prototypical application of static modelling is to find the stable structure of a molecular system which corresponds to minimum potential energy. This process produces a motionless molecule of idealised geometry. The properties of the molecular system such as the electrostatic potentials and reaction energies can be then obtained. In a molecular dynamics (MD) calculation, the system of molecules evolves over time by solving the positions of nuclear coordinates using Newtonian mechanics. This reflects the dynamical properties of the system: transport coefficients, molecular structural transformations, time-dependent responses to perturbations, rheological properties and spectra [3]. Unlike the static modelling, MD is not based on potential energy minimization bringing it to the closest equilibrium conformation. This thesis is limited to the static version of molecular modelling.

In accordance with relevant theories and experimental data, the molecular modelling is applicable to investigate the properties of the molecular system such as the number and types of atoms, nature of the bonds, bond lengths, angles and dihedral angles, molecular energy, geometry optimisation, enthalpy, and vibrational frequency [2]. Moreover, it can also be applied to describe the nucleophilicity, electrophilicity, electrostatic potentials, and predict molecular and biological properties for understanding the structure-activity relationships [2]. Among these properties, the molecular geometry optimisation can be achieved via the molecular mechanics (MM) method or quantum mechanical (QM) methods, which are frequently applied in molecular modelling.

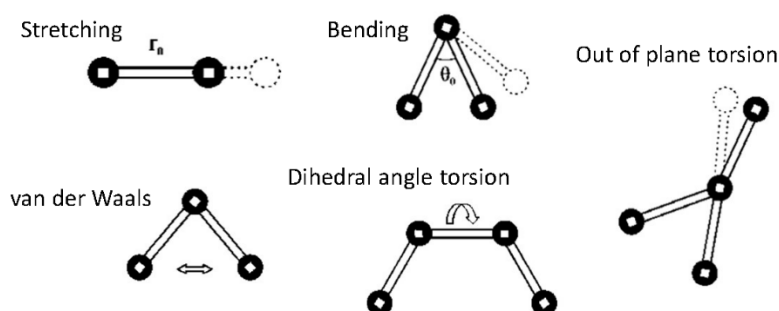
In this thesis, the approach of computational modelling of protein and polyelectrolyte under real conditions (aqueous solution, finite temperatures) are to be included with preliminary modelling results. For a better understanding of the work performed in these modelling work, a brief introduction to the concept and theories of molecular modelling (mainly MM and QM) is presented in this chapter.

Molecular mechanics

Molecular mechanics (MM) describes the total steric energy of a molecule regarding deviations from referenced unstrained bond lengths, angles and torsions as well as nonbonded interactions and Coulombic interactions [4, p. 13-15, 5, p. 265, 6, p. 165-166]. Thus, the total potential energy is contributed by the bond-stretching, bond-bending vibrations, dihedral motions, out-of-plane angle potential and van der Waals interactions (non-bonded interactions and Coulomb interactions). An illustration is given in AppxB-Figure 1. A molecular mechanics force field can be written as shown in AppxB-Equation 1.

$$U = \sum_{stretch} U_{ab} + \sum_{bend} U_{abc} + \sum_{dihedral} U_{abcd} + \sum_{out-of-plane} U_{abcd} + \sum_{non-bonded} U_{ab} + \sum_{Coulomb} U_{ab} \quad \text{AppxB-Equation 1}$$

Where U represents the potential energy, the letters a,b,c,d represent the atoms to which the potential is assigned. There is no physical meaning of the calculated total energy regarding that it is merely an indication of molecular strain in comparison with the hypothetical strain-free molecule [4, p. 14].



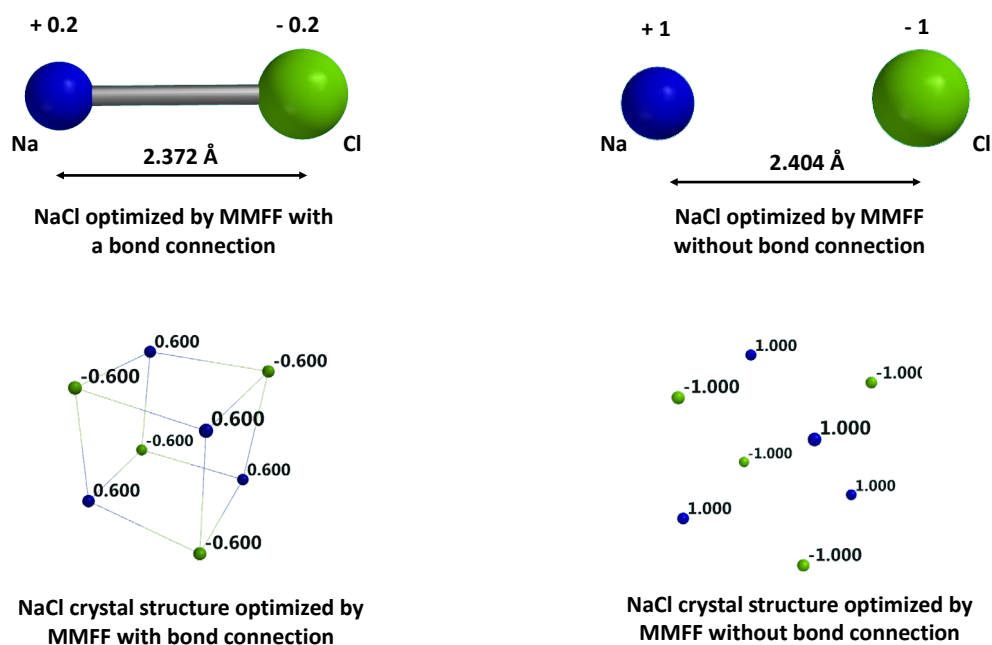
AppxB-Figure 1. Interatomic interactions in molecular mechanics according to [7, 8].

The behaviour of molecules is well modelled based on the developed force fields. A force field is a set of functions and constants used to find the potential energy of the molecules [9, p. 206]. Using the force field established based on the data of other relevant molecules, the geometry and property of a new molecule can be derived [10, p. 80].

The force fields are usually determined in two ways, i.e. calibrating the parameters against calculations of quantum mechanics on small molecules, and against data from analytical experiment on the properties such as crystal structure, infrared absorption, X-ray adsorption, density, enthalpy of vaporisation and Gibbs energies of solvation [10, p. 59]. The particularity of design for a force field is the factor to be considered when selecting it for a specific type of molecular system. For example, the force fields calibrated against the solution properties of amino acids are the ones suitable for the modelling of solvated proteins [10, p. 59]. The applications of some common force fields, differed by the functional forms and parameters, are listed in AppxB-Table 1. Among the popular MM forcefields, Merck Molecular Force Fields (MMFF) is a full periodic table force field suitable for a broad range of chemicals, with parameters extracted from quantum mechanics calculations. This force field applies to proteins and other similar biological systems and is transferable to treat conformational energetics and non-bonded interactions [9, p. 219-221]. The results of the MMFF calculation depend on the pre-definition of the molecular structure and bond type. An example of NaCl is given in AppxB-Figure 2. When the diatomic NaCl is built with a bond connection in-between, the MMFF-optimised structure shows a lower absolute value of electrostatic charge on sodium and chloride and a lower inter-atom distance than the one built without a bond connection. The latter calculation shows the electrostatic charge of Na and Cl of +1 and -1 respectively, which fit more to the practical situation. A difference in the atom charge is also observed for the modelled NaCl crystal built with and without bonds. During the finding of the minima of the molecular potential energy, there is no bond formation or break, and the atom connectivity specified in the input file is obeyed [11].

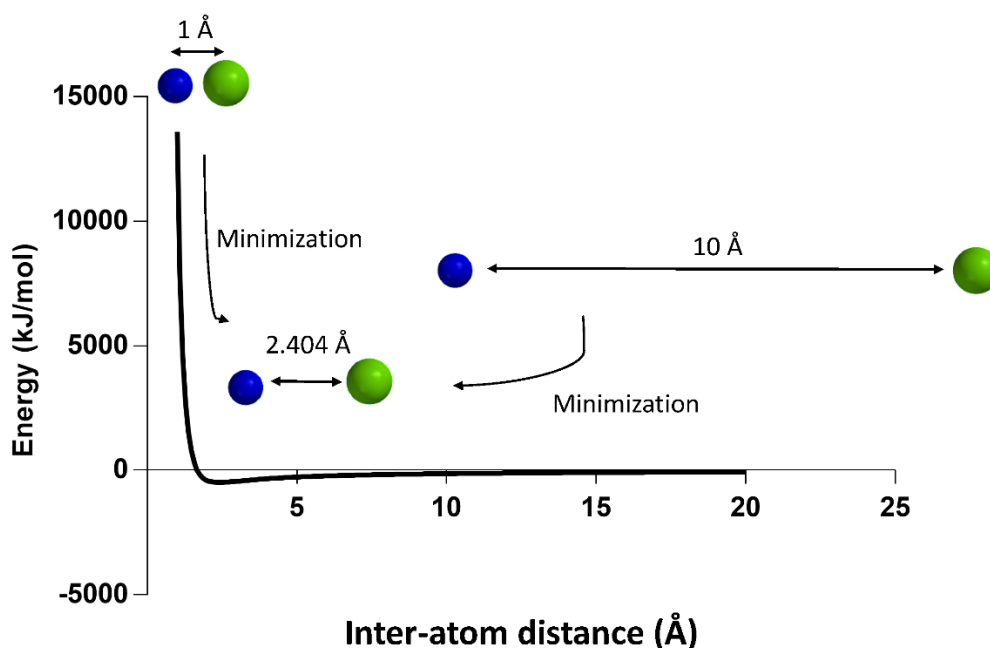
AppxB-Table 1. Example of MM force fields and their applications

Force field	Application	Reference
MM2 & MM3 & MM4	For calculations on small hydrocarbons.	[12-14]
OPLS	To reproduce liquid state thermodynamic properties; and for calculations on amino acids and proteins.	[10, 15, 16]
Dreiding	For calculations on organic, biological, and main-group inorganic molecules.	[17]
CFF	Parameterised for acetals, acids, alcohols, alkanes, alkenes, amides, amines, aromatics, esters, and ethers.	[18]
UFF	Full periodic table force field and performs well with inorganic materials, and organometallic materials.	[19, 20]
MMFF	Particularly well with organic compounds such as alkanes, alcohols, phenols, ethers, aldehydes, ketones, ketals, acetals, amines, amides, peptide analogs, ureas, imides, carboxylic acids, esters, carboxylate anions, ammonium cations, disulfides, halides (chlorides and fluorides), and amine N-oxides; applicable to proteins and other systems of biological significance.	[9, 20-25]



AppxB-Figure 2. The calculated electrostatic charge and inter-atom distance of NaCl optimised by MMFF with and without bond connections.

Based on the force fields, the studied molecular geometry is optimised iteratively [5, p. 457], in which a newly optimised geometry is calculated based on the energy and the first derivative of the energy with respect to all geometrical coordinates of the last geometry. This process terminates when the gradient closely approaches zero with a restricted change of geometrical parameter and energy between successive iterations [5, p. 457]. A simple scheme example of the one-dimensional optimisation is shown in AppxB-Figure 3 to find the equilibrium geometry of a diatomic molecule (e.g. NaCl). Usually, in molecular modelling, the objective functions have multivariable, representing a molecular potential energy surface, of which the minima are searched [9, p. 229-230]. The corresponding molecular structures are some of those with the local minimum energy on the potential surface [10, p. 65-68]. There were several frequently-used energy minimisation algorithms such as Steepest Descent Minimiser, Conjugate-Gradient Method and Newton-Raphson Minimiser [9, p. 229-241].



AppxB-Figure 3. Example scheme of the one-dimensional optimisation to minimise the strain energy of the NaCl, as a function of the inter-atom distance, to find the equilibrium geometry of NaCl with the energy minima.

Unlike some complicated methods such as the QM (described in the following), the electrons and nuclei of the atoms are not explicitly included in the MM calculations [4, p. 13]. Instead, in the MM, the atomic composition of a molecule is regarded as a collection of interacting masses driven by

harmonic forces [4, p. 13]. This enables the MM a relatively fast computational method practicable for both small molecules and larger molecules, and even oligo-molecular systems [26]. The MM is also advantageous in dealing reasonably accurately with van der Waals interactions at non-bonded distances, while for quantum mechanics it is notoriously difficult to solve [11]. More information on the Pros and Cons of MM are summarised in [11].

Quantum mechanics

A well-parametrised force field can calculate the molecular properties such as the geometry and relative conformational energies with high accuracy [4, p. 19]. However, when there is a lack of specific parameters for a structure, quantum mechanical (QM) methods, as a substitute, can be used for geometry optimisation [4, p. 19]. Additionally, the QM can deal with the calculation of transition states or reaction paths, polarisation effects and electron distribution [4, p. 19]. Moreover, QM can supply information on infrared and Raman spectra, UV/visible spectra and NMR spectra and complement existing experimental data, for example, the intermolecular potentials for molecular mechanics [5, p. 16]. The computation costs and the limitation to small molecules are the inferior aspects of the QM methods [4, p. 16].

QM describes the energy of a molecule regarding interactions among nuclei and electrons as given by the Schrödinger equation (see AppxB-Equation 2).

$$H\Psi = E\Psi \quad \text{AppxB-Equation 2}$$

The wave function is represented by ψ , which describes the system state and is a function of the Cartesian coordinates of all electrons and ions, depending on time. E and H represent the energy of a system and the corresponding operator (Hamiltonian operator (H)) describing the kinetic energies, electron-electron interaction energy, and the potential energy due to interaction with external potentials [5, p. 444, 27]. The time-independent Schrödinger equation for a single particle moving in an electric field in the case of three dimensions is shown as AppxB-Equation 3, in which the first part on the right side represents the kinetic term (\hbar represents the reduced Planck constant, m the mass, ∇^2 the Laplacian, r the position) and V the potential term [9, p. 41-43]. It is impossible to use elementary methods to derive the time-dependent Schrödinger equation, which is generally given as a postulate of quantum mechanics [9, p. 41-43].

$$-\frac{\hbar}{2m} \nabla^2 \Psi(r) + V(r)\Psi(r) = E\Psi(r) \quad \text{AppxB-Equation 3}$$

To make it possible to solve the Schrödinger equation, approximate solutions are needed, and one of them is the Hartree-Fock (HF) molecular orbital model. Three approximations were made to the Schrödinger equation [5, p. 445-446]: i) ignore nuclear motions; ii) restrict electron motion to one nucleus; and iii) use atom-centred functions to describe the one-electron solution to molecular orbital. A correlation is needed to bridge the HF energy and the experimental energy even with these assumptions.

Unlike HF model which calculates (one electron) wave functions, the density functional theory (DFT) derives the energy directly from the electron probability density. DFT and HF are coupled by using functionals (functions of another function), i.e. the total energy is a function of the electron density, and the electron density is a function of the coordinates [27, 28]. Here the 3N-dimensional problem (N represents the number of electrons) is reduced to a 3-dimensional one, and accurate results can be obtained with higher computation efficiency than the HF model [27]. One of the frequently used functional is the B3LYP hybrid functional (Becke's three-parameter Lee-Yang-Parr hybrid functional) [27, 29-31] which employs parameters determined through the reference to experimental thermochemical data.

Further approximations can be introduced to the Schrodinger equation to reduce the computational cost while keeping the formalism of quantum mechanics. Semi-empirical models are proposed with the following features [5, p. 450-451]: i) eliminate overlap between functions on different atoms; ii) restrict to a minimal valence basis set of atomic functions; and iii) incorporate empirical parameters into formalism and calibrated against reliable experimental or theoretical reference data. Semi-empirical function usually works as a start option for DFT calculations.

There are several software packages available in the market containing some validated QM codes, such as Gaussian [32], Turbomole [33], Materials Studio [34] and Spartan [5]. Most of the available product suites work based on a user-friendly graphical user interface from which the user can access all QM codes and calculation options.

For both the QM and MM methods, there were calculation errors of the molecular properties compared to experimental measurement. A list of the accuracies of the methods used for molecular modelling in this study is shown in AppxB-Table 2. MM tends to outweigh QM (semi-empirical PM6) and be comparable with QM (B3LYP with 6-31+G* basis set) in predicting the geometry of molecules. Regarding the energy accuracy, although the average error is small, it can accumulate for large molecular systems such as proteins and polymers and thus reducing the accuracy of the calculations such as reaction energy and activation barriers. To alleviate the error, the idea of isodesmic reactions was introduced to the molecular modelling in which the type and the number of bonds before and

after the chemical reaction are kept the same. Under this condition, the errors caused by the inaccuracies of the MM or QM methods are cancelled out, and theoretical energy data that are comparable with experimental measurement are resultantly obtained.

AppxB-Table 2. List of the accuracies of methods used for molecular modelling in this thesis.

Methods	Error on bond lengths (Å)	Error on bond angles (degree)	Error on hydrogen-bond energy (kJ/mol)	Error on the conformational energy (kJ/mol)	Reference
MM (MMFF)	0.014*	1.2*	-	1.59*	[21]
QM (semi-empirical PM6)	0.091**	7.86**	7.11**	9.83**	[35]
QM (B3LYP with 6-31+G* basis set)	0.0093**	1.29**	1.51**	16.54% (relative) **	[36]

*RMSE: root mean squared error

** MUE: mean unsigned error

Solvation for molecular modelling

Molecular modelling implicitly is carried out at zero K under vacuum conditions. With proper thermodynamic corrections, the properties of the molecular modelling system at room temperature and atmospheric conditions can be yielded. Moreover, the solvation should not be overlooked considering that chemistry usually occurred in the presence of solvent.

During solvation, solvent and solute molecules interact with each other and lead to changes in energy, stability, and molecular orientation (distribution) [9, p. 250]. The solvation effect on the molecular modelling of macromolecular (e.g. protein) behaviours, is an inevitable factor to be considered when investigating the locations of the functional site, characterising ligand-binding sites in proteins, docking of small molecules into protein binding sites and protein-protein interaction studies [2].

Under vacuum condition, the relative permittivity ϵ is 1. For non-polar hydrocarbons, the difference between the calculations with gas phase and with solvent is negligible [4, p. 18]. However, for polar molecules, the solvent effects need to be considered (e.g. in water, the relative permittivity ϵ is about 80) to avoid overestimation of conformations affected by strong electrostatic interactions [4, p. 18].

There are two options for the correction of the solvation effect: one is to apply a general field to model the solvent as a continuum in which no specific interactions occur between the solute and solvent; the

other is to introduce an explicit number of water molecules to the molecular systems in which the solute molecules interact with the solvent molecules. The former option treats the Coulombic terms of solvated molecules using a uniform relative permittivity, assuming that the electrostatic field of the molecules, especially the small ones, is homogeneous. Here the solvent is considered as a continuum with a given dielectric constant, and in accordance, several models were proposed such as the SM series solvation model (e.g. SM5.4), Onsager Model, Tomasi Polarized Continuum Model (PCM) and Isodensity Surface Model (IPCM) [5, p. 524, 9, p. 250-252]. The latter option to demonstrate the solvent effect is to add discrete solvent molecules around the solute molecules. Under this condition, there is no correction needed for the Coulombic terms of the applied force fields, and the local molecular-solvent interactions, such as the formation of hydrogen-bridges, can be clearly illustrated. However, the increased number of water molecules can lower the computation efficiency.

When it comes to the modelling of macromolecules such as proteins and polyelectrolytes, the surrounding environment can strongly affect the molecular conformational flexibility. The optimisation process performed in vacuo tends to overestimate the interactions among charged groups, and as a result, the non-polar hydrophobic groups are squeezed and artificially collapses [4, p. 137]. This does not make sense in reality when solvent molecules are involved.

The simulation of macromolecules in a solvent environment with thousands of water molecules requires immense computation effort. However, during the energy minimisation, incorporating structural water molecules explicitly into the macromolecular structure is essential for the functionality and conformation maintenance.

References

1. Jones, L.L. and R.M. Kelly, Visualization: The Key to Understanding Chemistry Concepts, in Sputnik to Smartphones: A Half-Century of Chemistry Education. 2015, American Chemical Society. p. 121-140.
2. Saleh, N.A., H. Elhaes, and M. Ibrahim, Design and Development of Some Viral Protease Inhibitors by QSAR and Molecular Modeling Studies, in Viral Proteases and Their Inhibitors. 2018, Elsevier. p. 25-58.
3. Kim, J., M. Jamil, J.E. Jung, J.E. Jang, A. Farzana, W.L. Jin, W.P. Sang, M.K. Woo, J.Y. Kwak, and Y.J. Jeon, Investigating the calculation of rotational viscosity of the mixture comprising

- different kinds of liquid crystals: molecular dynamics computer simulation approach. Chinese Journal of Chemistry, 2011. **29**(1): p. 48-52.
4. Holtje, H.-D. and G. Folkers, Molecular modeling: basic principles and applications. 1997, Weinheim: Wiley-VCH.
 5. Wavefunction, Inc., Spartan 16 Tutorial and User's Guide. 2016; Available from: <http://downloads.wavefun.com/Spartan16Manual.pdf>.
 6. Leach, B.A.R., Molecular modelling: principles and applications (second Edition). 2001: Pearson Education Limited.
 7. Li, C. and T.-W. Chou, A structural mechanics approach for the analysis of carbon nanotubes. International Journal of Solids and Structures, 2003. **40**(10): p. 2487-2499.
 8. Lengvarský, P. and J. Bocko, Prediction of Young's modulus of graphene sheets by the finite element method. American Journal of Mechanical Engineering, 2015. **3**(6): p. 225-229.
 9. Ramachandran, K., G. Deepa, and K. Namboori, Computational chemistry and molecular modeling: principles and applications. 2008: Springer Science & Business Media.
 10. Hinchliffe, A., Molecular modelling for beginners (second edition). 2008: John Wiley & Sons.
 11. Techniques of Molecular Modelling: Molecular Mechanics. [accessed: 2018 5 October]; Available from: https://www.ch.ic.ac.uk/local/organic/mod/mo_3.html.
 12. Allinger, N.L., Conformational analysis. 130. MM2. A hydrocarbon force field utilizing V1 and V2 torsional terms. Journal of the American Chemical Society, 1977. **99**(25): p. 8127-8134.
 13. Allinger, N.L., Y.H. Yuh, and J.H. Lii, Molecular mechanics. The MM3 force field for hydrocarbons. 1. Journal of the American Chemical Society, 1989. **111**(23): p. 8551-8566.
 14. Allinger, N.L., K. Chen, and J.H. Lii, An improved force field (MM4) for saturated hydrocarbons. Journal of computational chemistry, 1996. **17**(5-6): p. 642-668.
 15. Jorgensen, W.L. and J. Tirado-Rives, The OPLS [optimized potentials for liquid simulations] potential functions for proteins, energy minimizations for crystals of cyclic peptides and crambin. Journal of the American Chemical Society, 1988. **110**(6): p. 1657-1666.
 16. Jorgensen, W.L., D.S. Maxwell, and J. Tirado-Rives, Development and testing of the OPLS all-atom force field on conformational energetics and properties of organic liquids. Journal of the American Chemical Society, 1996. **118**(45): p. 11225-11236.

17. Mayo, S.L., B.D. Olafson, and W.A. Goddard, DREIDING: a generic force field for molecular simulations. *The Journal of Physical Chemistry*, 1990. **94**(26): p. 8897-8909.
18. Niketic, S.R. and K. Rasmussen, *The consistent force field: a documentation*. Vol. 3. 2012: Springer Science & Business Media.
19. Rappé, A.K., C.J. Casewit, K. Colwell, W.A. Goddard III, and W. Skiff, UFF, a full periodic table force field for molecular mechanics and molecular dynamics simulations. *Journal of the American chemical society*, 1992. **114**(25): p. 10024-10035.
20. Avogadro: Molecular Editor and Visualization, *Molecular Mechanics & Force Fields*. [accessed: 2019 10 January]; Available from: <https://avogadro.cc/docs/optimizing-geometry/molecular-mechanics/>.
21. Halgren, T.A., Merck molecular force field. I. Basis, form, scope, parameterization, and performance of MMFF94. *Journal of computational chemistry*, 1996. **17**(5-6): p. 490-519.
22. Halgren, T.A., Merck molecular force field. II. MMFF94 van der Waals and electrostatic parameters for intermolecular interactions. *Journal of Computational Chemistry*, 1996. **17**(5-6): p. 520-552.
23. Halgren, T.A., Merck molecular force field. III. Molecular geometries and vibrational frequencies for MMFF94. *Journal of Computational Chemistry*, 1996. **17**(5-6): p. 553-586.
24. Halgren, T.A. and R.B. Nachbar, Merck molecular force field. IV. Conformational energies and geometries for MMFF94. *Journal of computational chemistry*, 1996. **17**(5-6): p. 587-615.
25. Halgren, T.A., Merck molecular force field. V. Extension of MMFF94 using experimental data, additional computational data, and empirical rules. *Journal of Computational Chemistry*, 1996. **17**(5-6): p. 616-641.
26. Levita, J., E.P. Istyastono, A. Mutholib, I.J. de Esch, and S. Ibrahim, Analyzing the interaction of andrographolide and neoandrographolide, diterpenoid compounds from *andrographis paniculata* (Burm. F) nees, to Cyclooxygenase-2 enzyme by docking simulation. *Journal of Mathematical and Fundamental Sciences*, 2009. **41**(2): p. 110-119.
27. Jacobsen, H. and L. Cavallo, *Directions for Use of Density Functional Theory: A Short Instruction Manual for Chemists*, in *Handbook of Computational Chemistry*. 2017. p. 226-267.

28. Density functional theory for beginners. [accessed: 2018 19th December]; Available from: http://newton.ex.ac.uk/research/qsystems/people/coomer/dft_intro.html.
29. Becke, A.D., Density-functional thermochemistry. III. The role of exact exchange. *The Journal of chemical physics*, 1993. **98**(7): p. 5648-5652.
30. Stephens, P., F. Devlin, C. Chabalowski, and M.J. Frisch, Ab initio calculation of vibrational absorption and circular dichroism spectra using density functional force fields. *The Journal of Physical Chemistry*, 1994. **98**(45): p. 11623-11627.
31. Becke, A.D., A new mixing of Hartree–Fock and local density-functional theories. *The Journal of chemical physics*, 1993. **98**(2): p. 1372-1377.
32. Foresman, J.B. and Æ. Frisch, *Exploring chemistry with electronic structure methods* (third edition). 2015: Gaussian, Inc.: Wallingford, CT.
33. Furche, F., R. Ahlrichs, C. Hättig, W. Klopper, M. Sierka, and F. Weigend, *Turbomole*. Wiley Interdisciplinary Reviews: Computational Molecular Science, 2014. **4**(2): p. 91-100.
34. Accelrys Software Inc., *Materials Studio*. 2013; Available from: <http://accelrys.com/products/materials-studio/>.
35. Stewart, J.J.P. Accuracy of PM6 [accessed: 2018 5 October]; Available from: http://openmopac.net/manual/index_accuracy.html.
36. Riley, K.E., B.T. Op't Holt, and K.M. Merz, Critical assessment of the performance of density functional methods for several atomic and molecular properties. *Journal of chemical theory and computation*, 2007. **3**(2): p. 407-433.

Appendix C

Supplementary material for Chapter 5

Supplementary information of the direct collision simulation

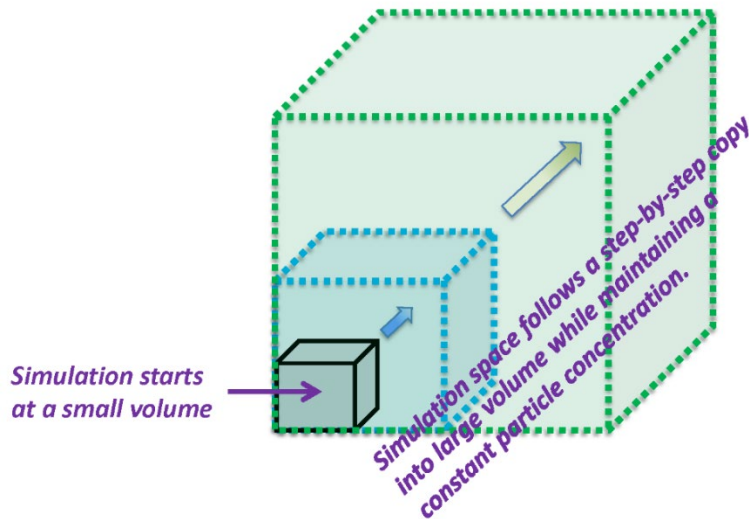
The direct collision (DC) simulation was performed to describe the particle agglomeration profile while differentiating the properties of the colliding particles and enabling the specificity of collision conditions among them.

The procedure of the DC simulation is as follows:

1. The information of each virtual particle in the simulation is stored in a pre-defined matrix, in which the particle position, particle size, and the state of presence of the particle are included.
2. Build the simulation domain with a specified size and distribute the particles randomly in the domain.
3. Initiate a time step and start the particle displacement. During each time step, the collisions among the primary particles are firstly evaluated, followed by the collisions between the primary particles and the agglomerates, and then among the agglomerates. At each time step, the particles displace within a predefined distance and in a random direction. The displacement of particles as a function of time follows the Einstein-Stokes law in a 3D case.
4. The progress of the simulation (e.g. the number of the remaining particles in the simulation domain) is updated every time step.

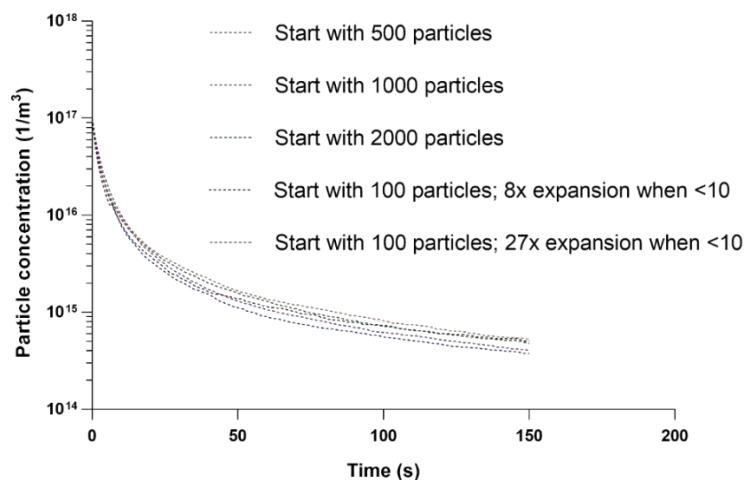
Periodic boundary conditions were employed to the wall of the cubic domain such that particles that have left the control volume at the end of a time step are replaced, for the next time step, by image particles that enter from the opposite side. This type of boundary condition is commonly employed in Monte Carlo simulations and allows for an infinite homogeneous system to be modelled approximately by a finite volume [1, 2]. In the DC simulation, a (pseudo-) random number, which was uniformly distributed on the interval $[-1,1]$, was generated and used for the directional vectors of the stepwise particle displacement.

The DC simulation was performed in a way of multi-scale, the scheme of which is displayed in AppxC-Figure 1. Whenever the number of the particles in the current volume decreases below a pre-set value, e.g. 10, the current simulation volume will expand several times, copying the status of the particles into the expanded volume. The procedure of volume expansion, as well as particle copying, is consistent with the hypothesis that the particle collision status in the smaller volume is crudely representative of the status in the whole volume of the system.



AppxC-Figure 1. Scheme of the multi-scale approach for the DC simulation.

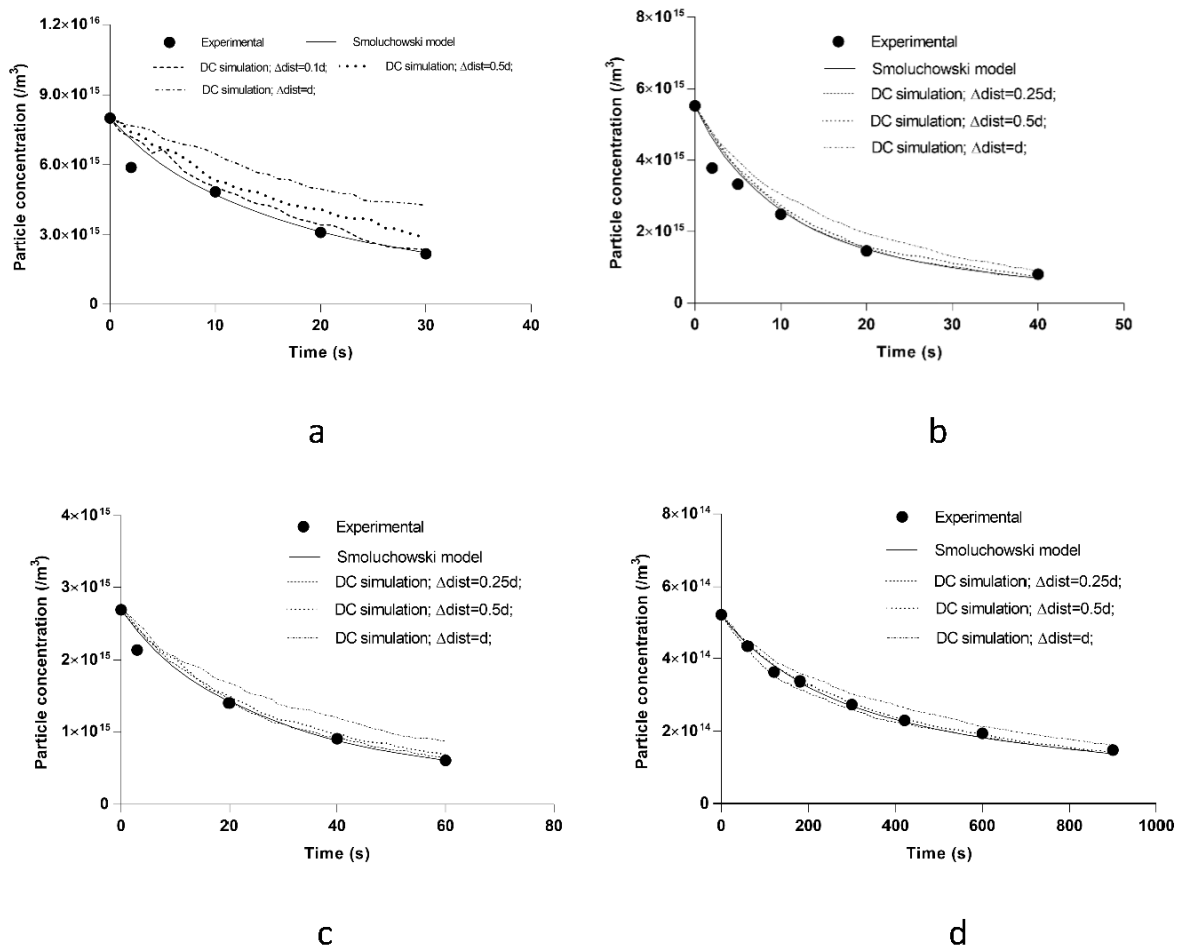
The precision of the multi-scale approach is checked by performing the simulation of different cases for 20 times and check the statistical significance of the differences among the cases, which reflects the consistency of these simulations. The results are displayed in AppxC-Figure 2, in which the concentrations of particles (number of particles in the simulation domain divided by the simulation volume) as a function of time with and without multi-scale are shown. Based on a Student's t-test, there are no statistically significant differences in the simulated particle concentrations ($p > 0.05$) in the different cases.



AppxC-Figure 2. The particle concentration as a function of time of simulations starting with different numbers of particles in the simulation domain with and without multi-scale. The starting particle concentrations were the same for all these simulations. The simulations started with the volume of 1×10^{-15} to $1 \times 10^{-14} m^3$, corresponding to the particle concentration of $1 \times 10^{17}/m^3$.

AppxC-Figure 3 shows the comparison of the DC simulation results with those of classical Smoluchowski's model on the gold nanoparticle agglomeration. The DC simulations were performed with the conditions and assumptions employed by the Smoluchowski's model reported in [3]. The primary particle (see AppxC-Figure 3 (a), (b) and (c)) and total particle (see AppxC-Figure 3 (d)) concentration ($1/m^3$) as function of time are displayed. In Smoluchowski's publication [3], the Smoluchowski's model fits the referenced experimental data (see AppxC-Figure 3 the square markers and solid line). The DC simulation was performed using different particle displacement distance per time step. It was found that there is an influence of the step-wise displacement distance ($\Delta dist$) of the simulated particles on the results of the simulation. The shorter the $\Delta dist$, the more comparable of the simulation result to the Smoluchowski's model. This might be due to the underestimation of particle collision frequency as the two colliding particles may miss each other at a long displacement step. These comparisons serve as a sort of validation of the DC simulation to assure that there are no artefacts or numerical errors to this simulation.

Based on the above tests of the DC simulation, in later studies, further investigations will be performed on the application of the DC method to simulate P-PE agglomeration.



AppxC-Figure 3. The data of experimental measurement, Smoluchowski model and DC simulation on the gold nanoparticle agglomeration. The primary particle ((a), (b) and (c)) and total particle ((d)) concentration as function of time are displayed. It shows that the smaller the displacement distance per time step in the DC simulation, the closer the simulation results to the Smoluchowski's model.

Supplementary information of the probability-based method

The Uchiyama's function was verified by comparing with the results of numerical simulations on the collisions of pairs of particles. Five thousand pairs of particles sharing the same primary conditions, such as particle size, were created with a uniform initial inter-particle distance between each two in one pair. The particles displaced stochastically in a 3D space. Whenever the distance between the two particles in one pair was shorter than the effective agglomeration distance, the two particles merge into one. Over a certain period, the probability of particle collision is calculated as the ratio of the number of pairs of collided particles divided by the total number of particle pairs.

AppxC-Table 1 shows a comparison of the calculated inter-particle collision probability with the numerical simulation. The calculated probability is listed as a function of the particle size, the starting inter-particle distance and the value of α (collision efficiency factor). The analytical solution and our numerical solution are well comparable, and the Uchiyama's formula is validated to predict the inter-particle collision probability.

AppxC-Table 1. The inter-particle collision probability calculated by Uchiyama's formula and the numerical simulation as function of particle radius, starting inter-particle distance and α .

r1 (nm)	r2 (nm)	Inter-particle dist (nm)	α	P_{Uchiyama}	$P_{\text{simulation}}$
96	96	250	2.56	0.97	0.97
96	96	250	2.34	0.83	0.82
96	96	250	2.16	0.74	0.74
96	96	300	2.56	0.70	0.70
96	96	400	2.56	0.37	0.38
96	96	500	2.56	0.19	0.19
96	121	400	2.56	0.46	0.46
96	121	400	2.82	0.56	0.56
96	121	400	2.34	0.38	0.38
96	121	400	2.16	0.33	0.32
96	121	500	2.56	0.24	0.24
121	121	500	2.56	0.29	0.30
121	121	500	2.82	0.37	0.38
121	121	500	2.34	0.23	0.22
121	121	500	2.16	0.19	0.20
121	121	700	2.56	0.063	0.063
121	138	500	2.56	0.34	0.34
121	152	500	2.56	0.39	0.39
121	192	500	2.56	0.54	0.55
152	152	500	2.56	0.50	0.50
152	152	500	2.82	0.65	0.66
152	152	500	2.34	0.38	0.38
152	152	500	2.16	0.31	0.30
152	152	800	2.56	0.041	0.039
192	192	600	2.56	0.50	0.506
192	192	800	2.56	0.089	0.084
192	192	1000	2.56	0.0079	0.0078
220	220	800	2.56	0.16	0.16

A method, named as the Cloud method, was developed to simulate particle agglomeration using the Uchiyama's function to predict the collision probability. In the simulation, the interaction among

clouds of particles rather than pairs of particles was considered. The particles in the simulation were divided into several groups based on their composition, e.g. monomer, dimer, trimer.... oligomers. The number of collisions among these groups of particles was calculated. The collision probability can be calculated by integrating Uchiyama's formula over an infinite distance, as shown in AppxC-Equation 1.

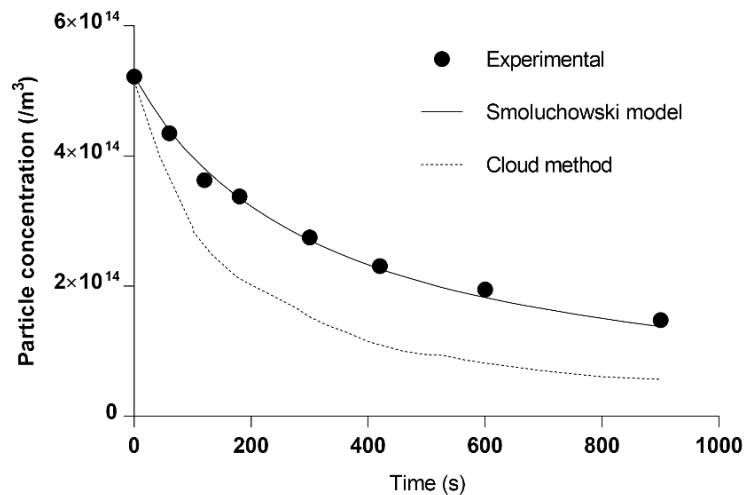
$$P_c(x, t) = \int_{r_{min}}^{\infty} \frac{x-a}{\sqrt{2\pi t^2}} e^{-\frac{(x-a)^2}{2t}} \left(\frac{a}{x}\right) dx \quad \text{AppxC-Equation 1}$$

Where r_{min} stands for the minimum distance between the colliding particles. Via this integration, the probability is only dependent on the time. Within a specific time interval, the average number of colliding particles can be determined by AppxC-Equation 2:

$$N_c = N_{tc} * P_c(x, t) \quad \text{AppxC-Equation 2}$$

Where N_c stands for the average number of collisions among the particles, N_{tc} the total number of possible collisions, $P_c(x,t)$ the probability of collisions calculated by the integration. During the simulation, the real number of collisions follows a Poisson distribution, where the rate parameter, λ , is replaced by N_c .

It was found that the Cloud method overestimates the particle agglomeration rate compared to Smoluchowski's model (see AppxC-Figure 4). Whether the algorithm is appropriate to describe particle collision and agglomeration still needs further evaluation.



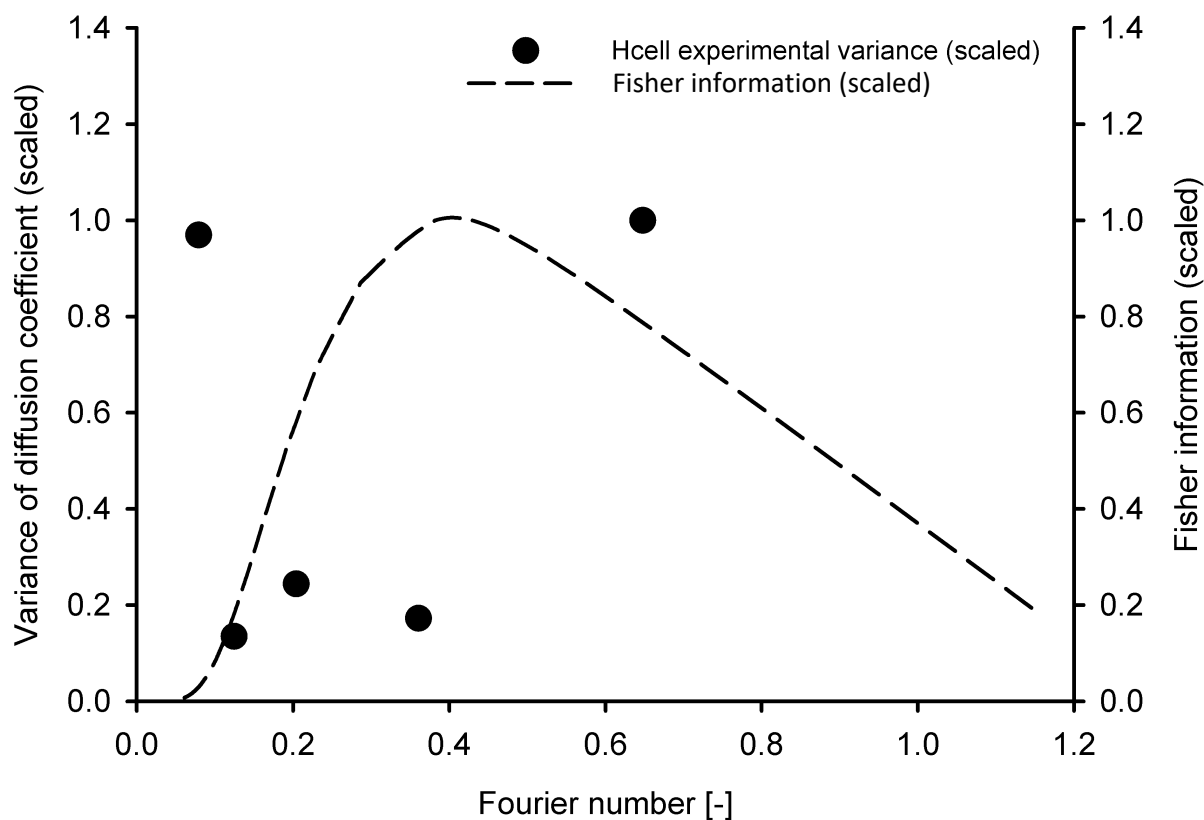
AppxC-Figure 4. Simulating gold nanoparticle agglomeration (particle concentration as function of time) using Cloud method and compare with the experimental values and Smoluchowski's model.

References

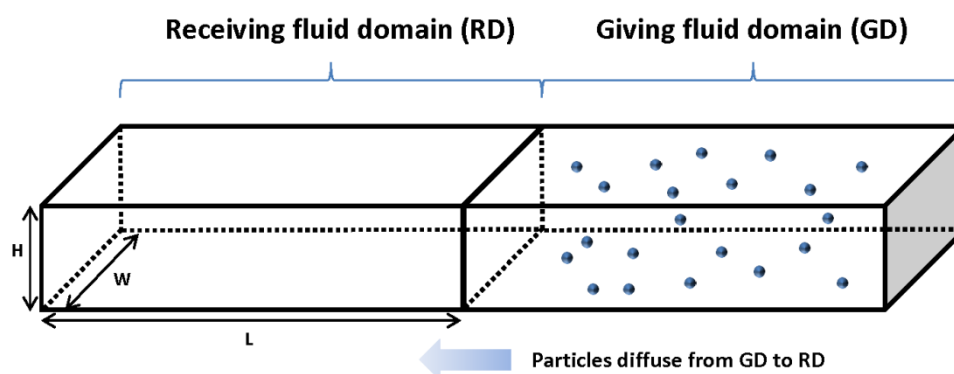
1. Alder, B.J. and T.E. Wainwright, Studies in molecular dynamics. I. General method. The Journal of Chemical Physics, 1959. **31**(2): p. 459-466.
2. Pearson, H., I. Valioulis, and E. List, Monte Carlo simulation of coagulation in discrete particle-size distributions. Part 1. Brownian motion and fluid shearing. Journal of Fluid Mechanics, 1984. **143**: p. 367-385.
3. Smoluchowski, M., Versuch einer mathematischen Theorie der Koagulationskinetik kolloider Lösungen. Zeitschrift Für Physikalische Chemie, 1917. **92**(1): p. 129-168.

Appendix D

Supplementary material for Chapter 6



AppxD-Figure 1. Calculated Fisher information (scaled) and measured diffusivity data variation (scaled) of lysozyme in water as a function of the dimensionless Fourier number. The variances of the measured lysozyme diffusion coefficients are low and almost similar within the range of Fourier number from about 0.1 to 0.4. When out of this range, the measured lysozyme diffusion coefficients have high variances.



AppxD-Figure 2. Geometrical scheme of Comsol Multiphysics particle tracing simulation. A three-dimensional simulation is performed. Two contacting domains are built, being a donor fluid domain (DD) and receiver fluid domain (RD), where the simulated particles transport from the DD with a higher initial particle concentration to the RD with a lower initial particle concentration.

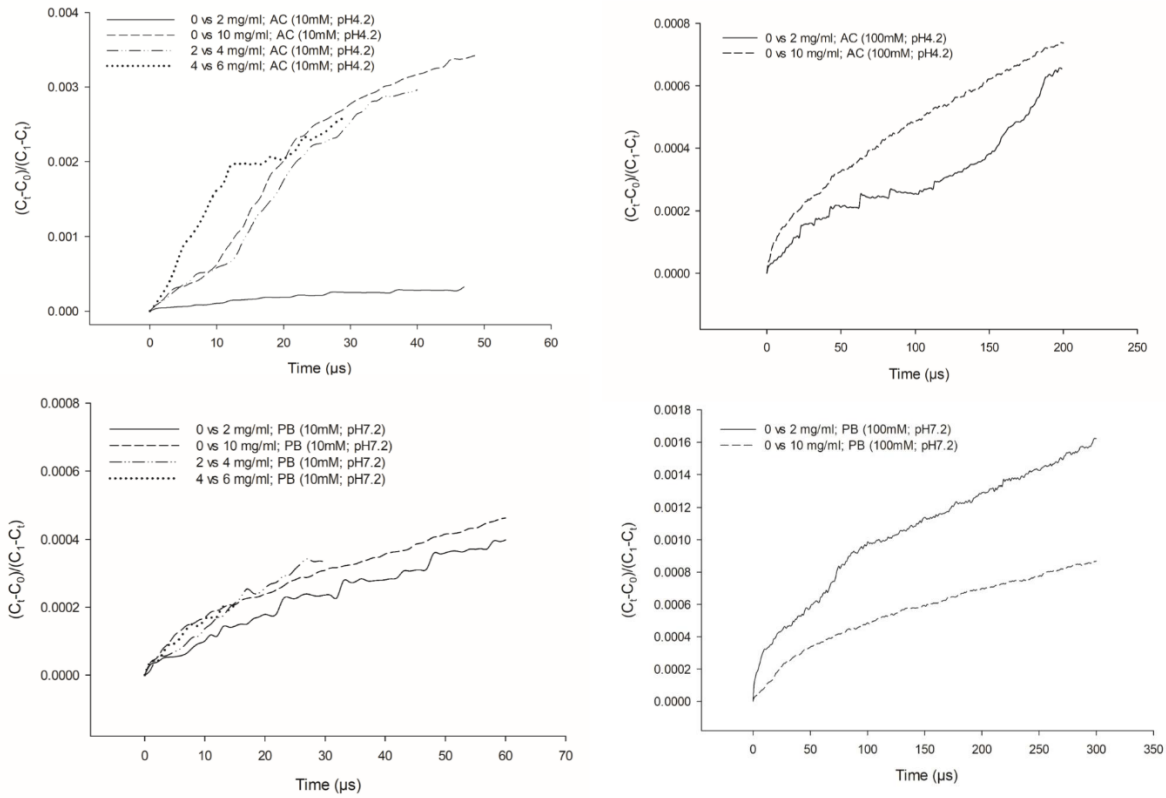
This simulation aims to describe the diffusion behaviour of protein molecules under practical microfluidics experimental conditions. However, due to the limit of computational power, the simulation geometry is unable to be fully in accordance with the practical geometrical dimension of the microfluidics device at full-time scale. Instead, a simplified simulation is conducted at a down-scaled geometry and a simulation period up to a few microseconds is performed. This period of simulation corresponds to the starting diffusion period under the working microfluidics experimental condition.

In the case of 0 vs X mg/ml (here X stands for the initial particle concentration in DD), “Bounce” wall condition is applied as the boundary condition except for the wall at the end of the RD domain (the wall at the left end), where a “Pass Through” wall condition is applied. As to the “Bounce” wall condition, the particles are reflected from the wall with conserving momentum. As to the “Pass Through” wall condition, the particles pass the boundary and disappear in the simulation. The dimensions of the DD and RD are $2000 \times 300 \times 70$ nm ($L \times W \times H$) respectively.

In the case of simulating particle diffusion at X_1 vs X_2 mg/ml (here X_1 and X_2 are non-zero values and stand for the initial particle concentration in the RD and DD respectively): “Bounce” wall condition is applied as the boundary wall condition. The dimensions of the DD and RD are $4000 \times 300 \times 70$ nm ($L \times W \times H$) respectively.

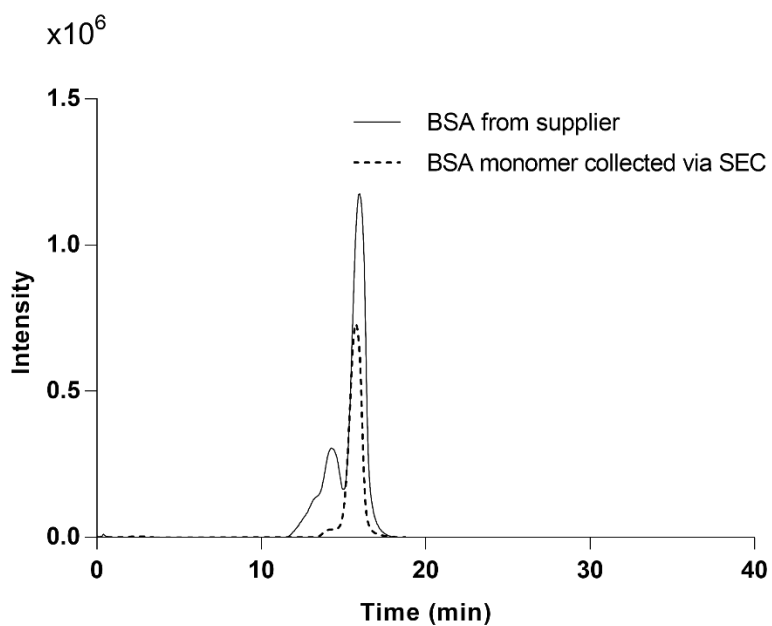
The density and diameter of the particles are set at 1120 kg/m^3 (based on the density of lysozyme solutions [1]) and 4 nm , respectively. The particle number concentration is calculated based on the mass concentration and molecular weight of lysozyme (14.3 kDa).

The particle transport from DD to RD (obtained from the simulation) is used to represent the particle transport in the case of full geometry.



AppxD-Figure 3. Particle tracing simulation results: concentration profiles as function of time *.

* Explanations later.



AppxD-Figure 4. Size-exclusion chromatogram of BSA obtained from the supplier, and the BSA monomer separated and collected via preparative size-exclusion chromatography (SEC). The monomeric BSA was separated using a Discovery BIO Gel Filtration column (Sigma–Aldrich, St. Louis, USA) with the LC-20AT LC pump and FRC-10A fraction collector (Shimadzu, Tokyo, Japan). Chromatograms were recorded with an SPD-20AV UV-Vis detector (Shimadzu, Tokyo, Japan) at a wavelength of 280 nm. The BSA obtained from the supplier was dissolved in PB (10 mM, pH 7.2) and applied onto the column at a flow rate of 0.5 ml/min. The collected monomeric BSA fraction was stored at room temperature for 24 h, remeasured by SEC and shown to maintain its monomeric character. The diffusion coefficient of the collected monomeric BSA was measured by H-cell microfluidics within 24 h.

AppxD-Table 1. Particle tracing simulation results *.

Simulation conditions	Slope of $\frac{C_t - C_0}{C_1 - C_t}$ as a function of t	
	Acetate buffer	Phosphate buffer
	(pH 4.2)	(pH 7.2)
0 vs 2 mg/ml protein; 10 mM buffer	7.6	7.3
0 vs 10 mg/ml protein; 10 mM buffer	82.1	8.8
2 vs 4 mg/ml protein; 10 mM buffer	81.2	12.6
4 vs 6 mg/ml protein; 10 mM buffer	105.4	15.6
0 vs 2 mg/ml protein; 100 mM buffer	2.9	6.3
0 vs 10 mg/ml protein; 100 mM buffer	4.3	3.4

* C_t represents the particle concentration in the receiver fluid domain at time t , C_0 the initial particle concentration in the receiver fluid domain, and C_1 the initial particle concentration in the donor fluid domain. The slope of $\frac{C_t - C_0}{C_1 - C_t}$ as a function of t represents the diffusion rate; the higher the slope value, the faster the particles diffuse. The slope is calculated by a linear trend line function (Excel 2016) with the y-intercept set to 0. These simulations are used to describe the diffusion behaviour of charged particles between the two domains at the starting period (up to a few microseconds).

AppxD-Table 2. The average recovery of the proteins in the streams passing through the H-cell, the standard deviation of triplicated measurements and the error of the calibration curve. Lysozyme (LYS) was tested in water, NaCl solution, PB (10 mM, pH 7.2) and AC (10 mM, pH 4.2) while the other proteins were measured in neutral PB medium (10mM, pH 7.2; except for etanercept in placebo buffer). Recoveries of about 100% are achieved for all proteins. In water, LYS shows a recovery of about 97% - 108%. The value higher than 100% is assumed to be due to the error given by the calibration curve for concentration determination. An error analysis of the calibration curve is also displayed. The recovery of LYS is not much influenced by the ionic strength and pH. For the other proteins, the recoveries also deviate slightly from 100%.

Protein	Medium	RS vs DS (mg/ml)	Average recovery	Standard Deviation	Error of calibration curve
LYS	H ₂ O	0 vs 2	96.7%	1.3%	1.8%
LYS	H ₂ O	0 vs 5	108.4%	0.3%	5.5%
LYS	H ₂ O	0 vs 10	103.4%	6.3%	4.6%
LYS	NaCl solution (10 mM)	0 vs 2	103.8%	3.3%	1.7%
LYS	NaCl solution (0.5 M)	0 vs 2	103.1%	1.2%	0.9%
LYS	NaCl solution (1 M)	0 vs 2	99.0%	0.6%	1.7%
LYS	PB (10mM pH7.2)	0 vs 2	109.1%	5.5%	3.1%
LYS	AC (10mM pH4.2)	0 vs 2	105.9%	2.1%	3.0%
CC	PB (10mM pH7.2)	0 vs 2	98.7%	4.3%	1.0%
MYO	PB (10mM pH7.2)	0 vs 2	107.1%	0.4%	5.0%
OVA	PB (10mM pH7.2)	0 vs 2	99.5%	1.7%	2.3%
BSA	PB (10mM pH7.2)	0 vs 2	103.1%	0.4%	0.9%
etanercept	Enbrel placebo buffer	0 vs 2	101.9%	2.8%	5.7%

Reference

1. Giordano, R., A. Salleo, S. Salleo, and F. Wanderlingh, Viscosity and density of lysozyme in water. *Physics Letters A*, 1979. **70**(1): p. 64-66.

Appendix E

Supplementary material for Chapter 8

FlowDensi 1.0

Convert csv database to matlab matrix

Calculation task
 Calculation of displacement rate
 Calculation of density

Optional plot
 Plot 1: x axis [v] y axis [v]
 Plot 2: x axis [v] y axis [v]
 Plot 3: x axis [v] y axis [v]

Parameters

Range of camera view (pixels)
 Left : 0 Right : Top : 0 Bottom :

Delta X
 Absolute (um)
 Relative (fraction)

Delta area
 Absolute (um²)
 Relative (fraction)

Delta AR
 Absolute
 Relative (fraction)

Delta Y
 Absolute (um) Relative (fraction) ~

Delta SIN Edge gradient
 ~

Med density (kg/m³)

Med viscosity (Pa*s)

Grav acc (m/s²)

Type of cell

Correction for wall effect
 Yes Drag coefficient
 No

Result export criteria
 Min number of dots per trajectory

 Coverage Y (absolute (um))
 Coverage Y (relative (fraction)) ~

Start !

Graphical user interface of *FlowDensi*

Experiment

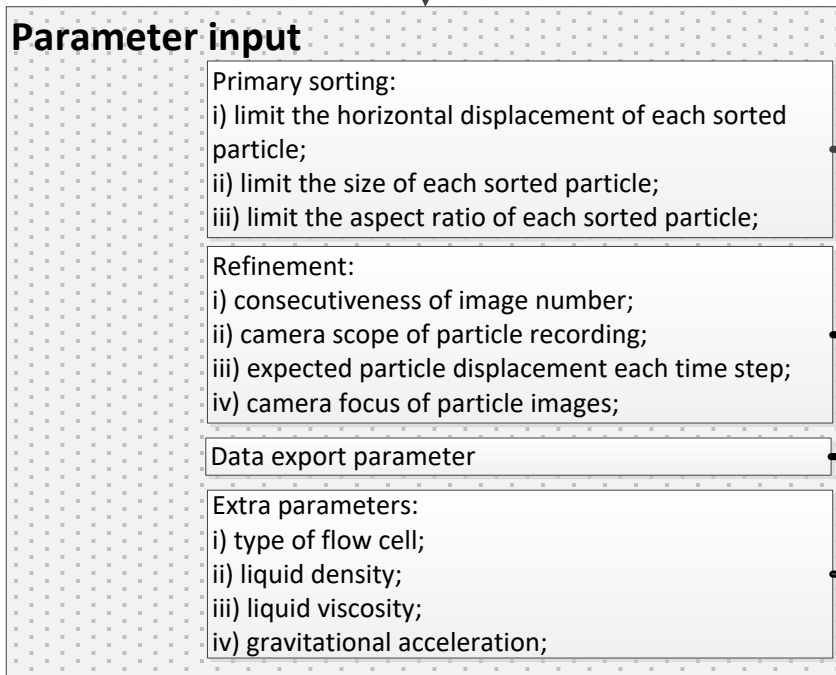
Preparation and equilibration of particle suspension

Particle displacement in stationay liquid

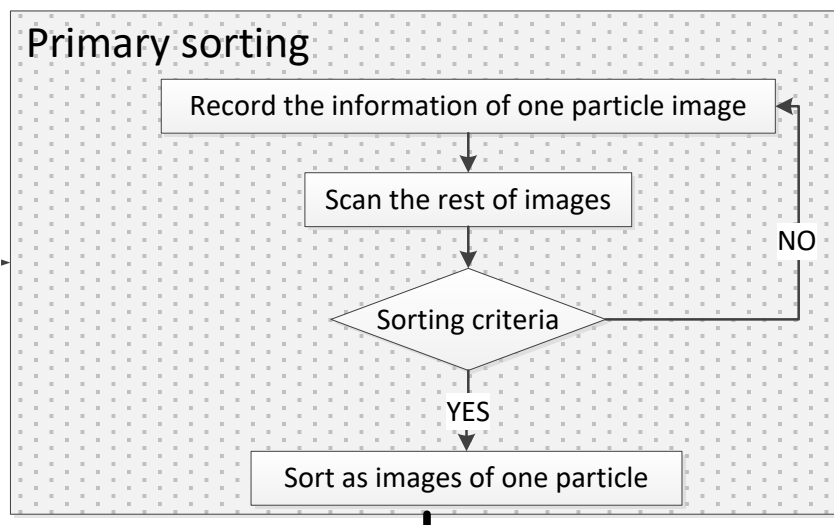
FlowCAM[®] imaging & recording

Export FlowCAM[®] data in CSV format;
 each row includes information of one of the images
 of a particle;

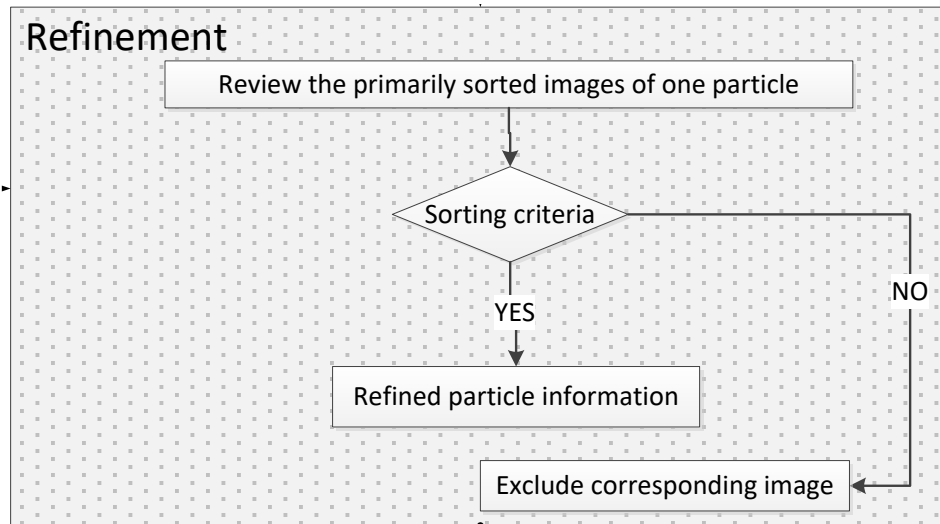
FlowDensi algorithm: Experiment section



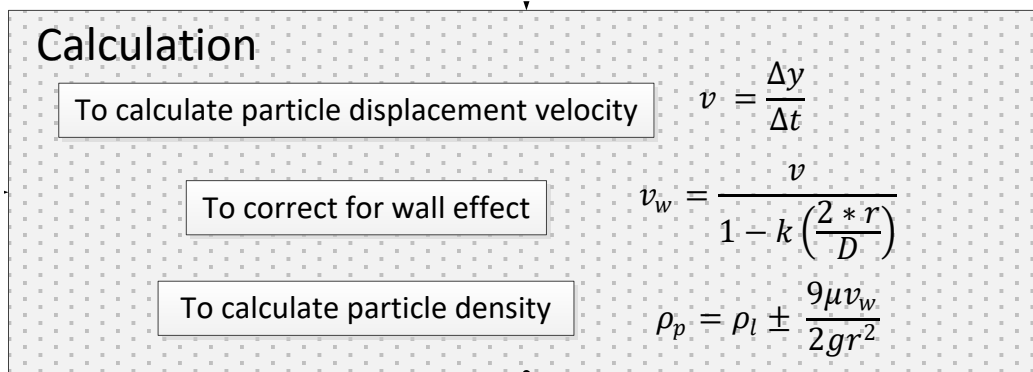
FlowDensi algorithm: Parameter input section



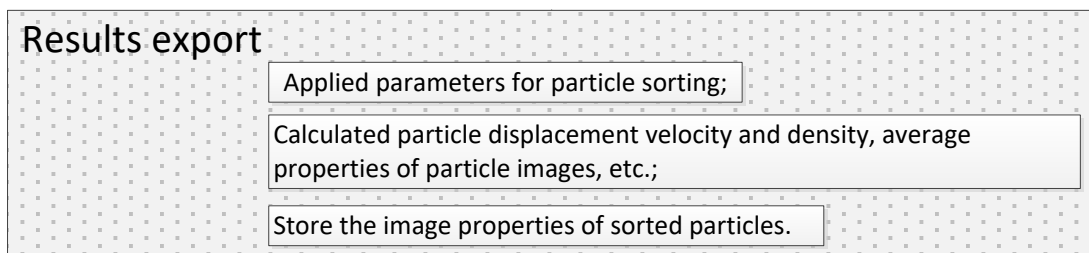
FlowDensi algorithm: Primary sorting section



FlowDensi algorithm: Refinement section

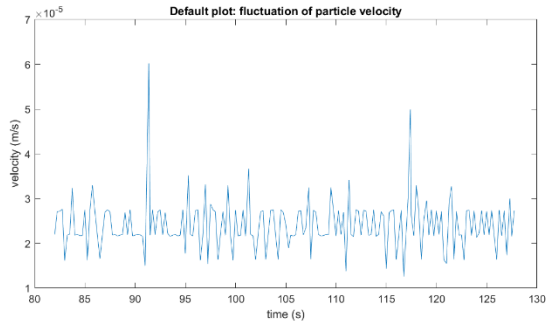
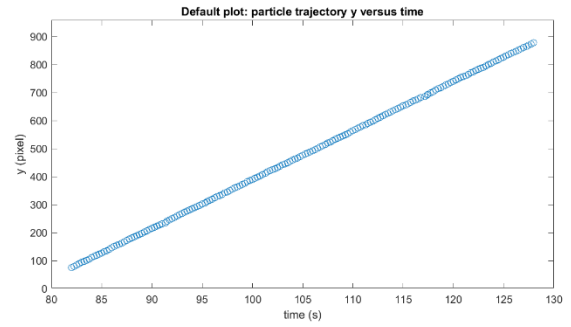
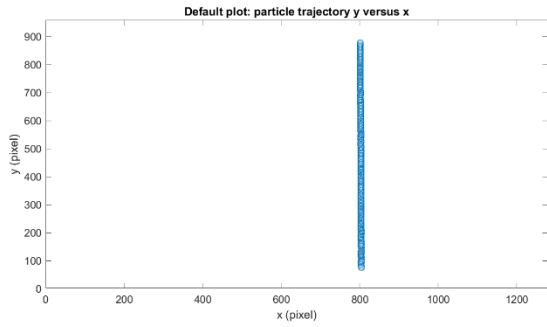


FlowDensi algorithm: Calculation section

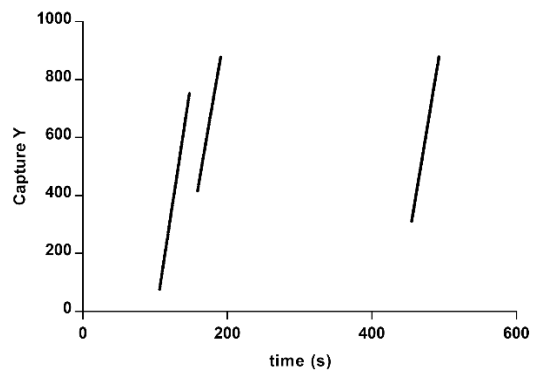
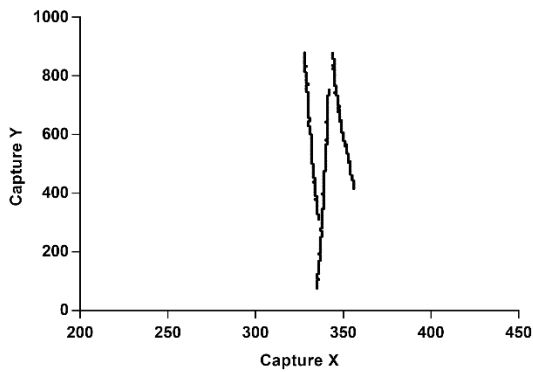


FlowDensi algorithm: Results export section

AppxE-Figure 1. Magnified view of the *FlowDensi* graphical user interface and the key sections of *FlowDensi* algorithm.



AppxE-Figure 2. Example of the plot of the data of a sorted particle exported by *FlowDensi*.



AppxE-Figure 3. An example of the mistaken consolidation of trajectories of particles obtained during primary sorting. This data is obtained via processing the 30 μm PS bead database with the *Delta X* of 40 μm , the *Delta area* of 0.15 (relative), the *Delta SIN* of 100, the *Delta Y* of 0-10 and the *Edge gradient* 0-255. All the particles in the graphs have similar x coordinates and size, and *FlowDensi* sorted them as one particle. However, the y coordinate as a function of time indicates that the sorted trajectory is composed of three particles' trajectories occurring at different time. Capture X and Capture Y represent the coordinates of the particles in the original FlowCAM[®] image.

Acknowledgement

How time flies! Finally, when I am almost at the end of my PhD study, I would like to show my heartfelt acknowledgement to all these people accompanying me during my PhD journey in the past several years.

First of all, I would like to express my gratitude to Prof. Geert-Jan Witkamp and Prof. Wim Jiskoot for offering me this opportunity to join this enthusiastic research group and work on this facilitating project. Thanks for your trust and giving me the freedom to do the scientific exploration. You have walked me through all the stages of my PhD research. Your patient instruction, expert guidance, insight criticism, and illuminating suggestions helped me overcome the challenges through the project and achieve the completion of my thesis. I also acknowledge my daily supervisor, Dr. Hayley Every, whom I closely worked with. I appreciate your instructive advice on my research and your detailed feedback for the improvement of my papers and thesis. Thanks also to my great colleagues and friends and brothers/sister, Dr. Reza Nejadnik, Dr. Ahmad Sediq and Dr. Onanong Nuchuchua, for your help in my experimental and thesis work, and for all the fruitful meetings with you. I also would like to thank Dr. Gerard Hofland. Although we did not have much time to communicate and discuss, I appreciate your guidance in the starting period of my PhD project. Also, my gratitude goes to STW, for providing financial support for this project, and to the STW users' committee members for their inputs and critical involvement in the project. My sincere thanks also go to Prof. Peter Verheijen, Prof. Wim Buijs, Dr. Cristian Piciooreanu and Dr. Marcel Ottens for your advice and help on particle agglomeration simulation, molecular modelling, multiphysics simulation and bioprocessing technology. The finalisation of my PhD project and the thesis could not have been achieved without your help.

Of course, I cannot forget the contributions from the MSc and BSc students to this project: Shiduo Zhang, Ruben van Duijvenvoorde, Andries van Opstal, and Tiago Castanheira Silva. It has been a great pleasure working with you in various interesting topics.

It would be impossible to perform experimental work without help from the technician and workshop support. I want to show my acknowledgement to the technicians, researchers and lab managers who gave me much support during my study. I thank Michel van der Brink, Jaap van Raamt, Aad Beeloo from the Process & Energy Engineering Department to provide support for my experimental work and for the lab relocation. Also Ben Abbas, Udo van Dongen, Yi Song, Max Zomerdijk, Stef van Hateren, Linda Otten from the Department of Biotechnology for your help on equipment build-up, experimental analysis and lab arrangement. Also Jeroen Koning, Ruud van Tol, Marcel Langeveld from DEMO for your help on the design of a new high-pressure reactor. Also Stefen Romeijn from the Division of Drug

Delivery Technology, Leiden University, for your great support on protein characterisation and analysis. Also the FeyeConers, Daniela Trambitas, Georgiana Ion, Reyes Menéndez González, Rob van der Veer and Gerben-Jan Boland from whom I received technical support on high-pressure equipment.

I would also like to extend my appreciation to the secretary groups for your kind help on administration issues: Leslie van Leeuwen, Eveline van der Veer, Ilona Holstein-Pouwels from the Process and Energy Engineering Department; and Miranda Verhulst, Kawieta Ramautar, Maita Latijnhouwers, Mieke van der Kooij from the Biotechnology Department.

I enjoyed the friendly working atmosphere in the last several years of my PhD study as there are many colleagues and friends to work with. It was a nice experience to work as a course assistant with Simon Feltz, Emma Korkakaki, Robin Schumacher, Leonie Marang, Helena Junicke, Gerben Stouten, with the help of Dr. Peter-Leon Hagedoorn, Dr. Adrie Straathof and Prof. Sef Heijnen. I would also thank my colleagues for questions, discussions, experience-sharing and I enjoy the time with you for meetings, cookies, cakes, lunch time and coffee breaks: Jure Zlopasa, Yaya Wang, Yimeng Bao, Ka Ying Florence Lip, Mario Pronk, Monica Conthe Calvo, Viktor Haaksman, Jules Rombouts, Danny de Graaff, Marissa Boleij, Mohammad Jafari, Maaïke Hoekstra, Hugo Kleikamp, Dmitrii Sorokin, Ingrid Pinel from the section of Environment Biotechnology; and Bianca Consorti Bussamra, Deborah Gernat, Joana Castro Gomes, Victor Koppejan, Monica Moreno Gonzalez, Shima Saffariopour, Rita da Costa Basto, Chema Jimenez Gutierrez, Joana P. Carvalho Pereira, Marcelo Henriques da Silva, Susana Pedraza de la Cuesta, Carlos Cabrera-Rodríguez, Silvia Pirrung, Erik Häusler, Karla Mayolo Deloisa, David Mendez Sevillano from the Bioprocess Engineering section. And all the others I cannot mention here, as the list would be too long.

I would also like to thank for the support from Dr. Rob van Haren and all the others from Hanze University of Applied Sciences during my research and thesis writing.

Finally, in this section, I would like to show my gratitude to my family. Thanks, Manna, for accompanying me during the last several years. Your optimistic attitude towards life inspires me to face any problems I encounter and to get rid of any depression and upset. Thanks, my mother and father, even though you are far away on the other side of the Europe-Asia continent, your unconditional support and prayer always give me the courage to move forward to take on challenges one by one in my life. Thanks also to my other relatives and friends for your support during the last several years.

List of publications

Journal publications

Miao Yu, Ahmad S. Sediq, Shiduo Zhang, M. Reza Nejadnik, Hayley A. Every, Wim Jiskoot, and Geert-Jan Witkamp, Towards the development of a supercritical carbon dioxide spray process to coat solid protein particles. *The Journal of Supercritical Fluids*, 141 (2018): 49-59.

Miao Yu, Hayley A. Every, Wim Jiskoot, Geert-Jan Witkamp, and Wim Buijs, Molecular structure of dextran sulphate sodium in aqueous environment. *Journal of Molecular Structure*, 1156 (2018): 320-329.

Miao Yu, Tiago Castanheira Silva, Andries van Opstal, Stefan Romeijn, Hayley A. Every, Wim Jiskoot, Geert-Jan Witkamp, and Marcel Ottens, The investigation of protein diffusion via H-cell microfluidics. *Biophysical Journal*, 116, (2019): 595-609

Miao Yu, Hayley Every, Wim Jiskoot, Geert-Jan Witkamp, and Wim Buijs, Molecular modelling of the interactions between lysozyme and dextran sulphate. Under preparation.

Miao Yu, Tiago Castanheira Silva, Hayley A. Every, Wim Jiskoot, Geert-Jan Witkamp, and Marcel Ottens, The determination of polyelectrolyte diffusion coefficients via microfluidic H-cell. Under Preparation.

Miao Yu, Ahmad S. Sediq, Ruben van Duijvenvoorde, M. Reza Nejadnik, Hayley A. Every, Wim Jiskoot, and Geert-Jan Witkamp, FlowDensi: a user-friendly Matlab-based toolkit for the density calculation of microparticles analysed by Flowcam®. Under preparation.

Conference contributions

Miao Yu, Ahmad S. Sediq, Hayley A. Every, M. Reza Nejadnik, Peter Verheijen, Wim Jiskoot, Geert-Jan Witkamp, Brownian dynamics simulation of protein-polyelectrolyte particle formation and growth. Poster, 30th Marian Smoluchowski Symposium on Statistical Physics, September, 2017, Krakow, Poland

Miao Yu, Ahmad S. Sediq, Shiduo Zhang, Hayley A. Every, M. Reza Nejadnik, Wim Jiskoot, Marcel Ottens, Geert-Jan Witkamp, Towards the development of controlled delivery systems for protein drugs by supercritical fluid processes. Oral presentation, Netherlands Biotechnology Conference, May 2017, Wageningen, the Netherlands

Miao Yu, Ahmad S. Sediq, Shiduo Zhang, Hayley A. Every, M. Reza Nejadnik, Wim Jiskoot, Geert-Jan Witkamp, Towards the development of controlled delivery systems for protein drugs by supercritical fluid processes. Oral presentation, 16th European Meeting on Supercritical Fluids (EMSF), April 2017, Lisbon, Portugal

Miao Yu, Ahmad S. Sediq, Hayley A. Every, M. Reza Nejadnik, Wim Buijs, Marcel Ottens, Wim Jiskoot, Geert-Jan Witkamp, Towards the development of controlled release protein drugs via a supercritical fluid process. Poster, BioDay symposium, March, 2017, Delft, the Netherlands

Miao Yu, Ahmad S. Sediq, M. Reza Nejadnik, Hayley A. Every, Wim Jiskoot, Geert-Jan Witkamp, Brownian dynamics simulation of protein-polyelectrolyte particle formation and growth. Oral presentation, 24th International Conference on Bioencapsulation, September 2016, Lisbon, Portugal

Miao Yu, Hayley A. Every, Wim Jiskoot, Geert-Jan Witkamp, Wim Buijs, Molecular structure of dextran sulphate. Poster, 21st European Symposium on Quantitative Structure-Activity Relationship, September 2016, Verona, Italy

Miao Yu, Ahmad S. Sediq, M. Reza Nejadnik, Hayley A. Every, Gerard Hofland, Geert-Jan Witkamp, Wim, Jiskoot. Supercritical carbon dioxide spray dried lysozyme-dextran sulphate complexes show ionic strength dependent release. Poster, Freeze Drying Conference: Freeze Drying of Pharmaceuticals and Biologicals, September, 2014, Garmisch-Partenkirchen, Germany

Curriculum Vitae

Miao Yu was born on 10 August 1988 in Qufu City, Shandong Province, China. After he finished his university education in 2010, he came to Wageningen University for the MSc study in Environmental Sciences. For his MSc thesis, he worked on the development of an energy storage system based on electro dialysis and reverse electro dialysis techniques. Afterwards, he did an internship at Wetsus (Center of Excellence for Sustainable Water Technology), where he investigated the influence of foreign ions, antiscalant and ultrasound on calcium carbonate crystallisation, towards the development of a technique to detect scale formation in drinking water treatment equipment. From 2013 onwards, he started working as a PhD candidate at the Department of Biotechnology, Delft University of Technology, under the supervision of Prof. Dr. Geert-Jan Witkamp, Prof. Dr. Wim Jiskoot and Dr. Hayley Every. He worked on the project 'Controlled release of protein pharmaceuticals from biodegradable, hydrophilic microcapsules produced by supercritical fluid processing' with the research purpose of developing a controlled drug delivery system for proteins via supercritical carbon dioxide processing. From November 2017, he is working as a postdoc researcher at Hanze University of Applied Sciences, Groningen, the Netherlands.

